Experimental Assessment of Charge Flow in Electrospinning

A thesis submitted in partial fulfilment of the requirements for the Degree of

Doctor of Philosophy in Mechanical Engineering

to the Department of Mechanical Engineering

University of Canterbury

by

Jonathan Jeffrey Stanger

2013

Supervisors:

Dr. Mathieu Sellier

Dr. Nick Tucker

Dr. Mark Staiger

Dr. Alan Wood

Overcome with giddiness he flew too close to the sun

~Myth of Icarus

I'm going down in a blaze of glory

~Bon Jovi

I. Table of Contents

II. Acknowledgments

I would like to thank Dr. Mathieu Sellier, Dr. Nick Tucker, Dr. Mark Staiger, and Dr. Alan Wood for their supervision and support of this work. You encouraged me in the good times and supported me through the hard times. When the will to continue began to fail you all lent me your support. For funding and hosting my research I would like to thank the Foundation for Research, Science and Technology (FoRST), University of Canterbury, Dr. Nigel Larsen and The New Zealand Institute for Plant & Food Research Limited, and Dick and Mary Earle. The generous funding from the Foundation and Plant & Food Research allowed me to briefly taste what living on a real wage was like. When financial times were hard Dick and Mary Earle were kind enough to offer me an additional scholarship beyond what they normally provide that demonstrated their belief in me and this work. This money made a world of difference at just the right time.

I would like to thank Neil Buunk and Simon Fullick for providing the apparatus is used in this thesis and gathering experimental work respectively. I would like to thank my parents Paul and Jill Stanger and my wife Tingyi Lee Stanger. Without the near-infinite support of my wife this thesis may have never made it to completion. This thesis is dedicated to the memory of my nanna, Dulcie Elizabeth Stanger who recently passed away. It was her dream that I would follow in the footsteps of her youngest son, my uncle, and complete the highest level of education possible.

Finally I would like to thank the remaining members of the Electrospinning team, Pablo Lepe, Nurfaizey Hamid, and Deborah Le Corre for being available for intense discussions regarding this work and all my friends and family for their continuedous support.

III. Abstract

Electrospinning is a method of using high voltage electric fields to transform polymer solutions into nano-scale fibres. The field has seen significant work on processing different polymers and their resulting fibres but less work has focused the electrospinning process itself. The aim of this thesis is to present experimental observations of charge behaviour in the electrospinning process in the context of the underlying physics typically used to describe electrospinning. This thesis presents a review of existing methods of measuring aspects of the electrospinning process, and reviews published mathematical models of the process as representative examples of the current understanding of the underlying physics that drive the electrospinning phenomena. A novel measurement technique is introduced — high frequency data capture of the electric current flow simultaneously at the high voltage and collector electrode. This is used in three ways: to examine bulk charge density, to measure fibre flight time, and to quantify charge lost from the fibre in flight. Charge density is studied by comparing current and mass flow at the Taylor cone under a wide range of conditions. For 8% PVOH in water a constant bulk charge density was found of 7.7 C/kg. Flight time is studied by determining the time from the application of high voltage to the charged fibre first arriving at the collector electrode. It was found that for 8% PVOH the flight time depended strongly on applied voltage while electrode distance had a negligible effect. Charge loss was studied by comparing the magnitude of the simultaneous current flows in the quasi-steady state to determine if the charge flowing into the Taylor cone arrives with the fibre at the collector. For 8% PVOH, 8% PVOH with ionic salt, 9% PVOH in water and 18% PVB in ethanol, it was found that charge is always lost.

IV. Glossary of Symbols Used

Electrical

Symbol	Description	Units
E	Electric field	$\left[{}^{V}/_{m}\right]$
ϕ	Voltage	$[V]$
q	Electric charge	$[C]$
α_q	Linear electric charge density	$\left[{}^{C}/_{m}\right]$
δ_q	Surface electric charge density	$\left[{}^{C}/_{m^2}\right]$
ρ_q	Volume electric charge density	$\left[{}^{C}/_{m^3}\right]$
I	Electric current	$\left[{}^{C}/_{s}\right]$
σ	Fluid conductivity	$\left[{}^{S}/_{m}\right]$
ϵ	Dielectric constant	

Dimensional

Symbol	Description	Units
d	Distance	$[m]$
ℓ	Length	$[m]$
r	Radius	$[m]$
x, y, z	Cartesian co-ordinates	$[m]$
χ	Aspect ratio	
V	Volume	$[m^3]$
A	Area	$[m^2]$
t	Time	$[s]$
κ	Curvature	$\left[{}^{1}/_{m}\right]$
ω	Frequency	$\left[{}^{1}/_{s}\right]$

Physical

Symbol	Description	Units
m	Mass	$[kg]$
γ	Surface tension	$\left[{}^{N}/_{m}\right]$
Q	Mass flow rate	$[kg/s]$
v	Fluid velocity	$\left[{}^{m}/_{s}\right]$
g	Acceleration due to gravity	$\left[{}^{m}/_{s^2}\right]$
G	Modulus	$[Pa]$
η	Viscosity	$[Pa \cdot s]$
η_0	Zero shear rate viscosity	$[Pa \cdot s]$
λ	Relaxation time	$[s]$
p	Internal fluid pressure	$\left[{}^{N}/_{m^2}\right]$
ρ	Fluid density	$[kg/m^3]$
τ	Stress	$\left[{}^{N}/_{m^2}\right]$
F	Force	$[N]$

CHAPTER 1

INTRODUCTION

1 Introduction

The electrospinning process is a low-cost, continuous method of producing nano-scale material. It has wide ranging applications as a technology to fill the materials size gap between traditional microfibers and carbon nanotubes. Electrospinning has also been shown to be able to process a wide range of materials and shows promise for biopolymers as it does not require extreme pH, temperatures or pressures that can damage sensitive molecules. To date much work has focused on exploring different materials that can be processed by electrospinning and studying the resulting fibres. However, there is a lack of work exploring the electrospinning process itself which adds to the challenges faced in the transition from the laboratory to industry.

The aim of the work presented in this thesis was to explore some of the as-yet untested assumptions about the phenomenon of electrospinning. To demonstrate the implications of the conclusions drawn from this exploration, they will be presented in the context of a generalized discussion of the electrospinning phenomenon, including existing literature. There are three assumptions tested in this thesis. First, that the charge carried by the electrospinning fluid depends on processing conditions such as applied voltage or electrode distance. Second, that the flight time of the electrospinning jet also depends on the processing conditions of applied voltage and electrode distance. Last, assuming there is no visible corona discharge, that while in flight the jet can be considered a closed system with respect to charge conservation (i.e. that there is no interaction between the environment and the jet in terms of charge flow).

Chapter 2 provides a general literature review of the electrospinning process and established techniques for measuring aspects of the process. The novel work in this thesis is a high-speed measurement technique that allows for quantitative observation of aspects of the electrospinning process. Chapter 3 reviews generalized mathematical models of the electrospinning phenomenon. These models are discussed in detail to summarize the present state of understanding of the electrospinning phenomenon. Much of the existing literature focuses on specialized cases with only limited attempts at describing the underlying physical mechanisms that govern the electrospinning process. Discussion of these models is broken into the 1D axisymmetric region and the 3D quasi-stable whipping instability region. For each region, the underlying physics is presented without describing the numerical methods used to solve the model. This is followed by a critical appraisal of refinements that have been proposed in literature. While accounting for solvent loss results in the conservation of mass being realistically satisfied, there have been no attempts to address the presence of corona discharges, the existence of which demonstrate that electrospinning is not a closed system for charge as well as mass.

Chapter 4 introduces the technique used throughout this thesis to test the above mentioned assumptions. This technique is the use of high frequency data capture of the electric current flow simultaneously at the high voltage and collector electrode. Two alternative methods of measuring the electric current at the high voltage electrode were compared with the high frequency data capture. It was found that the results were comparable but lacking in both the detail and efficiency provided by the data capture method. There is no previously reported example of measuring the electric current at the high voltage electrode known to the author[1]. This measurement technique could be used as a feedback signal for industrial automation of electrospinning when used in context of the results presented in this thesis. Chapter 5 demonstrates the failure of the parallel plate approximation of electric field conditions to predict an outcome in electrospinning using the data obtained in Chapters 4 and 6.

Chapter 6 uses the data capture technique to examine the flow of both mass and charge at the Taylor cone under a range of electric field conditions. The electric field is varied by using different combinations of the applied voltage and electrode distance. From the flow of mass and the flow of charge a bulk charge density can be determined. Chapter 7 uses higher frequency data capture to estimate the flight time of the electrospinning jet by measuring the time from applying power to the impact of the jet arriving at the collector. This estimation is validated by high speed video demonstrating that jet initiation time is approximately constant and jet initiation forms a similar flight path to that formed in the quasi-steady state of electrospinning. Chapter 8 takes advantage of the ability to make measurements at both the high voltage and collector electrode to examine the flow of charge from one electrode to the other. This is done when the jet is in the quasi-steady state under conditions that do not produce visible or audible corona discharges. A total of 234 different combinations of applied voltage and electrode distance were examined from conditions just above jet initiation to just below corona discharge onset. This allowed the quantification of any charge flow from the jet into the surrounding environment. A set of four different solutions were used to examine how any charge loss might be affected by changes to viscosity, conductivity or non-aqueous solvents.

Chapter 9 revisits the review presented in Chapter 3, providing a qualitative discussion of the underlying physical mechanisms that govern the electrospinning process. The aim is to provide an exhaustive qualitative description of the electrospinning process with sufficient detail so that models may be improved but limited to not offering specific methods to solve the physics for predictive

[1] **The concept of measuring the current at the high voltage electrode was originally proposed to us by its originator Prof. nzw. dr hab. inż. Tomasz Ciach of the Wydział Inżynierii Chemicznej i Procesowej Politechniki Warszawskiej. Prof. Ciach's method used a floating current measurement module that transmitted the analogue current flow data by an LED-photo-diode pair optical link.**

purposes. Specific attention is paid to the consequence of charge loss and its impact on the formation of electrospun fibre. This is important as the forces due to the charge carried by the fibre are the main difference between electrospinning and traditional fibre forming techniques. The detailed description of the electrospinning process along with the electric current measurement provides a technique that can be used as a feedback signal, and so this thesis forms another step towards proper control in the industrial manufacture of electrospun fibre. Chapter 10 provides a brief concluding summary of the results presented in this thesis.

The novelty of the work described is that, for the first time, the relationship between charge flow, mass flow, applied voltage and electrode distance has been quantified by high speed data capture and high speed imaging at various points in the electrospinning process and thus a new contribution to the understanding of the process has been made. These quantified measurements allow for the validation of existing and future theoretical models proposed to describe the process. In practical terms, the techniques developed here have already begun to be applied to industrial process control for the production of high quality electrospun fibre. Specific cases of these applications are the development of a system for automatic detection of electrospinning and in the development of methods to use auxiliary electric fields to influence the flight path of electrospun fibre.

CHAPTER 2

LITERATURE REVIEW

2 Literature Review

2.1 Electrospinning – An Introduction

Electrospinning is a method using high voltage electric fields to transform polymer solutions into nano-scale fibres. Fibre diameters range from ~10 nm to over 5 µm (Costolo et al., 2007, Pham et al., 2006). Fibres can be electrospun from a polymer melt or solution. There are fibre-forming solutions for many synthetic and naturally occurring polymers (Stanger et al., 2009b). All electrospinning apparatus depends on an electric field set up between two electrodes. Typical electric field strengths required for electrospinning are on the order of 1 kV/cm when estimated using the parallel plate approximation (Stanger et al., 2009b). Typically one electrode is a narrow tube or spinneret connected to a polymer supply and the other electrode acts as a collector for the fibres. The polymer solution or melt can be supplied to the spinneret using a constant pressure or constant flow rate system. The shape formed by the polymer droplet at the end of the spinneret was first described in detail by Sir Geoffrey Taylor and hence has become known as the Taylor cone, with Figure 1 being a typical example (Taylor, 1969). The shape of the Taylor cone is due to a combination of the surface simultaneously being driven towards a surface maximizing hemispherical shape and a surface minimizing conical shape.

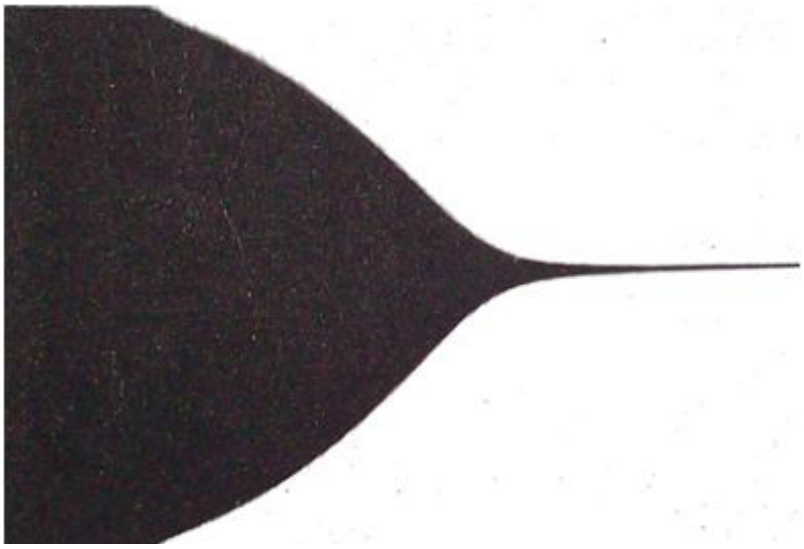

Figure 1: The original Taylor cone (Taylor, 1969).

Some systems favour constant pressure as it directly balances the forces that form the Taylor cone, whereas others favour a constant flow rate where the replenishment rate of the meniscus and Taylor cone must be matched to the loss of material by fibre production. The Taylor cone evolves upon application of a suitable electric field, where the small radius of curvature tip of the cone allows for sufficient concentration of electric stress that liquid is ejected from the cone to form a freely suspended fluid jet (Reznik et al., 2004). This jet undergoes a thinning process due to the external electric field and the surface charges carried by the jet. The thinning process is axisymmetric

for a short distance until the jet becomes unstable and takes on the characteristic whipping (also known as bending) instability. This instability is one that is quasi-stable as despite the random path the jet takes, the zone of space this path lies within is relatively constant, similar to the behaviour of an electron in an atomic orbital. Examples of the random nature of the jet path have been described in the literature (Shin et al., 2001a), with a full colour example given in Figure 2.

Figure 2: Typical Jet Path (Photo Credit: Robert Lamberts, Plant & Food Research, New Zealand).

As the jet travels through space, solvent (or heat in the case of a polymer melt) is lost, leading to the jet eventually becoming a solid polymer fibre. At this stage the rate of thinning is expected to decrease due to an increase in mechanical strength. These fibres are often collected on the opposite electrode to the one that is connected to the polymer supply as the fibres are naturally attracted to this electrode. In the simplest form the fibres are collected in a circular mat (Yang et al., 2009) which is expected to steadily decrease in density as one moves further from the axis of symmetry (Buchko et al., 1999). Typically the tip to collector distance (TCD) is chosen such that dry/solid fibres are collected. If the TCD is too short, fibres will coalesce where they are in contact with each other forming a porous film rather than a fibre mat such as seen in Figure 3 (Hong et al., 2006). Other fibre morphologies are also possible such as beads on a string (Fong et al., 1999), ribbon (Koombhongse et al., 2001) and hollow (Li et al., 2004) with examples shown in Figure 3.

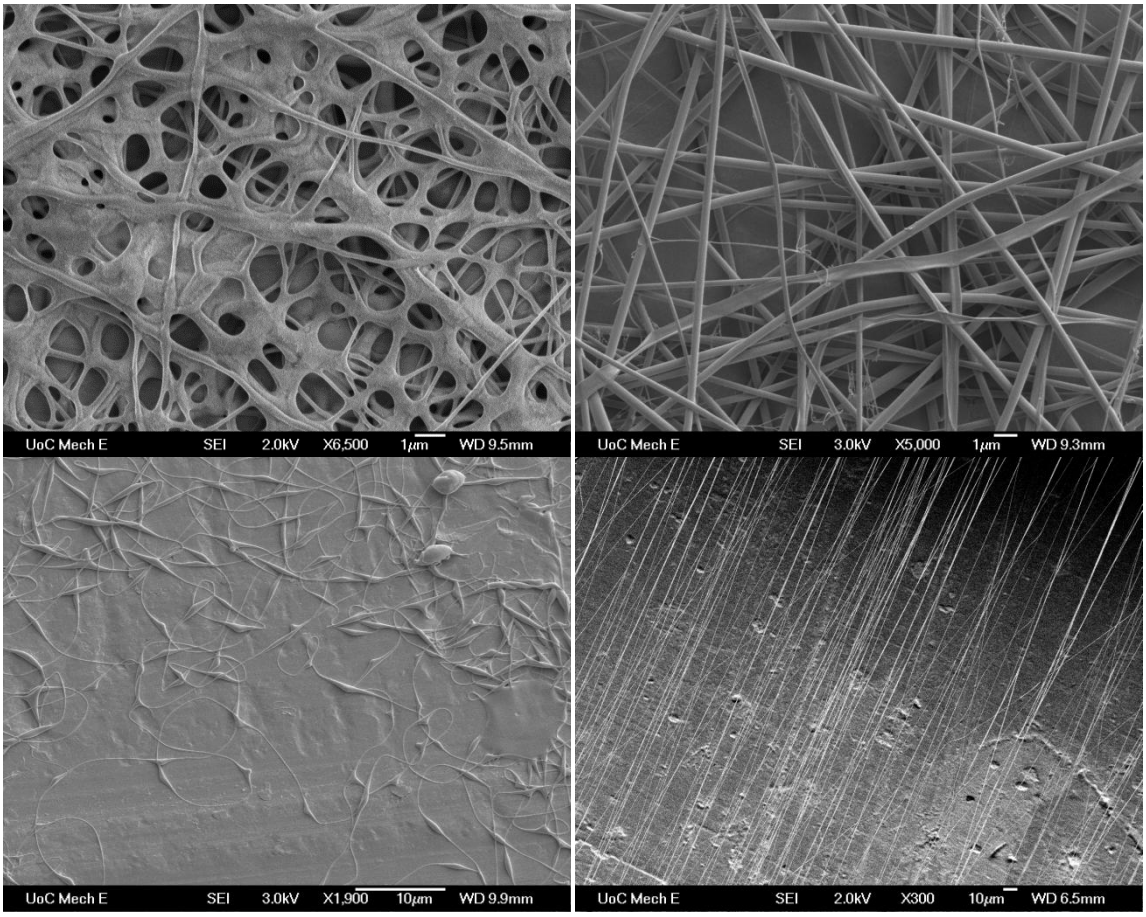

Figure 3: Wet electrospun fibre deposition morphology and other morphologies from Plant & Food Research. Top left: Wet fibres, Top right: Ribbon morphology, Bottom left: Beaded fibre morphology, Bottom right: Aligned fibre morphology

2.1.1 History

Electrospinning and the study of electricity interacting with fluids have a long history. The earliest known mention of electrospinning is by Charles Vernon Boys in 1888 who described the process as "the old, but little known experiment of electrical spinning" (Boys, 1887). Unfortunately, the polymers available at that time were unable to provide him with a suitable fibre for the construction of the torsion balance he was building. The earliest patent known to describe electrospinning was by John Frances Cooley in 1900 (Cooley, 1900). His sequence of patents describes a conventional electrospinning spinneret, a co-axial spinneret, an air assisted spinneret and a rotating spinneret. Later, between 1907 and 1920, John Zeleny studied the effects of strong electric fields on fluid surfaces (Zeleny, 1907, 1917, 1920). His systematic work began the theoretical study of electrospinning and electrospraying. During the period leading up to and during the Second World War a German inventor named Anton Formhals filed 22 patents covering many aspects of the process (Formhals, 1934, 1937, 1938, 1943, 1944). Formhals proposed innovations such as a rotating saw toothed spinneret, a tapered nozzle spinneret and the collection of fibre staples. His designs also proposed the use of coagulation baths to assist solidification, the use of external electric fields to manipulate fibres in flight and the co-spinning of oppositely charged fibres. In 1938 two Russian

scientists Igor' Vasil'evich Petryanov-Sokolov and Natalya D Rosenblum developed an electrospun filter material known as Petryanov filters (Filatov et al., 2007). These filters represent the earliest known commercial success of electrospun fibre. The scale-up to production level was rapidly undertaken in a factory in Tver' which produced a gas mask filter for smoke protection and later the Lepestock (Petal) filter for use as personal protection by aerosol removal in the nuclear industry. Sir Geoffrey Ingram Taylor spent the final years of his life (the period from 1964 to 1969) furthering the theoretical description of the electrohydrodynamic processes that result in the formation of liquid jets (Taylor, 1964, 1966, 1969). His work attempted to describe the shape adopted by the liquid droplet in the presence of electric fields by considering the forces of internal fluid pressure, surface tension and mobile charges in a fluid. His work resulted in the shape of the droplet being named after him. A more complete and detailed history of electrospinning can be found elsewhere in literature (Tucker et al., 2012).

2.1.2 Applications

The products of electrospinning find applications due to a small number of important properties: high aspect ratio, high surface area to volume ratio, micro- to nano-scale fibre diameters and good molecular orientation. These properties lead to important potential applications in the biomedical field such as tissue engineering, regenerative medicine, bioremediation, biosensors, genome analysis, drug delivery and wound dressings. Electrospun fibre also finds potential applications in the emerging nanomaterials industry such as air and water filtration, long fibre composites, super hydrophobic surfaces, self cleaning surfaces, antifouling coatings, stain resistant textiles, transparent composites and catalytic membranes. There are also numerous applications in the electronics industry such as high capacity lithium ion batteries, super capacitors, transparent electronics, gas sensors, solar and thermal energy generation and thermal dissipation. A more detailed discussion of some of these applications follows in the next sections.

2.1.2.1 Biomedical

Coaxial electrospinning has been used for encapsulation, both of living cells (Klein et al., 2009, Townsend-Nicholson et al., 2006) and enzymes (Dror et al., 2008). It has been shown that living cells in a suitable medium can survive the electrospinning process when encapsulated in this way (Townsend-Nicholson et al., 2006). Culturing the resulting cells showed no significant detrimental effect either in short-term viability or long-term morphology changes. This technique was further developed to produce porous microtubes by blending with poly(ethylene glycol) (Klein et al., 2009). This process immobilized cells while maintaining their ability to enzymatically interact with an aqueous environment. The same porous fibres were used to encapsulate enzymes (Dror et al., 2008). It was found that the pore size could trap large enzymes within the hollow fibre while

allowing small molecules (i.e. small enzymes or reactants) to pass through the shell. Blending of multiple polymeric fibres into a cross-linked tubular structure allowed McClure et al. (2012) to create biomimetic vascular grafts. These grafts could function as a tissue scaffold while also replicating the mechanical properties of native artery tissue. This was achieved by replicating the tri-layered structure of native artery tissue using different blends of bioresorbable polymers (McClure et al., 2012). It has been suggested that the axial stretching of the electrospinning jet could be used for genomics applications (Bellan et al., 2006b). Embedding DNA molecules in a poly(ethylene oxide) matrix would allow the study of the DNA molecule at a later date. This opens up possibilities for new sequencing techniques and characterization of the elastic properties of sections of DNA.

2.1.2.2 Materials

The inclusion of sulfonated polyimide electrospun fibres into a solid membrane of the same material improved the proton conductivity of the membrane (Tamura et al., 2010). The inclusion of 10% by weight aligned nanofibres increased the cell voltage and power density at high current densities. One direct use of electrospun ceramic nanofibres is for the catalytic generation of hydrogen gas from water (Chuangchote et al., 2009). It was found that TiO_2 nanofibre ground into a power was superior in performance to commercially available TiO_2 powder (Ishihara ST-01). These photocatalytic materials have potential use as high-surface area catalytic filters or as textiles with self cleaning, antibacterial or photochromic properties (Lombardi et al., 2011). The calcination process used to make ceramic fibres can also be used to create superhydrophobic silica fibres (Lim et al., 2007). By including silica nanoparticles (50 nm and/or 700 nm) with a polymer carrier and calcinating the resulting fibres, a fabric can be produced that has a contact angle of over 150^{o} and a sliding angle of less than 2^{o}. To achieve this, the fibres were plasma coated with a fluorinated monomer while exploiting the electrospinning process to produce a suitable microstructure.

Electrospun fibres offer potential benefits due to their intrinsic size. Nylon-4,6 electrospun fibres with diameters in the range of 50–200 nm are smaller than photons in the visible light spectrum (400–700 nm) (Bergshoef et al., 1999). Adding less than 5% wt of these fibres to an epoxy matrix allowed the creation of a transparent composite sheet which showed a Young's modulus over 30 times that of unreinforced epoxy and improved fracture strength (Bergshoef et al., 1999). The fibre addition did, however, decrease the elongation at fracture. Similar results were seen with electrospun polybenzimidazole (PIB) fibres in an epoxy matrix where the Young's modulus and fracture energy increased with increasing fibre content (Kim et al., 1999). These fibres at 15% by wt also outperformed commercially available PIB whiskers at 17% wt. Using a chopped electrospun fibre reinforcement (at a level of 10 parts per hundred) in styrene-butadiene rubber increased the Young's modulus by ten times and doubled the tear strength (Kim et al., 1999). This is a significant

improvement compared with a conventional filler (e.g. carbon black at 10 parts per hundred) which is only able to double the Young's modulus.

2.1.2.3 Electrical

Depositing electrospun fibres composed of a blend of poly(vinyl acetate) and poly(acrylic acid) on quartz crystal microbalances enabled the production of a usable NH_3 gas sensor (Ding et al., 2004). By tuning the blend composition a sensor could be produced that was fully reversible and could clearly detect gas concentrations at 50 ppm. The use of electrospun fibre for sensor applications is desirable as the increased surface area to volume ratio compared with thin films increases sensitivity (Wang et al., 2002). Using a membrane composed of poly(acrylic acid)-co-poly(pyrene methanol) showed a 2 to 3 order of magnitude increase in sensitivity when detecting metal ions or nitro aromatic compounds (Wang et al., 2002). This gives a practical sensitivity in the range of 10 ppb.

Electrospun fibre has been shown to be a suitable material to increase the surface area of dye-based liquid-junction photovoltaic cells (Drew et al., 2002). Electrospun fibre was compared with spin-coating as a method of depositing a polymer/chromophore blend membrane that forms one electrode. It was found that the increased surface area of the electrospun fibre resulted in a higher current flow per concentration of Congo Red dye (Drew et al., 2002). A similar process using Ruthenium-based dyes and calcinations of polymer/titanium isopropoxide composite fibres produces a dye-loaded metal oxide fibre-based photovoltaic cell (Onozuka et al., 2006). Without process optimization the efficiency was found to be 4.2% compared with an optimized nanocrystalline-TiO_2 matrix which achieved 10%. Similar ceramic fibres have also been demonstrated to be capable of the conversion of thermal energy into specific wavelengths of light (Tomer et al., 2005). This could have application in thermo-photovoltaics for harvesting power from waste heat. The technique of converting electrospun fibre into nano-scale ceramics has also found use in the field of lithium ion batteries (Wang et al., 2012). It was found that compared with a bulk $Li_2CoTi_3O_8$ ceramic particle (~400 nm in size), calcined electrospun fibres (~300 nm in diameter) performed at close to theoretical capacity for low discharge currents. Even at high discharge currents of 2000 mA/g the calcined electrospun fibre retained almost 30% higher storage capacity.

2.2 Variables Controlling the Electrospinning Process

In traditional electrospinning, numerous parameters (Stanger et al., 2009b) have been identified as affecting the final properties of the electrospun fibre. Parameters that influence the electrospinning process can be broken down into three categories:

- *environmental conditions* that are dictated by atmospheric and local processing environment parameters;

- *solution parameters* that are dependent on the properties of the solution used as the feedstock; and
- *processing parameters* that are associated with the design, geometry and operation of the electrospinning apparatus.

Table 1 is a list of commonly quoted parameters. This list excludes parameters that are specific to more exotic electrospinning methods. It should be noted that these parameters cannot be viewed as entirely independent as interaction effects are prominent (Patra, 2010, Patra et al., 2009a, 2009b, 2010a, 2010b).

Table 1: Processing parameters that are known to affect the electrospinning process (Stanger et al., 2009b).

Solution parameters	Process parameters	Environmental conditions
Concentration	Electrostatic potential	Temperature
Surface tension	Electric field strength	Atmospheric composition
Conductivity	Electrostatic field shape	Local atmosphere flow
Dielectric constant	Working distance	Atmospheric pressure
Solvent vapour pressure	Mass flow rate	Humidity
Polymer entanglement	Fluid pressure	
Viscoelastic properties	Charge flow rate	
	Orifice diameter	

2.2.1 Environmental Parameters

Environmental parameters can be divided into those that relate to the local spinning conditions or properties of the atmosphere in which the spinning process takes place. Many do not directly affect the electrospinning process but act to modify the solution parameters.

2.2.1.1 Temperature

The temperature of the atmosphere and the electrospinning solution/melt affects the final fibre properties. There is evidence that this is not due to an intrinsic interaction of electrospinning and temperature but as a result of the material properties changing in response to temperature (Cooley, 1902, Kim et al., 2006, Kong et al., 2008, Pakravan et al., 2011). Increasing temperature typically reduces the viscosity of a flowing polymer melt or solution which appears to result in a decrease in fibre diameter (Kong et al., 2008, Pakravan et al., 2011). For melt electrospinning this applies to both the initial melt temperature and the temperature of the atmosphere (Kong et al., 2008). The decrease in fibre diameter was far larger when the atmosphere temperature was changed from the initial melt temperature which indicates that for melt electrospinning the freezing time is probably more important that melt viscosity (Kong et al., 2008). Solution electrospinning showed a similar response to initial solution temperature increasing; however, above a certain temperature the trend reversed (Pakravan et al., 2011). This is probably due to the added complexity of temperature interaction with both evaporation rate and surface tension (Pakravan et al., 2011). When a solvent is heated the rate of evaporation increases, effectively behaving like a more volatile solvent, which

results in a shorter drying time for electrospun fibre. The shorter drying time can help with low vapour pressure solvents (Kim et al., 2006). This can equally create a problem as solvents with a high vapour pressure can evaporate fast enough to clog the spinneret due to the Taylor cone forming an unspinnable solid skin (Cooley, 1902, Kim et al., 2006). Some polymer solutions show the additional complexity of changing surface tension with increasing temperature which in addition to changing fibre diameter can also introduce or remove beading behaviour(Pakravan et al., 2011), where fibres are formed with significant variation in thickness, resembling a string of beads.

2.2.1.2 Atmospheric Composition and Local Atmosphere Flow

It is possible to introduce a local flow of gas saturated with the solvent around the cone to prevent evaporation at the cone (Larsen et al., 2004). Electrospinning within a dry gas has also been used to control the evaporation rate of the solvent in the jet (Buchko et al., 1999). A flow of pressurized air has been used to improve the formation of electrospun fibres (Hsiao et al., 2012, Lin et al., 2007, Wang et al., 2009). Increasing the rate of the local airflow was shown to reduce beading by additional stretching of the fibre (Hsiao et al., 2012, Wang et al., 2009); increasing the amount of fibre draw in this fashion also reduced the fibre diameter (Hsiao et al., 2012, Lin et al., 2007). However, at high airflow rates the increase in solvent loss rate resulted in faster drying of the fibre and a consequent increase in fibre diameter (Hsiao et al., 2012). Electrospinning with an atmosphere composed of a high breakdown strength gas would enable much higher field strengths to be reached. Baumgarten (1971) found that using Freon-12 (CCl_2F_2), a gas with a high dielectric strength resulted in an increase in the fibre diameter.

2.2.1.3 Atmospheric Pressure

It was asserted by Ramakrishna et al. (2005) that “generally, reduction in the pressure surrounding the electrospinning jet does not improve the electrospinning process”. However, the removal of air from the electrospinning chamber would allow for higher electric fields to be obtained without catastrophic discharges (Reneker et al., 1999). Also, due to the lower vapour pressure under a vacuum, solvent loss would be faster and could solve the problem of low vapour pressure solvents. Solvent-based electrospinning under a vacuum was shown to produce larger fibre diameters and smaller deposition area, which was attributed to the lower pressure transmitting a smaller perturbation amplitude that generates the whipping instability (Yang et al., 2009). However, this effect could also be attributed to the faster rate of solvent loss which would cause faster drying, appearing to reduce the extent of the whipping instability.

2.2.1.4 Humidity

Increasing humidity will reduce the solvent vapour pressure for aqueous solutions in electrospinning (Tripatanasuwan et al., 2007). Since this increases drying time, the fibres formed become thinner

with increasing humidity. At higher humidity the reduction in solvent loss rate is sufficient to introduce the formation of beads on the fibres (Tripatanasuwan et al., 2007). A similar effect can be generated by introducing solvent into the atmosphere to slow down solvent loss (Larsen et al., 2004). For solvents that can absorb water from the environment, a high humidity can slow down the drying process or prevent drying entirely resulting in thicker fibres or fused fibre films (De Vrieze et al., 2009). Theoretical analysis of the effects of humidity on electrospun fibre diameter predicts an increase in fibre diameter with increasing humidity (Thompson et al., 2007). Humidity has been shown by Kim et al. (2005), Casper et al. (2004) and Megelski et al. (2002) to control the formation of micro pores on the surface of the individual fibre.

2.2.2 Solution Parameters

Solution parameters are highly interrelated. A key property that controls electrospinning behaviour and fibre properties is the viscoelasticity of the solution. This can be modified by changing polymer concentration, polymer structure, solvent, diluent or other additives. Additives used to modify a solution's viscoelasticity will often have an effect on other parameters such as surface tension or conductivity.

2.2.2.1 Polymer Concentration

Varying polymer concentration has been often studied with examples such as Jarusuwannapoom et al. (2005), Eda et al. (2007) and Koski et al. (2004). These works show the strong effect of varying polymer concentration in the solution. As discussed above the electrospinning process has a strong dependence on the viscoelastic properties of the solution. This is due to the requirement for a sufficient level of intermolecular interaction that will help to damp the fluid instabilities and prevent jet breakup. Without sufficient elasticity, long wave perturbations remain undamped and result in bead formation (Hohman et al., 2001). This often occurs when the concentration is too low, resulting in electrospraying. As the concentration is raised a "bead-on-a-string" morphology (Fong et al., 1999) is observed with the beads slowly becoming more spindle-like and merging into the fibre as concentration increases. At a suitable concentration a smooth fibre is obtained. Using a theoretical model it was shown that increasing polymer concentration resulted in thicker fibres (Thompson et al., 2007). This matches observations by Koski et al. (2004). However, the work by Eda et al. (2007) focuses more on the entanglement concentration which represents the concentration of entanglements a single polymer molecule will experience on average with its neighbours.

2.2.2.2 Surface Tension and Conductivity

A theoretical study by Thompson et al. (2007) has shown that surface tension has almost no effect on the final properties of the electrospun fibre. This finding is consistent with the work of Hohman et al. (2001) and Yarin et al. (2001a) who both find that once the bending instability begins the electric

stresses are significantly larger than the capillary stresses. However, Fong et al. (1999) show that modification of surface tension (by the addition of surfactant or co-solvents/non-solvents) can assist in the formation of smooth fibres. The introduction of additives to the solution, often ionic salts, enables the modification of either the solution conductivity (Zhang et al., 2005) or surface tension (Zeng et al., 2003). For solutions with very low conductivity adding ionic salts to increase the solution conductivity has been shown to enable jet formation to occur but further addition beyond this has been shown to negatively affect the ability to form fibres (Stanger, 2008). It was also shown that the addition of mono atomic ionic salts to increase conductivity resulted in an increase in fibre diameter (Stanger et al., 2009c).

2.2.2.3 Solution Volatility and Dielectric Constant

The solution volatility, dielectric constant, solution conductivity and surface tension are typically dependent on the choice of solvent when other additives are not present. Jarusuwannapoom et al. (2005) provides an excellent study of the effects of using different solvents with a wide range of properties. When a solvent with a very low volatility is used wet fibres (i.e. appearance of a film with pores rather than a fibre mat) are collected.

However, the Taylor cone will solidify if the solvent is too volatile, halting fibre production. The same study also found that the dipole moment of the solvent and solution conductivity must both be of a sufficient level for electrospinning to occur. The theoretical study by Thompson et al. (2007) found that increasing the volatility of the solvent would increase the fibre diameter. It has been found that increasing the dielectric constant of the solution will increase the charge relaxation time and screening of the charge carried inside the jet (Sun et al., 2012). These changes to the charge behaviour in the jet are expected to suppress the formation of the whipping instability which in turn should produce thicker fibres but would allow better alignment of electrospun fibres (Sun et al., 2012).

2.2.2.4 Polymer Entanglement

It has been shown that the optimal solvent for electrospinning is not necessarily based on its solvating power for a particular polymer (Luo et al., 2010). Counter-intuitively, solvents with a high solubility can bind too well to the polymer molecule interfering with the viscoelastic properties and in turn affecting the electrospinability of the polymer solution. This can be corrected for by choosing binary solvent mixtures of a poor co-solvent or a diluent to reduce the overall solvating power of the mixture (Luo et al., 2010). This effect is highlighted in the work by Eda et al. (2007) where the ability to form fibres is examined in the context of intermolecular entanglements. It was found that at polymer concentrations too low to enable sufficient entanglement fibre formation was not possible.

As entanglement increased (with concentration, molecular weight/structure or solvent interaction) beaded fibres could be formed and eventually smooth uniform fibres.

2.2.2.5 Viscoelastic Properties

Directly linked to the polymer concentration is the solution viscosity which has been shown to be important in both the jet initiation and the final fibre properties (Deitzel et al., 2001a, Megelski et al., 2002). As the solution viscosity increases the fibre diameter increases (Demir et al., 2002). When varying viscoelastic properties in a theoretical model it was found that increasing the solution relaxation time increased fibre diameter while increasing elongation viscosity would decrease fibre diameter (Thompson et al., 2007). It is claimed that increased elongation viscosity correlates with stronger stretching that decreases fibre diameter (Thompson et al., 2007). Theoretical study of the response of a thinning jet under non-Newtonian viscoelastic behaviour showed that the zero-shear rate viscosity cannot sufficiently describe the polymer solution's behaviour in electrospinning (Feng, 2002). Under shear thinning the thinning rate at the Taylor cone is decreased while in the jet it is increased (Feng, 2002). A similar behaviour can be achieved by increasing the polymer's relaxation time (Feng, 2003). If the polymer solution undergoes strain hardening then the Taylor cone experiences a high level of stretching, appearing less like the traditional Taylor cone, while the jet undergoes less thinning due to the higher viscous resistance resulting in thicker fibre (Feng, 2002).

2.2.3 Processing Parameters

When trying to describe the underlying mechanisms that drive electrospinning, it is the processing and solution parameters that offer insight into this electrohydrodynamic process. Varying the solution parameters will reveal much of how the fluid dynamics affect the electrospinning process. To study the electrostatic aspects of electrospinning, experiments examining the effects of the non-material based processing parameters on electrospinning are required. The operation of a typical electrospinning apparatus will involve the modification of the applied electrostatic potential, the working distance and the feed rate.

2.2.3.1 Electric Field

Variation of the applied electrostatic potential and the working distance will also cause variation of the electric field strength. Typically, researchers will look at either the electrostatic potential (Lee et al., 2004) or the electric field strength (Buchko et al., 1999). Direct experiments with respect to electric field strength are difficult due to the non-linear nature of the electric field for needle-plate geometries (Stanger, 2008). Often the parallel plate approximation is used ($E = V/d$). However, this has been shown to be a poor predictor of electrospinning behaviour (Stanger, 2008). If the localized electric field value exceeds the dielectric strength for the atmosphere then a corona will be generated. The observation of this corona has been reported by Tripatanasuwan et al. (2009) but

the effects are yet to be quantified. It has been found that increasing the electrostatic potential will result in thinner fibres (Megelski et al., 2002).

In some cases increasing the working distance results in thinner fibres (Reneker et al., 2000) due to an increased time-of-flight after the onset of the bending instability and hence more time for the jet to be stretched. In other cases increasing the working distance results in a reduction of the electric field so will result in thicker fibres (Lee et al., 2004). However, jet initiation becomes difficult at excessively short or long distances due to the electric field being too strong or weak respectively. The electrode geometry and addition of secondary electrodes can be used to control deposition patterns or the extent of the bending instability. Work such as that by Teo et al. (2005) shows that the modification of the electric field allows control over the fibre flight and hence the modification of the final fibre alignment.

2.2.3.2 Mass Flow Rate and Fluid Pressure

There are comparatively few experiments done examining the feed rate (Rutledge et al., 2001, Zong et al., 2002), likely due to feed rate being used as a control parameter for stabilization of the Taylor cone. However, a low feed rate was shown to form very thin and dry fibres in a study by Yuan et al. (2004). Rutledge et al. (2001) demonstrated that with increased feed rates the fibres became much thicker and beads-on-a-string fibres were formed. The work by Druesedow et al. (2009) showed that without proper control of the fluid pressure, defects in the electrospun mat are formed from dripping droplets (or intermittent electrospraying). Correct control was found to produce stable electrospinning over a 24 hour period.

2.2.3.3 Charge Flow Rate and Orifice Diameter

The design consideration of the orifice diameter for the spinning head has been examined by some authors (Mo et al., 2004, Thompson et al., 2007). It was found that larger orifices resulted in thicker fibres (Mo et al., 2004). When the orifice size was very large it was difficult to obtain a stable Taylor cone and very small orifices become impractical as the Taylor cone dries out or the polymer is too viscous to flow through (Zhao et al., 2003). The electric current (which is analogous to the flow rate of charge) observed at the collector has been shown to follow a power law relationship with respect to applied voltage (Demir et al., 2002, Doshi, 1994, Fallahi et al., 2008). Fridrikh et al. (2003) showed that the final fibre diameter depends on the ratio of charge and mass flow rates. When measuring electric current at the collector a non-linear relationship between charge flow rate and mass flow rate was found (Fridrikh et al., 2003, He et al., 2005). When electric current was measured at the high voltage electrode this relationship was found to be linear (Stanger et al., 2012).

2.3 Process Measurement Techniques

When trying to compare one electrospinning experiment with another an obvious problem quickly becomes evident. Many reports that discuss an electrospinning experiment focus either on the polymer solution (Jarusuwannapoom et al., 2005) or the fibre produced (Koombhongse et al., 2001). For those that do try to quantify the process itself, it is common to only refer to a flow rate (when using a syringe pump) and the applied voltage and working distance (Wang et al., 2009). It has been proposed that a more detailed reporting of the electrospinning process might help connect different electrospinning experiments together making the mechanisms by which fibre formation occurs more obvious (Stanger et al., 2010). The benefit of easier comparison between experiments assumes that the fluid and environmental properties are also reported with sufficient detail. Additional processing parameters that can be measured are the electric current flow, the whipping frequency and the geometry of the Taylor cone, straight jet and the whipping envelope (Figure 4). These parameters can be divided into the Taylor cone region, the straight jet region, the whipping instability region and the collector region, which are each discussed in more detail below.

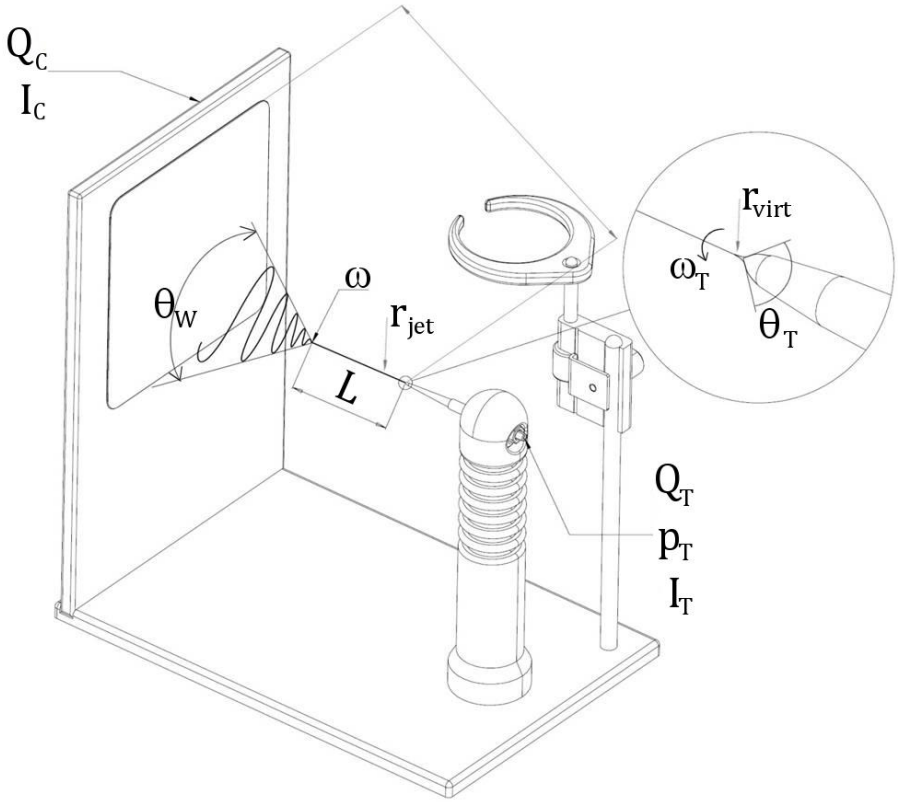

Figure 4: Observable properties of the electrospinning process.

2.3.1 Taylor Cone

The first stage of any electrospinning experiment is the polymer supply mechanism. As mentioned in Section 2.1 polymer melt or solution can be supplied using a constant flow rate or constant pressure method. A syringe pump is commonly reported as the mechanism for the supply of a constant flow rate (Theron et al., 2004), whereas a gravity feed mechanism can be used to provide a constant

pressure (Stanger et al., 2009d). The quantification of polymer delivery to the Taylor cone requires that the mass flow rate (Q_T) and the fluid pressure (p_T) be recorded. Briefly, this is because the Taylor cone can be considered to be a static fluid surface governed by the surface tension, surface electric charge, viscoelastic fluid properties and the internal fluid pressure (Stanger et al., 2009b). As such, the flow rate is connected to the fluid pressure through the viscoelastic properties of the fluid. The relationship may be further complicated by the expectation that the surface charge is dependent on the surface geometry adopted by the Taylor cone. Therefore, simply reporting of the flow rate (Q_T) alone does not adequately describe the experiment.

When using a syringe pump it is trivial to quantify Q_T. To record the pressure it is possible that a pressure sensor could be placed in-line with the polymer flow to record p_T simultaneous with Q_T. However, due to the weakly conducting nature of the polymer along with the high voltages employed by electrospinning this becomes challenging. The same problem is observed when trying to record the electric current flow which will be discussed in more detail later. The use of a constant pressure device offers its own problems. The typical Q_T used in electrospinning is of the order of 1 mm^3s^{-1} (Kowalewski et al., 2005) which makes using non-contact flow meters impractical. The use of in-line flow meters poses the same problems as the in-line pressure sensors. Invoking conservation of mass with the assumption that all polymer ejected from the Taylor cone deposits onto the collector provides a potential method to measure Q_T (Stanger et al., 2009d). This simply requires an accurate known concentration for solvent-based systems to enable the calculation of the solution flow rate from the deposition of solid polymer on the collector.

The next stage of an electrospinning experiment is the high voltage electric current, I_T. This is a widely neglected measurement as most measurements of the electric current flow are done at the collector (Demir et al., 2002, Fallahi et al., 2008, Theron et al., 2004). Likely this is due to the difficulties in placing an ammeter in-line with the high voltage supply to the Taylor cone. First, there is concern that any typical off-the-shelf ammeter would not be designed to insulate against the very high voltages (>5,000 V). This concern can be addressed by allowing the ammeter to 'float'. Floating in this case refers to raising the entire ammeter to the electric potential of the high voltage that is being measured. This prevents the electric potential exceeding the insulating capacity as the entire device is now at a similar potential. The ammeter must be battery powered to allow it to float. A second concern is now generated: how to record the data. Any contact with the external world (i.e. non-high voltage) would potentially provide a path for the floating ammeter to catastrophically discharge. Two options are left: optical and radio communication of data. Radio communication requires the construction of custom hardware and hence this method is not known to have been used. Optical communication via some variant of fibre optics can be done; however, this also

requires custom hardware and hence has not been used in published literature. Optical recording of a display is a simple solution. This method restricts the sample rates to an approximate order of 10 Hz at best due to the refresh times of displays and the ability to record the numbers using visual observation or video. This problem applies to any sensor application where high voltage is concerned. One way to sidestep this challenge is to use a high voltage supply that has an internal feedback that reports the electric current supplied (Stanger et al., 2012).

With suitable application of polymer supply and electric current the characteristic Taylor cone can be formed. It has been suggested that the shape of the Taylor cone determines some of the behaviour of jet formation and polymer solution flow rate. A number of studies have used photography to measure the shape of the Taylor cone (Feng, 2002, Han et al., 2008b, Helgeson et al., 2008, Shin et al., 2001b, Taylor, 1969, Yarin et al., 2001b, Zeleny, 1917). Obtaining photos of a Taylor cone (diameter approximately 0.5 mm) with sufficient resolution and clarity to obtain a usable trace of its geometry is a non-trivial task. Far more challenging than the technical difficulties is the challenge of converting a trace of the Taylor cone geometry into a usable metric that can be used to compare between different experimental conditions. One obvious option is the 'half angle' of the cone geometry, θ_T, as described by Taylor (1969) and later by Yarin et al. (2001b). Another option would be to define an arbitrary metric such as the radius of a 'virtual orifice' where the jet attaches to the Taylor cone, r_{virt} (Stanger et al., 2009a). Here a given distance is measured from the simulated surface of the hemispherical droplet (i.e. the volume without electrical forces deforming it) and the jet diameter at this point is measured. This is required as there is currently no known transition point that can be physically defined and subsequently measured that separates the Taylor cone and the liquid jet. However, the technical challenges of photographing the jet to obtain a diameter are even greater than those of the Taylor cone.

2.3.2 Straight Jet

The next part of the process that can be characterized is the straight jet. Analysis of the equations that describe the physics of the jet show that the thinning of the jet should follow an inverse power law for regions close to the Taylor cone (Helgeson et al., 2008). From this perspective the straight part of the electrospinning jet could be described fairly accurately by an initial diameter and an exponent for the inverse power law describing the thinning of the jet. The initial diameter has been described in the previous section. The power law exponent could be obtained by fitting the function to a series of accurate and precise measurements of the jet diameter. As was discussed in Section 2.3.1, there are technical difficulties in using standard optical photography for these measurements. Optical methods are the only ones available at this stage in the process. This is because the introduction of any physical object into the space near the jet will disrupt the electric field,

destroying the ability to measure the experiment being undertaken. Despite these challenges some studies have produced sufficient data that a power law function could be fitted (Feng, 2002, Han et al., 2008b, Helgeson et al., 2008, Shin et al., 2001b). As the jet diameter is on the order of < 10 µm, an alternative method to optical photography is laser diffraction to measure the jet diameter (Doshi, 1994). This allows the jet diameter to be measured along the entire length of the straight part, providing a much better description of the jet.

Another aspect of the straight jet that is not always present in electrospinning but is also very rarely reported is the pendulum like motion of the straight jet with angular frequency, ω_T (Han et al., 2008a). In this case the straight jet is ejected not from the centre of the droplet that forms the Taylor cone but off to one side. As a result the jet is unstable in position and will rotate around the centre. This motion can be characterized by a stable frequency of the oscillation (ω_T). It should be explicitly stated that this motion is distinct from the motion of the whipping instability and its frequency is much lower (~250 Hz or less compared with over 1 kHz for the whipping instability). The simplest characterization of the straight jet is that of its length, L. This can be done using simple optical photography and measured using standard image analysis (Kowalewski et al., 2005, Wu et al., 2012). The simplicity comes from the stable nature of the straight part of the jet (assuming no pendulum motion) and the ease of illuminating the whipping instability cone with a suitable light source (such as halogen bulbs). This allows easy detection of the position of the Taylor cone and the position of the onset of the instability making the straight line distance between these two points trivial to measure.

2.3.3 Whipping Instability

As measuring the straight jet length requires sufficient illumination of the whipping instability, these same photos can be used to obtain information about the instability itself. The whipping instability initially is composed of a set of expanding rings of the liquid jet (Eda et al., 2007, Reneker et al., 2000). As the rate of expansion is initially quite consistent this forms a cone or envelope that the whipping instability is contained within (Wu et al., 2012). The instability is chaotic as the jet motion is unpredictable but the motion is confined within a fairly stable region of space. Hence defining this region of space will somewhat describe the nature of the instability. The simplest method is to measure the full angle of the cone that is formed by these expanding rings, θ_W (Kowalewski et al., 2005, Wu et al., 2012).

One aspect of electrospinning that received much attention during the early stage of development (pre 2001) was the splitting or splaying of the jet. Due to the high speeds of the jet in the whipping envelope standard optical camera systems captured jets that appeared to bifurcate (Shin et al., 2001b). Once researchers had access to high enough speed photography it became clear that in

most cases the electrospinning jet completes its journey as a single jet. However, some cases have been found were the produced fibre shows strong evidence of repeated bifurcation (Filatov et al., 2007). Bifurcation is likely an important observation to characterize the whipping behaviour. Further characterization of the whipping instability can be done if high speed video facilities are available. With a capture frame rate of approximately 7,500 frames per second or more it becomes feasible for the measurement of the time taken for a ring to form. This can then be converted to a frequency of the whipping instability (ω), either the rotational speed (Reneker et al., 2000) or the number of rings formed per second. As with all the other optical photography methods this poses a significant technical challenge, often requiring sufficient light levels that the heat produced will definitely have changed the process being observed.

2.3.4 Collector

The final stage of the electrospinning process is the collection of the fibre. Many of the characterization methods here are similar to those discussed in Section 2.3.1, excluding of course those specific to the Taylor cone. These measurements can either rely on conservation laws or can check that the conservation assumption is valid in the experiment. In the case of checking validity, this is not challenging the conservation law, rather determining if the electrospinning experiment is a closed system to which the conservation law can be applied. The first case of this would be measuring the deposition rate (Q_C) which would be directly related to the flow rate (Q_T) at the Taylor cone by the known solid polymer concentration. When dealing with constant pressure polymer solution supply it is challenging to measure Q_T directly compared with measuring Q_C (Stanger et al., 2009d). Q_C can be measured using a four figure balance and weighing the collector electrode before and after (Stanger et al., 2009d). Making the assumption that all polymer ejected from the Taylor cone lands on the collector this allows Q_T to be calculated. If Q_T is known then the measurement of Q_C can be used to test the assumption that all the polymer lands on the collector. The second conservation law that can be tested at the collector is the conservation of charge. If the electric current flow at the Taylor cone (I_T) is known, then measuring the electric current flow at the collector (I_C) will reveal any loss of charge. This would test if electrospinning is a closed system with regard to the flow of charge. This is an important value to quantify as corona discharges have been observed (Tripatanasuwan et al., 2009). Charge on the jet is the driving force in electrospinning and hence understanding it is vital to describe the jet dynamics.

2.4 Novel Measurement Techniques

This thesis aims to introduce a novel measurement technique for characterizing electrospinning. As discussed in Section 2.3.1 measurements of I_T have not been published. This thesis will present methods to obtain measurements of I_T either using a rudimentary method of 'floating' an ammeter

or by using the current feedback signal available on some high voltage power supplies. When 'floating' the ammeter the use of video observation was used to enable the recording of data in an accurate fashion. One can think of the electrospinning process as a circuit and as such once I_T can be measured the more trivial I_C can be measured to test the assumption that the process is a closed circuit. This provides another novel method of observing the electrospinning process. If all the electrospun fibre is collected and weighed over a known time period, conservation of mass can provide a value for Q_T in a constant pressure polymer delivery system. Comparing the flow of mass, Q_T, and the flow of charge, I_T, it is possible to calculate a bulk charge density for the Taylor cone for a given condition. This further extends the method above to provide another observation of the electrospinning process. Finally, the flight time of the jet offers significant challenges in measuring due to the electrospinning process relying on the charged jet flying through free space. Any physical probe would disturb the flight path while optical methods of tracking particulate in the jet are limited when fibre diameters drop below the wavelength of visible light. High speed data capture of the collector electric current allows the identification of the time when power is switched on and the time when the jet first arrives at the collector electrode. The difference between these two times is shown to be a reasonable estimate of the flight time of the jet.

CHAPTER 3

MODELS OF ELECTROSPINNING

3 Models of Electrospinning

3.1 Introduction

The electrospinning process is a phenomenon within the field of electrohydrodynamics (EHD). As early as 1940 attempts were made to apply theoretical understanding of electrohydrodynamics to the observations made from electrospinning in order to understand the phenomenon (Filatov et al., 2007). The best known example of these early attempts is the work of Sir Geoffrey Taylor after whom the Taylor cone is named (Taylor, 1969). When attempting to describe the physics that drive the electrospinning phenomenon, electrospinning is typically divided into two distinct regions. The first is the axisymmetric region that is typically taken to extend from the orifice through the Taylor cone and out to the onset of the whipping instability (Carroll et al., 2006, 2008, 2009, Feng, 2002, 2003, Gañán-Calvo, 1997, Ganan-Calvo, 1997, Helgeson et al., 2008, Hohman et al., 2001, Reznik et al., 2004, Spivak et al., 1999, 2000, Turnbull, 1989, Yarin et al., 2001b). The second is the whipping region which covers the chaotic jet path from the onset of the instability to the collector electrode (Blonski et al., 2005, Carroll et al., 2011, Kowalewski et al., 2005, 2009, Reneker et al., 2000, 2008, Theron et al., 2005, Thompson et al., 2007, Yarin et al., 2001a).

The reason for the split is simple; in the axisymmetric region the mathematics can be reduced to a much simpler form and solved with significantly less computational power. Solution of the mathematics for the chaotic jet path of the whipping instability is non-trivial and requires resorting to a 3D discretized complex simulation which is computationally intensive. As both regions have the common root of electrohydrodynamics, the mathematical descriptions are often similar though their final form varies depending on the intended method of solving.

As there is no work the author is aware of in the field that attempts a general process description, a review of state-of-the-art mathematical models as a proxy for complete descriptions of the electrospinning process will be presented. It is not expected that these mathematical models will include all knowledge within the field of electrospinning; however, they should contain a description of the key phenomena that represent the electrospinning process. The preceding chapter has reviewed the techniques from literature for studying the electrospinning process. Therefore, the models will be explored as representations of the understanding of the electrospinning process itself while the following chapters will explore experimentally some of the individual aspects of the electrospinning process. The primary focus will be on the axisymmetric model of Feng (2002) and the whipping region model of Reneker et al. (2000). These models will be presented in enough detail that they could be reconstructed with the aid of expert knowledge. However, the details of the underlying methods for solving the problem will be omitted unless required to understand the conceptual construction of the model. Throughout the description, the implications of the

mathematical equations used to construct the models will also be discussed in a qualitative sense. All equations presented here use the symbols presented in the data dictionary (see Section IV) rather than those used by the original authors.

3.2 Axisymmetric Region

3.2.1 Early Work

Melcher et al. (1971) worked closely with Taylor to produce a generalized theory of the electrohydrodynamics (EHD) of a steady, semi-insulating liquid jet under the influence of an electric field. This work provided the analytical methods used by Taylor (1969) to describe the eponymous cone. This work introduced the assumptions that the charge relaxation time was small compared with the hydrodynamic relaxation time, meaning charge will reorganize faster than the fluid in response to applied forces. However, this work also assumed a linear external electric field and failed to account for the electric field generated by the ejected jet. It also only accounted for bulk conduction of electric charge (where charge is carried by the fluid) and ignored surface convection (where charge flows along the surface). As foundation work, this has led to a number of subsequent models requiring the electric current to be an initial input (Feng, 2002, Reneker et al., 2000, Spivak et al., 2000, Turnbull, 1989).

Later work by Ganan-Calvo (1997) introduced the electric field generated by the ejected jet and convection electric currents as well as bulk conduction. This model includes capillary forces, hydrodynamic pressure, electric forces and momentum in the normal and tangential EHD balance equations; however, it explicitly excludes ion emission or corona discharges and chooses conditions where viscous effects are negligible. Derived from standard EHD theory, this model assumes that the internal tangential electric field is very small compared with the external tangential field. The electric current in the jet is assumed to be dependent on the fluid properties and flow rate. As would be expected, the governing equations are given by the conservation of mass, charge and momentum.

From the same EHD origins, the work by Spivak et al. (2000) developed a similar model starting with the same three conservation laws. This model chooses to include viscoelastic effects in the momentum equation in the form of the Oswald-deWaele model. As with the previous model, Spivak et al. (2000) reduced the problem to a one-dimensional description justified by invoking axysymmetric geometry. Work by Reznik et al. (2004) is one of the few examples that retained a higher dimensionality. This model used the boundary element method to simulate the time evolution of the radially symmetric droplet in two dimensions. The incompressible form of the Navier-Stokes equation is used to describe the motion of the fluid while the Laplace equation is solved to describe the electric field due to the surface charge distribution. This model, like the previously described models, points to the relative charge and hydrodynamic relaxation times and

claim a conductive behaviour. This places most of the charge in the fluid on the boundary layer at the surface.

3.2.2 Feng Model of Axisymmetric Region

The work by Feng (2002) draws from the same roots as the previously discussed models, i.e. electrohydrodynamic theory. This model has seen further development in the following years, making it one of the most discussed (Carroll et al., 2006, 2008, 2009, Feng, 2003, Helgeson et al., 2008). This first section will present the original model in detail with the subsequent section discussing the changes and improvements.

3.2.2.1 Governing Equations

Like all the previously discussed models, four equations govern the axisymmetric steady state jet by representing the conservation of mass, conservation of charge, conservation of momentum and Coulomb's law for the $E(z)$ field. Given four equations we need to choose four unknowns so that the equations can be rearranged entirely in the form of these four unknowns so that the system can be solved. Initially, reduction of the four equations to be in terms of these four unknown functions — $r(z)$, $v(z)$, $E(z)$ and $\delta_q(z)$ — is attempted. For the sake of simplicity solvent loss is ignored, but it is acknowledged by the entire electrospinning field to be a prominent feature in fibre production from solutions. As this model examines the Taylor cone, ignoring solvent loss is justified by claiming that solvent loss is not significant before the jet region. The charge conservation accounts for both conduction and convection as seen in Ganan-Calvo (1997) and Reznik et al. (2004).

Mass conservation is given by:

$$\pi r^2 v = Q \tag{3.1}$$

Charge conservation is given by:

$$\pi r^2 \sigma E + 2\pi r v \delta_q = I \tag{3.2}$$

Momentum conservation is given by:

$$\frac{d}{dz}(\pi r^2 \rho v^2) = \pi r^2 \rho g + \frac{d}{dz}\left(\pi r^2(-p + \tau_{ZZ})\right) + \frac{\gamma}{r} 2\pi r r' + 2\pi r(t_t^e - t_n^e r') \tag{3.3}$$

where $r(z)$ is the jet radius, $v(z)$ is the average cross section velocity, $E(z)$ is the average cross section electric field, $\delta_q(z)$ is the surface charge density, $p(z)$ is the internal fluid pressure, $\tau_{zz}(z)$ is the axial stress and $t_t^e(z)$ and $t_n^e(z)$ are the tangential and normal surface tractions due to surface charge. The constant Q is the volumetric flow rate, σ is fluid conductivity, ρ is the fluid density, g is gravitational acceleration and γ is the surface tension. Equation (3.3) is formed by considering the forces on a short segment of the jet as shown in Figure 5. As this is a one dimensional axisymmetric

steady state (i.e. not time dependent) model, all primes indicate a derivative with respect to z as this simplifies notation.

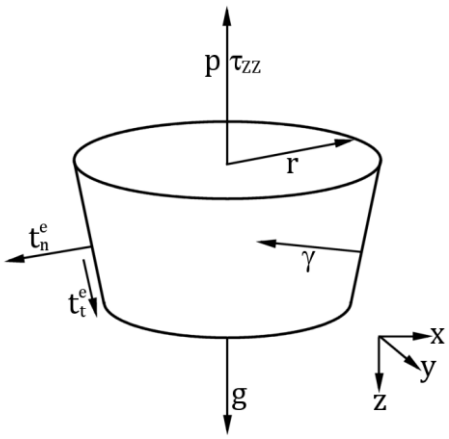

Figure 5: Forces considered acting on the jet used to construct this model.

The model considers forces due to gravity, Newtonian viscosity, surface tension and surface charge, which are presented in that order in the momentum conservation equation (see Equation (3.3)). In this model, the ambient pressure is set to zero, which is gauge pressure in engineering terms. The electrostatic surface tractions can be re-written in terms of surface charge and the electric field, removing two of the unknown functions from the equations:

$$\begin{aligned} t_n^e &= \left\| \frac{\epsilon}{2}(E_n^2 - E_t^2) \right\| \approx \frac{\delta_q^2}{2\bar{\epsilon}} - \frac{\bar{\epsilon} - \epsilon}{2} E^2 \\ t_t^e &= \delta_q E_t \approx \delta_q E \end{aligned} \tag{3.4}$$

where $\|*\|$ represents the step change of a given quantity across the surface of the jet and the overscore represents the equivalent value outside the jet (i.e. in ambient air). This model uses the step change conditions for E_n and E_t: $\|\epsilon E_n\| = \bar{\epsilon}\bar{E}_n - \epsilon E_n = \delta_q$, $\|E_t\| = \bar{E}_t - E_t = 0$ and assumes that $\epsilon E_n \ll \bar{\epsilon}\bar{E}_n$ and $E_t \approx E$. This exactly mirrors the surface conditions used by Ganan-Calvo (1997) where the internal electric field was assumed to be very small and most charge was found on the surface. The pressure $p(z)$ is determined by a radial momentum balance and applying the normal force balance at the surface of the jet gives:

$$-p + \tau_{rr} = t_n^e - \frac{\gamma}{r} \tag{3.5}$$

where $\tau_{rr}(z)$ is the radial stress. Using a generalized Newtonian constitutive relation for the viscous normal stress difference yields:

$$\tau_{zz} - \tau_{rr} = 3\eta v' \tag{3.6}$$

where η is the viscosity, allowing the elimination of the last two unknowns and transforms Equation (3.3) into Equation (3.7) using Equations (3.4) – (3.6):

$$\rho v v' = \rho g + \frac{3}{r^2}\frac{d}{dz}(\eta r^2 v') + \frac{\gamma r'}{r^2} + \frac{\delta_q \delta_q'}{\bar{\epsilon}} + (\epsilon - \bar{\epsilon})EE' + \frac{2\delta E}{r} \tag{3.7}$$

Finally the electric potential along the central axis of the jet can be determined by free and induced charges on the surface. Induced charges are given by E_n and $\bar{E}_n$: $\delta_{ind} = (\epsilon - \epsilon_0)E_n - (\bar{\epsilon} - \epsilon_0)\bar{E}_n$ where δ_{ind} is the induced charge in the jet. This means that not only are free ions being accounted for but also any dielectrically induced charges. The normal electric field E_n is related via Gauss's law to the axial electric field E by:

$$2\pi r E_n + \frac{d}{dz}(\pi r^2 E) = 0 \tag{3.8}$$

Given $\bar{\epsilon}\bar{E}_n - \epsilon E_n = \delta_q$, we can express $\bar{E}_n$ in terms of E. Hence, the potential along the z axis due to the total surface charge $\delta_q + \delta_{ind}$ may be obtained by Coulomb's law:

$$\phi(z) = \phi_\infty(z) + \frac{1}{2\bar{\epsilon}}\int \frac{\delta_q r d\zeta}{\sqrt{(z-\zeta)^2 + r^2}} - \frac{\beta}{4}\int \frac{d[Er^2]/d\zeta}{\sqrt{(z-\zeta)^2 + r^2}} d\zeta \tag{3.9}$$

where $\phi(z)$ is the electric potential, $\beta = \epsilon/\bar{\epsilon} - 1$ and integration is over the entire distance between the two electrodes. To simplify the problem it is possible to use an asymptotic estimate to remove the integral component of this integro-differential equation which leads simply to the axial electric field equation:

$$\begin{aligned} \phi(z) &\approx \phi_\infty(z) + \ln\chi\left(\frac{1}{\bar{\epsilon}}\delta_q r - \frac{\beta}{2}\frac{d[Er^2]}{dz}\right) \\ E(z) &= E_\infty(z) - \ln\chi\left(\frac{1}{\bar{\epsilon}}\frac{d[\delta_q r]}{dz} - \frac{\beta}{2}\frac{d^2[Er^2]}{dz^2}\right) \end{aligned} \tag{3.10}$$

where $\ln\chi$ is the natural log of the aspect ratio, $\chi = \ell/r_0$. Unless otherwise stated the parallel plate approximation electric field E_∞ is assumed to be spatially uniform. However, as seen above this model is explicitly including the electric field generated by the jet as well as the external electric field. Equations (3.1), (3.2), (3.7) and (3.10) then form the fundamental description of the dynamics modelled in this system. There are four equations for four unknown functions $r(z)$, $v(z)$, $E(z)$ and $\delta_q(z)$.

3.2.2.2 Dimensionless Parameters

The following characteristic quantities are used to make the four unknowns dimensionless.

Electric Field	$E_0 = \dfrac{I}{\pi r_0^2 \sigma}$
Length	R_0
Surface charge density	$\delta_{q0} = \bar{\epsilon}E_0$
Velocity	$v_0 = \dfrac{Q}{\pi r_0^2}$

Combining the above characteristic quantities to scale the unknowns with the following dimensionless groups we are able to take Equations (3.1), (3.2), (3.7) and (3.10) and make them dimensionless.

Aspect ratio	$\chi = \frac{\ell}{r_0}$
Beta (significance of induced charges)	$\beta = \frac{\epsilon}{\bar{\epsilon}} - 1$
Electric Peclet number (indicates the importance of charge convection relative to conduction)	$Pe = \frac{2\bar{\epsilon}v_0}{\sigma r_0}$
Epsilon (ratio of electrostatic force to inertia)	$\varepsilon = \frac{\bar{\epsilon}r_0^2}{\rho v_0^2}$
Froude number (ratio of inertia to gravity)	$Fr = \frac{v_0^2}{g r_0}$
Reynolds number (ratio of inertia to viscous forces)	$Re = \frac{\rho v_0 r_0}{\eta_0}$
Weber number (ratio of inertia to surface tension)	$We = \frac{\rho v_0^2 r_0}{\gamma}$

Solving the equations in dimensionless form is done in most models (Reneker et al., 2000, Reznik et al., 2004, Spivak et al., 2000). The following is Equations (3.1), (3.2), (3.7) and (3.10) in their dimensionless form, where the symbols have been kept the same as the dimensional symbols:

$$r^2 v = 1 \tag{3.11}$$

$$Er^2 + \mathrm{Per}v\delta_q = 1 \tag{3.12}$$

$$vv' = \frac{1}{\mathrm{Fr}} + \frac{3}{\mathrm{Re}}\frac{1}{r^2}\frac{d}{dz}(\eta r^2 v') + \frac{1}{\mathrm{We}}\frac{r'}{r^2} + \varepsilon\left(\delta_q\delta_q' + \beta EE' + \frac{2E\delta_q}{r}\right) \tag{3.13}$$

$$E = E_\infty - \ln\chi\left(\frac{d(\delta_q r)}{dz} - \frac{\beta}{2}\frac{d^2[Er^2]}{dz}\right) \tag{3.14}$$

3.2.2.3 Boundary Conditions

Equations (3.11) and (3.12), mass and charge conservation, allow v and δ_q to be expressed in terms of r and Er^2. This requires two boundary conditions. Equations (3.13) and (3.14), momentum conservation and axial electric field, can be rearranged as equations for r'' and $(Er^2)''$, each requiring an additional boundary condition.

First, exit point boundary conditions ($z = \chi$) are formed using asymptotic thinning conditions. Namely as R and δ_q drop to zero and E approaches E_∞, stretching of the jet is governed by a balance of inertia, gravity and tangential electric force. This is effectively defining the exit conditions such that the jet ceases to exist in the limit of stretching (see Figure 6). The following equation gives two of the four required boundary conditions:

$$r(\chi) + 4\chi r'(\chi) = 0$$
$$Er^2(\chi) = E_\infty r(\chi)^2$$

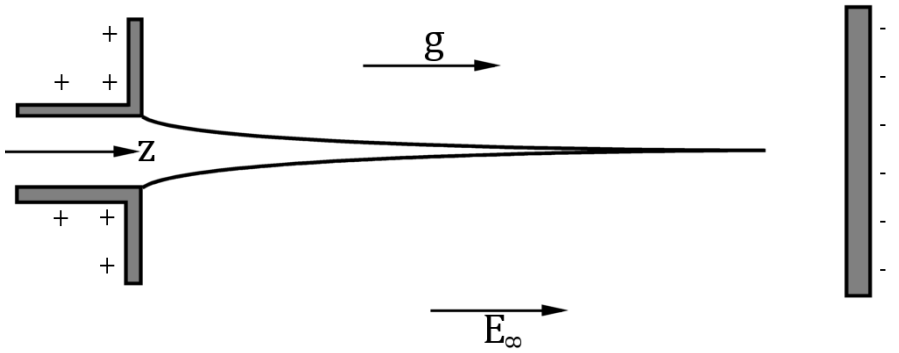

Figure 6: Schematic of the limit of stretching boundary conditions as given by Feng (2003).

It should be noted that the whipping instability is not addressed by this model and therefore no definite conclusions concerning the exit conditions can be drawn. Estimating the true exit conditions is difficult because of the chaotic nature of the whipping instability and therefore the model solution may not be valid along its entire length. However, assuming that at a sufficient distance from the Taylor cone the effect of the whipping fibre is small compared with the local effects of the straight jet seems reasonable. At the origin ($z = 0$) an easy boundary condition is the following:

$$r(0) = 1$$

The final boundary condition is much harder to define. To use the variables r and Er^2 we need to define $\delta_q(0)$ to give $Er^2(0)$ via the equation for charge conservation for any given I. This is difficult because the geometric details of the electrodes and the applied electric field will determine $\delta_q(0)$. As this model does not use such detailed descriptions of the geometry of the electrospinning arrangement an *ad hoc* definition of $\delta_q(0)$ is required. Ganan-Calvo (1997) and Hartman et al. (1999) circumvented defining $\delta_q(0)$ by specifying the slope $r'(0)$. However, this results in the problem of determining what point of the jet $z = 0$ actually corresponds to in the real world. Feng (2002) states that Hohman et al. (2001) takes a pragmatic approach by fitting the model to experimental results to determine $\delta_q(0)$. Feng (2002) goes on to point out that the surprising outcome of this approach coupled with the more complex representation of the electric potential is that stable solutions can only be found if $\delta_q(0)$ is zero or very small. When high $\delta_q(0)$ is used then the jet bulges into a balloon soon after exiting the nozzle.

To solve the apparent problem of defining the final boundary condition, Feng (2002) initially tried solving the model for an arbitrary series of different values for $\delta_q(0)$ and σ. The results showed that the profile for $\delta_q(z)$ was only modified by $\delta_q(0)$ within a very small boundary layer (on the order of 0.025% of total distance or ~5% of the orifice radius) and is practically independent of $\delta_q(0)$ outside of this boundary layer. As $\delta_q(0)$ has little effect on the final solution our *ad hoc* definition of $\delta_q(0)$ is chosen to be the intercept at $z = 0$ of the slope formed by $\delta_q(z)$ outside of the boundary layer. This is due to the assumption that a sharp transition of charge density within this boundary layer is

unlikely. To add weight to the argument for this choice Feng (2002) points out that the result here resembles the case in conventional fibre spinning where the normal stress condition $\tau_{rr}(0)$ has to be defined *ad hoc* but also turns out to have little effect on the solution. This effectively results in defining the final boundary condition as:

$$E(0) = E_0$$

Such that at the nozzle, the effective electric field is that generated by the application of high voltage to the electrodes and is independent of the Taylor cone presence. This prevents the formation of a sharp electric field gradient inside the Taylor cone.

3.2.3 Further Refinements

3.2.3.1 Viscoelastic Models

Part two of the first work by Feng (2002) introduces non-Newtonian viscoelastic behaviour. First the introduction of an empirical formula accounts for extension thinning or thickening. This empirical formula is taken from (Song et al., 1994):

$$\bar{\eta} = \eta_0 \left[1 + \left(\lambda\sqrt{\frac{\mathrm{II}}{2}}\right)^2\right]^{\frac{n-1}{2}} \cdot Tr(\mathrm{III}) \qquad (3.15)$$

$$Tr(\mathrm{III}) = Tr_\infty + (3 - Tr_\infty)(1 + \mu^3|\mathrm{III}|)^{\frac{m-1}{3}}$$

where λ and μ are the relaxation times for shear and extension, η_0 is the zero shear rate viscosity, $\bar{\eta}$ is the dimensionless viscosity, n and m are the corresponding power law indices. Of the two dimensionless numbers, Tr is the Trouton ratio and Tr_∞ is the asymptotic Trouton ratio at high strain rate. Finally $\mathrm{II} = 6(dv/dz)^2$ and $\mathrm{III} = 6(dv/dz)^3$ which are the second and third invariants of the rate-of-strain tensor. This allows the direct replacement of the term 3η in Equation (3.13) by the following dimensionless function:

$$\bar{\eta} = (1 + De^2 v'^2)^{\frac{n-1}{2}}\left[Tr_\infty + (3 - Tr_\infty)(1 + \overline{De}^3 v'^3)^{\frac{m-1}{3}}\right] \qquad (3.16)$$

where De is the dimensionless Deborah number defined as $De = \sqrt{3}v_0\lambda/r_0$ and $\overline{De} = \sqrt{6}v_0\mu/r_0$. The result of introducing extension thinning to a severely stretched jet enhances the "onion dome" shape typically observed in electrospinning of polymer solutions. The jet diameter is much thicker at the base of the Taylor cone (providing the "onion dome") however the ejected jet is a similar diameter to the Newtonian case. Under a mild stretching condition that is not representative of typical electrospinning, the effect of extension thinning was found to be far less. Extension thickening under severely stretched conditions reduces the "onion dome" shape towards the inverse power law shape of a Newtonian fluid. However, the jet diameter does not reduce as quickly within the Taylor cone as the Newtonian case due to the increasing shear leading to increased viscosity

which also leads to a thicker ejected jet. This work also briefly examined strain hardening which was found to eventually produce thicker fibres due to increasing resistance as the jet is stretched.

Later work by Feng (2003) replaces the empirical relationships with the Giesekus model which is molecular theory-based rather than phenomenological description-based (Giesekus, 1982). This model provides a satisfactory prediction of the elongational rheology of polymer solutions (including the plateau at high strain) without adding sufficient complexity to make computation impossible. To include this viscoelastic model into the governing equations the viscoelastic term (second term in Equation (3.7)) is replaced by $T'/\pi r^2$ as shown below:

$$\rho v v' = \rho g + \frac{T'}{\pi r^2} + \frac{\gamma r'}{r^2} + \frac{\delta_q \delta_q'}{\bar{\epsilon}} + (\epsilon - \bar{\epsilon}) E E' + \frac{2\delta_q E}{r} \tag{3.17}$$

where the tensile force (T) is given by:

$$T = \pi r^2 (\tau_{zz} - \tau_{rr}) \tag{3.18}$$

where τ is the stress, either in the axial direction along the z axis or in the radial direction, and is related to the strain rates by a constitutive equation obtained from the Giesekus model (Giesekus, 1982):

$$\begin{gathered} \boldsymbol{\tau} = \boldsymbol{\tau}_p + \eta_s (\nabla \boldsymbol{v} + \nabla \boldsymbol{v}^T) \\ \boldsymbol{\tau}_p = \lambda \boldsymbol{\tau}_{p(1)} + \alpha \frac{\lambda}{\eta_p} \boldsymbol{\tau}_p \cdot \boldsymbol{\tau}_p = \eta_p (\nabla \boldsymbol{v} + \nabla \boldsymbol{v}^T) \end{gathered} \tag{3.19}$$

where α is the mobility factor, the subscript p represents the polymer while the subscript s represents the solvent and the subscript (1) represents the upper convected derivative. This equation results in converting Equation (3.13) in the following form:

$$\begin{aligned} v v' = {} & \frac{1}{\mathrm{Fr}} + \frac{3(1-\eta_r)}{\mathrm{Re}} \frac{(r^2 v')'}{r^2} + \frac{1}{\mathrm{Re}} \frac{T_p'}{r^2} + \frac{1}{\mathrm{We}} \frac{r'}{r^2} \\ & + \varepsilon \left(\delta_q \delta_q' + \beta E E' + \frac{2E\delta_q}{r} \right) \end{aligned} \tag{3.20}$$

where the viscosity ratio is defined as $\eta_r = \eta_p / \eta_0$, and adds two more governing equations:

$$\begin{aligned} \tau_{prr} + \mathrm{De}\left(v \tau_{prr}' + v' \tau_{prr}\right) + \alpha \frac{\mathrm{De}}{\eta_r} \tau_{prr}^2 &= -\eta_r v' \\ \tau_{pzz} + \mathrm{De}\left(v \tau_{pzz}' - 2v' \tau_{pzz}\right) + \alpha \frac{\mathrm{De}}{\eta_r} \tau_{pzz}^2 &= 2\eta_r v' \end{aligned} \tag{3.21}$$

This leaves the original boundary conditions in place but add in the requirement to define the radial and axial stress due to the polymer, τ_{prr} and τ_{pzz}, at the Taylor cone. The chosen boundary conditions assume that the shear inside the nozzle is ineffective in stretching polymer molecules (unlike that in the jet) and as such the initial stress is purely Newtonian:

$$\tau_{prr} = -\eta_r v' = 2\eta_r \frac{r'}{r^3} \tag{3.22}$$

$$\tau_{pzz} = -2\tau_{prr}$$

Numerical experiments found that at distances greater than $10r_0$ changes to the initial stress conditions have minimal effect on the jet profile solution. Indeed, non-Newtonian conditions were found often to under- or overshoot a reasonable jet profile whereas conditions close to Newtonian provide the best agreement with experimental observations. Comparing this description to mechanical stretching (conventional fibre spinning), there is no die swell. This is because the electrostatic forces at the surface of the jet continue to stress the jet such that the polymer molecules are prevented undergoing elastic recovery. This is proposed as part of the reason why electrospinning produces much thinner fibres. Another difference between electrospinning and conventional spinning seen in simulations is that electrospinning has most of its thinning occurring at the Taylor cone. Here the thinning is extreme compared with conventional spinning; however, conventional spinning has continuous thinning along its length. This result is only valid for the axisymmetric part of the jet, whereas the whipping instability may be responsible for subsequent thinning (Reneker et al., 2000). It was found that increasing strain hardening by decreasing molecular mobility resulted in thicker jets. Increasing the Deborah number (the ratio between stress relaxation time and characteristic time of the process) also results in thicker jets. This model also separates the contributions of the polymer from the solvent and finds that as the polymer becomes more dominant the effect of strain hardening increases resulting in thicker jets.

3.2.3.2 Axisymmetric Stability Analysis

Taking this basic model it is possible to apply stability analysis of the governing equations analogous to the work done by Rayleigh on describing the Rayleigh-Plateau instability (Strutt, 1879). Inspired by the work of Hohman et al. (2001), Carroll et al. (2008) modified the original model for non-Newtonian fluids to introduce perturbations and study their growth or damping rates. The aim was to describe the 'beading' phenomenon observed in electrically driven jets, also known as the axisymmetric instability. This work showed that the formation of these 'beads' occurs a short distance from the Taylor cone where the jet has effectively become a straight column of fluid (i.e. thinning rate is very small). As was found by Hohman et al. (2001) there are two unstable modes, a capillary driven mode (like the Rayleigh-Plateau instability) and a 'conducting' mode driven by surface charges. It is noted that for low conductivity solutions the 'conducting' mode is dominated by the capillary instability. However, in a further developed work by Carroll et al. (2009), in highly conducting polymers this 'conducting' mode becomes dominant due to the higher surface charge carried by the jet.

It was found that increasing the flow rate or the viscosity, or decreasing the applied voltage stabilized the jet and decreased the instability growth rate (Carroll et al., 2008). Increasing the

relaxation time destabilizes the jet up to a critical point where it becomes a significant stabilizing force. The explanation for this is that the polymer molecules undergo relaxation within the jet, where increasing relaxation time leads to less stability. However, once the relaxation time is longer than the ongoing stretching rate the molecules can no longer relax within the jet and this leads to the stabilizing effect. This effect is seen strongly in the work studying conductive PEO solutions, where the solution with a shorter relaxation time leading to low axial stress in the jet produces 'beads' while the longer relaxation time solution has significantly higher stabilizing axial stress and produces a smooth jet (Carroll et al., 2009).

Performing an energy analysis of the equivalent of Equation (3.20) shows that for low conductivity solutions the electrical, charge and viscoelastic forces all absorb perturbation energy while the capillary force reinforces the perturbations. This shows that it is the capillary mode that is creating the axisymmetric instability for low conductivity solutions (Carroll et al., 2008). The same analysis for conductive solutions shows that the capillary and Newtonian viscoelastic forces both absorb perturbation energy. The non-Newtonian viscoelastic forces generally absorb energy except for specific conditions where it strongly reinforces the instability. The electrical and charge forces reinforce the formation of the instability demonstrating that it is driven by the interaction of surface charge on the jet.

3.3 Whipping Region

Models of the chaotic whipping instability have been challenging to produce. Due to the lack of symmetry this requires the problem to be described mathematically in its entirety. Without the ability to reduce the problem to a simpler form this leaves it very computationally intensive; providing limited opportunities for development in the last century when computer power was limited. As such the model described by Reneker et al. (2000) is the first to attempt a description of the 3D path of the chaotic instability. This model has then been further developed (Blonski et al., 2005, Carroll et al., 2011, Kowalewski et al., 2005, 2009, Reneker et al., 2008, Theron et al., 2005, Thompson et al., 2007) and criticized by others in literature (Carroll et al., 2011, Kowalewski et al., 2005, 2009).

3.3.1 Reneker Model of Whipping Instability

The easiest way to build an accurate concept of how this model is constructed is to start with the simplest case and steadily extend it. Consider a charged straight fluid jet segment that is in an electric field parallel to its central axis. Now divide this jet into two equal sized segments. If we now consider the forces acting on these jet segments to be acting on a single mass point, where the mass point has the position at the base of the column on the centre axis of each segment, then we can say that each point has a mass m and a charge q. Let us name the mass points that represent the

segments A and B respectively. From the perspective of the jet this is effectively a 1D discretized description that can accommodate a 3D jet path with respect to fixed co-ordinates. Now let us choose a frame of reference where mass point A has no motion. For a visual representation see Figure 7. It should be noted that due to there being only two points and the segments are fixed as being straight this is a one-dimensional model. Once three points come into existence it is possible for a three-dimensional system to exist.

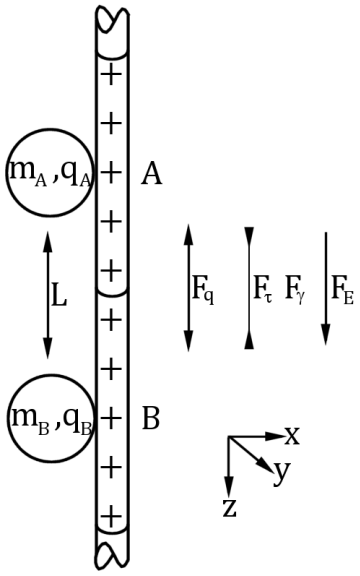

Figure 7: Discretization of a liquid jet column to allow 3D simulation.

We can now describe the system by examining the forces acting on B only. The forces chosen to govern the interactions of B with A are the Coulomb force ($\boldsymbol{F}_q$), the viscoelastic force ($\boldsymbol{F}_\tau$), the capillary force ($\boldsymbol{F}_\gamma$) and the Lorentz force ($\boldsymbol{F}_E$) (which is valid as the charge is treated as a point charge). In the original work by Reneker et al. (2000) the capillary force is treated as only affecting fluid jets that have a non-zero curvature (i.e. a bent jet) and so in this simple model it is excluded.

The Coulomb force is named such because even in the three-dimensional generalization this force, representing the interaction between the charged mass points via their electric fields, takes on the form of Coulomb's Law for two point charges. As such in this simple system the force is given by $\boldsymbol{F}_q = -k_e(q^2/\ell^2)$ where k_e is the electrostatic constant. Here ℓ is defined as the distance between point A and point B. The other electrostatic force involved in this system is the Lorentz force, named because it takes its form from the Lorentz force law where the magnetic field is set to zero. As the force depends on an interaction between the charged mass point and a constant external electric field, the force is the same for this simple system and for the more complex ones introduced later. This force is given by $\boldsymbol{F}_E = q(\phi_0/h)$ where ϕ_0 is the applied electric potential and h is the tip to collector distance. Finally the viscoelastic force represents the effect of the stretching of the viscoelastic jet by using the definition of nominal stress in a material. The force due to nominal stress

is defined by $\boldsymbol{F}_\tau = A\tau$ where A is the cross sectional area and τ is the axial stress. As this model does not include any tangential stress the term stress shall hereafter refer only to nominal stress. The stress behaviour over time is modelled using Maxwellian viscoelastic material (i.e. a spring and dashpot in series) and as such the viscous and elastic behaviour doesn't need to be included into the forces acting on the jet. This force is then given by $\boldsymbol{F}_\tau = \pi r^2 \tau$.

The differential equations that govern this system are then formed by taking Newton's second law (i.e. $\boldsymbol{F} = m\boldsymbol{a}$, where m is mass and $\boldsymbol{a}$ is acceleration) and equating this with the sum of the forces described above. In order to solve a system of first order ODEs (ordinary differential equations), the equations need to be in the form below. The stress equation (Equation (3.24)) describes the spring and dashpot in series that represents our viscoelastic Maxwellian material. These equations can then be solved using $\frac{d\ell}{dt} = -v$ and the conservation of volume (and hence mass) given by $\pi r^2 \ell = \pi r_0^2 \ell_0$.

$$\begin{aligned} \frac{dx}{dt} &= v \\ \frac{dv}{dt} &= \frac{1}{m}\left(-\frac{k_e q^2}{\ell^2} - \frac{q\phi_0}{h} + \pi r^2 \tau\right) \end{aligned} \tag{3.23}$$

$$\frac{d\tau}{dt} = \frac{G}{\ell}\frac{d\ell}{dt} - \frac{G}{\mu}\tau \tag{3.24}$$

where G is the storage modulus of the polymer. This model effectively presents the phenomenological explanation of jet thinning in electrospinning as being driven by interactions between the charges on the jet with the electric field and which is restrained by the viscoelastic properties of the fluid. The electric field has a gradient running from the high voltage electrode to the collector which is the sum of the external electric field from the electrodes (in this case assumed to be uniform) and the electric field generated by the charges on the jet. The charge carried by the jet is more concentrated near the Taylor cone than the collector due to stretching of the jet segments which leads to a non-uniform electric field (stronger at the Taylor cone) that further enhances stretching. This effect is finally balanced against the other forces that resist stretching, primarily viscoelasticity.

3.3.2 Dimensionless Parameters

All lengths in the model are scaled by the electric length scale to render them dimensionless (see Equation (3.25)). It is asserted by Reneker et al. (2000) that L_{el} is also assumed "to be the initial filament length which is not restrictive". Time is made dimensionless by dividing by the viscoelastic relaxation time η/G. Stress is made dimensionless by dividing by G. The velocity is then made dimensionless by $L_{el}\eta/G$. The radius, unlike all other lengths, is made dimensionless by dividing by r_0. Now the three forces involved in the above simple equation are made dimensionless using a set of three dimensionless parameters (see Equation (3.26)). Here Q can be used to remove the

dimensionality of the Coulomb force, likewise V can be used for the Lorentz force and F_{ve} can be used for the viscoelastic coupling force. It is noted by Reneker et al. (2000) that $Q \equiv F_{ve}$ which can be used to reduce the number of initial conditions specified when solving the dimensionless form. Using these dimensionless parameters, Equations (3.23) and (3.24) now take on the form shown in Equation (3.27). Additional dimensionless parameters are required to extend this model to three dimensions however these will be introduced later, in Section 3.3.4, following the generalization of Equations (3.23).

$$L_{el} = \left(\frac{q^2}{\pi r_0^2 G}\right)^{1/2} \tag{3.25}$$

$$\begin{aligned} Q &= \frac{q^2\eta^2}{L_{el}^3 mG} \\ V &= \frac{q\phi_0\eta^2}{hL_{el}mG} \\ F_{ve} &= \frac{\pi r_0^2\eta^2}{L_{el}mG} \end{aligned} \tag{3.26}$$

$$\begin{aligned} \frac{d\bar{x}}{d\bar{t}} &= \bar{W} \\ \frac{d\bar{W}}{d\bar{t}} &= V - F_{ve}\frac{\bar{\tau}}{\bar{\ell}} + \frac{Q}{\bar{\ell}^2} \\ \frac{d\bar{\tau}}{d\bar{t}} &= \frac{\bar{W}}{\bar{\ell}} - \bar{\tau} \end{aligned} \tag{3.27}$$

3.3.3 Long Three Dimensional Discretized Jet

Following the method outlined in Section 3.3.1 we begin with the discretization of our jet. Consider a long fluid jet that exists in an electric field that runs parallel to the z axis. This jet is then divided into a series of segments, each represented by a point of mass, m, which carries a charge, q. Each mass point represents a straight column of liquid extending from the location of that point to the location of the point above it in the jet. The jet is modelled as a system of viscoelastically connected point masses that are acted on by the four forces outlined in Section 3.3.1. These four forces are the Lorentz force ($\boldsymbol{F}_E$), the Coulomb force ($\boldsymbol{F}_q$), the viscoelastic force ($\boldsymbol{F}_\tau$) and the capillary force ($\boldsymbol{F}_\gamma$).

The Taylor cone is not assigned a charge as the force due to this charge is assumed to be accounted for by the electrostatic field that extends from the Taylor cone to the collector electrode. In this case the electrostatic field is simplified using the parallel plate approximation (ϕ_0/h_{int}). This approach is valid to a point due to the superposition principle for electric fields (i.e. one can add two separate fields together where they overlap). Hence it is possible to calculate the force due to the different electric fields (i.e. from the charge on the electrodes and the charges on the mass points) and sum the forces rather than sum the electric field for each point in space. Computationally this saves time

as it does not require a solution to the Laplace equation at each time step. The two electrostatic forces are the Lorentz force ($\boldsymbol{F}_E$) and the Coulomb force ($\boldsymbol{F}_q$) where the Lorentz force represents the electrostatic field from the two electrodes.

The Coulomb interactions are attributed to the formation of the bending instability, i.e. considering a series of charged point masses that are interacting via the Coulomb force the system is intrinsically unstable such that any deviation from the equilibrium point (i.e. not on the axis) will result in a wildly varying solution that will not return to the equilibrium point as per Earnshaw's theorem (Earnshaw, 1842). Earnshaw's theorem can be summarized as any system of more than two bodies interacting purely by Coulomb forces cannot reach an equilibrium solution that is stable with respect to perturbations. The interactions are given by a modification of Coulomb's law (Equation (3.28)) as demonstrated in Equation (3.29). The difficulty in calculating these forces is in the fact that each bead interacts with each other bead. As a result a summation is required. In practice the three dimensional forces that act on these mass points are split into their *x*, *y* and *z* components as per the unit vectors.

$$\boldsymbol{F}_q = k_e \frac{q_1 q_2}{r^2} \tag{3.28}$$

$$\boldsymbol{F}_q = k_e q^2 \sum_{\substack{j=1,N \\ j \neq i}} \frac{1}{\ell_{ij}^2} \left[\mathbf{i} \frac{x_i - x_j}{\ell_{ij}} + \mathbf{j} \frac{y_i - y_j}{\ell_{ij}} + \mathbf{k} \frac{z_i - z_j}{\ell_{ij}} \right] \tag{3.29}$$

where **i**, **j** and **k** are the unit vectors and

$$\ell_{ij} = \left[\left(x_i - x_j\right)^2 + \left(y_i - y_j\right)^2 + \left(z_i - z_j\right)^2 \right]^{1/2}$$

This form of the Coulomb force represents the assumed phenomenological mechanism of a self-repelling jet being intrinsically unstable so therefore must undergo a bending instability in flight. This model does not account for what might generate the instability; rather it relies on a limited growth rate near the Taylor cone due to axial stretching providing a stabilizing force which once the axial stress in the jet starts to relax the bending instability can then grow at a faster rate.

For the viscoelastic interactions, modelling using the Maxwellian material equation (see Equation (3.24)) as in Section 3.3.1 is still valid as the stress is still acting in one dimension along the jet. However, the equation for the force affecting a mass point now must include a normal vector pointing along the jet segment axis (see Equation (3.30)). Modelling of the viscoelastic forces in this system is simplified by considering each mass point to be a linear approximation of the true jet path. By keeping the distance between each mass point small enough this approach is valid. The force applied to each mass point is found by considering the effects of the stress in the jet both above and below the mass point in question (see Equation (3.30)). The form of the equation is taken from the definition of stress (i.e. $\boldsymbol{F}_\tau = A\tau$) where the area is taken from the radii of the jet above and below.

$$\boldsymbol{F}_{\tau} = \pi r_{ui}^2 \tau_{ui}\left[\mathbf{i}\frac{x_{i+1}-x_i}{\ell_{ui}} + \mathbf{j}\frac{y_{i+1}-y_i}{\ell_{ui}} + \mathbf{k}\frac{z_{i+1}-z_i}{\ell_{ui}}\right] - \pi r_{di}^2 \tau_{di}\left[\mathbf{i}\frac{x_i-x_{i-1}}{\ell_{di}} + \mathbf{j}\frac{y_i-y_{i-1}}{\ell_{di}} + \mathbf{k}\frac{z_i-z_{i-1}}{\ell_{di}}\right]$$

where both l_{ui} and l_{ud} are given by:

$$\ell_{ui} = [(x_{i+1}-x_i)^2 + (y_{i+1}-y_i)^2 + (z_{i+1}-z_i)^2]^{1/2}$$
$$\ell_{di} = [(x_i-x_{i-1})^2 + (y_i-y_{i-1})^2 + (z_i-z_{i-1})^2]^{1/2} \quad (3.30)$$

and r_{ui} and r_{di} are given by

$$r_{ui} = \sqrt{\frac{r_0^2 L_{el}}{\ell_{ui}}}\,, r_{di} = \sqrt{\frac{r_0^2 L_{el}}{\ell_{di}}}$$

The capillary force due to surface tension is calculated in a similar way to the viscoelastic force in that a contribution from the jet above and below the mass point in question is used. This force is the action of the surface tension to restore any bent part of the jet to a straight jet. The equation used is given by Equation (3.31) where it should be noted that the inclusion of a jet curvature (κ_i, calculated from the position of mass point (*i-1*), *i* and (*i+1*)) explicitly accounts for the non-straight nature of the jet during the bending instability.

$$\boldsymbol{F}_{\gamma} = -\frac{\gamma\pi(r^2)_{av}\kappa_i}{\left(x_i^2+y_i^2\right)^{\frac{1}{2}}}[\mathbf{i}|x_i|sign(x_i) + \mathbf{j}|y_i|sign(y_i)]$$

where the function *sign(x)* is given by

$$sign(x) = \begin{cases} 1 \;\; if\; x > 0 \\ -1\; if\; x < 0 \\ 0 \;\; if\; x = 0 \end{cases} \quad (3.31)$$

and $r_{av} = \frac{r_{ui}+r_{di}}{2}$

Gravity and aerodynamic forces have been excluded as they are orders of magnitude smaller than the above forces and hence are assumed to have a minimal impact on the mass point dynamics.

Now following the path from Section 3.3.1, the system of first order differential equations can be constructed by using Newton's second law and equating it to the summation of all the above forces (see Equation (3.32)). This combined with the equation from Section 3.3.1 used to model the one-dimensional stress in a Maxwellian material (see Equation (3.24) and (3.33)) completes the set of equations required to model the electrospinning jet as proposed by Reneker et al. (2000). For the sake of rigor Equations (3.32) and (3.33) have been expanded to show the full system of first order differential equations that are solved as part of this model (see Equation (3.34)).

$$
\begin{aligned}
m\frac{d^2\boldsymbol{r_i}}{dt^2} &= \left(\boldsymbol{F}_q + \boldsymbol{F}_\phi + \boldsymbol{F}_\tau + \boldsymbol{F}_\gamma\right) \\
m\frac{d^2\boldsymbol{r_i}}{dt^2} &= k_e q^2 \sum_{\substack{j=1,N \\ j\neq i}} \frac{1}{\ell_{ij}^3}\left(\boldsymbol{r}_i - \boldsymbol{r}_j\right) - q\frac{\phi_0}{h}\mathbf{k} + \frac{\pi r_{ui}^2 \tau_{ui}}{\ell_{ui}}\left(\boldsymbol{r}_{i+1} - \boldsymbol{r}_i\right) \\
&\quad - \frac{\pi r_{di}^2 \tau_{di}}{\ell_{di}}\left(\boldsymbol{r}_i - \boldsymbol{r}_{i-1}\right) \\
&\quad - \frac{\gamma\pi\left(r_i^2\right)_{av}\kappa_i}{\sqrt{x_i^2 + y_i^2}}\left[\mathbf{i}|x_i|sign(x_i) + \mathbf{j}|y_i|sign(y_i)\right]
\end{aligned}
\tag{3.32}
$$

$$
\frac{d\tau}{dt} = G\frac{d\ell}{\ell dt} - \frac{G}{\eta}\tau \tag{3.33}
$$

where $\frac{d\ell}{dt}$ is given by $\frac{d\ell_{ui}}{dt} = \frac{(\boldsymbol{r}_{i+1} - \boldsymbol{r}_i)(\boldsymbol{V}_{i+1} - \boldsymbol{V}_i)}{\ell_{ui}}$

$$
\begin{aligned}
\frac{dx_i}{dt} &= u_i \\
\frac{dy_i}{dt} &= v_i \\
\frac{dz_i}{dt} &= w_i \\
\frac{du_i}{dt} &= \frac{1}{m}\left(k_e q^2 \sum_{\substack{j=1,N \\ j\neq i}} \left[\frac{x_i - x_j}{\ell_{ij}^3}\right] + \pi r_{ui}^2 \tau_{ui}\frac{x_{i+1} - x_i}{\ell_{ui}} - \pi r_{di}^2 \tau_{di}\frac{x_i - x_{i-1}}{\ell_{di}} \right. \\
&\quad \left. - \frac{\gamma\pi(r^2)_{av}\kappa_i}{\sqrt{x_i^2 + y_i^2}}\left[|x_i|sign(x_i)\right] \right) \\
\frac{dv_i}{dt} &= \frac{1}{m}\left(k_e q^2 \sum_{\substack{j=1,N \\ j\neq i}} \left[\frac{y_i - y_j}{\ell_{ij}^3}\right] + \pi r_{ui}^2 \tau_{ui}\frac{y_{i+1} - y_i}{\ell_{ui}} - \pi r_{di}^2 \tau_{di}\frac{y_i - y_{i-1}}{\ell_{di}} \right. \\
&\quad \left. - \frac{\gamma\pi(r^2)_{av}\kappa_i}{\sqrt{x_i^2 + y_i^2}}\left[|y_i|sign(y_i)\right] \right) \\
\frac{dw_i}{dt} &= \frac{1}{m}\left(k_e q^2 \sum_{\substack{j=1,N \\ j\neq i}} \left[\frac{z_i - z_j}{\ell_{ij}^3}\right] + \pi r_{ui}^2 \tau_{ui}\frac{z_{i+1} - z_i}{\ell_{ui}} - \pi r_{di}^2 \tau_{di}\frac{z_i - z_{i-1}}{\ell_{di}} + q\frac{\phi_0}{h_{int}} \right) \\
\frac{d\tau_{ui}}{dt} &= G\frac{d\ell_{ui}}{\ell_{ui}dt} - \frac{G}{\eta}\tau_{ui}
\end{aligned}
\tag{3.34}
$$

3.3.4 More Dimensionless Parameters

Following from Section 3.3.2, the discussion of dimensionless parameters is continued with the introduction of the dimensionless parameter, A (see Equation (3.35)), associated with the capillary force ($\boldsymbol{F}_{\gamma}$). The final dimensionless parameter for the equations is given by Equation (3.36) which is used to find the total distance from the Taylor cone to the collector in the new dimensionless co-ordinates. This then allows the system of differential equations outlined in Equation (3.34) to be reduced to the form shown in Equation (3.37) where the dimensionless nature is emphasized by the bar.

$$A = \frac{\gamma \pi r_0^2 \eta^2}{m L_{el}^2 G^2} \tag{3.35}$$

$$H = \frac{h}{L_{el}} \tag{3.36}$$

$$\begin{aligned}
\frac{d\bar{x}_i}{d\bar{t}} &= \bar{u}_i \\
\frac{d\bar{y}_i}{d\bar{t}} &= \bar{v}_i \\
\frac{d\bar{z}_i}{d\bar{t}} &= \bar{w}_i \\
\frac{d\bar{u}_i}{d\bar{t}} &= Q \sum_{\substack{j=1,N \\ j\neq i}} \left[\frac{\bar{x}_i - \bar{x}_j}{\bar{\ell}_{ij}^3}\right] + F_{ve}\bar{\tau}_{ui}\frac{\bar{x}_{i+1} - \bar{x}_i}{\bar{\ell}_{ui}^2} - F_{ve}\bar{\tau}_{di}\frac{\bar{x}_i - \bar{x}_{i-1}}{\bar{\ell}_{di}^2} \\
&\quad - A\frac{\left(\bar{r}_i^2\right)_{av}\kappa_i}{\sqrt{\bar{x}_i^2 + \bar{y}_i^2}}[|\bar{x}_i| sign(\bar{x}_i)] \\
\frac{d\bar{v}_i}{d\bar{t}} &= Q \sum_{\substack{j=1,N \\ j\neq i}} \left[\frac{\bar{y}_i - \bar{y}_j}{\bar{\ell}_{ij}^3}\right] + F_{ve}\bar{\tau}_{ui}\frac{\bar{y}_{i+1} - \bar{y}_i}{\bar{\ell}_{ui}^2} - F_{ve}\bar{\tau}_{di}\frac{\bar{y}_i - \bar{y}_{i-1}}{\bar{\ell}_{di}^2} \\
&\quad - A\frac{\left(\bar{r}_i^2\right)_{av}\kappa_i}{\sqrt{\bar{x}_i^2 + \bar{y}_i^2}}[|\bar{y}_i| sign(\bar{y}_i)] \\
\frac{d\bar{w}_i}{d\bar{t}} &= Q \sum_{\substack{j=1,N \\ j\neq i}} \left[\frac{\bar{z}_i - \bar{z}_j}{\bar{\ell}_{ij}^3}\right] + F_{ve}\bar{\tau}_{ui}\frac{\bar{z}_{i+1} - \bar{z}_i}{\bar{\ell}_{ui}^2} - F_{ve}\bar{\tau}_{di}\frac{\bar{z}_i - \bar{z}_{i-1}}{\bar{\ell}_{di}^2} + V \\
\frac{d\bar{\tau}_{ui}}{d\bar{t}} &= \frac{d\bar{\ell}_{ui}}{\bar{\ell}_{ui}d\bar{t}} - \bar{\tau}_{ui}
\end{aligned} \tag{3.37}$$

3.3.5 Generating the Instability

As was alluded to in Section 3.3.3, the bending instability will not be self generating under this mathematical model. Unless the mass beads have a position that is not exactly on the central axis (i.e. $[x, y] \neq [0,0]$) then there is no force acting in the x, y plane as per Equation (3.36). As the Enershaw theorem suggests that this straight jet solution should be a highly unstable solution the

model introduces small perturbations of the form below. The amplitude of these perturbations is assumed to be freely chosen with the only requirement that it is small.

$$x = 10^{-3} L_{el} \sin(\omega t)$$
$$y = 10^{-3} L_{el} \cos(\omega t) \quad (3.38)$$

where ω is the frequency of the whipping instability. From here simulations could be performed in two ways as discussed by Reneker et al. (2000). The initial condition is either two or three beads followed by the gradual introduction of new beads representing the flow of polymer into the jet, or a guess of the jet profile is made and divided into suitable mass beads, allowing the model to evolve over time without introducing new beads. Accordingly, the above perturbation can be introduced with each new bead or can be uniformly applied at the beginning of the simulation to the entire jet of beads suspended in space. In both cases the perturbation is applied to each bead only once and the resulting dynamics occur due to the off axis forces generated from the jet's Coulombic self interaction. Hence the phenomenological explanation given for the jet dynamics is that drawing the jet in a straight line is an intrinsically unstable state and the smallest of "laboratory noise" would cause the deviation into a whipping motion. It is proposed that a string of charges along the central axis is effectively sitting on a local maxima of stability and that any deviation from that state would result in a rapidly growing instability. With the assumption of rapid growth for the instability resulting from any deviation of the stable state it is not required to propose a source for this deviation.

3.3.6 Objections and Refinements

From the initial paper published by Reneker et al. (2000) there have been a number of refinements (Carroll et al., 2011, Kowalewski et al., 2005, 2009, Reneker et al., 2008, Yarin et al., 2001a). Some of these refinement result from direct objections to the original proposed model. These objections are usually that the original form was overly simplistic and hence did not fully account for the physics of an electrohydrodynamic jet.

3.3.6.1 Surface Tension

In the work by Kowalewski et al. (2009) the surface tension force is expanded to account for the thinning of the jet as well as the curvature created by the bending of the jet. These two curvatures are demonstrated in Figure 8. To extend this the surface tension force is extended to the form shown in Equation (3.39). The original form of surface tension only accounted for the resistance to bending in the jet whereas the new version also accounts for the resistance to high rates of thinning.

$$\boldsymbol{F}_{\gamma} = \pi\gamma r^2 \kappa \hat{\boldsymbol{n}} + \pi\gamma r \hat{\boldsymbol{t}} \quad (3.39)$$

Similarly, the work by Carroll et al. (2011) which attempts to connect the two different models presented here (Section 3.2.2 with Section 3.3.1) introduces a similar surface tension term. This term

accounts for the curvature due to thinning of the jet. The form of the force is given below. Here the curvature is given by the rate of thinning (i.e. $^{dr}/_{dz}$) while ℓ represents the length of the segment.

$$\boldsymbol{F}_{\gamma} = 2\pi\gamma\frac{dr}{dz}\ell \tag{3.40}$$

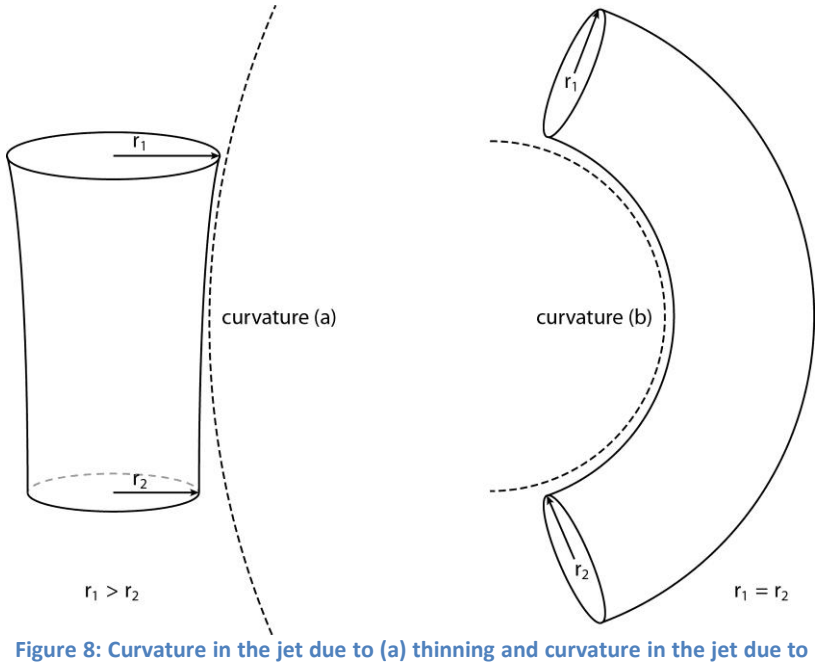

Figure 8: Curvature in the jet due to (a) thinning and curvature in the jet due to (b) bending.

3.3.6.2 Coulomb Force Tends to Infinity in the Continuous Limit

In two published works by the team at the University of Warsaw in Poland (Kowalewski et al., 2005, 2009) it was pointed out that using the simple Coulomb interactions leads to a model that is inconsistent in the continuous limit. They state that the "electrostatic force exerted by a fibre portion of length L_1 on a contiguous fibre portion of length L_2, assuming a constant linear charge density α_q" is as given by Equation (3.41). The solution to this integral is infinite. As such the model in the limit as ℓ (distance between two mass points) tends to zero (i.e. as the jet being modelled becomes continuous rather than discrete mass points) is that where the force generated by the Coulomb interactions chosen becomes infinite. As such this choice of electrostatic interactions causes errors when one attempts to keep the distance between mass points small to improve accuracy. The team proposes a different electrostatic interaction model that they call "ring charges" where one takes the charge on the mass point (q) and spreads it evenly over a ring with a radius equal to the jet diameter (r) and calculates the interaction between two rings aligned on a common axis. The alternative electrostatic interaction takes the form given in Equation (3.42). In this case as ℓ tends to zero the force between two rings tends towards a finite value. This can be seen in Figure 9 where only when ℓ is larger than r does the function asymptotically approach the same value as

Coulomb's law for point charges. Hence now the length of the segments can be reduced to improve the model accuracy.

$$F_{1\to 2} = \int_{-L_1}^{0} dz_1 \int_{0}^{L_2} dz_2 \frac{k_e \alpha_q^2}{(z_2 - z_1)^2} \tag{3.41}$$

$$dF_{2\to 1} = -k_e \frac{dQ_1 dQ_2}{(z_2 - z_1)^2} \times \frac{2}{\pi} \int_{0}^{\frac{2}{\pi}} \frac{d\varphi}{\left[1 + \left(\frac{2r}{z_2 - z_1}\right)^2 \sin^2 \varphi\right]^{3/2}} \tag{3.42}$$

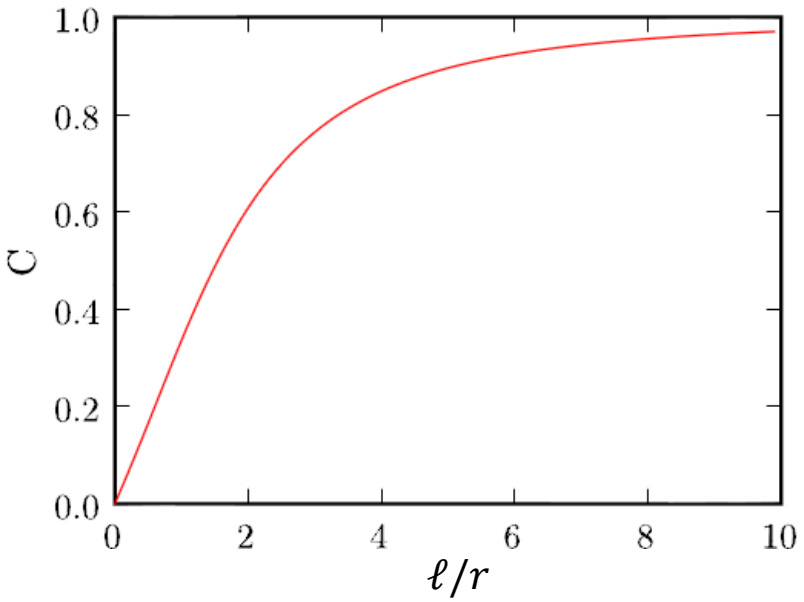

Figure 9: Function introduced to modify the magnitude of the Coulomb force to prevent trending to infinity Kowalewski et al. (2009).

3.3.6.3 Solvent Loss and the Change of State for the Polymer Jet

Shortly following the work published by Reneker et al. (2000) additional work by Yarin et al. (2001a) presented an extension to the above described model that included evaporation of the solvent. As a first approximation an empirical relationship was used to describe the saturation vapour concentration of water at a given temperature. This was compared with the atmospheric relative humidity to provide a solvent mass loss rate over time. This was then combined with another empirical relationship between the polymer viscosity and solvent concentration to allow the viscoelastic properties to vary throughout the jet evolution. Including change of state from solution to solid polymer delayed the onset of the bending instability overcoming the stabilizing forces in the jet. The growth rate of the bending loops was also reduced to a level more consistent with experimental observations. The empirical relationship was used to calculate the viscosity in the jet at a given time. It was found that the viscosity rapidly increases to its plateau region (forced by the model) from the onset of the bending instability. It is suggested that although the model keeps

simulating the jet as a liquid with high viscosity, once the bending instability sets in the jet becomes dry and hence unable to stretch significantly. The empirical relationships could not account for this but experimental observations suggest this may be the case. The key part of this work relating to the phenomenological description is that solvent loss and hence the change of state is vital to suppressing the electrostatic forces driving the bending instability and preventing rapid and uncontrollable growth. Indeed, as the loss of solvent is related to surface area as the jet thins solvent loss would increase resulting in a faster drying jet. This then becomes a natural mediator for the growth rate of the bending instability.

3.3.6.4 Perturbation Uniformity

The three main works that were incorporated into this model (Reneker et al., 2000, 2008, Yarin et al., 2001a) all work with a perturbation that drives an axisymmetric bending instability (see Equation (3.38)). By perturbing jet segments with a set frequency the bending loops naturally form a series of symmetrical loops that expand around the central axis. Experimental observations, however, have shown that this is not how electrospun fibre behaves. Figure 10 and Figure 11 both clearly show that for the first short distance the uniformity exists but after that the jet path decays into a non-uniform chaotic behaviour. The jet path always resides within the whipping envelope, but its path is effectively random. The work by Kowalewski et al. (2005) addresses this by introducing a random perturbation rather than one defined by a frequency. The form of this is given in Equation (3.43), where ϵ is the size of the perturbation. The resulting jet paths appear to match much closer to that seen in Figure 11.

$$x = \epsilon \sin(rand)$$
$$y = \epsilon \cos(rand) \tag{3.43}$$

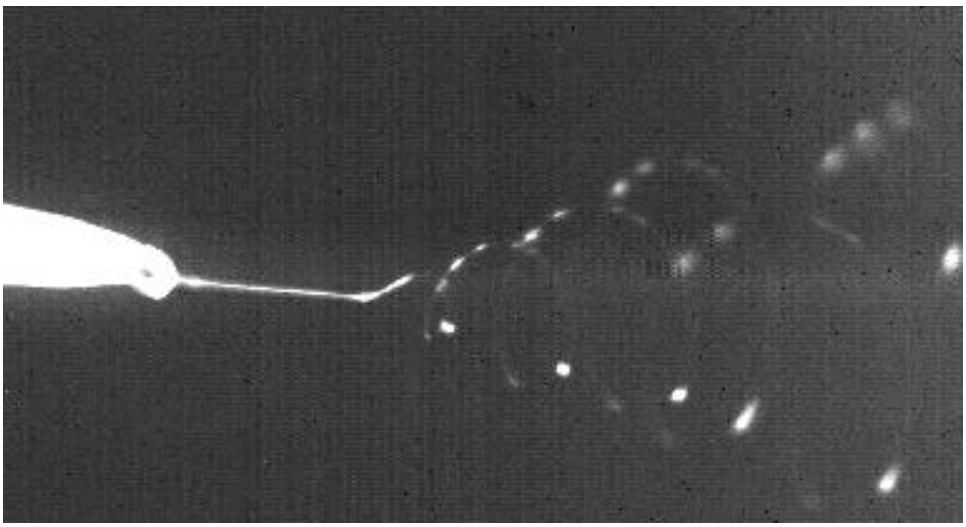

Figure 10: High Speed Image of Electrospinning Jet. 10,000 fps, 10% poly(vinyl alcohol) in water.

Figure 11: High Speed Image of Electrospinning Jet. 1/1000 s shutter speed, 10% poly(vinyl alcohol) in water. Photographer – Robert Lambert, Plant & Food Research, New Zealand

3.3.7 Further Developments

3.3.7.1 Multiple jets

Having a simulation of the path of a self interacting electrically charged jet in three dimensional space the natural extension of this is to put a second copy of the simulation next to the first to study jet-jet interactions. This is what was attempted by Theron et al. (2005) where a simulation consisting of a 3x3 grid of jets or a single line of nine jets was studied. Qualitatively it was found that the jets near the outside of any nozzle arrangement would be bent away from the internal jets. Additionally the internal jets would be confined by the outer jets, making the whipping envelope smaller relative to a single jet. The only quantitative test was to measure the envelope angles for the single line of nine jets along the line of jets and across the line of jets. It was found that the whipping envelope was confined by its neighbours and would balloon outwards on its unconfined sides.

3.3.7.2 Debye Layer for Conductive Fluids

In the attempt to create a correlation between the model by Feng (2002) (Section 3.2.2) and the model by Reneker et al. (2000) (Section 3.3.1), Carroll et al. (2011) found that for highly conductive fluids the bending instability model required two modifications. The first was a simple one, accounting for the two methods of charge transport in a fluid system, convection and conduction. This is done by introducing a charge conservation equation of the form below. This is analogous to Equation (3.2) used in Section 3.2.2.

$$\pi r^2 \sigma E + 2\pi r v \delta_q = I \tag{3.44}$$

Introducing this charge conservation equation for highly conductive fluids results in all the charge being transported in the conducting mode (hence not on the surface) within the Taylor cone resulting in no electrical-based thinning. This does not match physical observations as there is a clear difference in the thinning of the jet with and without the electrical field for all cases where a jet can

be generated. It is then proposed that the conducted charges that are near the surface sufficiently to interact with external fields will also participate in electrically driven thinning. A reasonable estimate of the portion that may interact with external electric fields is the charges within the Debye layer. One can calculate the thickness of the Debye layer and using the known radial symmetry determine the volume fraction of the charge that can interact. In the case of highly conductive polymers this could account for as little as 0.1% of the total charges.

3.3.7.3 Parameter Sensitivity Analysis

The model defined above (Section 3.3) includes many initial conditions and dimensionless parameters. Taking the assumption that the model approximates the real world results it can be informative to study how changing each initial condition changes the resulting fibre as was done by Thompson et al. (2007). This work found a number of trends of which some of the more relevant ones will be discussed here. Increases in charge density were predicted to increase the fibre diameter. This implies that counter to the intuition that more charge would increase stretching, the jet travels as a whole unit across the gap with less stretching, in some cases even suppressing the onset of the bending instability. Increases in collector distance were predicted to decrease the fibre diameter. This is likely due to more time for thinning and whipping to occur. This explanation would depend on flight time being linked to flight distance. Increasing the initial jet radius was predicted to increase the fibre diameter. This seems to imply that the forces dictating the thinning rate of the jet will not increase in proportion to an increase in initial jet diameter resulting in a thicker overall jet. Rheologically speaking, increasing the relaxation time or decreasing the extensional viscosity was predicted to result in a thicker fibre. This again points to the importance of rheological properties in electrospinning. It would appear that in this case a higher relaxation time in the polymer results in more resistance to stretching, while lower initial extensional viscosity will result in more initial stretching but as a result a lower overall level of stretching due to a thinner jet having less self-repulsion.

3.3.7.4 Secondary Bending Instability

Observations have been made of microscale-diameter coiled fibres on collectors (Reneker et al., 2008). It is proposed that this is due to an additional bending instability that occurs after the first. This secondary instability would treat the axis of the jet in the first instability as its central axis and whip around that axis. This instability would occur after most of the solvent is lost and hence is of significantly smaller amplitude than the original, resulting in small coils of fibre. Some photos of this instability have been obtained (Theron et al., 2005) which demonstrate its existence. The extension of the identical dynamics from the above model (see Section 3.3) to be applied to the already whipping jet normal to its central axis results in a simulation approximating the dynamics theorised.

Additionally the possibility of a tertiary instability is proposed. This proposes that the phenomenon of the electrospinning bending instability is not limited to the simple case of a straight jet in air but potentially to any electrically charged fluid jet. This would make it the electrical analogue to the aerodynamic instability.

3.4 Conclusion

There has been extensive work done in attempt to simulate the process of electrospinning. This chapter has provided a detailed review of these attempts in simulation. Each model represents state-of-the-art understanding regarding the underlying physics that are responsible for the electrospinning process. As such they can be considered examples of attempts to produce a generalized model of electrospinning. However, the continued development of these models, without restriction to specific cases, indicates that they are yet to be considered complete. Specifically, existing models generally focus on describing a generic viscoelastic electrohydrodynamic fluid in a vacuum with a uniform electric field. The focus of further development has been on solvent loss, bead formation or jet stability and more complex viscoelastic behaviour. Without a theory to describe the accumulation of charge within the fluid the models are forced to use charge conservation and treat the electric current as an initial variable. There have been observations of corona discharge published in literature indicating the possibility that this may constitute missing underlying physics of the process. This would require the removal of the vacuum assumption. No model has explored the possibility that electric charge may not be conserved within the jet throughout the process despite the fact that charge on the fibre is the primary force driving electrospinning. It is clear that these models would benefit from further experimental observations of the electrospinning process being reported, specifically regarding the behaviour of charge in the process, to improve the understanding of the primary underlying physics of electrospinning.

CHAPTER 4

CURRENT MEASUREMENT IN THE ELECTROSPINNING PROCESS

4 Current Measurement in the Electrospinning Process

4.1 Introduction

The electrospinning process is driven by the application of electric charge to the surface of a polymer solution. To understand the behaviour of the process it is important to start with understanding the flow of charge in the system. As the electrospinning jet is a highly charged, large specific surface area object moving quickly through space it is plausible that charge might be lost due to interaction between the jet and the environment.

The electric current flowing between the high voltage power supply and the nozzle electrode is, by definition, the flow of charge ($I = \frac{\partial q}{\partial t}$) through the system (Figure 12). Similarly the electric current flowing between the collector electrode and ground is the flow of charge leaving the system (Figure 12). By comparing the electric current measured at the nozzle and at the collector one can determine if the charge entering the system survives to exit the system. Note that charge conservation is not being questioned, simply the conservation of charge in the limited system of two electrodes with a polymer flow between them in an infinite vacuum.

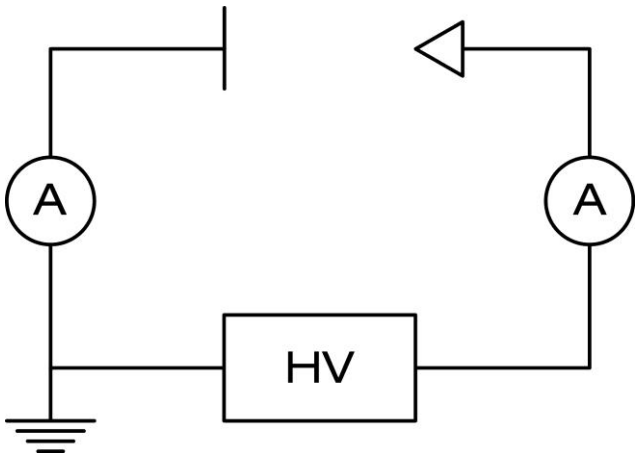

Figure 12: Diagram of electric current flow in the electrospinning system.

Due to the very high voltages involved, traditional methods of measuring the voltage drop across a resistor are difficult. However, it is possible to isolate the measurement device and "float" the device to get a reading. "Floating" refers to raising the entire measurement apparatus to the high voltage of the electrode which will generally eliminate the possibility of damage to the measurement hardware. This raises the question of the validity of the reading in terms of the current being drawn by the process rather than any current drawn due to the introduction of the measurement hardware. As the measurement is sought to establish a difference in current flow at points in the system care must be taken to ensure that the measurement technique does not affect the accuracy of the data.

4.2 Experimental Details

4.2.1 Materials

Electrospinning was carried out using an aqueous solution of poly(vinyl alcohol) (PVOH) (Chemiplas NZ limited, Wellington, NZ). The PVOH had an average molecular weight of 118,000 $gmol^{-1}$ and degree of hydrolysis (DH) in the range of 85–90%. The polymer solution was prepared by dissolving PVOH in distilled water for approximately 2 h at 60°C with constant stirring using an impeller blade in an overhead stirrer running at 500 rev/min. The final stock polymer concentration was determined by drying a small sample in a convection oven at 80°C to find the weight of solids. The stock solution was then diluted to a final PVOH concentration of 8 wt.% using distilled water.

4.2.2 Apparatus

All samples were electrospun using a Model ES4 electrospinning platform (Electrospinz Ltd, New Zealand). The pressure of the polymer solution at the spinning head (varied by a gravity feed system) was used as the control variable. Once stable spinning was attained the pressure was kept constant. The high voltage electrode was a nominally 30 mm o.d. stainless steel tube with a 2 mm wall thickness. The spinning tip was an Axygen T-200-Y 200 µL pipette tip with a nominal inner nozzle diameter of 0.5 mm. The high voltage electrode was held in an adapter to allow the inline resistor to be connected between the electrode and the high voltage supply (Figure 13). Clean 150 mm square sheets of stainless steel were used as collector electrodes.

All digital multimeters used were Digitech model QM-1500 (RS Electronics Ltd, New Zealand). The inline resistors used were high precision (0.01% tolerance) 10 kΩ resistors (RS Electronics Ltd, New Zealand). An additional Glassman MK50P1.5 high voltage power supply was used to provide direct current feedback for data logging experiments as the EMCO power supply included with the Electrospinz Ltd platform does not include current feedback.

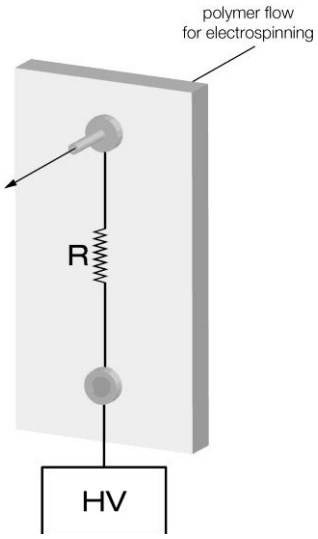

Figure 13: Diagram of inline resistor for current measurement.

4.2.3 Methods

The current drawn at the high voltage electrode was measured in two ways. First, the high voltage electrode was separated from its intrinsic connection to the high voltage supply then reconnected using a high precision resistor to allow the current to be measured (Figure 13). The electric current could then be determined using Ohms law ($V = IR$). If an appropriate value is chosen for this inline resistor then the voltage drop measured across it will be in the millivolt range for the current flow expected. Considering the entire electrospinning process as a circuit, this means that the applied voltage at the Taylor cone will be effectively identical with or without the resistor inline.

Measurement of the voltage drop across this resistor can then be done in a number of ways. One method used was to take a digital multimeter and "float" it at high voltage, ensuring that the leads and case were kept free in air or on an insulating bench (Figure 14). This provided quite a lot of disturbance to the electric field and added the risk of accidental discharges due to the large additional surface area with sharp edges and corners being charged along with the high voltage electrode. This method was improved in terms of quality of the results and safety of measurement by building a digital or analogue panel meter into the adapter shown in Figure 13, resulting in the device shown in Figure 15.

Finally, depending on the availability of suitable equipment it is possible to use the current feedback output of the high voltage power supply such as that available on the Glassman MK50P1.5 high voltage supply. This is a voltage obtained using a voltage divider circuit internally within the power supply. It is measured before the output of the high voltage and so is representative of the total load that is applied at the end of the high voltage cable.

Figure 14: Photo of multimeter mounted to allow meter to float at high voltage.

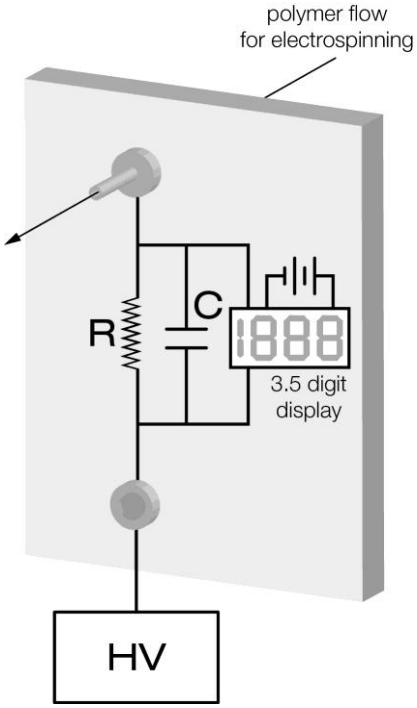

Figure 15: Built in meter for measurement of current at high voltage. Capacitor, C, represents the intrinsic capacitance of the meter. Note: this will effectively act as a high pass filter to eliminate quickly changing signals.

Measuring the current drawn by the collector electrode is essentially the same as the process outlined above with the inline resistor. Again a resistor with sufficient precision is chosen and placed inline between the collector electrode and ground (Figure 16). This effectively lifts the collector electrode to a voltage above ground. If the resistor is correctly chosen, however, then this should be less than approximately 50 mV which in the scale of the electric fields applied in the system is negligible.

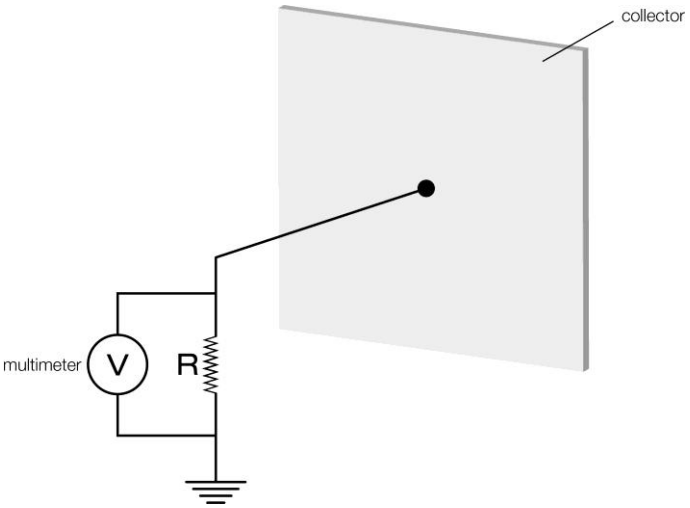

Figure 16: Photo and diagram of resistor used to measure current flowing from collector to ground.

In all cases the experimental method to determine if there is a difference in electric current and hence charge at the high voltage electrode compared with the collector electrode involves fixed distance, polymer and environmental conditions and changing the voltage from onset of spinning to an upper limit where stable electrospinning is difficult to maintain. In the work described in this chapter the distance was fixed at 100 mm and the voltage started at 5 kV and swept up to 18 kV.

If there is a low voltage signal from a current feedback output on the high voltage supply and the inline resistor to ground available then computer data logging becomes feasible. Using a compactDAQ platform (National Instruments Corporation, Austin, Texas, US) for high speed data acquisition it is possible to collect signals representative of the electric current leaving the high voltage supply and arriving at the collector electrode. It is also possible to automatically step the output high voltage and collect a signal representative of the supply output voltage (full program details given in Appendix A). This allows for rapid data collection, and thus the collection of many data points over a period of time. Taking an average of the significantly larger set of observations for a single condition gives a more accurate representation of the long-term current draw by the process rather than the transient current associated with events such as changing the constant head pressure or cleaning the spinning tip. This also gives the opportunity to perform statistical analysis and give a standard deviation of the observed signal and hence an indication of the error associated with the measurement. Further discussion of error in the current measurements will follow later.

4.3 Results and Analysis

4.3.1 Ohms Law

Before making observations of the electrospinning process itself it is prudent to determine if the assumptions regarding methods proposed hold true. To this end using both the floating multimeter method and the compactDAQ platform described above, the value of a chain of resistors was determined (See Figure 17). This chain consisted of 28 3.3 MΩ resistors (10% tolerance) giving an expected resistance of 92.4 MΩ ± 9.24 MΩ. Using $V = IR$ the observed current can be plotted against the high voltage applied to determine R. The voltage used was 0–5 kV for the floating meter and 0–3 kV for the compactDAQ method. As Ohms law is a linear function, a non-linearity cannot physically happen. So any non-linearity would indicate that the measurement apparatus is not recording either the true voltage, electric current or both. This would require the apparatus and method to be revisited. A value of resistance outside of the tolerance would suggest that there is a systematic error introduced in the method that needs to either be characterized or eliminated. It can be seen from Figure 17 that both methods give linear relationships, but each method gives a slightly different value. The compactDAQ/Glassman supply pair gives a resistance of 94.5 MΩ whereas the floating meter/EMCO supply pair gives a slightly higher resistance of 99.9 MΩ. As each method uses

a slightly different approach and a different high voltage supply it is not surprising that the results are slightly different. However, each method gives a result within the expected tolerance of the resistor chain (i.e. >101.6 MΩ).

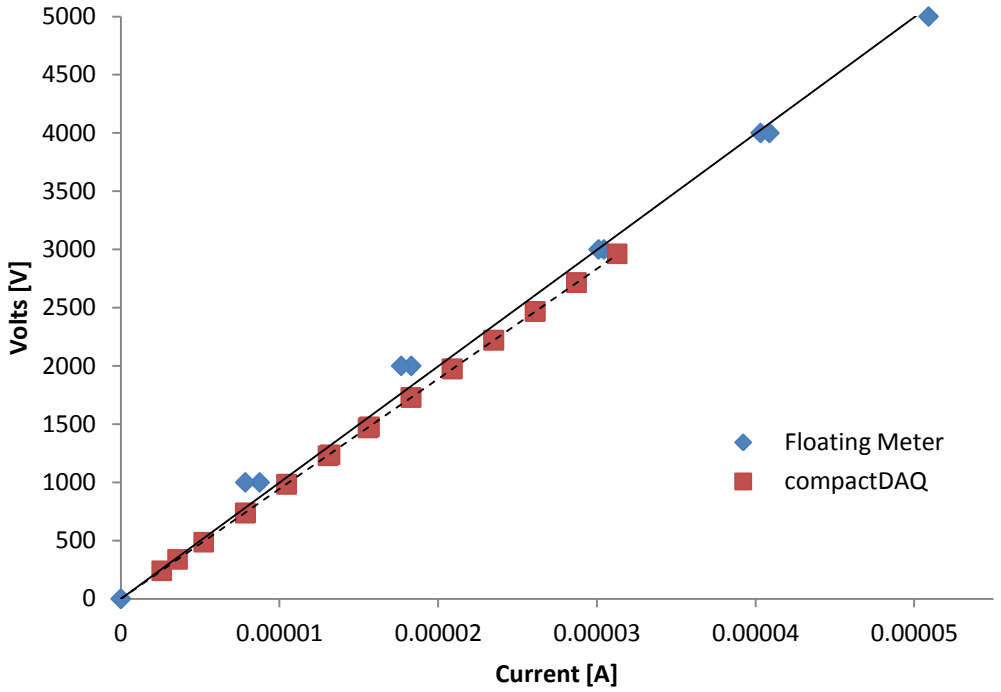

Figure 17: Ohmic relationship observed using data logging methods. The floating meter method gives a resistance of 99.9 MΩ (R^2 = 0.994). The compactDAQ method gives a resistance of 94.5 MΩ (R^2 = 1.00).

4.3.2 Signal Noise

It should be noted that initial trials with the compactDAQ/Glassman supply pair showed such significant noise that it was difficult to determine if the desired signal existed under the noise. It was found that there was a high frequency signal overlaid on the voltage and current feedback signals (see Figure 18). This signal appeared to be invariant with the magnitude of the feedback signal. This signal overlaying the feedback signal had a frequency in excess of 50 kHz and a magnitude of up to 0.4 V peak to peak. As the signal being measured was less than 0.2 V for current it is not surprising that this additional signal generated such large noise on the output. The example shown in Figure 19 demonstrates the effects of filtering. The blue signal is the current observed at the high voltage electrode while electrospinning is occurring with no filtering. The voltage changes over time according to Figure 20. The red signal shows the effects of the simple first order RC filter (see Appendix B for a more detailed description) with a cut off frequency of 50 kHz (sample rate is typically 1 kHz which exceeds the Nyquist-Shannon sampling frequency required to observe any signal that passes through the filter).

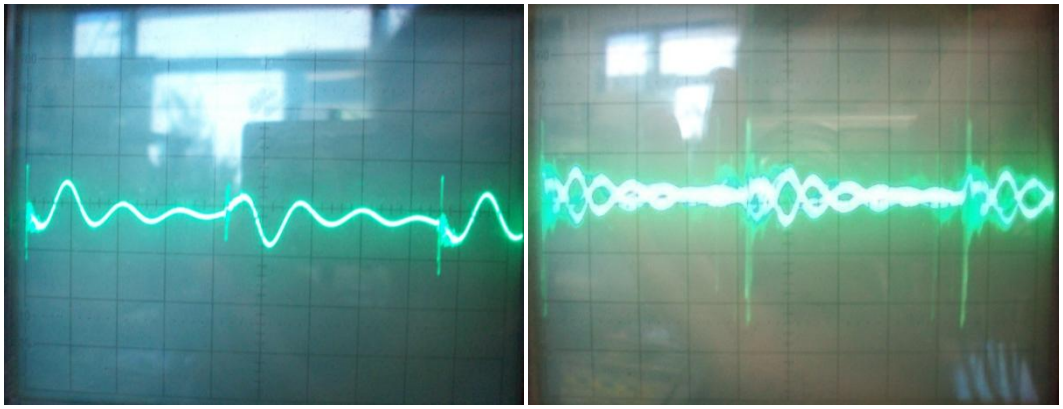

Figure 18:Left: Noise on a constant voltage feedback signal. Time base is 2 µs with voltage divisions of 0.2 V. Right: Noise on a constant current feedback signal. Time base is 2 µs with voltage divisions of 0.1 V.

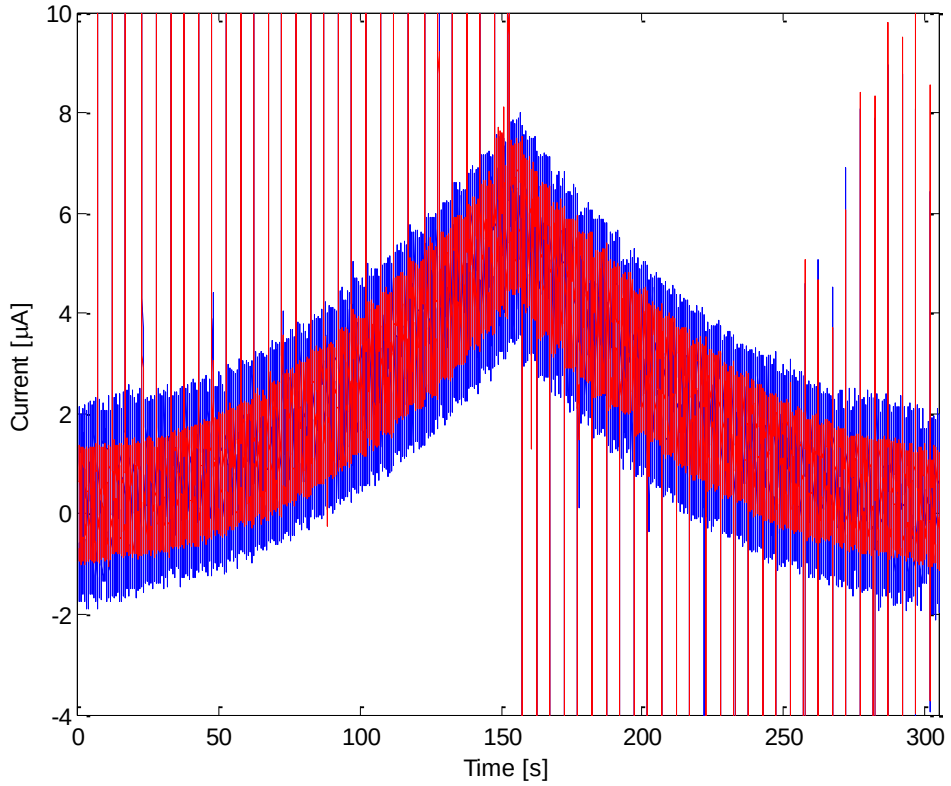

Figure 19: Example of the raw data for high voltage current vs time. The larger blue trace represents the pre-filtered raw data. The smaller red trace represents the same data passing through the physical signal filter. The spikes represent the transition between applied voltages and hence are not relevant data.

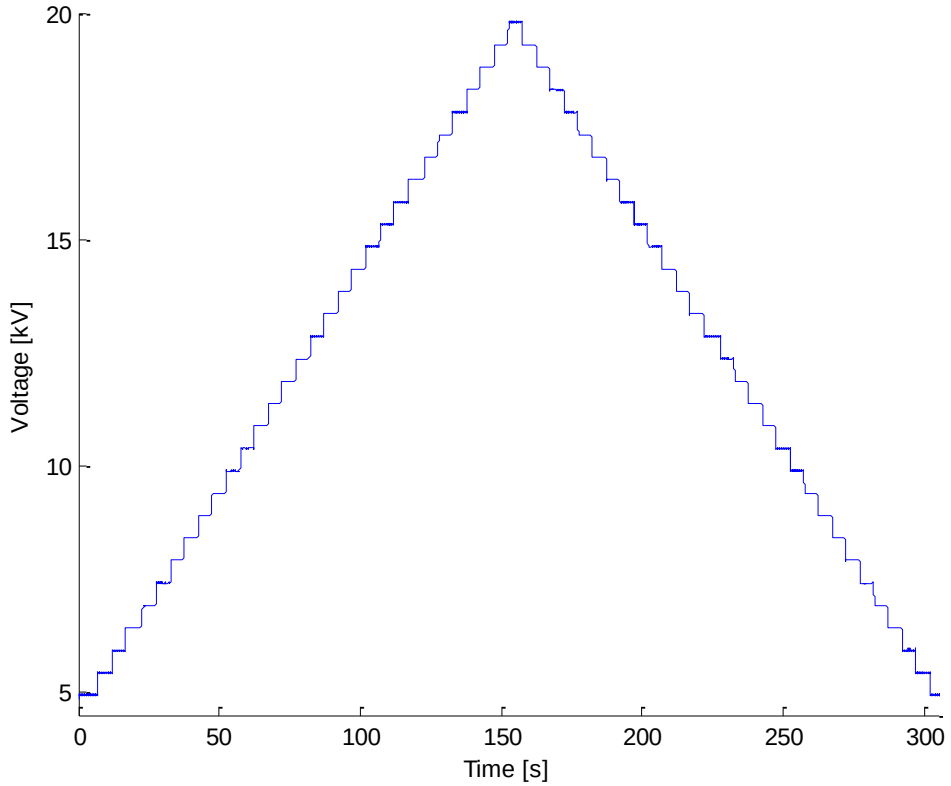

Figure 20: Example control signal sent to Glassman power supply to observe current drawn by electrospinning at different voltages.

The vertical lines occur at each step increase in voltage. For our purposes we are only interested in the steady state so a MATLAB™ script was devised to drop approximately 1 second of data centred on these spikes (see Appendix A). Although this region is currently treated as unusable data, future chapters will examine this phenomenon more closely. Using the MATLAB script to extract a portion of data from both signals, representing a zone where a constant voltage is applied, we can examine the statistical distribution of the current measurement. A typical dataset approximates a normal distribution. To demonstrate the effect of the filtering we can show the expected normal distribution for pre-filtering and post-filtering, effectively showing that the filtering helps the signal to converge on the mean (see Figure 21).

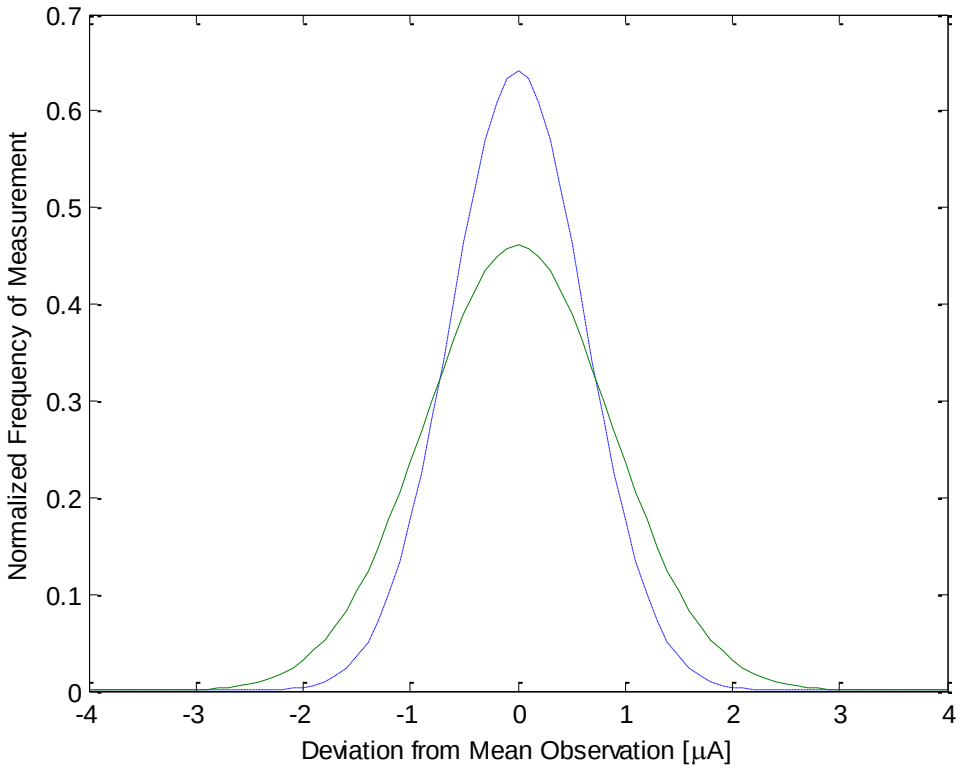

Figure 21: Representation of a typical normal distribution of the observations made during a constant current experiment in electrospinning. This shows the normalized expected frequency of observations that deviate by a known amount of microamps from the expected mean. The solid green line shows the pre-filtering typical distribution. The dashed blue line shows the post-filtering typical distribution.

4.3.3 Calibrate High Voltage Measurements

After eliminating the signal noise the next important stage is to ensure that the voltage measured is calibrated. To do this a Tektronix High Voltage Probe (P6015A) was used to measure directly the voltage on the output terminal. This probe has a reported accuracy of 3% of the voltage measured. The scaled output voltage from the probe was measured using either an oscilloscope or the compactDAQ platform. As can be seen in Figure 22 the required linear relationship was found between the recorded voltage from the high voltage supply and the real voltage seen on the output terminal. The EMCO power supply (Figure 22) has a real voltage 98.19% of the recorded voltage corresponding to approximately 200 V lower than indicated on the display. In Figure 23 we see again the excellent linear response with the real voltage now being 113.3% of the recorded voltage. As each power supply reports voltages shifted in opposite directions it is important to correct for this to prevent unexpected differences in the reported current measurements at a specific voltage.

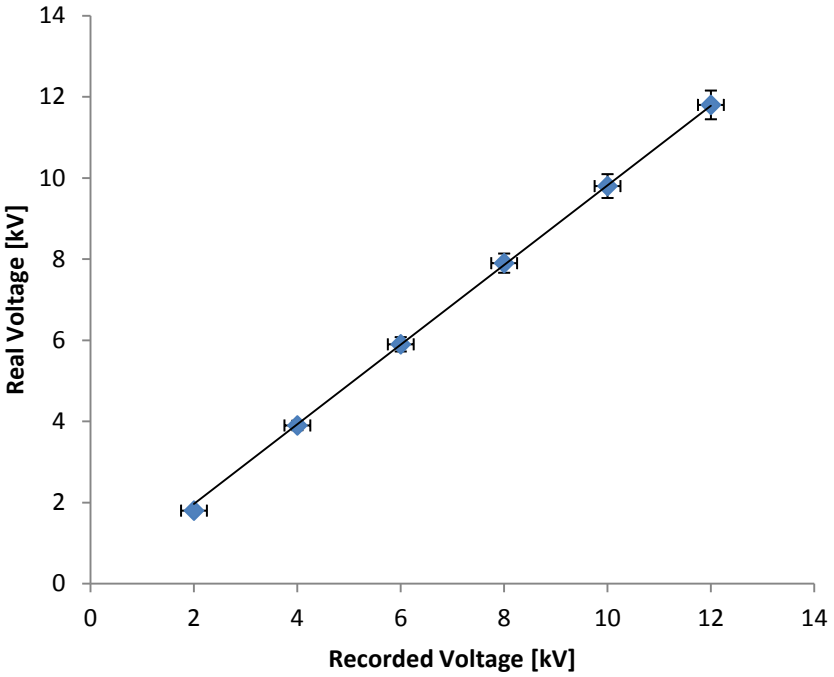

Figure 22: Calibration curve of recorded voltage against actual voltage for the EMCO power supply in the Electrospinz Doris Platform. Note that the recorded voltage has an uncertainty of ±250 V due to the analogue meter that the kV is read from. Linear trend is $V_{Real} = 0.9819\ V_{Recorded}$ ($R^2 = 0.9996$).

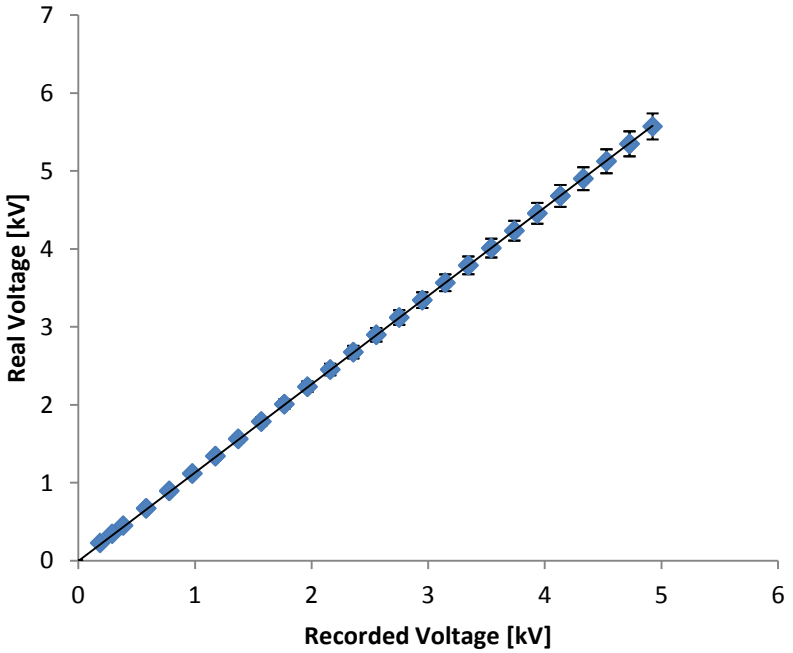

Figure 23: Calibration curve of recorded voltage against actual voltage for the Glassman power supply used with the compactDAQ system. Linear trend is $V_{Real} = 1.133\ V_{Recorded}$ ($R^2 = 1$). Error in the compactDAQ reading of the recorded voltage is marginal and an equivalent error exists on top of the reported error for the real voltage so is omitted.

4.3.4 Does each method return the same results?

The next question to be answered is if we use each method to measure the same phenomena are the results the same? This is effectively asking; does the measurement method matter? If the

current drawn by the high voltage electrode is plotted against the voltage applied for each of the three methods described in the experimental details (Section 4.2.3) we can see that the results differ slightly (see Figure 24). The main difference is between the built in meter and the other two methods. The compactDAQ appears to give results that are very close to the floating multimeter and so these two methods are comparable. This indicates that a different experimental method may produce slightly different results. A number of reasons can be put forward to explain why these differences might exist: solution inhomogeneity, environmental conditions, power supply electronics, measurement electronics and discharge/charge bleed caused by measurement apparatus being introduced. As with all experiments the first question to ask is if the experimental design or equipment has introduced a systematic or random error. All solutions are made to 1 dp precision, which is approximately the precision that can be obtained with a 2-figure balance. The experimental runs aggregated for Figure 24 cover three separate dilutions across a time period of 3 weeks. Across this whole period the data from the compactDAQ was being collected giving us the opportunity to see if different days and solutions make a significant difference. Plotting each run collected using the compactDAQ we can see that all the runs return similar results (Figure 25). The results of Figure 25 were collected across a narrow range of humidities with no discernable effect on the results related to change in humidity and with variation explained by experimental noise. As all runs were done at a controlled temperature of 20–22^{o}C there is no consideration of temperature. The results of the floating multimeter and the compactDAQ shown in Figure 24 were both collected in the low narrow humidity range presented in Figure 25. However, the results of the built in meter shown in Figure 24 were recorded under higher humidity conditions (i.e. >50 %RH) and this may have contributed to the higher readings.

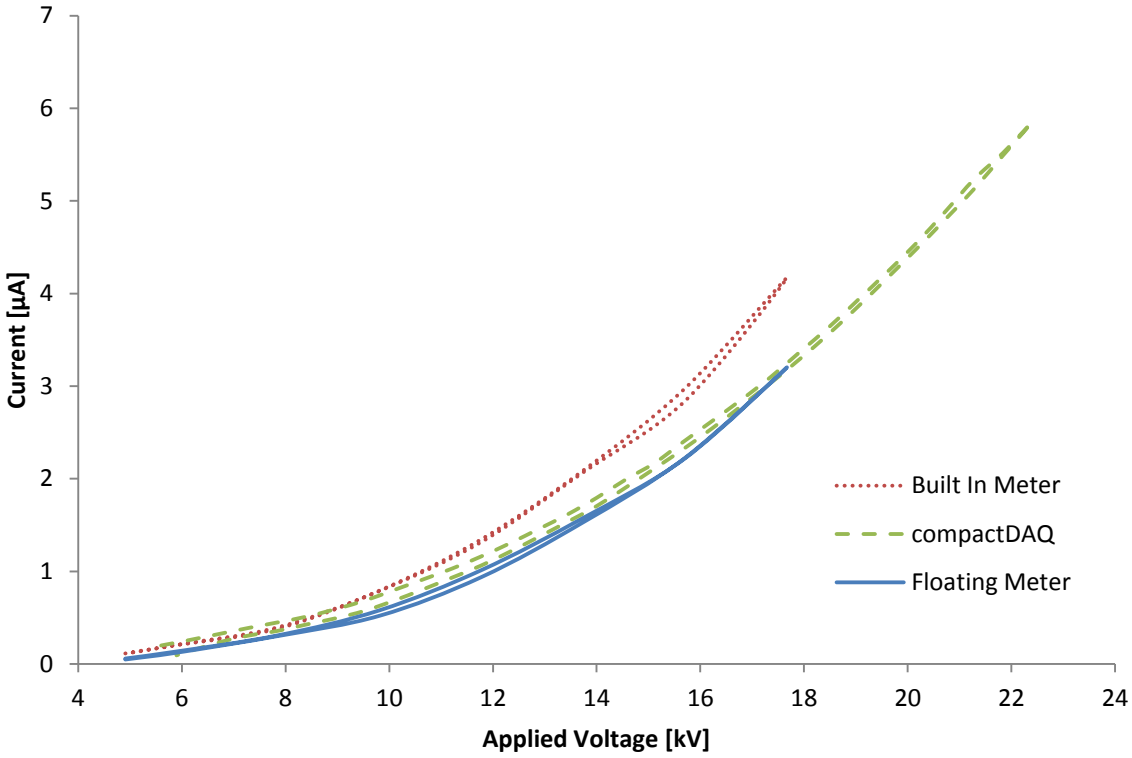

Figure 24: Aggregate plots of each method at 100 mm distance with 8% PVOH. For each method all data recorded under the same conditions was averaged to provide a curve that is representative of typical measurements.

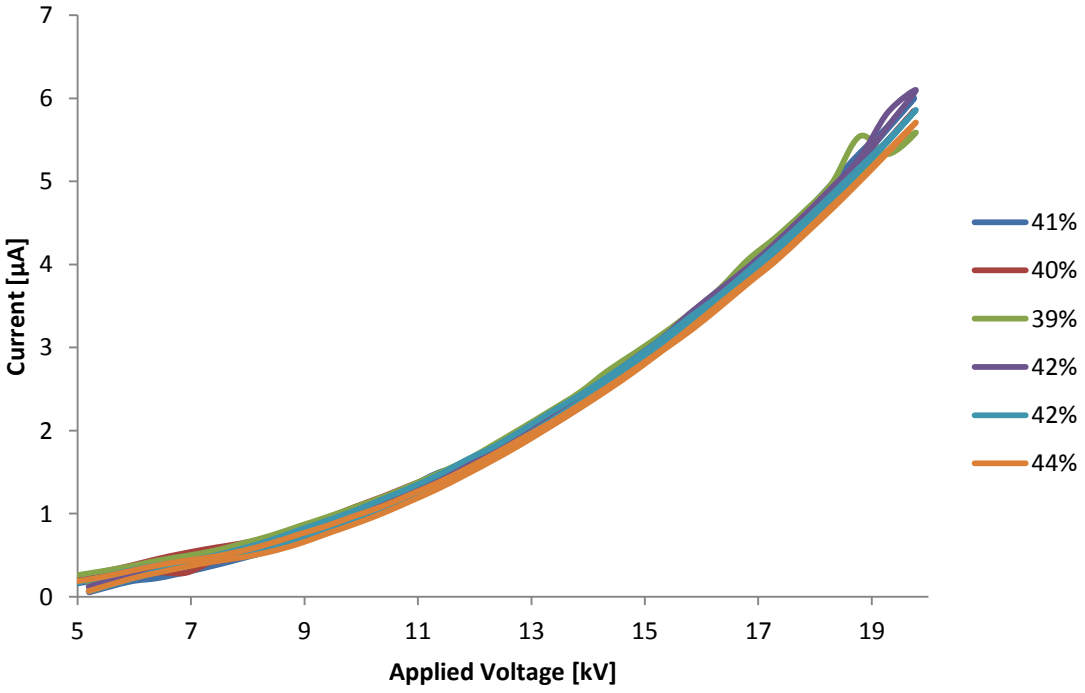

Figure 25: Raw data from the compactDAQ for 8% PVOH electrospun at 100 mm distance for a range of humidities.

As the different measurement methods use different high voltage power supplies (EMCO and Glassman) some of the variation seen in Figure 24 might be explained by the differing power electronics in the supplies. However, the fact that the floating meter and the compactDAQ results overlap in Figure 24 indicates that this is unlikely to be the case. To further explain the difference

one might propose that the electronics used to collect the data may cause a difference in the current observed. In order to answer this question an experiment was done using the compactDAQ and Glassman supply where the built in meter is put inline with the high voltage supply as per Figure 26. The results of this experiment are shown in Figure 27. It appears that the current measured at the high voltage electrode by the compactDAQ is consistently higher than that measured by the floating built in meter. This may be due to the fact that the current signal is measured first by the compactDAQ then the subsequent signal is measured by the floating built in meter (see Figure 26) giving the opportunity for some current to be lost (such as by discharges on the floating built in meter). This shows that measuring the same current with different instruments produces predictably similar results (even when under high voltage conditions).

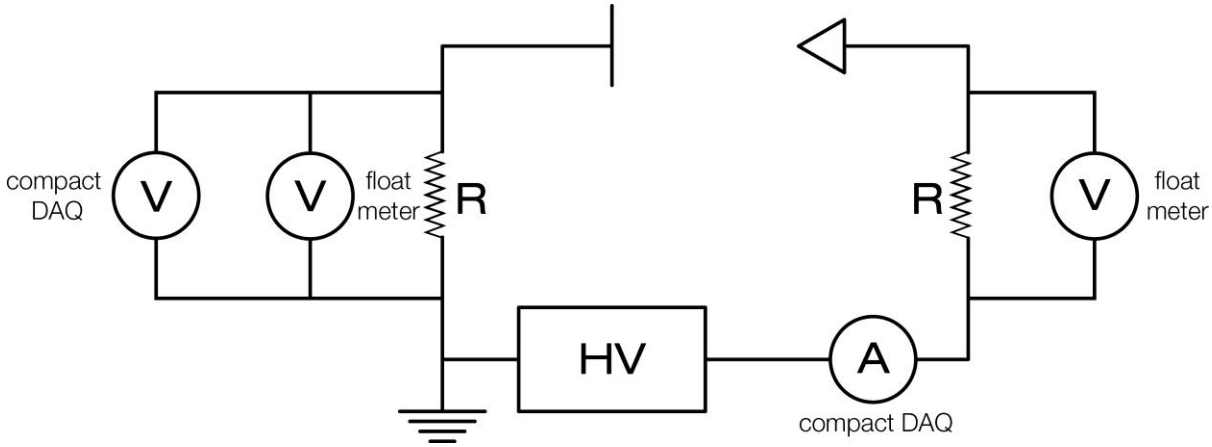

Figure 26: Simplified circuit diagram of the measurement of electric current using two methods simultaneously.

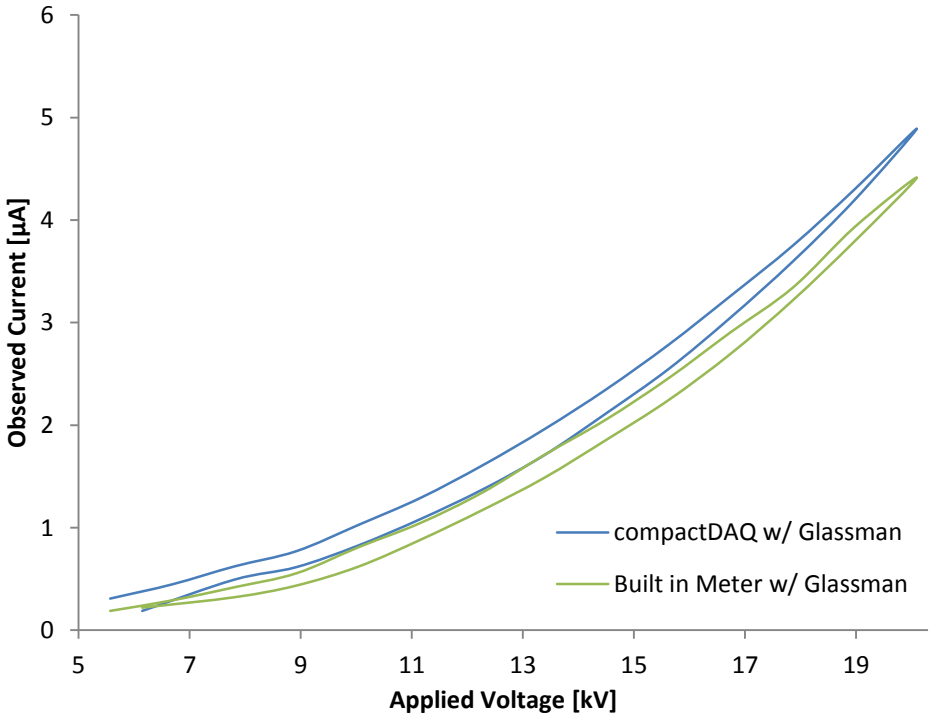

Figure 27: Observed current at the high voltage electrode while electrospinning is occurring using 8% PVOH, 100 mm distance to collector. In line with the compactDAQ/Glassman data logging the built in meter is recording the current.

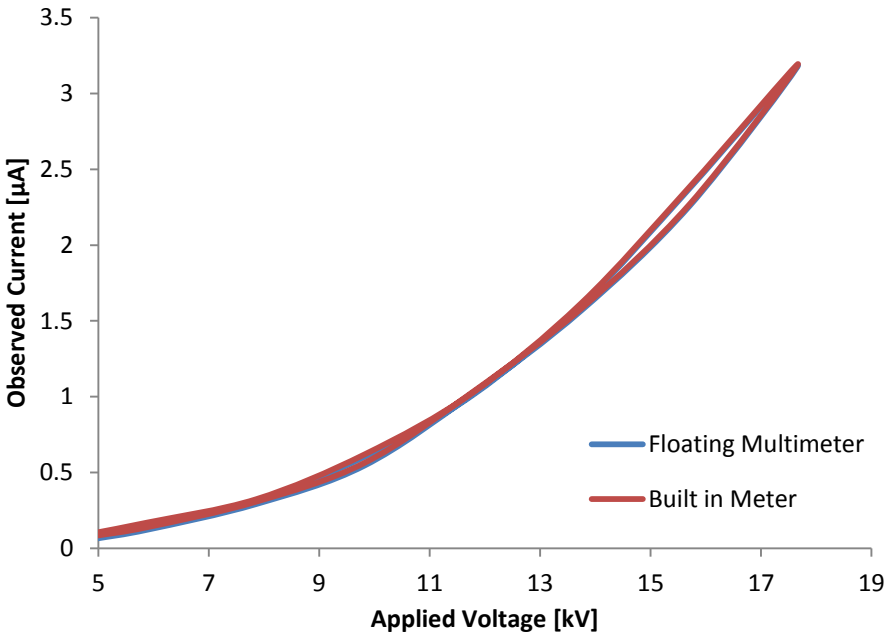

Figure 28: Observed current at the high voltage electrode while electrospinning is occurring using 8% PVOH, 100 mm distance to collector. Both the floating multimeter and the built in meter are measuring the same process simultaneously.

The final question to answer is if there is some kind of discharge or charge bleed process occurring that might explain the difference seen in Figure 24. The easiest way to determine this is to compare the results obtained using the built in meter under different conditions with a "typical" response curve. In this case using the aggregate curve from the compactDAQ method for the "typical" response curve seems reasonable. The results presented in Figure 29 show the importance of humidity control to suppress excessive discharges. The aggregate results for the built in meter were recorded with an ambient humidity as high as 60 %RH whereas later experiments using the same equipment were below 50 %RH. The later experiments undertaken in the lower humidity conditions all overlap nicely with the aggregated compactDAQ data. The built in meter was constructed using "free form" electronics techniques and hence has a number of unavoidable sharp points (see Figure 15). Under higher humidity conditions where the meter floats at voltages in the kilovolt range it is not unexpected that there would be charge leakage from these points or even corona discharges which would significantly increase the observed electric current. For the voltage range considered all experiments should be ideally done when the absolute humidity is controlled below the level present at a temperature of 22^{o}C and 50 %RH.

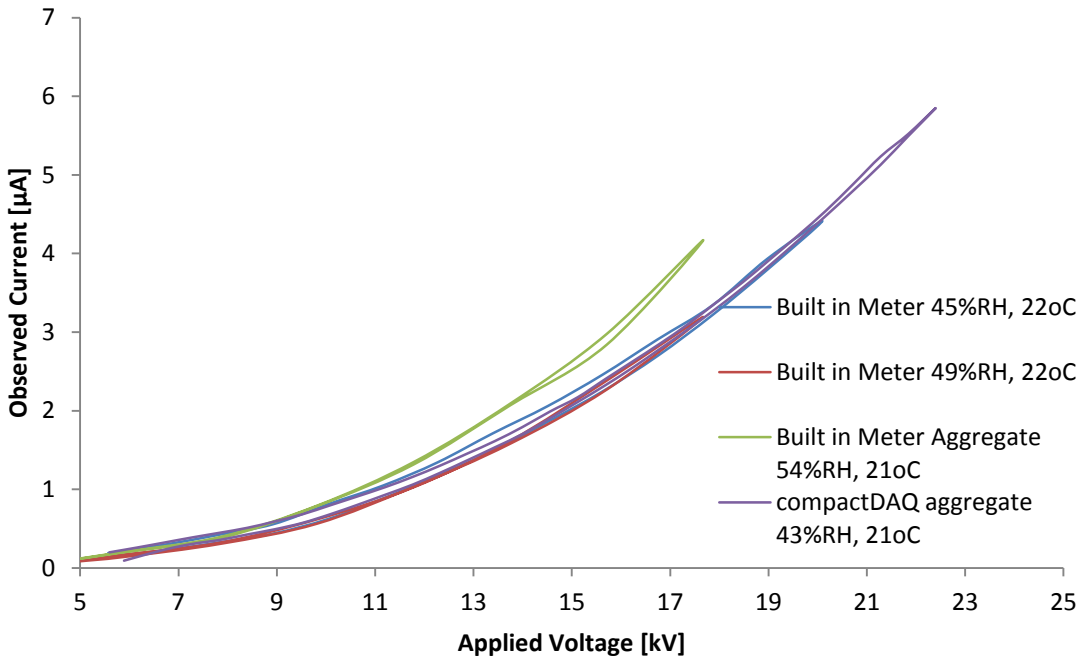

Figure 29: Observed current at the high voltage electrode while electrospinning is occurring using 8% PVOH, 100 mm distance to collector. Both the floating multimeter and the built in meter are measuring the same process simultaneously.

4.3.5 Are the Measurements Repeatable?

Once it was established that each method of measurement returns similar results, it became important to establish if each experiment is repeatable. Performing an analysis of variance (ANOVA) on the data presented in Figure 25 allows us to quantify the variance associated with different factors that change between experiments. This includes a factor that separates each experiment to compare what should be identical runs. The atmospheric pressure was also recorded but had such a small variation (range 1017-1026) that the term was not orthogonal to other terms in the model. As all seven runs were done on three separate days (two groups of three and a single). Day was attempted as a factor, but was found to be non-orthogonal as well. In the context of an ANOVA if a parameter is non-orthogonal then it is not independent of other parameters in the ANOVA model. These non-orthoginalities are likely because of the limited range of environmental conditions and hence one term implies another. Hence from Table 1 the conclusion can be drawn that environmental conditions have a significant response ($p < 0.01$) in the current observed at the high voltage electrode. However, the magnitude of this variance is in the order of the magnitude of the residual variance associated with the data. Within reason, changing the applied voltage accounts for the variation in the data (99.8% of variance). The variance associated with different days is likely to be attributed to the changing environmental conditions. It should be noted that, as per Table 1, once variation due to environmental conditions has been controlled for the variation between runs is not longer significant ($p > 0.05$), so the measurements are repeatable.

Table 2: ANOVA results from the analysis of observed electric current for a range of repeated experiments with 8% PVOH, 100 mm distance.

Source of variation	d.f.	s.s.	m.s.	v.r.	F pr.
Applied voltage	32	1,172	36.63	2082.47	<.001
Temperature	1	0.0499	0.04988	2.84	0.098
Humidity	4	0.4634	0.11580	6.59	<.001
Ambient pressure	4	0.0267	0.00667	0.38	0.822
Experimental run	6	0.0014	0.00024	0.01	1.000
Applied voltage and humidity interaction	128	0.6362	0.00497	0.28	1.000
Applied voltage and experimental run interaction	192	0.1497	0.00078	0.04	1.000
Residual	52	0.9146	0.01759		
Total	419	1,174			

4.3.6 Is the Response Measured Related to the Electrospinning Process?

Knowing that the measurements are repeatable and of good quality, the next question is “are the observations an artefact of applying high voltage to a pair of electrodes?” Applying a high voltage to the electrodes when no polymer is the system does draw an electric current, as shown in Figure 30. This draw is likely due to a small amount of charge leaking at the edges and corners of the high voltage electrode with some being caught by the grounded electrode. It can be seen that the leakage is small (approximately 2–5%) in comparison to when electrospinning is occurring. This is by design as each electrode is carefully rounded to as large a radius as practically possible. However, Figure 30 does not represent the true electrostatic situation. This is because the electrospinning tip and polymer supply mechanism used on the ES4 is made of an insulating material while the polymer solution is a weakly conducting material. So without the polymer solution in the system the observation only represents the energy required to maintain a portion of the electrostatic field.

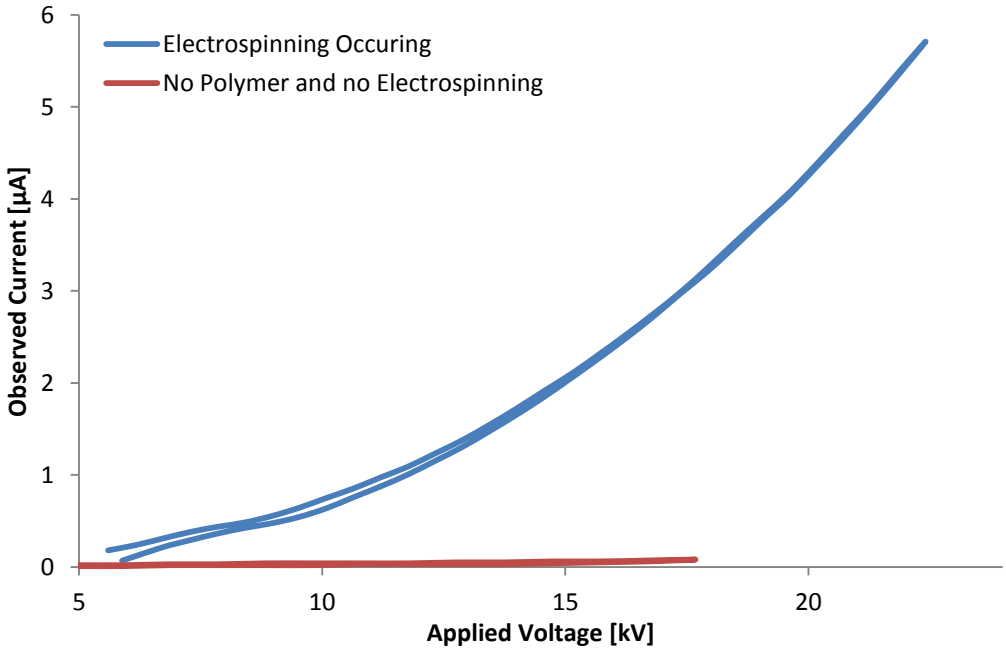

Figure 30: Observed electric current at the high voltage electrode when no polymer is in the system or when electrospinning is occurring. Data is the average of many readings.

To work with a better representation of the true electrostatic field the apparatus was filled with polymer solution but the spinning tip was blocked. The spinning tip tapers down to a sharp point and with the polymer in the system this tapered point is represented. However, to get a true representation one would need to have the Taylor cone established, which would naturally lead to electrospinning so this cannot be done. Performing a similar voltage sweep to Figure 30 when there was polymer in the system shows a markedly different response (see Figure 31). In this case it appears that under a certain critical voltage the response is similar to that seen in Figure 30, but above this critical voltage the electric current drawn is close to that seen when electrospinning occurs.

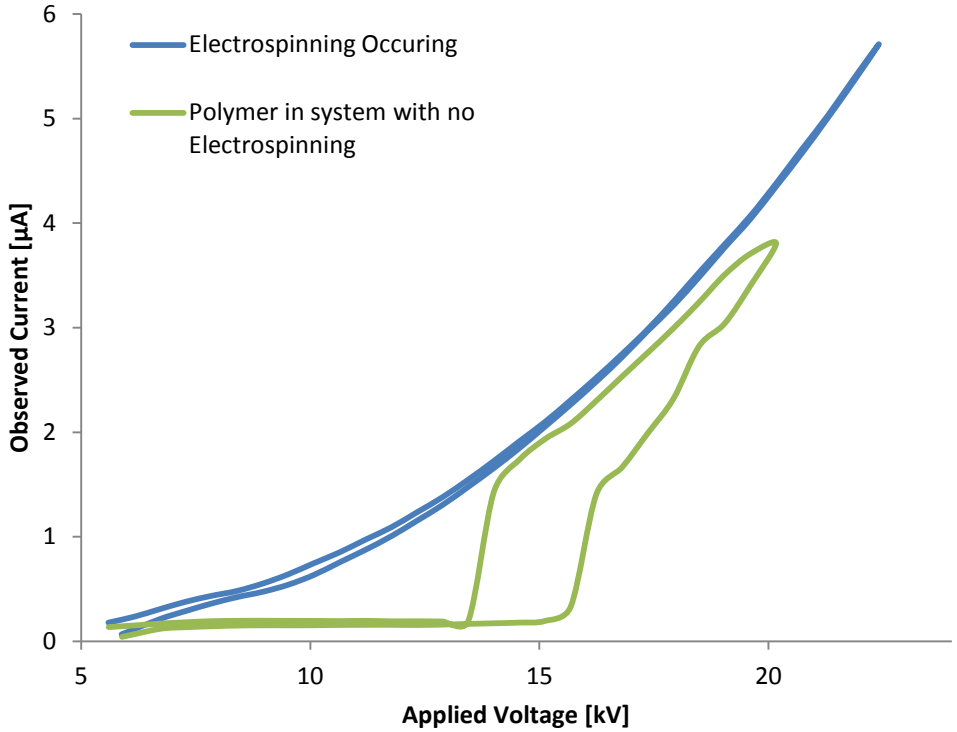

Figure 31: Observed electric current at the high voltage electrode with polymer is in the system but with the nozzle blocked so no electrospinning is occurring. Data is the average of many readings.

The reason for the current drawn at voltages approximately 15 kV and above is probably losses from the sharp points in the system. Once the charge density on the conductive parts of the electrospinning apparatus exceeds a critical level then charge will start to bleed off the surface. This charge bleed is very small compared with the charge contained on the surface but as can be seen is comparable to that drawn to sustain the electrospinning process. The electrospinning jet draws charge away from the highly charged spinning tip and so may act to prevent the build up of charge on a surface sufficient to cause the bleeding of charge into the atmosphere. However, it is likely that, given the energetic nature of an electrode charged to the kilovolt range, some of the current observed using this method is not being carried by the jet. There is no other apparent method to further separate the components contributing to the current drawn by the process so the total

current measured will be used, rather than attempting to define a zero point and subtract from the observations. This should allow for comparison but the limitation of the current measurement techniques should be kept in mind.

4.3.7 Is there More Current Flowing to HV than from Collector?

Having established that the method described in this chapter produces results that are meaningful and relevant to the movement of charge in the electrospinning process the question of whether charge is retained on the jet/fibre can now be addressed. Using the methods described in this chapter, a voltage sweep (5 kV to 20 kv) was performed using the compactDAQ equipment for 8% PVHO in water at a distance of 100 mm to determine if the steady state flow of charge through the high voltage electrode matched that flowing through the collector electrode. Figure 32 clearly shows a significant difference between the electric current observed at the high voltage electrode and that at the collector indicating that some charge is lost while the jet is in flight. Given the small radius (order of 100–500 nm) the jet eventually attains this is not surprising as this level of curvature would produce very high electric fields which is the pre-requisite for charge bleed and atmospheric breakdown. Due to the high charge density carried in the fibre (Stanger et al., 2012) even when the jet is initially ejected with a larger radius (order of 1–10 µm) it may have enough surface charge density to generate the required high electric fields for charge loss.

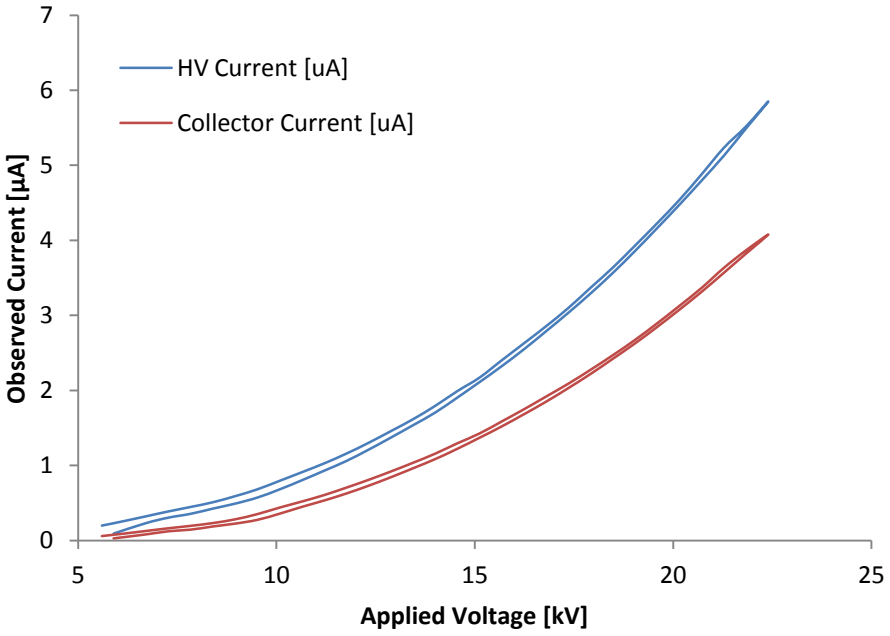

Figure 32: Observed electric current at the high voltage and collector electrodes for a range of applied voltages while electrospinning. Electrospinning was done using 8% PVOH in water at a distance of 100 mm. Data is the average of seven independent experimental runs.

This loss can be easily demonstrated by Figure 33 which shows the percentage of current lost as the applied voltage increases. For voltages below 10 kV the spinning process is difficult to maintain. This is due to the fact that the applied voltage is near the critical voltage that allows electrospinning to

occur. Near this cusp of jet initiation it seems the current drawn to form the static electric field and subsequently initiate the jet is very small. Any loss of charge in flight is likely to have a large impact on the current observed at the collector. Additionally with such a small signal to observe, errors in measurement are likely to play a larger role. However, this large loss is observed both when the experiment is started on the sweep up and at the end of the experiment on the sweep down. This means the large loss is not due to the time period of observation being too short for the process to reach a steady state. Beyond the initially high loss the loss reaches something close to a constant percentage, at approximately 35%. As such this shows that across the range from 12 to 22 kV the current observed at the collector is 35% smaller than that observed at the high voltage electrode, implying that 35% of the charge on the fibre has been lost.

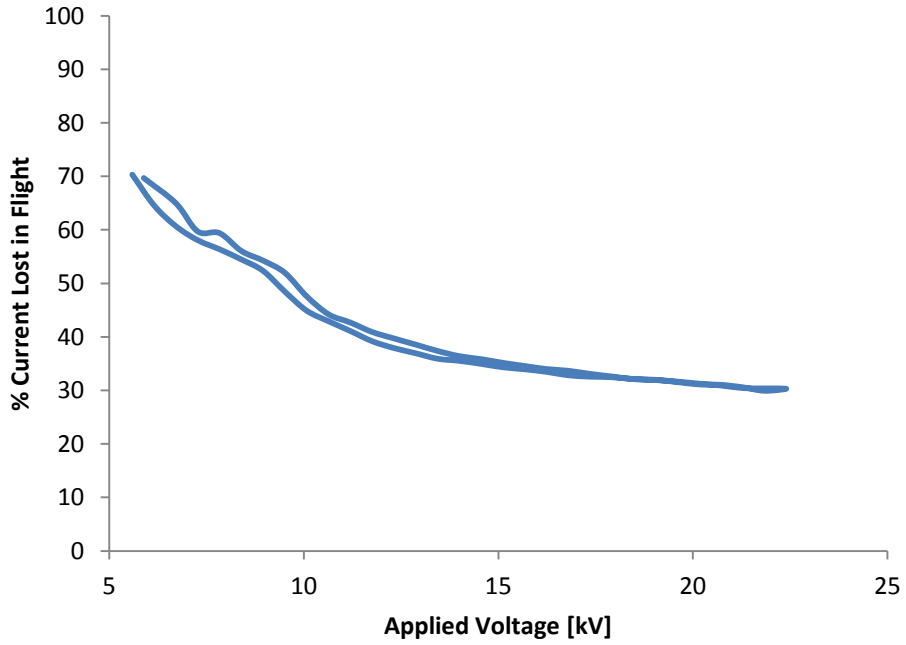

Figure 33: Loss of current flow observed between the high voltage electrode and the collector electrode. Loss is expressed as a percentage of the current observed at the high voltage electrode.

4.4 Summary and Conclusion

The aim of this chapter has been to determine if there is a difference between the electric current drawn from the high voltage power supply to initiate and sustain electrospinning and the electric current flowing to ground at the collector electrode to neutralize the charge on the incoming fibre. Section 4.3.7 shows there is a difference using the method outlined in Section 4.2. After first calibrating the high voltage supplies to ensure both were outputting the same voltage, followed by filtering the noise from the raw signal to eliminate high frequency switching noise it was established that the measurement method could reproduce the results of Ohms Law within expected error. This then led to showing that for low humidity conditions the results from multiple methods of observation were comparable. An analysis of variance of the data from the compactDAQ data

acquisition apparatus showed that the results were repeatable. There was considerable difficulty in establishing what portion of the signal was due to the electrospinning process itself and what portion was due to the application of high voltage to a series of electrodes. However, bearing this in mind, this limitation can be accepted and the results compared on a relative scale rather than an absolute scale. Hence there is a method that can be used to determine if there is a difference in the electric current flow from the high voltage source and from ground. This method demonstrated there is a difference between the high voltage electric current and collector electric current for 8% PVOH in water electrospun at 100 mm distance.

CHAPTER 5

FAILURE OF THE PARALLEL PLATE APPROXIMATION

5 Failure of the Parallel Plate Approximation

5.1 Electric Field Shapes and Electrode Distance

The parallel plate approximation of electric fields is derived from considering a capacitor composed of two infinitely large plates. The equation for the electric field between these two infinitely large plates is $E = V/d$. This approximation works quite well for similarly composed electrode geometries such as near the middle of real world capacitors (where edge effects are small). However, the parallel plate approximation is a poor description of the electric field conditions that influence the electrospinning process. Before examining various observed results a discussion of the electric field will be presented as it is an important quantity to understand when discussing electric charge flow. For simple cases of increasing the applied voltage the electric field will increase in proportion to the increased applied voltage. This is useful to remember, as changing the applied voltage for a fixed electrode geometry will demonstrate how the electrospinning process changes when the strength of the field changes in a predictable way. The situation becomes more complex when the electrode geometry changes. Often the electrospinning geometry resembles point-plane or needle-plane geometry. This geometry leads to a non-uniform electric field often with some elements of axial symmetry (see Figure 34). It is relatively easy to calculate the electric field for a given geometry using a commercial finite element software package such as COMSOL™ to solve the Laplace equation. There are challenges, however, when dealing with geometries of this type. Due to the very small size of the Taylor cone and its associated electrode compared with the tip to collector distance (TCD) the process of solving the Laplace equation leads to unrealistic concentrations of electric field very near the Taylor cone region. This could be avoided by refining the mesh to a much smaller size and accurately modelling the Taylor cone; however, this is somewhat impractical and unnecessary.

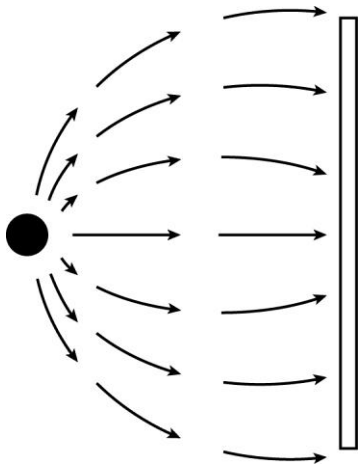

Figure 34: Electric field shape for a point-plane geometry.

Taking into account the likely axial symmetry we can simplify the presentation of the changing electric field strength with respect to TCD by plotting the axis between the centres of both

electrodes (see Figure 35). This figure has been truncated as the peak electric field strengths are unreliable (see discussion above) and obscure the detail where they flatten out. Figure 35 shows that the effect of changing the TCD influences the electric field strength more at short distances (50 mm) than at long distances (150 mm). It is also possible to infer from Figure 35 that the electric field becomes more uniform at longer distances. Uniformity here is taken to mean the variation of the strength of the electric field at points away from the axis of symmetry. Figure 35 also shows that the electric field strength does not vary proportionately to the TCD. This is all due to the concentration of electric field lines caused by the point or needle in the geometry.

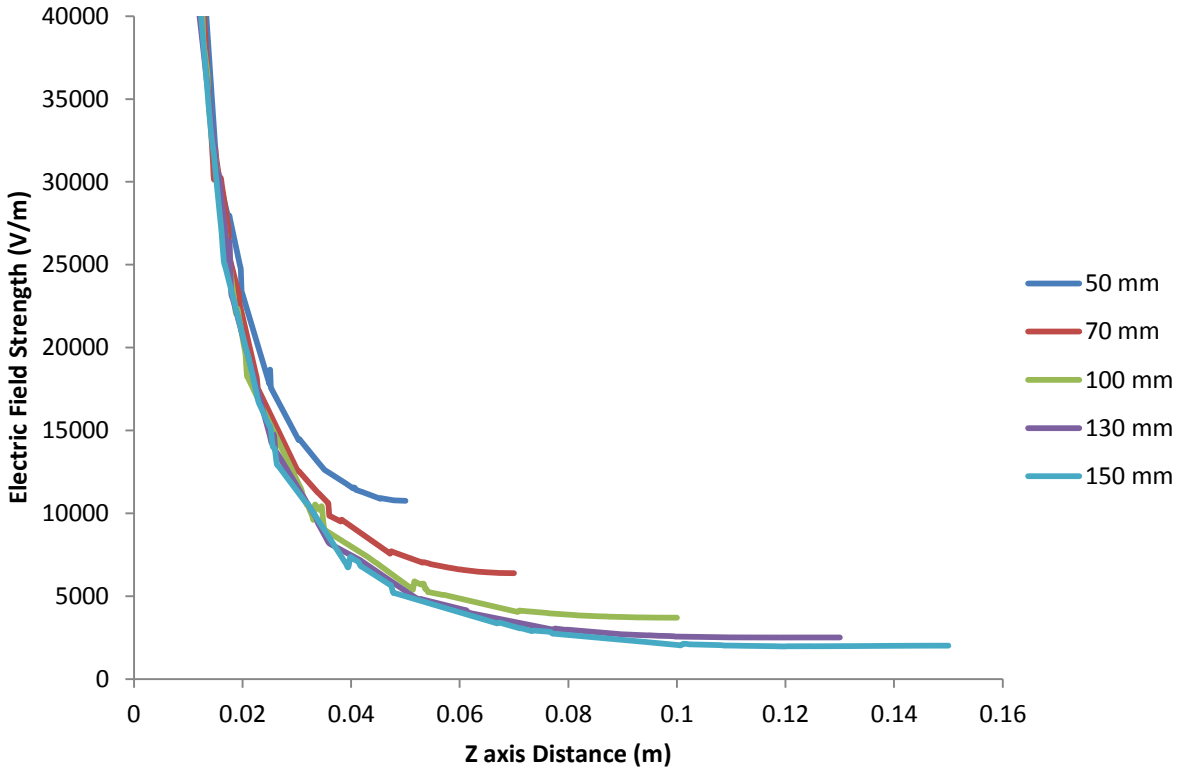

Figure 35: Axial electric field strength for different electrode distances of a needle-plate geometry with a potential difference of 5000 V.

5.2 Parallel Plate Approximation for the Electric Field

5.2.1 Materials and Methods

Electrospinning was carried out using an aqueous solution of poly(vinyl alcohol) (PVOH) as prepared in Section 4.2.1. Following the method outlined in Chapter 3 the electric current at the high voltage electrode was measured at 7 distances and 26 voltages potentially giving 182 different electric field conditions. Following the method used by Stanger et al. (2009d) the mass deposition rate (and by inference the mass flow rate) was measured at selected combinations of 3 distances and 4 voltages to potentially give a total of 7 different electric field conditions.

5.2.2 Results and Discussion

The nature of the electric field formed in a typical needle-flat plate electrospinning apparatus is difficult to quantify. Hence reports in literature often use the infinite parallel plate approximation to estimate the electric field strength that then drives the properties of the electrospinning process (Yarin et al., 2001a). Due to the simplicity it may be desirable to fit a response to the parallel plate capacitor approximation of the electric field; however, Figure 36 shows that this is not a valid approach. The three different mass deposition rates for a single predicted electric field condition (Figure 36) show that this representation of the field is not a valid description of the phenomenon. This cluster of three distinctly different deposition rates at 1 kV/cm indicates that although mass deposition rate responds to electric field strength the relevant electric field strength is not related to the parallel plate approximation. This is seen clearly in Figure 37 where the much larger dataset shows significant divergence the higher the parallel plate prediction of the electric field strength gets. At approximately 1.5 kV/cm there is a very wide variation in the electric current observed, with a shorter TCD giving higher electric currents than a longer TCD.

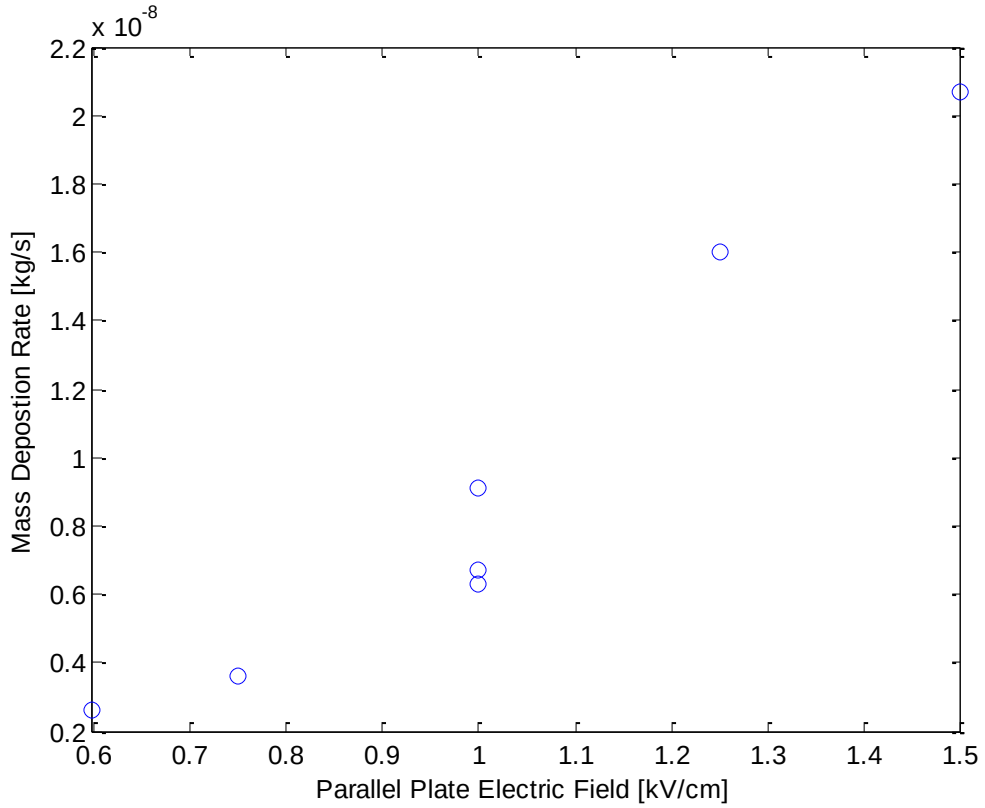

Figure 36: Mass deposition rate plotted against the parallel plate approximation of electric field strength. Note the cluster of points at 1 kV/cm resulting from the failure of the parallel plate approximation in representing the electric field strength. Error bars representing the standard error obtained from the linear regression as presented in Table 1 are smaller than marker for each data point.

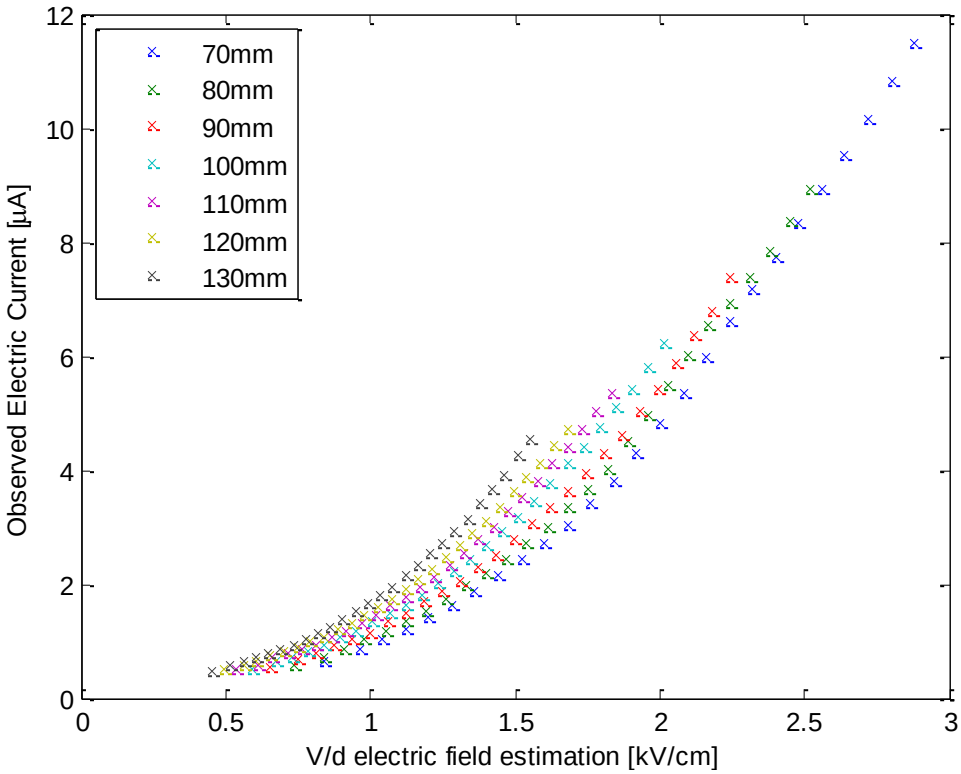

Figure 37: Observed electric current at the high voltage electrode for 8% PVOH showing that V/d is not a valid predictor of behaviour.

5.3 Conclusion

The parallel plate approximation of the electric field strength is a poor predictor of electric current and mass deposition rate in the electrospinning process. The difference in electric field geometry between a pair of infinite parallel plates and the typical point-plane electrospinning configuration suggests that it is a poor predictor for other aspects of the electrospinning process. Therefore, the parallel plate approximation will not be used in any of the discussions in this thesis.

CHAPTER 6

CHARGE DENSITY IN THE ELECTROSPINNING PROCESS

6 Charge Density in the Electrospinning Process

6.1 Introduction

Typically, the fibre mass deposition rate (also known as mass production rate) or flow rate (also known as feed rate) has been treated as a parameter that can be varied independently (Patra et al., 2010b). However, a constant internal pressure within the Taylor cone must be maintained to allow stable electrospinning from the Taylor cone that in turn establishes a constant flow rate (Stanger, 2008). It is possible when studying the process in a quasi-stable state to treat the mass deposition rate as a response variable related to processing conditions (such as voltage, electrode distance, humidity, polymer concentration, conductivity...) (Demir et al., 2002). Treating mass deposition rate as a response variable, it has been shown that both the mass deposition rate and electric current observed at the collector have a power law relationship to the applied voltage (Demir et al., 2002, Fallahi et al., 2008, Theron et al., 2004). Existing literature has varied the applied voltage to study the effect of different magnitude electric fields on the electric current at the collector electrode and the mass deposition rate. However, it is impossible to quantify the relationship with an applied electric field although, of course, the electric field is directly related to the electrospinning behaviour.

This chapter aims to relate variation in mass deposition rate and electric current at the high voltage electrode to variations in applied voltage and distance between the spinneret and the collector plate. In addition this chapter attempts to determine if there is a relationship between mass deposition rate and electric current flow. Mass deposition rate is measured as the amount of dry material deposited on the collector plate over time. When stable electrospinning is occurring this mass is entirely in the form of a nano-fibre. If the process is unstable, then spots of liquid polymer or sprayed particulates may also be deposited. The data presented in this chapter extends the empirical understanding of the relationship between processing variables and the resultant fibre and allows better control of the process.

6.2 Experimental Methods and Materials

6.2.1 Materials

Electrospinning was carried out using an aqueous solution of poly(vinyl alcohol) (PVOH). A stock solution was prepared as per Section 4.2.1. The stock polymer solution was diluted to an accurate final concentration of 8 wt% which is equivalent to 6.87 x 10^{-4} mol/L when using the average molecular weight.

6.2.2 Methods

The electric current flow was quantified by measuring the current flowing into the high voltage electrode in contact with the polymer solution. Throughout the experiments the solution properties

were kept constant. The variable used to control the electrospinning process was the internal fluid pressure inside the Taylor cone – this pressure is varied by raising or lowering the header tank. By controlling the internal pressure it was possible to obtain a stable Taylor cone and hence obtain comparable results between different voltages and distances.

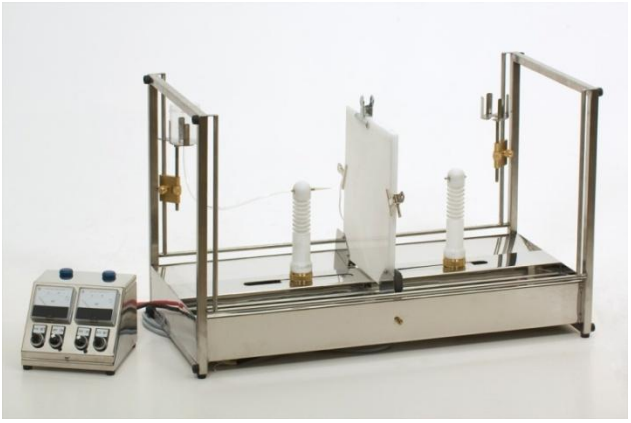

Figure 38: Photo of the Electrospinz ES4 electrospinning apparatus.

All samples were electrospun using a Model ES4 electrospinning apparatus (Electrospinz Ltd, New Zealand) as shown in Figure 38. The polypropylene pipette tip used was an Axygen T-200-Y 200 µL pipette tip with an orifice diameter of 0.5 mm. The processing parameters were measured to an accuracy of ± 1 mm for the working distance, ± 250 V for the potential difference and ± 0.5 mm for the head height allowing determination of hydrostatic pressure. Conductivity of the polymer solution was measured using a Eutech PC 510 conductivity meter.

The mass deposition rate was determined by depositing fibre onto collector electrodes made of cleaned, nominally 150 mm square sheets of 316 stainless steel connected to earth via a magnetic holder. After fibre deposition, samples were dried for 8 h (RH 40%, 25°C) before analysis. The mass deposited on each steel electrode was weighed using a 4-figure balance (Mettler Toledo AG204, measurement error of ±0.0001 g). For each set of voltage and distance conditions three replicates were produced by depositing fibre for a period of 1, 2, 3, 5, 10, 20 and 30 min. Each combination of conditions to produce a sample was randomized to eliminate any ordering bias. Using the conservation of mass it is possible to then convert the mass deposition rate to a mass flow rate at the Taylor cone.

Electric current was measured using a compactDAQ data acquisition platform (cDAQ-9172 with 9205 and 9263 modules, National Instruments) connected to a Glassman high voltage power supply. The compactDAQ platform was able to program a ramping voltage from just above the onset of electrospinning (typically ~5 kV) to an upper limit (~20 kV) in 0.5 kV steps every 5 s. During this time the current feedback output was logged with the 16 bit ADC module at a sampling rate of 1 kHz. The data were processed using a custom MATLAB script to provide the average current drawn for a given

voltage. Fluid pressure was adjusted by varying the height of the polymer header tank to maintain stable electrospinning throughout.

6.3 Voltage-Mass Flow Rate Relationship

Often the mass deposition rate or mass flow rate (depending on where it is measured), Q, is treated as an independent processing parameter that can be freely varied (Theron et al., 2004). Treating the mass deposition rate this way ignores the intrinsic nature of the Taylor cone, whereby to maintain a static Taylor cone shape one must balance the internal fluid pressure with the external forces of surface tension and surface electric charge. There is only one mass deposition rate that can satisfy the requirement of a static Taylor cone for any given set of processing parameters.

For a given voltage and distance the mass deposited on the collector electrode increases linearly with time. Figure 39 shows the increase in mass of fibre deposited over time on the collector. The gradient of the linear trend is the mass deposition rate. The linear relationship means that there is a constant rate of mass deposition and therefore mass flow rate (Q) over a period of up to 30 min. The y-intercept at t=0 is not at zero due to the interaction between the stainless steel electrode and the magnet used to hold it in place. A 316 stainless steel plate that is connected and removed from the magnetic specimen holder without having electrospun fibre deposited on it will appear gain an average of 0.005 g due instrumentation error caused by residual magnetism, which corresponds to the magnitude of the y-intercept observed in all cases.

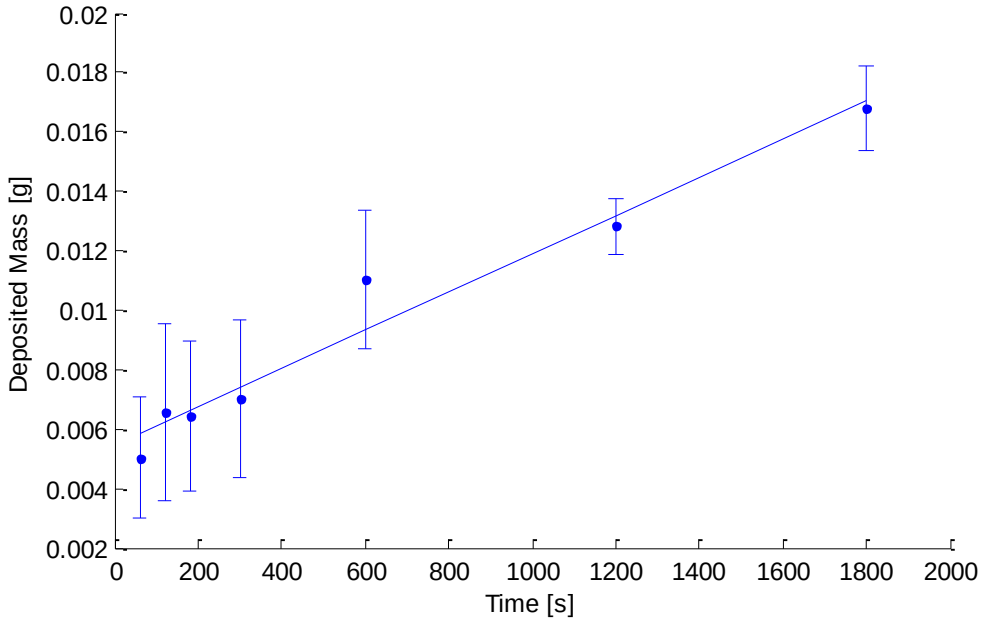

Figure 39: Mass increase of collector electrode over time with a fixed electrode distance of 100 mm and fixed applied voltage of 10 kV. The error bars represent one standard deviation of the measured data. The trend line equation is $m = 6.41\times10^{-6}\ t + 5.49\times10^{-3}$ ($R^2 = 0.964$).

Using conservation of mass, the mass deposition rate was converted to mass flow rate at the Taylor cone that will be used throughout. The mass flow rate was determined at 100 mm distance for the

voltages 7.5, 10, 12.5 and 15 kV, and at 75 mm and 7.5 kV with 125 mm and 7.5 and 12.5 kV (Table 3). Increasing the voltage or decreasing the distance between electrodes leads to an increase in the mass flow rate. This is consistent with the expectation that the flow rate at the Taylor cone increases with electric field strength. Past studies have only considered varying the applied voltage (Demir et al., 2002, Fallahi et al., 2008, Theron et al., 2004). The current study offers the possibility of examining the response in terms of the applied electric field. This can be done as varying the electrode distance at a constant applied voltage varies the applied electric field in a similar way as varying the applied voltage, but with the additional complexity of varying the electric field shape.

Table 3: Mass flow rate (g/s) for a range of voltages and electrode distances where each value represents the constant linear flow rate over time – as seen in Figure 39. The errors listed are the standard error obtained from the linear regression performed to find the linear mass flow rate.

		Electrode distance		
		75 mm	100 mm	125 mm
Applied voltage	7.5 kV	$8.38\times10^{-5} \pm 0.32\times10^{-5}$	$4.54\times10^{-5} \pm 0.08\times10^{-5}$	$3.24\times10^{-5} \pm 0.22\times10^{-5}$
	10.0 kV	-	$7.88\times10^{-5} \pm 0.15\times10^{-5}$	-
	12.5 kV	-	$19.98\times10^{-5} \pm 0.10\times10^{-5}$	$11.34\times10^{-5} \pm 0.12\times10^{-5}$
	15.0 kV	-	$25.87\times10^{-5} \pm 0.14\times10^{-5}$	-

Using the data presented in Table 3 we can look at the relationship between mass flow rate and the applied voltage which for a fixed distance linearly relates to electric field strength. These results are shown in Figure 40. Previous literature has reported several examples of power law relationships in similar circumstances for various polymers (polyurethaneurea, polyacrylonitrile and PVOH) (Demir et al., 2002, Fallahi et al., 2008, Theron et al., 2004). Both a linear relationship (R^2 = 0.958) or a power law (R^2 = 0.968) would fit with this data. However, with only four data points it is not valid to rely on a goodness of fit to determine a suitable function so the difference in fit is negligible. For the sake of comparison, fitting a power law produces the equation $m_{rate} = 1.99 \times 10^{-10} kV^{2.66}$. Figure 41 shows the relationship between the mass flow rate and increasing distance while the applied voltage is kept constant. This again shows that increasing the electric field strength (by decreasing the electrode distance) increases the mass flow rate.

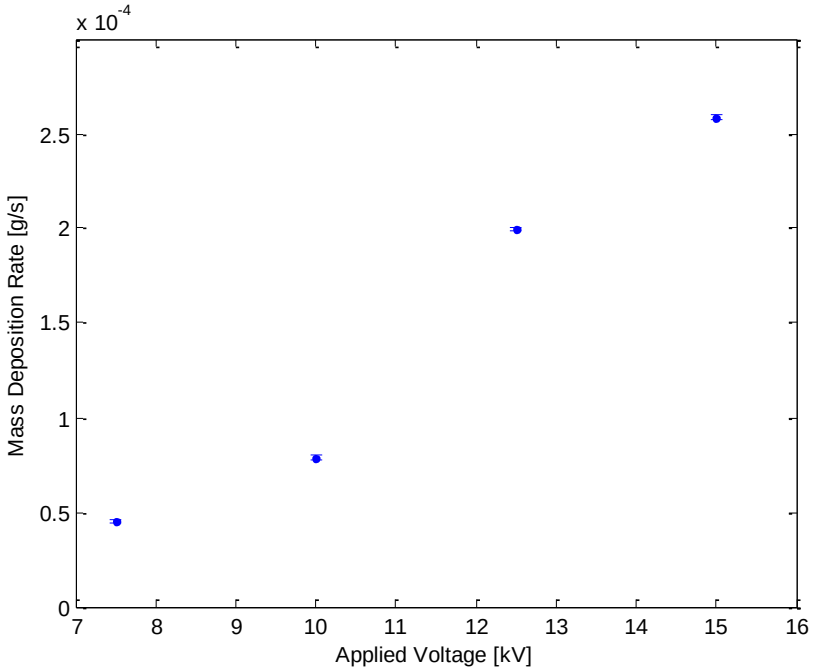

Figure 40: Mass flow rate response to applied voltage for the fixed electrode distance of 100 mm. Error bars representing the standard error obtained from the linear regression as presented in Table 3 are smaller than the marker for each data point.

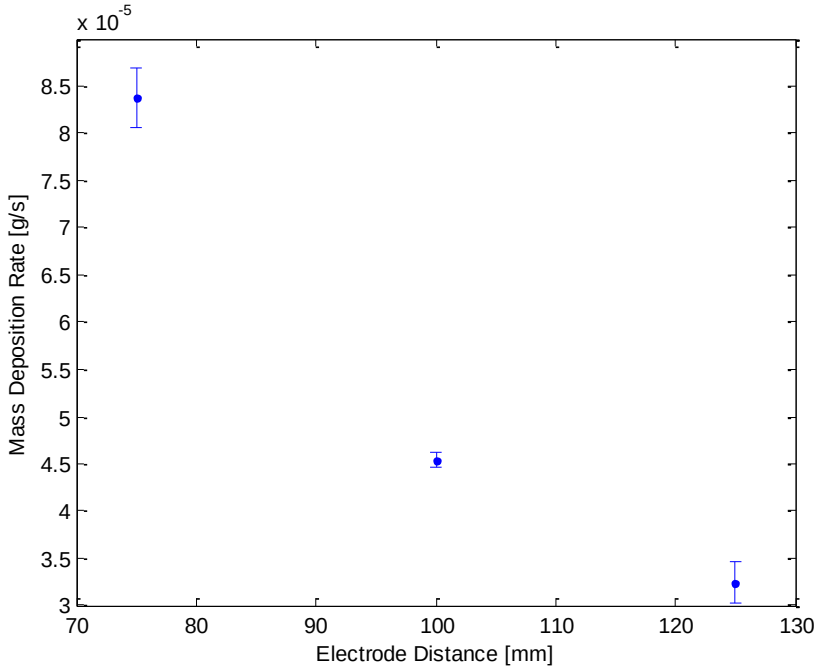

Figure 41: Mass flow rate response to electrode distance for a fixed applied voltage of 7.5 kV. Error bars representing the standard error obtained from the linear regression as presented in Table 3 are shown where some are smaller than the marker for the data point.

6.4 Voltage-Current Relationship

It is expected that the electric current observed at the high voltage electrode would increase with applied voltage. Figure 42 shows some typical high voltage electric current traces in response to increases in voltage. Like the mass flow rate, the electric current increases with applied voltage and decreasing electrode distance. Each trace is started approximately at the initiation voltage for electrospinning which is why the current is near zero. Traces were recorded for the electric current

response to applied voltage at electrode distances of 50 to 130 mm at 10 mm steps (along with traces at 75 mm and 125 mm to match the conditions the mass flow rates were measured under). The three traces that were recorded at 75, 100 and 125 mm allow the identification of the electric current being drawn when the mass flow rate was measured (Table 4).

Table 4: Electric current measured at the high voltage electrode (expressed in µA) for a range of voltages and electrode distances.

		Electrode distance		
		75 mm	100 mm	125 mm
Applied voltage	7.5 kV	0.432 ± 0.516	0.333 ± 0.513	0.284 ± 0.515
	10.0 kV	-	0.711 ± 0.515	-
	12.5 kV	-	1.281 ± 0.545	1.026 ± 0.558
	15.0 kV	-	2.073 ± 0.581	-

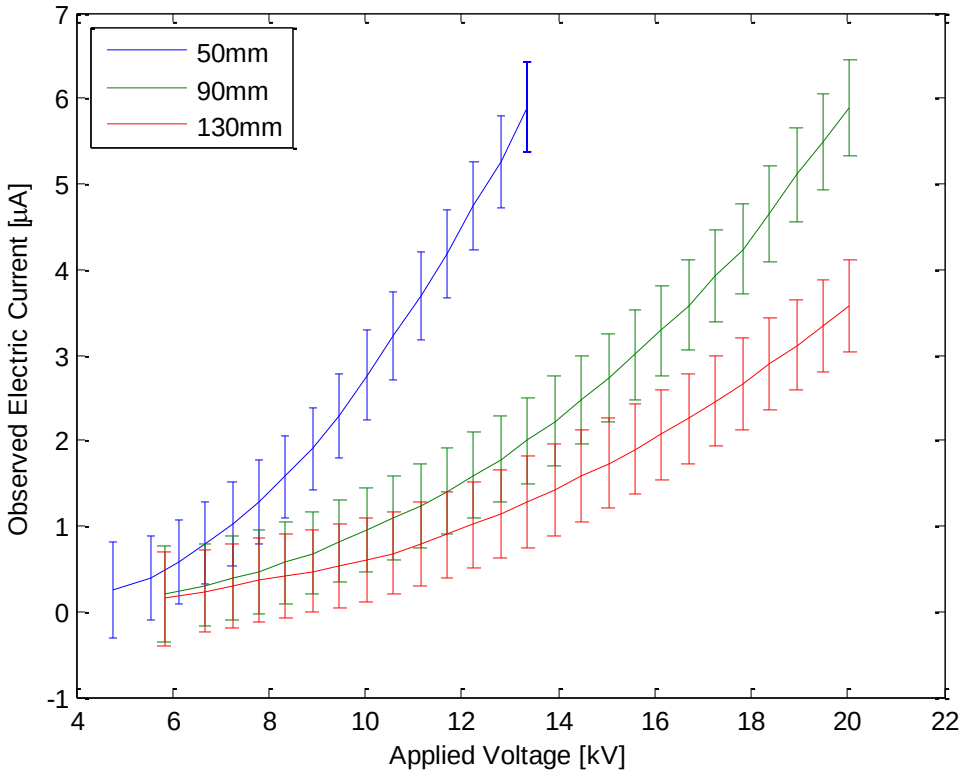

Figure 42: Observed electric current at the high voltage electrode in response to applied voltage at the fixed electrode distances of 50, 90 and 130 mm. The error bars represent one standard deviation of the measured data.

Visual inspection of Figure 42 suggests that the electric current drawn by the high voltage electrode follows a power law relationship with applied voltage. Where the relationships between electric current and applied voltage are studied specifically for PVOH (Theron et al., 2004), it was found that there were power law relationships between the electric current and applied voltage (Theron et al., 2004). A similar power law relationship has been reported for other polymer solutions (Demir et al., 2002, Fallahi et al., 2008). This relationship is given without a theoretical basis. The power law relationship can be simply tested by plotting the observed electric current for the nine distances, 50 to 130 mm, on logarithmic axis. The linear relationships seen in Figure 43 shows that a power law is

a good description of the data, particularly at high applied voltages. Performing a linear fit of the logarithmic transformed data for the high voltage electric current shows that for the power law function $I = aV^{\alpha}$, the exponent, α, is approximately 2.6 with a slight decline as distance increases. The average fitting value of the power law is an R^2 of 0.9992.

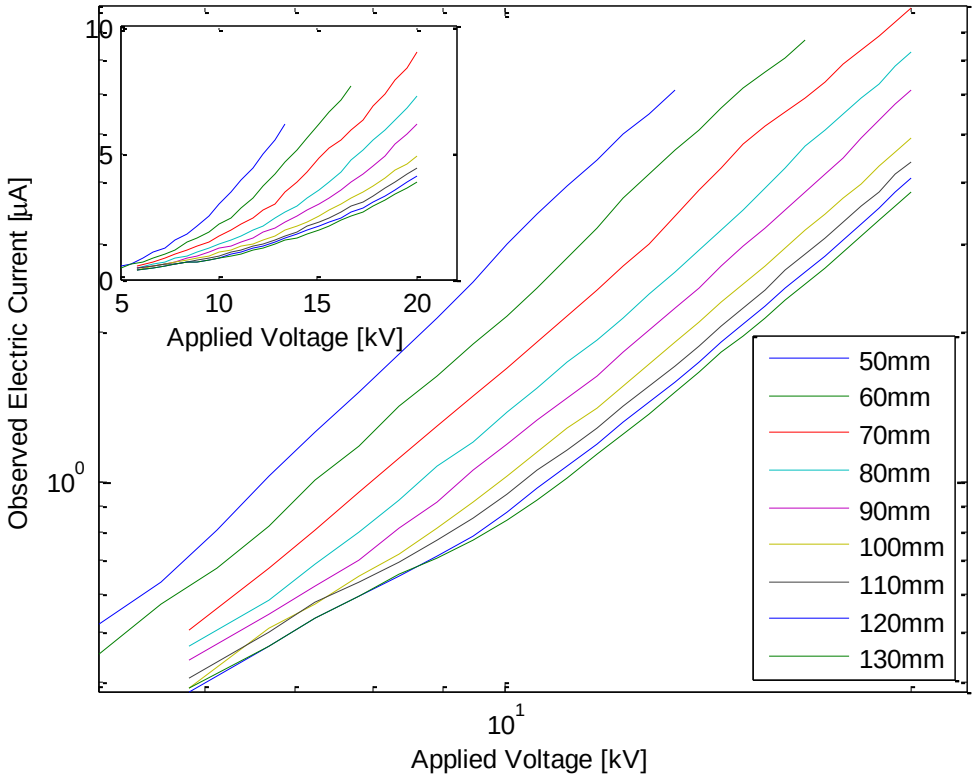

Figure 43: Observed high voltage electric current for 8% PVOH in water being electrospun at different applied voltages and distances. Primary graph is a log-log plot, insert graph is the same data on linear axes.

Study of the electrohydrodynamic phenomena that are responsible for the Taylor cone and the formation of the jet by Filatov et al. (2007) concluded a generalized voltage-current relationship of the form $I \sim V^2$ for the electric current measured at the collector (Filatov et al., 2007). This is similar to that from corona discharges and was found to be independent of the polymer supply method. For a needle-plate electrode arrangement immersed in transformer oil the high voltage current relationship was found to follow the equivalent relationship where a threshold voltage, V_{th}, was exceeded, $I = A(V - V_{th})^2$ (Atten et al., 1997). It is proposed that this charge flow is the result of a charge injection process, effectively the same as a corona formation where the fluid medium is the transformer oil as opposed to air (Collins et al., 2012). It is suggested that the electric current flow in the electrospinning process may appear like a corona discharge process (Collins et al., 2012). Previous reports have focused on the power law relationship as discussed above; however, plotting the observed high voltage electric current against V^2 shows a strong linear relationship (Figure 44). An arbitrary power law relationship has a very good fit to the data and despite the possibility that

the electrospinning process fits the power law relationship with a higher power, the fitting of electric current to established theoretical relationships has merit. The data fits the above discussed relationship with an average threshold voltage, V_{th} of 2.76 kV. The average goodness of fit, R^2 is 0.9985 which is of a similar quality of fit to the power law relationship.

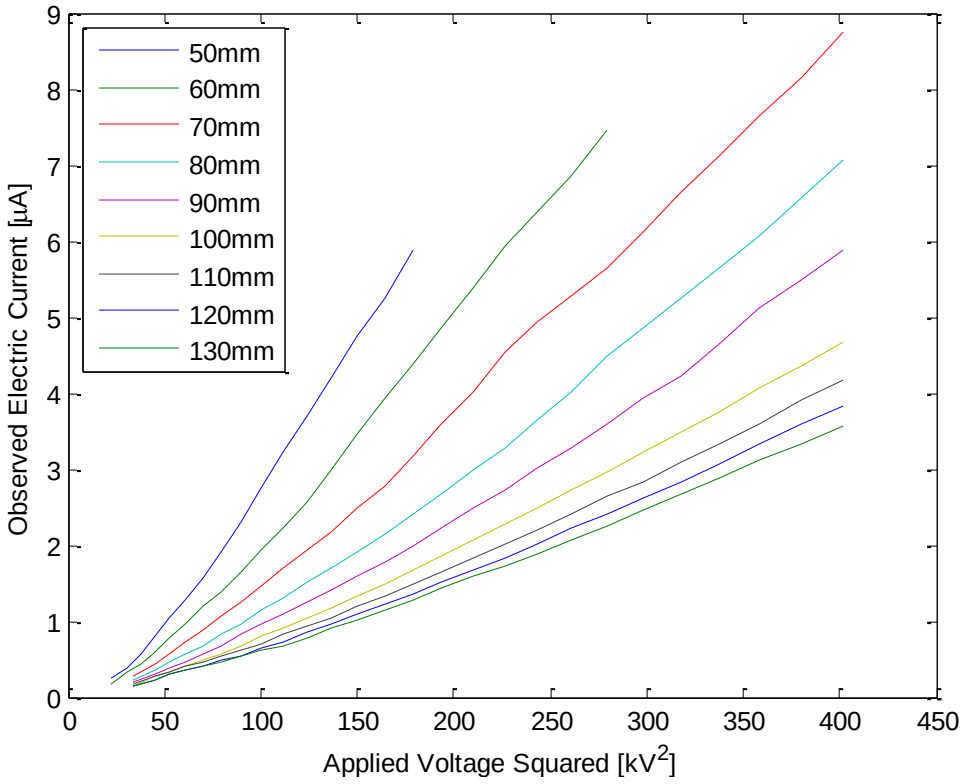

Figure 44: Observed high voltage electric current for 8% PVOH in water being electrospun at different applied voltages and distances.

The same process used above to investigate power law relationships can be applied to determine if a similar relationship exists between high voltage electric current and electrode distance. This power law, $I = Ad^{\beta}$, scales with an exponent, β, of approximately -1.5 for voltages above 10 kV. The average fitting value of this power law is an R^2 of 0.9835. With respect to variation of electric current with electrode distance the work by Theron et al. (2004) proposes a relationship of the form $I = Ae^{-d/H}$. The result of fitting this function to the available data gives a coefficient, H, of 66.3 with an average goodness of fit R^2 of 0.9656 which is worse than the power law relationship. Neither case has a theoretical basis.

Literature provides two models for the relationship between high voltage electric current and applied voltage (Equations (6.45) and (6.46)). Similarly, two models are presented for high voltage electric current and electrode distance, one from the literature, one from examining the form of the data collected (Equations (6.47) and (6.48)). Theron et al. (2004) proposes that a model of the collector electric current can be treated as a separable function. Although this work studies the high voltage electric current, the same assumption will be made. With two functions for each variable

(applied voltage and electrode distance) this gives four possible functions for $I(V,d)$. The quality of fit of these four functions is summarized by Table 5. From this table it is clear that the combination of Equation (6.46) and (6.47) to form Equation (6.49) is the best fit. This is also the function that includes the only function that has some theoretical basis (i.e. Equation (6.46)). Chapter 4 shows that when examining only the high voltage electric current it is very difficult to distinguish between electrospinning and a corona discharge formed from a similar electrode arrangement. This may explain why Equation (6.46) produces a better fit to the observed data. Regardless, any future data observed can be described using any of the four models if the four parameters, α, β, V_{th} and H are reported.

$$I(V) = AV^{\alpha} \tag{6.45}$$

$$I(V) = A(V - V_{th})^2 \tag{6.46}$$

$$I(d) = Ad^{\beta} \tag{6.47}$$

$$I(d) = Ae^{-\frac{d}{H}} \tag{6.48}$$

Table 5: Quality of fit for the possible separable functions that describe the high voltage electric current in response to applied voltage and electrode distance.

	Functions describing the high voltage electric current			
	$I = AV^{\alpha}d^{\beta}$	$I = AV^{\alpha}e^{-\frac{d}{H}}$	$I = A(V - V_{th})^2 d^{\beta}$	$I = A(V - V_{th})^2 e^{-\frac{d}{H}}$
R^2	0.9857	0.9333	0.9909	0.9446

$$I(V,d) = A(V - V_{th})^2 d^{\beta} \tag{6.49}$$

6.5 Polymer Bulk Charge Density

Figure 42 shows a power law relationship between high voltage electric current and applied voltage, with an average power law exponent of 2.60. As has already been shown (Figure 40) the relationship between mass flow rate and applied voltage is also a power law with an exponent of 2.66 (Figure 40). The similarity suggests a close relationship between the mass flow rate and high voltage electric current. Figure 45 shows that for a range of different voltages and distances there is a linear relationship between mass flow rate and high voltage electric current. Moreover, without requiring the intercept to be zero (no mass implies no current) the linear relationship gives an intercept nearly zero.

Figure 45 indicates that there is a linear relationship between the flow of mass and the flow of charge. As the mass flow rate has units of [kg/s] and the electric current has units of [C/s] this

constant would have units of [kg/C]. The value for the data observed in Figure 45 is 7.7 C/kg for the polymer solution at the Taylor cone. Using mass conservation, a theoretical bulk charge density of 98 C/kg can be found for the fibre as it arrives at the collector assuming no charge is lost in flight. This is nearly two orders of magnitude larger than that used for simulations by Kowalewski et al. (2009) (0.02–0.2 C/kg) or simulations by Carroll et al. (2011) (i.e. 0.001-0.55 C/kg) and nearly an order of magnitude larger than that used for simulations by Reneker et al. (2000) (i.e. 1 C/kg). As the charge on the fluid is the primary driving force for the electrospinning dynamics this is an important observation. It is possible that existing simulation work may not correspond to the physical situation of electrospinning PVOH.

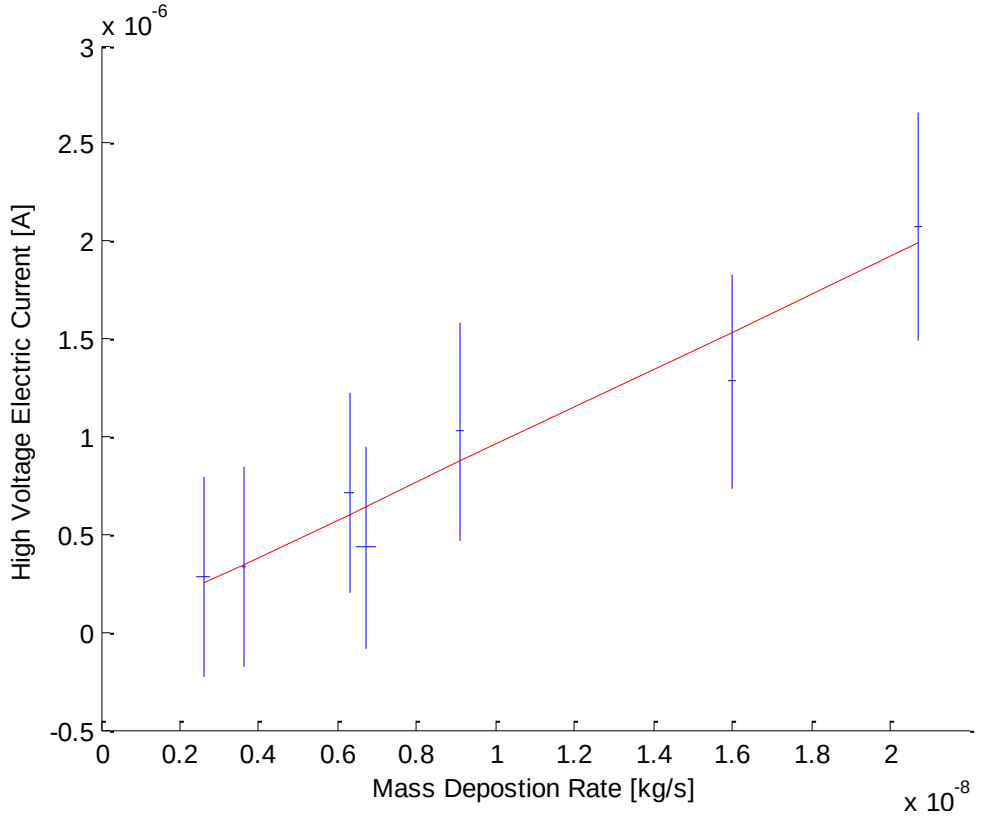

Figure 45: Mass flow rate as a response to electric current drawn by the high voltage electrode for all combinations of voltage and distance available in this chapter. The trend line is described by $I = 96\ m_{rate}$ ($R^2 = 0.9397$).

Given the complexity of the interactions around the Taylor cone during electrospinning (including local electric field, surface tension, surface charge, ionic charge, viscoelastic forces, etc.) it is surprising that a constant bulk charge density is so strongly indicated. However, it does indicate that this would be a useful variable for a closed loop electrospinning control system. This could also provide the basis for the study of how dissociated ions in solution participate in the charge transfer mechanism in electrospinning.

The charge carriers in electrospinning are often discussed as existing in the form of ionic-like charge carriers (Atten et al., 1997). Previous work has proposed a linear relationship between electric

current and mass flow rate based on the number of ions in solution giving rise to the flow of electric current (Stanger, 2008). This relationship is given in Equation (6.50), where F is Faraday's constant, c is the ion concentration, ρ is the solution density and m_{rate} is the mass flow rate. This equation can be fitted to the relationship shown in Figure 45 where the constant 7.7 C/kg (for the solution rather than dry polymer) is equivalent to $1000Fc/\rho$ allowing the calculation of the relevant ion concentration. For 8% PVOH, the ion concentration calculated was found to be 8.076x10^{-5} molL^{-1}. This is approximately one order of magnitude smaller than the estimated concentration of PVOH molecules (i.e. 6.87x10^{-4} molL^{-1}) and approximately two orders of magnitude higher than the concentration of ions found in pure water (i.e. 1x10^{-7} molL^{-1}). The solvent used in this case was distilled water with a higher conductivity (~2 µScm^{-1} compared to 0.55 µScm^{-1} for pure water). However, this is unlikely to provide sufficient ions to account for the bulk charge density observed in this chapter. Work by Keun Son et al. (2005) shows that solution pH modifies the protonation of PVOH molecules in solution, therefore changing the charge carried by each molecule in solution. This may allow for only a fraction of the PVOH molecules to act as charge carriers but without further work outside the scope of this thesis it is impossible to tell. If the process in this chapter was repeated for a range of polymers and for a range of ionic salt additions it may become clear if ion concentration is the limiting factor in determining the flow of electric current.

$$I = \frac{1000Fc}{\rho} m_{rate} \tag{6.50}$$

6.6 Discussion of Previous Work

6.6.1 Voltage-Mass Flow Relationship

Theron et al. (2004) studies the collector electric current for PVOH in response to mass flow rate or applied voltage. The study used a 50/50 solvent of water and ethanol with a POVH molecular weight of 10,000 (unknown degree of hydrolysis) at a concentration of 6% by weight. Theron et al. (2004) does not report an explicit relationship between flow rate and applied voltage but this may be determined algebraically as $Q = cV^{0.0563}$ from the reported relationship between electric current and flow rate and electric current and applied voltage. Since the exponent is less than 1 this means the function has a decreasing gradient with respect to increasing applied voltage. Other reports of flow rate in response to applied voltage in the literature used polyurethaneurea (PUU) (Demir et al., 2002) and polyacrylonitrile (PAN) (Fallahi et al., 2008) respectively. The relationships for PUU were found to be $Q = cV^3$. The relationships for PAN were found to be $Q = cV^{3.628}$. For the data presented in Section 6.3 the relationship is $Q = cV^{2.66}$ for PVOH 8%. Previous work has shown that the mass deposition rate can be sensitive to solution composition (such as conductivity), electrode polarity and substrate materials (Stanger, 2008, Stanger et al., 2009d). The observed exponent is

within an order of magnitude to those made for PUU and PAN but differs significantly from that previously reported for PVOH (Theron et al., 2004). The work by Theron et al. (2004) did not control the flow rate, but rather produced relationships for a wide range of flow rates and averaged the results. If a constant volume flow rate feed system is used it is possible to under- or over-feed the Taylor cone resulting in flow rates that do not represent stable electrospinning. The ability to achieve stable electrospinning underpins the work described in this paper. To derive the above power law, the resulting formula from two different experiments was combined. As this was never intended by Theron et al. (2004), this may explain why the exponent is so different from the result observed here and for PUU/PAN.

6.6.2 Voltage-Current Relationship

As was noted above, there are major differences between the work of Theron et al. (2004) and the work described here. The response of collector electric current to applied voltage was reported to be $I = cV^{4.565}$ where c is a constant (Theron et al., 2004). This exponent is much higher than that seen in Figure 42 of 2.60. This could be due to any of the differences described above, either in materials, measurement or electrode geometry. As previously described, the work by Theron et al. (2004) was done at a range of fixed flow rates which would cause over feeding at low voltages and underfeeding at high voltages interfering with the observed voltage-current relationship. Without knowing the precise details of the electrode geometry or the flow rate required to maintain stable electrospinning at each voltage it is not possible to offer a complete explanation as to the differences observed. Two other notable reports in the literature used polyurethaneurea (PUU) (Demir et al., 2002) and polyacrylonitrile (PAN) (Fallahi et al., 2008), respectively. The relationship of collector electric current for PUU was reported as $I = cV^{2.7}$ and the relationship for PAN was reported as $I = cV^{2.625}$. As no errors are given for the exponents the fact they are very similar implies the relationships for electric current are in good agreement with that shown in Figure 42 where the average power law exponent is 2.60.

6.7 Conclusions

This chapter aimed to find relationships between the processing variables of applied voltage and electrode distance and either the mass flow rate or the high voltage electric current for 8% PVOH in water. A relationship was found between the mass flow rate and the high voltage electric current for a range of different applied voltages and electrode distances for 8% PVOH in water. Previous reports have described a power law relationship between the mass flow rate or collector electric current and applied voltage. The same reports have described a relationship between the collector electric current and electrode distance as either a power law or inverse exponential function. It was found that the fitting of the high voltage electric current to an inverse exponential function as electrode

distance increases always resulted in a poorer fit than a power law relationship for 8% PVOH in water.

The work in this chapter found that a power law fits the high voltage electric current for 8% PVOH in water with an average exponent of 2.6. An alternative power law relationship of the form, $\sqrt{I} = A(V - V_{th})$ (I is in [A], V is in [kV], V_{th} is in [kV] and A is a constant with units [A^3s^2/J^2]), found a threshold voltage of 2.76 kV. This function was found to have a much better fit than a standard power law for 8% PVOH in water. The mass flow rate for 8% PVOH in water was also found to follow a power law with an exponent of 2.66. The relationship between mass flow rate and high voltage electric current for 8% PVOH in water was found to be linear for a wide range applied electric field conditions. The linear relationship was found to be $I = 7.7\, m_{rate}$ where m_{rate} is the polymer solution flow rate in [kg/s] and I is in [A]. This gradient corresponds to a constant bulk charge density of 7.7 C/kg for all combinations of applied voltage and electrode distance.

The constant bulk charge density found was at least an order of magnitude larger than that typically used in simulations (Carroll et al., 2011, Kowalewski et al., 2009, Reneker et al., 2000) suggesting that a higher charge density may be required to describe the physical reality of electrospinning. Additionally the constant charge density means that the flow rate can be controlled automatically by using the high voltage electric current as a feedback signal for continuous flow electrospinning.

CHAPTER 7

FLIGHT TIME IN ELECTROSPINNING

7 Flight Time of the Electrospun Fibre

7.1 Introduction

When trying to explain physical mechanisms for changes in the electrospinning process due to changes in solution properties, processing parameters or environmental conditions it is useful to be able to quantify the properties of the jet while in flight. Quantification of properties of the electrospinning jet while in flight unfortunately provides a complex problem. By its very nature the jet, being a freely suspended column of charged fluid in motion through air, will have its properties changed by any physical sensor that is introduced to measure these properties. This leaves only optical or related methods that can be done at a distance; however, these methods have another challenge, that of the scale of the jet being in the micron or less range. At an observation distance on the same order of magnitude as the inter electrode distance this poses challenges for gaining observations at a reasonable resolution. This leaves researchers with having to infer properties of the jet while in flight from observations at the Taylor cone or at the collector.

It is possible to use laser diffraction (Doshi, 1994) to measure the diameter of the jet while in flight without appearing to interfere with the process. This method can only be used on the jet before the whipping instability as the quasi-chaotic instability doesn't allow the laser to cleanly intersect the jet to get a diffraction pattern. With the jet diameter it is possible to infer a fluid velocity from the conservation of mass; however, with relatively volatile solvents there must be a change in mass of the jet even over short distances making the velocities obtained inaccurate. It is also possible to measure the mass deposition rate and the average fibre diameter to obtain the fibre lay down rate (Stanger, 2008, Stanger et al., 2009d). This rate, given in ms^{-1}, should be equivalent to the three dimensional velocity of a unit of mass in the jet. From these data alone it is impossible to separate the axial velocity towards the collector from the off axis velocities due to the whipping instability. As such the figure is of limited use in describing the process. The whipping instability also makes it currently impossible to measure the length of the jet while it is in flight.

Other than estimations from numerical models, there is no method established to estimate the time the jet spends in flight. This figure is a useful one as it is often invoked, based on assumptions as to how the flight time would change with processing variables, to explain a number of observed phenomena. If a method can be found, that does not necessarily directly measure the flight time of the jet but can estimate it, then the response of this estimate to processing parameters can be explored. This then gives empirical evidence to use in forming arguments about the physical phenomena of electrospinning.

7.2 Experimental Details

7.2.1 Materials

Electrospinning was carried out using an aqueous solution of poly(vinyl alcohol) (PVOH). A stock solution was prepared as per Section 4.2.1. The stock polymer solution was diluted to an accurate final concentration of 8 wt% which is equivalent to 6.87 x 10^{-4} mol/L when using the average molecular weight.

7.2.2 Methods

This chapter used the ES4 model electrospinning apparatus (Electrospinz Ltd, New Zealand) and the compactDAQ data acquisition platform (National Instruments Corporation, Austin, Texas, US) as described in Chapter 4. Electric current was measured using the Glassman high voltage power supply direct feedback and the high precision resistor between the collector electrode and ground. Both signals were logged using the compactDAQ platform. Unlike the method described in Section 4.2.3 of Chapter 4 the control signal for the applied voltage did not sweep from 5 kV to 18 kV and back again but rather started at 0 kV for a fixed time, then switched to a given kV for a fixed time before returning to 0 kV. This effectively provides a step change between no possible electrospinning and stable, well-formed electrospinning. To facilitate this step change the volume of the droplet that would form the Taylor cone was maintained at a level where jet initiation could occur as quickly as is possible. The work covered in this chapter also sampled the electric current at a rate of 10,000 Hz but still retained the passive 1,000 Hz filter. This higher sample rate allowed a more accurate picture of step changes in the electric current. This work explored step changes of 7.5, 10, 12.5 or 15 kV each at the electrode distances of 80, 100 and 120 mm. Each condition was repeated three times to provide some ability to check for errors in the measurement.

High speed video observations were done using a FASTCAM-1024PCI model 100K (Photron Inc., San Diego, California, US) camera. For the sake of improving visibility of the jet while recording the high speed video, electrospinning was undertaken using the stock solution. The same step change in voltage was used to start and stop the electrospinning process and select a clearly visible initiation cycle.

7.3 High Speed Video Observations

Using high speed photography it has been established that the electrospinning jet is typically a single continuous stream of fluid (Baumgarten, 1971). This was later confirmed using high speed video (Shin et al., 2001a). Using these techniques it would be possible to examine the jet initiation process rather than the steady state process. If the goal is to track a small unit of fluid mass and record the amount of time it takes to travel between the two electrodes then tracking the leading edge of the jet is an obvious candidate. The leading edge of the jet will only give a valid estimate of the flight

time if it follows a similar flight path to that of the steady state jet. The only alternative is to use some method to tag a unit of mass in the jet during the steady state. The sample frames shown in Figure 46 demonstrate that the leading edge of the jet undergoes the same whipping instability that characterizes the steady state. Frame 21 shows the newly formed jet extending straight from the Taylor cone. Frame 28 shows the onset of the first "whip" of the whipping instability. Frame 41 shows this instability continuing behind the leading edge, establishing the cone envelope of the whipping instability. Frame 175 demonstrates the steady state the system settles into; note the length of the straight jet becomes shorter. Although it is possible that the leading edge carries a larger amount of mass than the steady state jet or may not undergo as extreme off axis forces due to the lack of an established whipping instability it is still a reasonable estimation of the steady state. In determining the time of flight between the two electrodes, only the velocity along the central axis is relevant for which the leading edge results should be related to the steady state results.

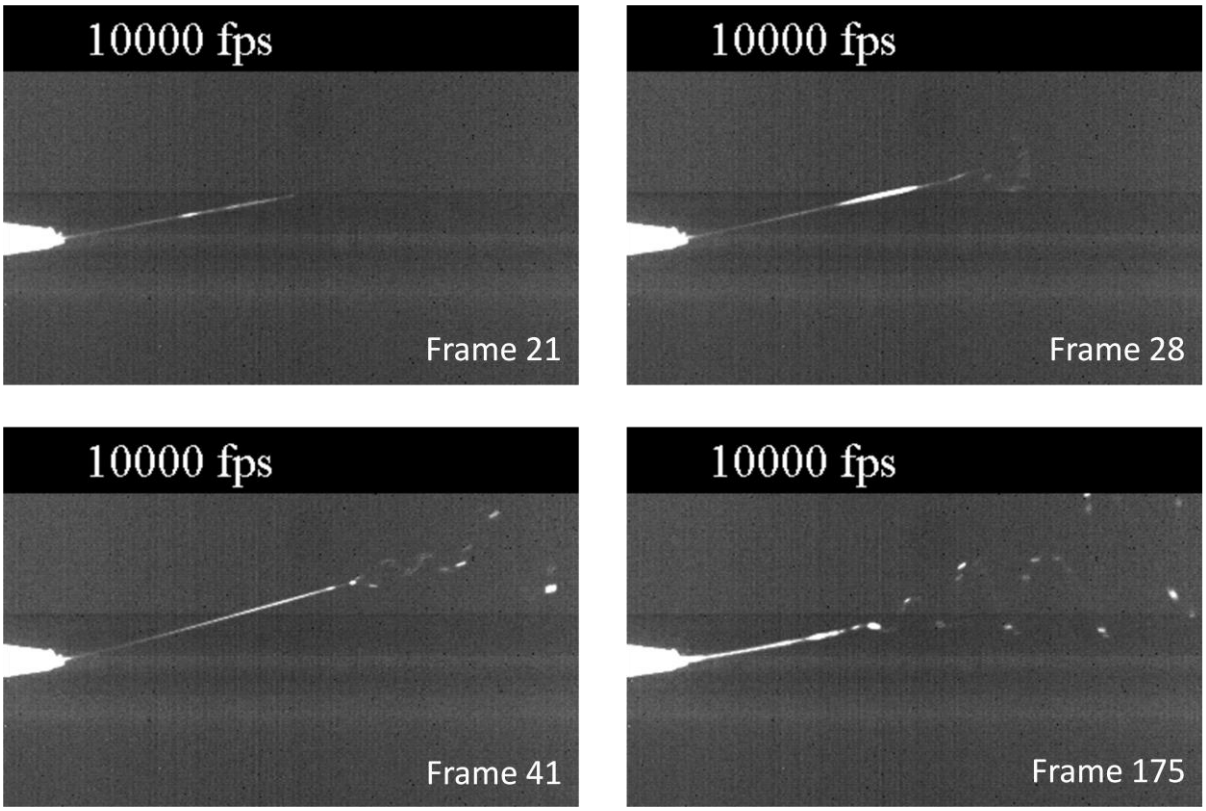

Figure 46: Frames extracted from a high speed video of the initiation of electrospinning. Video was recorded at 10,000 fps with the specific frame number marked.

7.4 High Sample Rate Electric Current Observations

Visual tracking of the leading edge leaving the Taylor cone is possible (Figure 46); however, visual tracking of the leading edge arriving on the collector is non-trivial. This is due to the large area where the fibre may land combined with the small scale the fibre reaches. This would require at least two high speed video cameras and introduces problems of synchronization as well as excessive cost. An alternative could be to measure a weight change in the collector; however, the mass deposition rate

(see Chapter 6, Section 6.3) is on the order of mg/hour. This would require an extremely sensitive load cell, which would be affected by strong electric and magnetic fields and hence would provide challenges isolating it from the applied electric field required for electrospinning.

7.4.1 Estimation of Flight Time

It has been well established in Chapter 6 that every unit of mass carries an equivalent unit of charge. The electrospinning process begins with an applied voltage to the high voltage electrode which causes a corresponding flow of charge into (or away from) any grounded nearby object, namely the collector electrode. This can be seen in Figure 47 at the point marked 'A' where the collector current shows a small peak that decays away back to zero. This represents the capacitive charging of the two electrodes. The fact that the electric current decays away back to zero indicates that no charged material has reached the collector. As the charged material travels through space it will continue to draw electric current from the high voltage electrode (hence the large peak not shown in the high voltage electric current) so as to establish the process; however, there will be no effect on the collector electrode. That is until mass reaches the collector at which point there should be a step change in the electric current flowing to (or from) the collector. This is seen in Figure 47 at the point marked 'B' which represents the first mass to arrive at the collector. The difference in time between the peak at 'A' triggered by the application of high voltage and the time at the step change 'B' triggered by the beginning of a flow of mass onto the collector will give the time of flight for the leading edge of the electrospun jet to travel between the electrodes.

It can be seen in Figure 47 that the step change at point 'B' is followed by the collector current rapidly adopting a steady current flow indicating that indeed the leading edge behaves similarly to the steady state. One obvious flaw in this method is that it has no way of estimating the amount of time taken for the Taylor cone to form and for the jet to be ejected post-application of high voltage. However, it is expected that if the time to form the Taylor cone and jet is significant it is approximately constant. This is because the polymer solution used is the same in all cases and care is taken to ensure that the droplet always has sufficient mass to form the Taylor cone without delay.

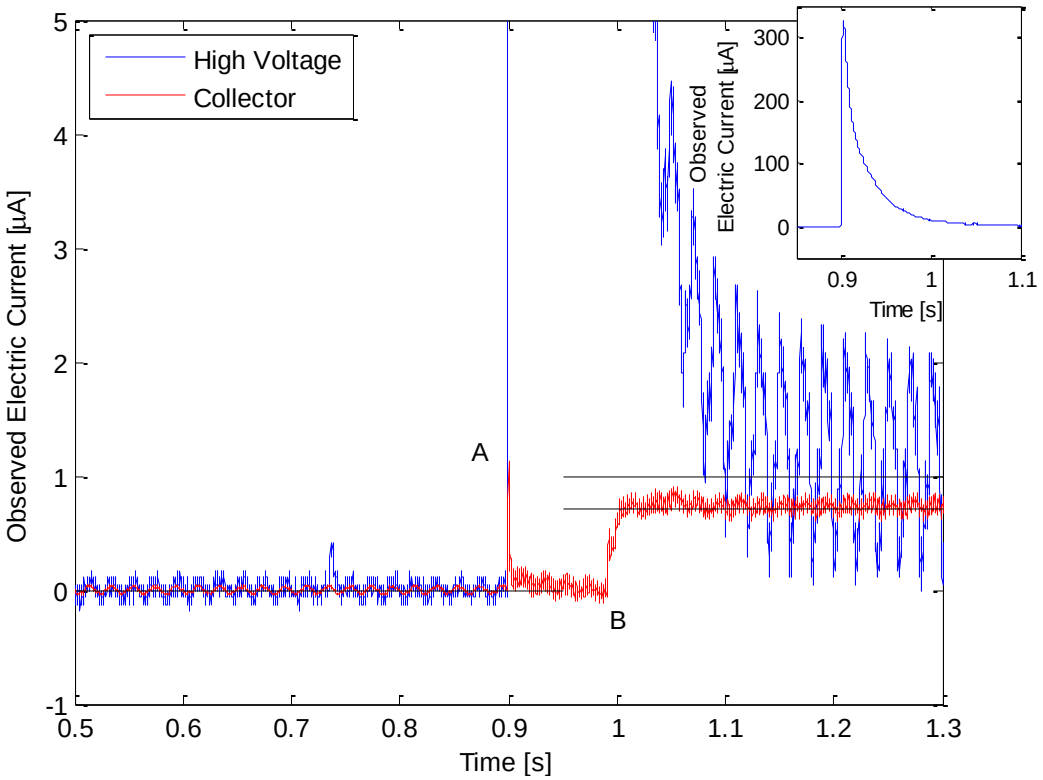

Figure 47: High voltage and collector electric current recorded under a step change in applied voltage. The applied voltage is 7.5 kV at an electrode distance of 100 mm. Point 'A' marks the initiation of the applied voltage. Point 'B' marks the arrival of fibre on the collector. Insert shows the unscaled high voltage electric current data showing the charging curve on initiation of electrospinning.

7.4.2 FFT Analysis of the Signal Noise

One obvious issue with the data presented in Figure 47 is the appearance of a significant amount of noise on the signal. This signal has already been filtered to remove much of the high frequency noise introduced by the high voltage power supply. The noise is most visible on the high voltage electric current signal (Figure 48) with the collector signal being approximately 1/5 of a wavelength out of phase, likely due to the distance between the two electrodes. It is possible to take a sample of the steady state electric current and apply a Fast Fourier Transform (FFT) using the inbuilt algorithm included with the software package MATLAB™. This transforms the time varying electric current signal into the frequency domain allowing the analysis of what frequencies contribute the most to the observed signal. The results show that the "noise" is primarily a 50 Hz oscillation with harmonics at 100, 150, 200 and 250 Hz where the harmonic at 150 Hz is the next largest contributor (see Figure 49). As the mains power in New Zealand operates at 50 Hz it is likely this is the source of the variation. There are no other major components other than very low frequency representing the direct current flow. The situation is the same for the collector current flow, but does include some higher frequency components above the 1000 Hz filter frequency. It should be noted that the current draw from (or into) the collector current also conforms to a direct current flow and does so for longer periods than typically analysed here. There are no sudden discharges as observed by

Filatov et al. (2007). As such it is possible that for polymers like PVOH, which may carry residual water, there is a mechanism that enables continual charge flow from the newly deposited fibres to the collector electrode.

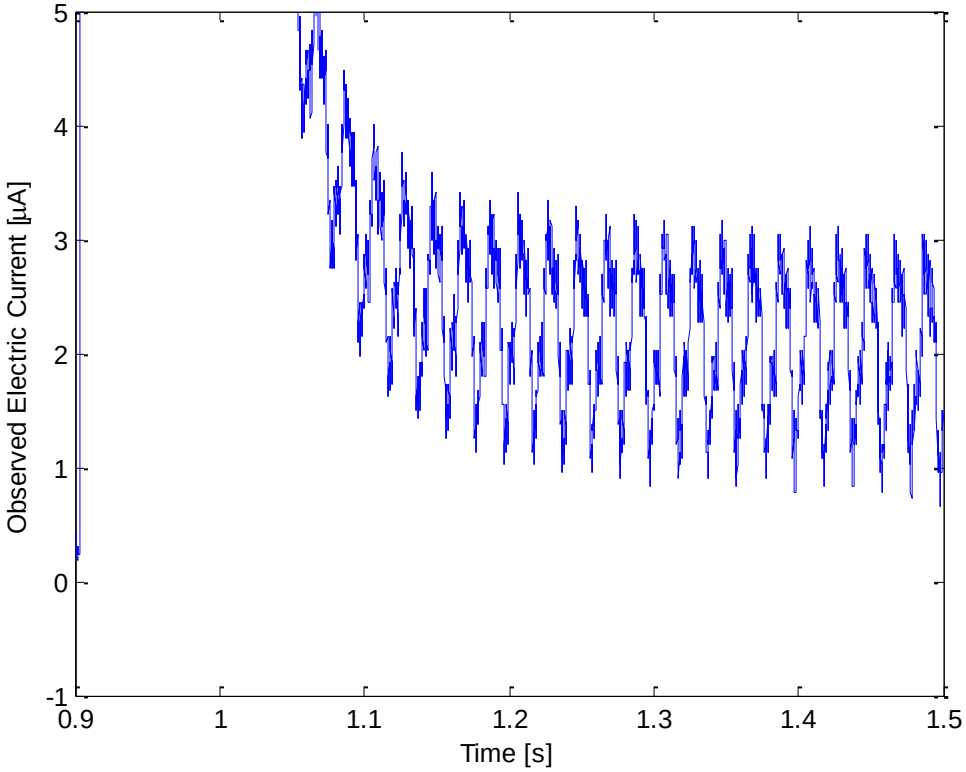

Figure 48: Extended detail of the noise present on the high voltage electric current signal with a voltage of 7.5 kV and a distance of 100 mm.

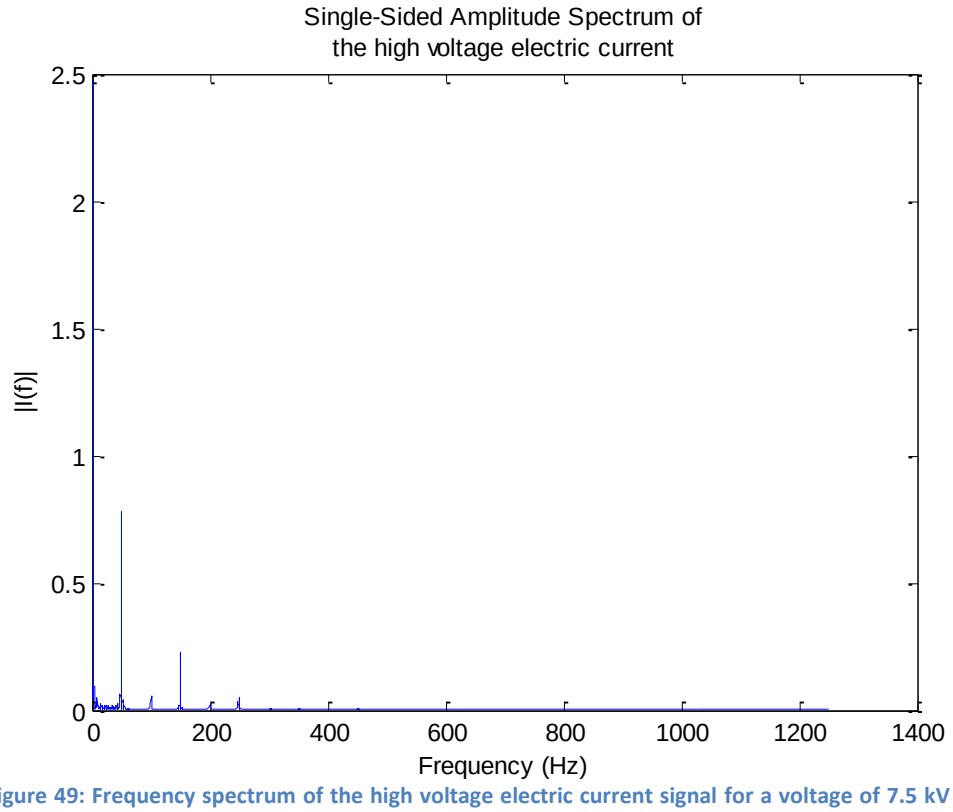

Figure 49: Frequency spectrum of the high voltage electric current signal for a voltage of 7.5 kV and a distance of 100 mm.

7.5 Jet Initiation Time

Having established a method for estimating the flight time for an electrospinning jet, it now stands that exploring the relationship between the processing parameters and the flight time is the next step. It is expected that an increase in the applied voltage should result in a shorter flight time due to the increased force experienced by the fibre. An increase in the flight distance provides a more complex problem. It is expected that an increase in the flight distance would decrease the electric field strength and hence the force on the fibre.

7.5.1 Distance

Under the conditions specified in the methods section, the flight times do not significantly vary with varying electrode distance as seen in Table 6. This is unexpected as the increase in flight distance should account for some variation if not the change in electric field strength. It is possible, however, that the change in flight distance results in such a small change in flight time that it doesn't register over the intrinsic error associated with this method. The intrinsic error in this method is high as the operator must reproduce the exact same initial meniscus so as to ensure identical conditions for jet initiation. It is interesting to note that although the variation due to distance is small, the flight times at 100 mm distance are always the smallest. This may represent an optimal point, yet the difference is typically within the reported errors so may simply be coincidence. This may be due to the forces exerted by a the external electric field being so high that the fibre will cross most practical electrode distances in approximately the same amount of time.

Table 6: Flight times for 8% PVOH under different electrospinning conditions. Reported error values are the standard deviation of the three repeats measured.

		Applied voltage			
		7.5 kV	10 kV	12.5 kV	15 kV
Electrode distance	80 mm	0.086 ± 0.008 s	0.054 ± 0.011 s	0.032 ± 0.003 s	0.0215 ± 0.001 s
	100 mm	0.086 ± 0.017 s	0.048 ± 0.005 s	0.030 ± 0.002 s	0.0202 ± 0.002 s
	120 mm	0.095 ± 0.011 s	0.053 ± 0.007 s	0.035 ± 0.003 s	0.0265 ± 0.004 s

7.5.2 Voltage

As the electrode distance appears to have no significant effect on the flight time it is reasonable to average the results for each applied voltage across the three distances. The averaged flight times follow a power law relationship ($t = 4.847kV^{-2.0}$) with respect to applied voltage (see Figure 50). This indicates that near the initiation voltage for electrospinning (approximately 5 kV for 8% PVOH) the flight times will be very long compared with the higher applied voltages where there will be less variation. It should be remembered that changing the applied voltage and hence the electric field exerting a force on the fibre will change the acceleration rate throughout the flight time. As such it would not be expected that doubling the force would halve the flight time. This is because the electric field is not uniform and varies with distance in the z axis, time spent in flight.

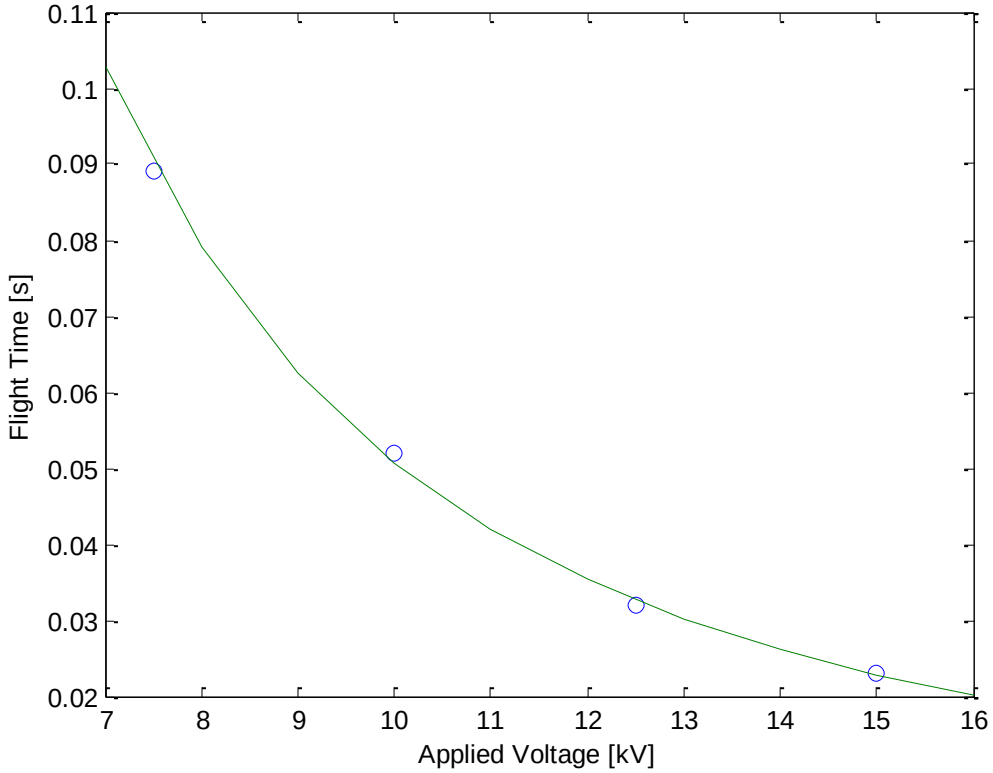

Figure 50: Flight time in response to applied voltage averaged over the three distances. Power law relationship is of the form t = 4.847 $kV^{-2.0}$.

7.6 Viscoelastic Damping of the Electric Stretching Force

In order to explore why changes in the electrode distance produce little variation in flight time, simulations were run to estimate the effect of changing either applied voltage or electrode distance on the flight time of the leading edge. The first simulation is the simplest one: the flight time of a charged particle is estimated with the same charge per unit mass as the electrospinning jet; that is 96 C/kg (see Chapter 6). This simulation uses the Lorentz equation (Equation (7.51)) to give the force experienced by the particle. From this, it is possible to solve Newton's second law of motion using an iterative method to approximate the solution to the ordinary differential equation (ODE). For this, one of the standard ODE solvers included with MATLAB is sufficient. In order to simulate the flight of this particle, a more accurate representation of the applied electric field than the parallel plate approximation is needed. The electric field was estimated using a point-plane configuration and simulated using COMSOL™. The electric field along the central axis of symmetry between the electrodes was then fitted to a power law function $E(d) = Ad^b$ where b is the exponent (see Figure 51). For an electrode distance of 50mm the power law exponent is -1.19, while for 100 mm and 150 mm the exponents are -1.31 and -1.41 respectively. This correctly represents the sharp decline in electric field strength with increasing distance from the Taylor cone. Simulating the particle flight time shows that the distance changes the flight time in a similar order of magnitude to the applied voltage (see Table 7). It can be seen that the flight times from the simulation are one or two orders of magnitude shorter than those seen experimentally in Table 6. Using this simulation, the flight

times respond to the applied conditions in the expected fashion. However, this simulation is a poor approximation of an elongating polymer jet as it neglects entirely the viscoelastic properties of the jet which would slow down the jet and reduce the flight time. Remembering that changing the applied voltage changes the forces acting on the jet throughout, this simulation does help explain the power law relationship to applied voltage seen in Table 6. Here, the power law description of the electric field strength obtained from COMSOL™ results in a power law relationship between flight time and applied voltage. The fitted power laws for the simulated results in Table 7 give an exponent of approximately -0.5 compared with -2.0 for the observed data. This difference is likely due to viscoelastic resistance to stretching in the real system, hence at low applied voltages (when the force is low) the flight times increase far more than the free particle case.

$$\boldsymbol{F} = q(\boldsymbol{E} + \boldsymbol{v} \times \boldsymbol{B}) \tag{7.51}$$

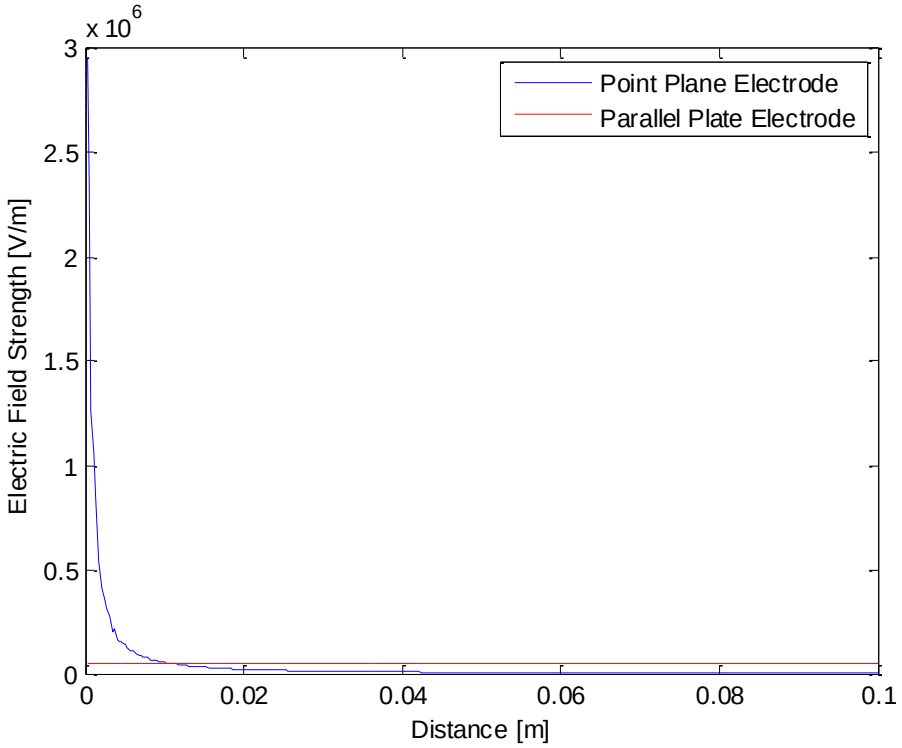

Figure 51: Electric field strength along the axis of symmetry for a point plate electrode arrangement for 5 kV potential difference and 100 mm electrode distance.

Table 7: Simply simulated flight times for 8% PVOH under different electrospinning conditions using non-linear electric fields.

		Applied voltage		
		5 kV	10 kV	15 kV
Electrode distance	50 mm	0.00088 s	0.00063 s	0.00051 s
	100 mm	0.00163 s	0.00115 s	0.00094 s
	150 mm	0.00234 s	0.00167 s	0.00137 s

A more suitable simulation would be one that includes some effect from the viscoelastic jet. The model presented in the paper by Reneker et al. (2000) and discussed in Chapter 3 provides us with

just such an option. However, despite the apparent simplicity of such a model the practical implementation is non-trivial. The set of differential equations are sufficiently unstable that without a detailed description of the algorithm as well as the equations and very specific initial conditions it is challenging to obtain a realistic solution. Without such a tool readily available the alternative is to analyse the relative size of the forces experienced by the fibres. The typical sum of forces in the jet is given in Equation (7.52) (see Chapter 3 for a full discussion). If considering a purely axisymmetric jet each force is individually defined in Equation (7.53) (Carroll et al., 2011).

$$\boldsymbol{F}_{sum} = \boldsymbol{F}_C + \boldsymbol{F}_E + \boldsymbol{F}_\sigma + \boldsymbol{F}_\gamma \tag{7.52}$$

$$\begin{aligned} F_C &= \sum_{i \neq j}^{N} \frac{q^2}{\left|z_i - z_j\right|^3}\left(z_i - z_j\right) \\ F_E &= qE(z) \\ F_\sigma &= \pi R_{di}^2 \sigma_{di} - \pi R_{ui}^2 \sigma_{ui} \\ F_\gamma &= -2\pi\gamma l \frac{dR}{dz} \end{aligned} \tag{7.53}$$

Without simulation, examination of Figure 51 shows that the force due to the electric field, F_E, will vary significantly across the distance between electrodes. At points close to the Taylor cone the jet will behave axisymmetrically. At the point of a typical whipping instability (~10–20 mm) the lack of axial symmetry is not as important as the field becomes more uniform through the z-plane due to the distance from the point source. As such the force experienced by the jet due to the external electric field can reasonably be assumed to be similar to the form shown in Figure 51, although if the charge carried by the jet were not constant, this force would decrease even further. This force would be like firing the jet from a cannon, with a very large initial push and little force afterwards. However, our existing simulation represents this force. The strength of the coulombic force, F_C, depends on the retention of charge and the distance between elements in the jet. As the jet is known to stretch this force must decrease along the length of the jet. Therefore the action of this force is similar to F_E, with a strong initial push that diminishes over time.

The surface tension force, F_γ, along with the viscoelastic force, F_σ, will resist stretching in the jet. These are the forces that will differentiate our discussion from the above simulation. F_γ is a simple force as it relates entirely to the rate of extension due to conservation of mass. As is discussed in Chapter 3, conservation of mass means that the radius of a segment of jet is dependent on the length of this segment. As the jet stretches the radius decreases, increasing the surface area of the jet. As such F_γ will be a force that strongly opposes the action of F_E and F_C in their initial phase when stretching is high but subsequently becomes less important as the stretching rate decreases.

Indeed, the thinning rate at a short distance from the Taylor cone has been shown to become much less and holds fairly constant (Carroll et al., 2006).

F_σ will depend on the difference in strain and strain rate along the jet either due to the elastic modulus or the viscosity of the liquid. Models of electrospinning typically use a simple Maxwell model of viscoelastic behaviour. Under this model there is a dashpot connected in series to a spring. Analysis of the equations used by Feng (2002) has shown that the rate of deformation is at its maximum near the Taylor cone and reduces considerably within the jet region. With the very strong initial forces F_E and F_C (and large deformation rate), stress will be instantly developed from the elastic component (directly proportionate to the strain), promoting thinning together with stretching. As the jet continues to deform and hence forces and strain rate decrease, the viscous component of the stress will develop and work against stretching while the overall stress will decay exponentially.

Carroll et al. (2006) observed that increasing the polymer's relaxation time ($\lambda = \Psi_{01}/2\eta_p$ where Ψ_{01} is the low shear rate limit of the first normal stress coefficient and η_p is the polymeric contribution to viscosity of the solution; which reflects its elasticity, and therefore the Deborah number $De = \lambda v/R$) causes the thinning radial compressive force to develop more rapidly. However, farther from the spinneret, the thinning forces die away more rapidly presumably due to larger extensional viscosity (as the polymer molecules uncoil) acting against the electric field. Similarly, stretching axial forces are developed sooner and are stronger for the more viscoelastic polymers. Note that increasing λ has the same effect as increasing the electric field (i.e. increased stretching) as it will result in higher De.

Under conditions such as these, the effect of a high initial force will be reduced compared with the effect of the smaller forces acting over a longer region. No matter if the electric field is increased by increasing applied voltage or the distance, in both cases that will results in an increased initial stretching rate. The effect of increased applied voltage and distance will be discriminated by the overall stretching.

Changes in distance will result in minimal changes in the electric field strength for most of the region of the fibre's flight but important changes at the point electrode (see Chapter 5, Section 5.2.2). This is due to the concentration of force caused by the point electrode in the point-plane electrode configuration. In traditional electrospinning the point is the syringe needle. As the distance decreases the point electrode will further focus the electric field lines resulting in a higher peak electric field but having less influence on the more uniform field further from the point electrode. In other words, the jet is strongly thinned initially but stretches more slowly. On the contrary, changes in applied voltage will result in a uniform increase of the forces experienced by the jet. In other

words, the jet will initially be strongly thinned but will also continue to stretch at higher rate. Hence changes in applied voltage would have more effect on the flight time than changes in electrode distance.

7.7 Jet Initiation Time

Upon completion of the previously discussed experiments additional high speed video equipment became available. This allowed the estimation of the time taken for a jet to be ejected from the Taylor cone once high voltage is applied. Estimating this time was achieved by placing a Light Emitting Diode (LED) in the camera field of view; this LED was switched by the same signal that initiated the high voltage that forms the Taylor cone. Recording the resultant jet initiation at 1000 frames per second allowed the estimation of the time from high voltage application (signalled by the LED light turning on) to the observed first ejection of mass in the form of a jet. However, it should be noted that high speed video capture requires very high light levels that also significantly heat the field of view of the camera. Hence these observations are not directly comparable with the previously discussed work. The reasons for this incompatibility may be environmental, due to variations in laboratory relative humidity and temperature affecting the solvent evaporation rate and leading to significant changes in the viscoelastic properties of the polymeric fluid.

This preliminary work indicated that at the distances of 80, 100, 120 mm and 10, 12.5, 15 kV the jet initiation time was constant within the estimated error values. For 7.5 kV at 80, 100 and 120 mm the jet initiation time was found to be slightly longer but still constant over the three distances. The tentative conclusion from this work is that that the jet initiation time is constant for a given polymer system, and that this novel method will add to the understanding of the effect of applied voltage and electrode distance on jet flight time. In terms of the previous tranche of experimental work these observations, although at quantitative variance with the earlier observations for the reasons outlined, do support the validity of the previously discussed method of using high speed current measurement at the collector to estimate the flight time. This is because the jet initiation time appears to be constant under most conditions with only slight variation when the voltage begins to approach the minimum initiation voltage.

7.8 Conclusions

This chapter establishes a novel method for estimating the flight time of an electrospinning jet. Observations were made for 8% PVOH in water. High speed video observations revealed that the jet initiation process closely mimics the quasi-steady state in electrospinning with the immediate formation of the whipping instability. Further observations found that the jet initiation time is approximately constant. The method is non-contact which overcomes previous difficulties in measuring the flight time of the jet. It was found that the flight time did not vary significantly with

increased flight distance. However, with increasing applied voltage the flight time decreased in a power law relationship ($t = 4.847kV^{-2.0}$). This is attributed to the viscoelastic properties of the jet resisting the large initial change in electric field strength caused by changing the electrode distance which leaves the bulk of the flight distance at similar electric field strengths. A simulation was performed using a charged particle with the same charge density as the electrospinning jet and an identical electric field. This simulation demonstrated the significance of the viscous forces in the flight time, increasing the jet flight time by up to two orders of magnitude and further increasing the flight time at low applied voltages.

CHAPTER 8

CHARGE LOSS IN THE ELECTROSPINNING PROCESS

8 Charge Loss in the Electrospinning Process – Observations

8.1 Introduction

Chapter 4 demonstrates that charge is lost to the surrounding environment between the high voltage electrode and the grounded collector electrode. It is thought that the charge carried with the electrospinning jet is associated with ions in the polymer solution and hence linked to conductivity of the solution (He et al., 2004, Reneker et al., 2000). A short distance from the Taylor cone the velocity of the fluid becomes sufficiently larger than the velocity of the ions (the drift velocity) that the ion velocity can effectively be thought of as the velocity of the fluid (Collins et al., 2012, Hohman et al., 2001, Reznik et al., 2004). This would lead to a situation where all the charge would be presented on the surface of the jet due to the self-repulsion of the charged ions. It has been shown that variation of processing conditions changes the current drawn from the high voltage source (Stanger et al., 2012). This chapter investigates the effects of processing conditions on the amount of charge lost from the fibre in flight.

To determine the charge lost in flight, the electric current will be observed at the high voltage electrode and the collector electrode. As electric current is a measure of the flow of electric charge any difference in the two electric currents would strongly indicate that charge is lost from the jet while it moves from one electrode to the other. As there are many inter-related factors that affect the electrospinning process it is important to limit the number of factors that change in any one experiment. The charge lost while the jet is in flight will be studied by varying the applied voltage and the electrode distance only while keeping all solution and environmental properties constant for a single set of experiments.

Changing the polymer concentration will change the rate of jet thinning (Deitzel et al., 2001a) and hence the surface area that charge is held on. To examine the effect of polymer concentration the same experiments described below are done using 9% and 8% PVOH. The typical working range for PVOH described in the materials section below (Section 8.2.1) is approximately 6–15%, limited in the upper range by the difficulty of dissolving additional PVOH. A change of 1% should show detectable variation if polymer concentration has an effect.

Previous work (Stanger, 2008) has shown that the addition of an ionic salt changes many of the properties of the electrospinning process and fibre properties such as jet diameter, mass deposition rate, fibre diameter and draw ratio. To determine if the concentration of ions in solution has a measurable impact on the observed electric currents and the charge loss, 0.3% wt sodium chloride was added to a solution of 8% PVOH in water. This is a similar quantity to that added in the previous work (Stanger, 2008).

All proposed experiments so far have been for PVOH, which is an aqueous system. An alternative polymer system is examined which is stable and controllable. Electrospinning of PVB in ethanol is not an entirely non-aqueous system but is sufficiently differentiated from aqueous PVOH to test if the charge loss phenomenon is a general phenomena or one that is specific to PVOH or aqueous systems. Electrospinning of PVB from ethanol can be kept stable, though it does require periodic removal of dried material at the Taylor cone to prevent the orifice from clogging. At the concentration proposed in the materials section below (Section 8.2.1) this is only required approximately every 1–2 min. The fibres formed are of reasonable quality and dry. This gives four different experiments that will show how the charge loss behaviour varies with solution composition and determine if this charge loss is a general part of the electrospinning process or only occurs under specific conditions.

8.2 Method and Apparatus

8.2.1 Materials

Electrospinning was carried out using an aqueous solution of poly(vinyl alcohol) (PVOH). A stock solution was prepared as per Section 4.2.1. The stock polymer solution was diluted to an accurate final concentration of 8 wt% which is equivalent to 6.87 x 10^{-4} mol/L when using the average molecular weight.

Ionic salt used in this chapter was Potassium Chloride (KCl) (BDH, NZ) AnalaR grade. The salt was added to the diluted polymer solution at a wt% relative to the weight of the diluted solution. Salt was added at a quantity of 0.3%wt which is equivalent to 0.019 $molL^{-1}$ for 8% PVOH in water. The salt was stirred into the solution and left for 4 h before use.

Subsequent electrospinning was carried out using poly(vinyl butyral) (PVB) (United Paints Ltd, Christchurch, NZ). The polymer solution was prepared by dissolving PVB in industrial ethanol (approximately 94%) (Thermo Fisher Scientific New Zealand Ltd, Auckland, NZ) at a concentration of 18% by weight. This was done at room temperature and left to sit in a sealed bottle for at least 4 h before use.

8.2.2 Apparatus

All samples were electrospun at using a Model ES4 electrospinning platform (Electrospinz Ltd, New Zealand). The pressure of the polymer solution at the spinning head (varied by a gravity feed system) was used as the control variable. Once stable spinning was attained the pressure was kept constant. The high voltage electrode was a nominally 30 mm o.d. stainless steel tube with a 2 mm wall thickness. The spinning tip was an Axygen T-200-Y 200 µL pipette tip with a nominal inner diameter of 0.5 mm. Clean 150 mm square sheets of stainless steel were used as collector electrodes.

National Instruments compactDAQ data logging system (as described in Chapter 4) was used to record the high voltage and collector electric current flow. For the collector electrode, the resistor used in-line with the connection to ground was a high precision (0.1% tolerance) 10 kΩ resistor (RS Electronics Ltd, New Zealand). The EMCO high voltage supply in the Electrospinz ES4 was bypassed to allow the use of a Glassman MK50P1.5 high voltage power supply to provide direct current feedback for data logging experiments as per Chapter 4.

8.2.3 Methods

All electric current measurements taken in this chapter followed the procedure outlined in Section 8.2.2 for the compactDAQ approach. Variation of the charge loss rates due to flight distance was examined by varying voltage as described in Section 8.2.2 at a range of distances. The distances chosen between the high voltage electrode and the collector electrode ranged between 50 and 130 mm in 10 mm steps giving a total of nine distances. For each tip to collector distance, electrospinning was undertaken at applied voltages ranging from approximately 5.6 kV to 20 kV with steps of approximately 0.55 kV giving 26 different applied voltages. This gives a total of 234 different electrospinning conditions. For each distance four repeats of each voltage sweep is recorded in a randomized order. Each voltage sweep begins by scanning upwards from 5.6 kV to 20 kV followed by scanning downwards from 20 kV to 5.6 kV. These results were then averaged giving a total of eight measurements per set of conditions where an average of ~4,500 samples constitute the steady state behaviour at each electrode distance and applied voltage. The above experiment exactly as described is repeated for the higher concentration of 9% PVOH and 8% PVOH with 0.3% wt. ionic salt. A similar experiment is performed for 18% PVB but the applied voltage starts at 6.9 kV and scans upwards to 20 kV followed by scanning back down to 6.9 kV. All other aspects of the experiment with PVB are kept the same as those for PVOH.

8.3 Data

8.3.1 Sources of Error

This work discusses the difference in the observed electric current at the high voltage electrode and the collector electrode. While it has been shown in Chapter 4 that the apparatus described in Section 8.2 can provide repeatable measurements with known levels of noise and a signal that corresponds to the electrospinning process, there are problems associated with comparing the observed pair of signals. It assumes that the electric current flowing through the collector is representative of the charge carried by the electrospinning jet. Due to conservation of charge, any charge lost must find an alternative circuit path (see Figure 52). In a typical laboratory there are many options for alternative circuit paths. However, one unavoidable option is the paths between the electrodes that bypass the electrospun jet itself and travel directly to the collector electrode (see

Figure 52). In this case charge would be lost from the electrospinning jet but is sufficiently close to the collector that it is energetically unfavourable to take any route other than through the collector. This would lead to a reported current flow that is higher than that carried by the jet. There is no electrode configuration or apparatus that can be built that will prevent this from happening without affecting the electrospinning process itself. Therefore all reported charge losses may be smaller than reality. Examining charge loss has not been undertaken in detail before. The focus is on demonstrating that under a wide range of conditions there is an observable charge loss occurring and that the quantity can be related to environmental, solution or processing parameters.

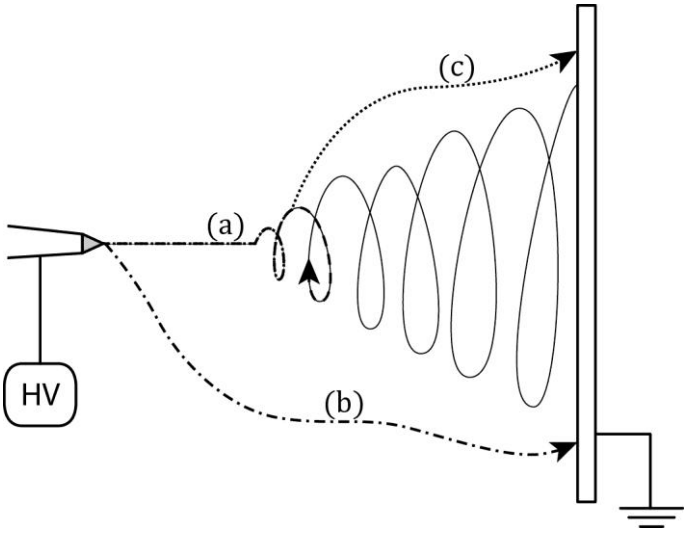

Figure 52: Examples of alternative circuit paths for charge lost from the jet i.e. a) is a direct path following the jet path or b) is an indirect path through the atmosphere or c) is an indirect path from part way through the jet through the atmosphere. All paths end at the collector.

8.3.2 Applied Voltage

As was seen in the previous chapter (see Chapter 6 Section 6.4) the observed electric current at the high voltage electrode and the collector electrode both vary with applied voltage at a fixed distance. It can be seen in Figure 53 that at all applied voltages for a fixed distance of 100 mm, the observed electric current at the high voltage electrode exceeds that at the collector electrode. The difference between these electrodes indicates a loss of charge being carried by a jet. The four polymer solutions examined all show a similar difference between the high voltage and collector electric current. For the three aqueous solutions of PVOH high voltage and collector electric current follow a similar pattern. The main difference between these polymer solutions is that for a given distance the observed electric currents follows the order 8% PVOH < 9% PVOH < 8% PVOH w salt (see Figure 54). This order is true both for the high voltage and collector electric current. This order also represents the order of increasing conductivity; however, with only three data points nothing can be concluded about the nature of the relationship between solution conductivity and electric current.

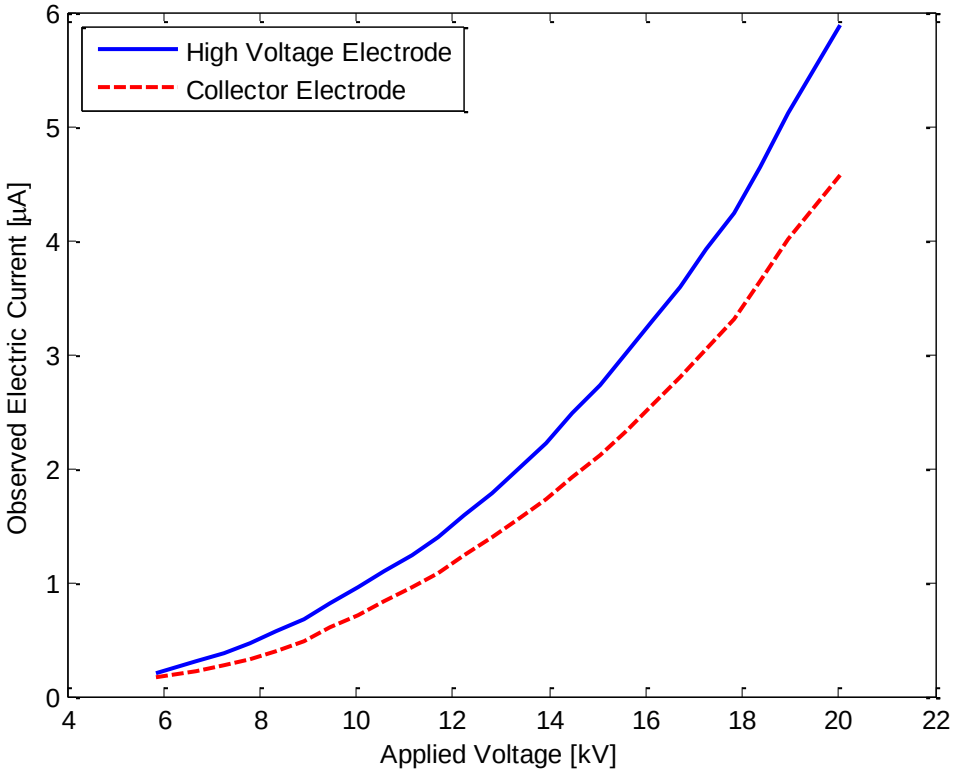

Figure 53: Observed electric current for 8% PVOH in water being electrospun at different applied voltages for a distance of 100 mm.

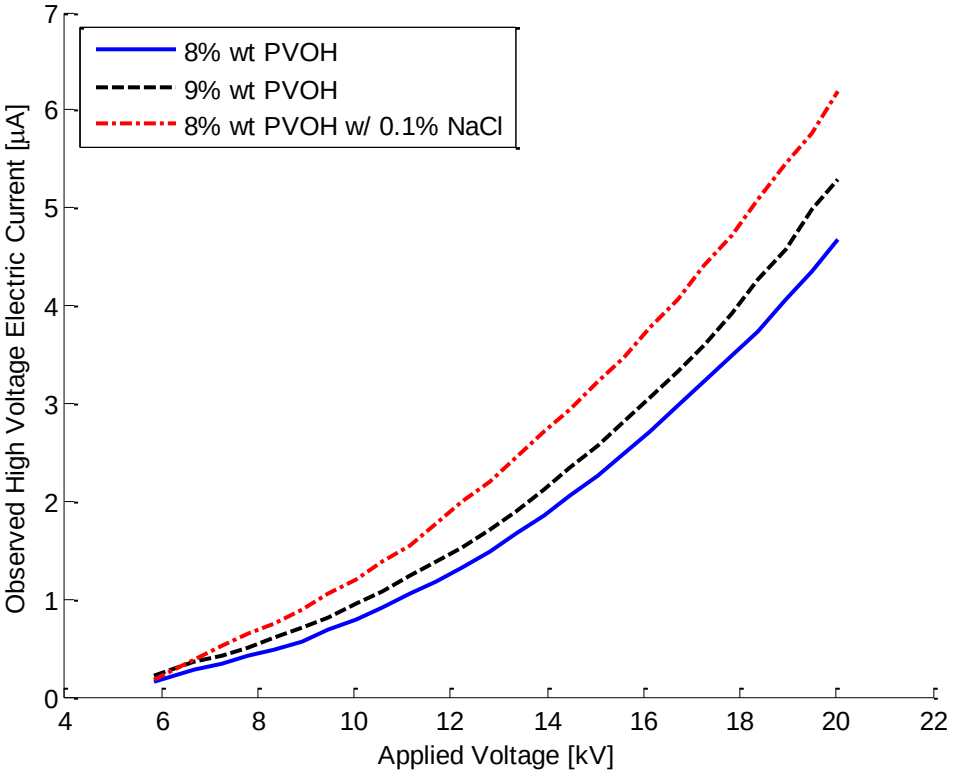

Figure 54: Observed high voltage electric current for 8% PVOH, 9% PVOH and 8% PVOH w/ 0.1% NaCl in water being electrospun at different applied voltages for a distance of 100 mm.

Figure 55 shows that for 8% PVOH the difference between the high voltage and collector electric current (ΔI) appears to increase with increasing applied voltage. This also corresponds to increasing

high voltage electric current. A similar relationship is seen for the other two PVOH based polymer solutions examined.

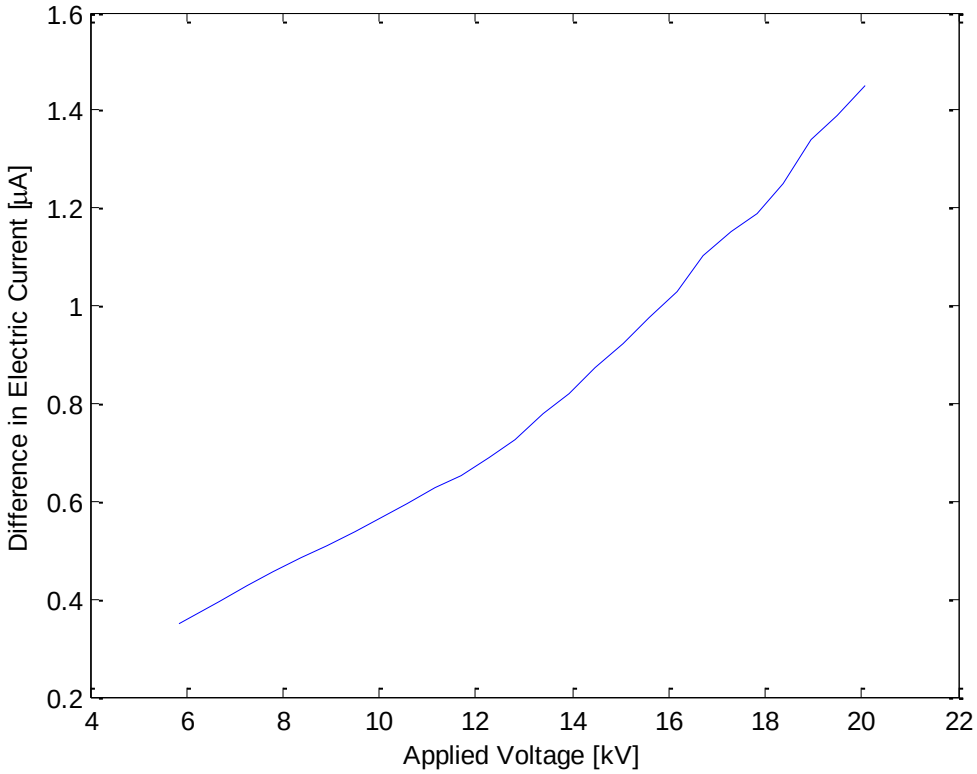

Figure 55: Difference between observed electric current at the high voltage electrode and the collector electrode for 8% PVOH in water being electrospun at different applied voltages for a distance of 100 mm.

8.3.3 Electrode Distance

As described in Section 4.2.3 8% PVOH was electrospun at nine different electrode distances ranging from 50 mm to 130 mm. Figure 56 show the currents at 50 mm, 90 mm and 130 mm. It can be seen that for all distances the electric current at the collector is consistently less than at the high voltage electrode. It is also clear that as distance increases the losses increase. The same trend is seen for the other two PVOH solutions where at all distances the observed electric current follows the same order previously seen: 8% PVOH < 9% PVOH < 8% PVOH with salt. The increasing difference with increasing distance is seen more clearly in Figure 57 which shows the difference in observed electric current between the two electrodes. In terms of absolute losses, more charge is lost when the distance is 130 mm.

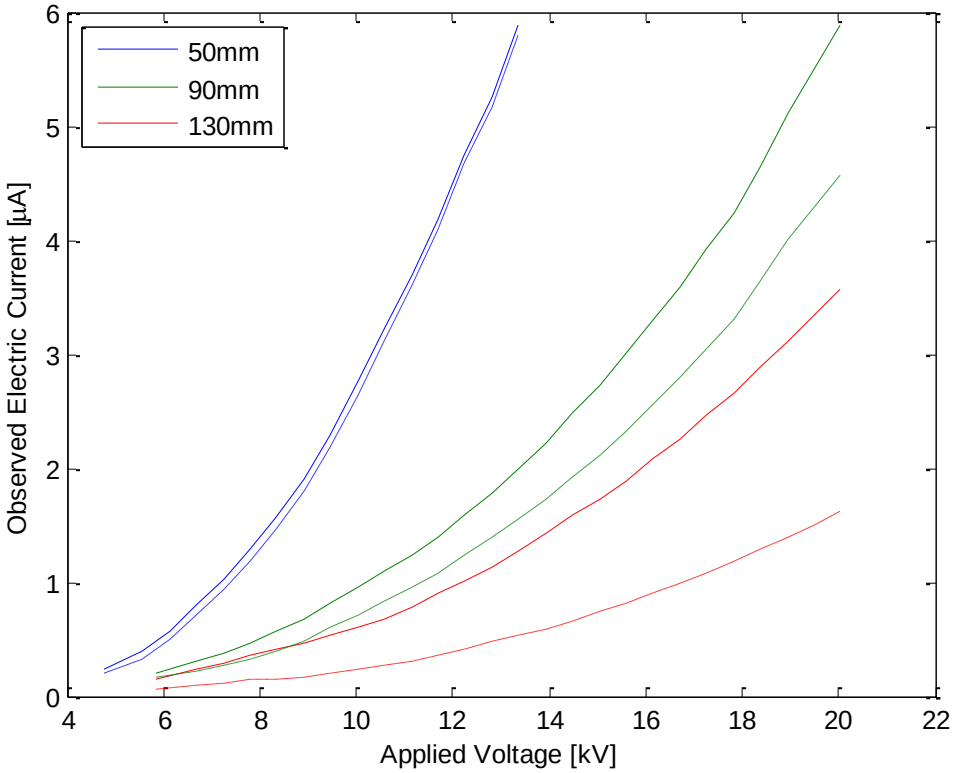

Figure 56: Observed electric current for 8% PVOH in water being electrospun at different distances. Solid lines represent the current observed at the high voltage electrode while dashed lines represent the current observed at the collector.

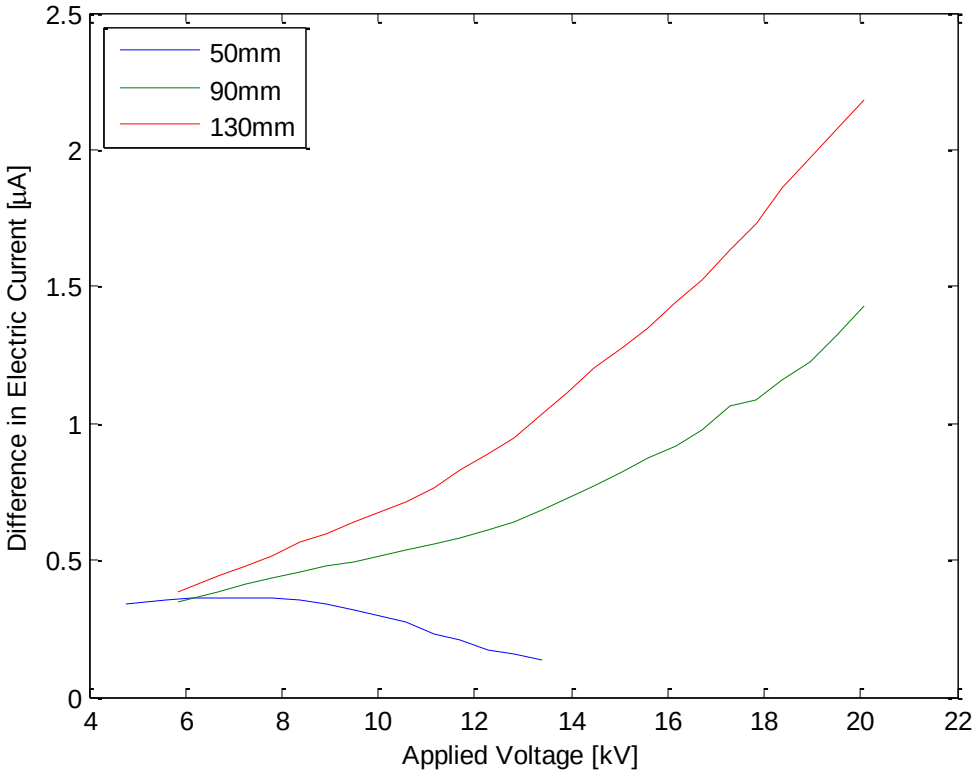

Figure 57: Difference between observed electric current at the high voltage electrode and the collector electrode for 8% PVOH in water being electrospun at different applied voltages for three distances of 50, 90 and 130 mm.

8.3.4 Loss Fraction

The aim of this chapter is to examine the nature of charge loss during electrospinning. There are two ways one can quantify a loss of charge. The most obvious is the one already discussed, i.e. the difference in the high voltage and collector electric current flow (ΔI). However, it is possible to examine the loss in terms of the fraction of the high voltage electric current that arrives at the collector. Figure 58 shows that this method of examining the losses reveals an almost constant loss rate for a given distance at all applied voltages. This is most obvious at voltages above 11 kV. At the longest tip to collector distance there is approximately only 42% of the high voltage electric current arriving at the collector. The applied voltage cannot act as a substitute for the local Taylor cone electric field when examining loss rates. This is because although the applied electric field changes with the applied voltage, so does the mass flow rate and hence the Taylor cone shape, which in turn modifies the local Taylor cone electric field. Near the initiation voltage for electrospinning (i.e. from 5 kV up to 11 kV) the losses increase followed by a decrease when near the reasonable limits of detection for the compactDAQ platform (i.e. signal is < 1 mV). A similar trend is seen with all three PVOH solutions. For PVOH solutions, 8% PVOH has the most loss of charge, followed by 9% PVOH with 8% PVOH and salt having the least loss of charge. This can be seen in Figure 59, which shows the fraction of the electric current arriving at the collector for a tip to collector distance of 130 mm. At tip to collector distances of 100 mm or less, the fraction arriving at the collector becomes effectively the same for each PVOH solution.

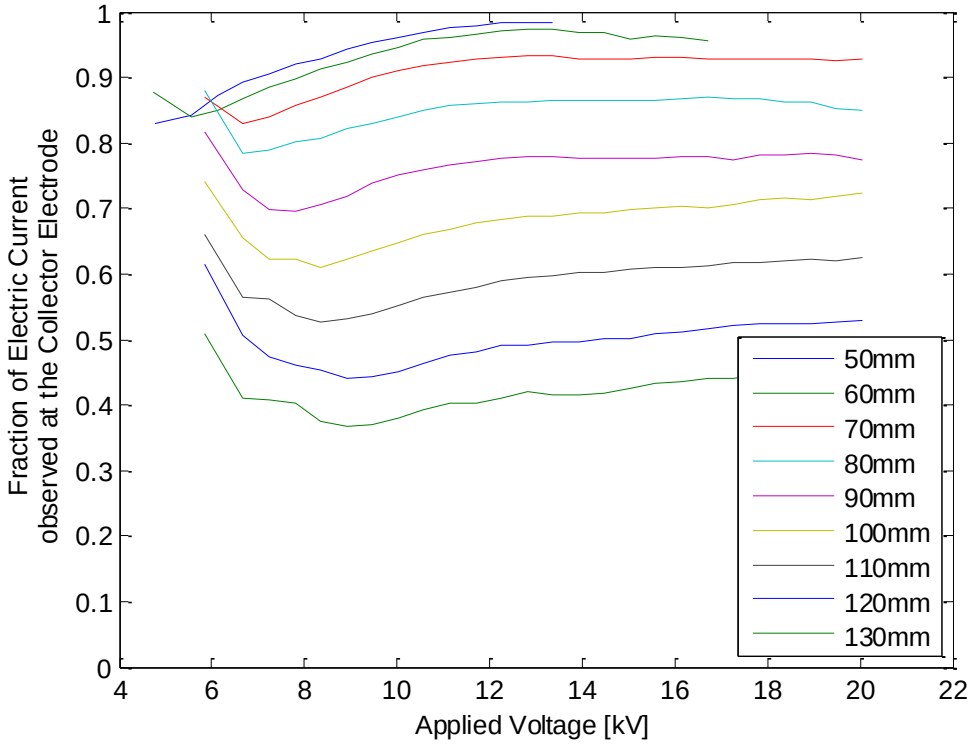

Figure 58: Fraction of electric current arriving at the collector electrode for 8% PVOH at all distances.

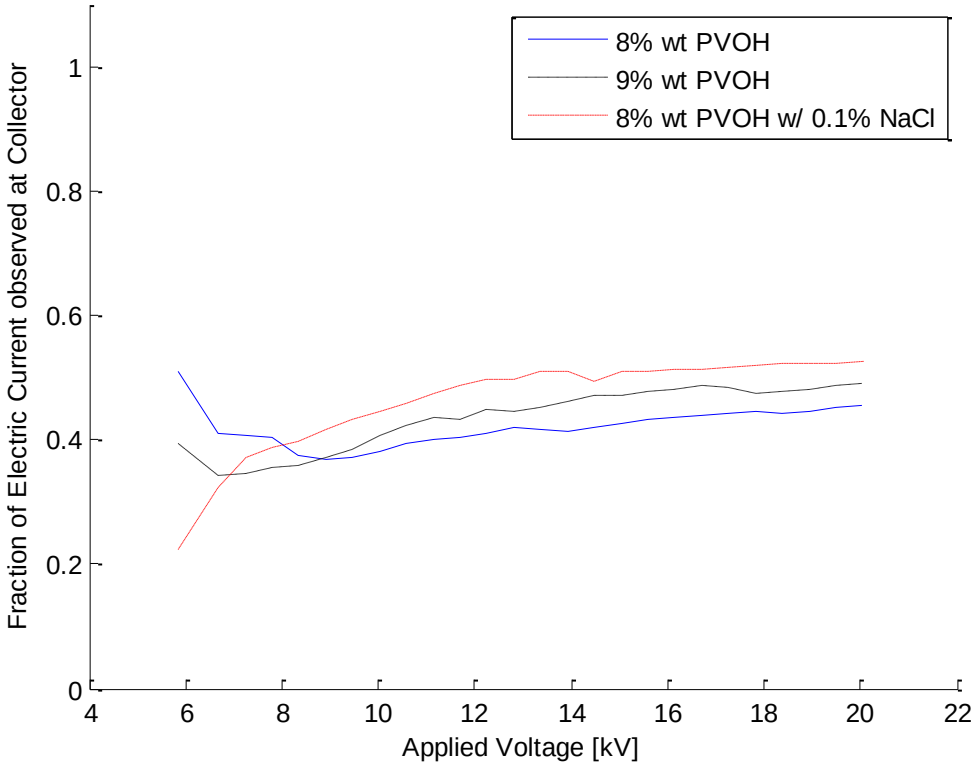

Figure 59: Fraction of electric current arriving at the collector electrode for 8% PVOH, 9% PVOH and 8% PVOH w/ salt at a distance of 130 mm.

8.4 Data Analysis

Any attempt to analyse the collected data faces the challenge that most of the variables in the electrospinning process are interrelated as seen in Section 8.3.4. Transforming the data from applied voltage to electrode distance is not trivial. This section therefore aims to use the high voltage electric current as a proxy measure of the local Taylor cone conditions and analyses charge loss for a range of flight distances (determined by electrode distance) associated with isomorphic Taylor cones. The goal is not to reproduce the exact same experiment (identical global conditions) but to reproduce identical initial conditions for the electrospun jet formation (local Taylor cone conditions). This can be justified as follows.

8.4.1 Taylor Cone Analysis

To achieve the transformation of the data from varying applied voltage to varying electrode distance there needs to be a method of determining what global conditions provide equivalent initial conditions in the local Taylor cone region. First it is possible to convert the high voltage electric current data into mass deposition rate data using the linear relationship from Chapter 6. This means that contour lines in the high voltage electric current data correspond to contour lines in the mass deposition rate (see Figure 60). To generate an equivalent mass deposition rate for an identical solution under different applied voltages or distances suggests equivalent local Taylor cone

conditions. This can only be true when the fluid pressure is controlled to maintain a stable Taylor cone rather than setting an arbitrary mass flow rate. Under this requirement the Taylor cone is always in a state where the forces are in a state of balance. Work by Demir et al. (2002) shows that the jet diameter increases with respect to applied voltage. This can be seen as equivalent to the Taylor cone shape changing in response to an increased mass flow rate. From Figure 60 it can be seen that for each distance there is only one voltage that can generate the same mass deposition rate. As such this is the unique local Taylor cone condition that corresponds to an equivalent experiment with a different flight distance available. This allows the charge loss to be studied with respect to changing flight distance. Summarizing, it can be reasonably assumed that for the same fluid, at the same flow rate, that the same local electric field is needed to form the same shaped Taylor cone. The data must be mined for electrospinning conditions that result in these isomorphic Taylor cones.

Using the high voltage electric current as a proxy for measuring local Taylor cone conditions, it is possible to examine the effect of flight distance on charge loss while maintaining an isomorphic stable Taylor cone and therefore identical initial conditions for the jet/fibre ejected. To further demonstrate the non-linear nature of the local Taylor cone conditions with respect to flight distance Figure 60 shows the contours of constant electric current that are observed in the electrospinning process. These lines are equally spaced on the domain of observed electric currents; they are not equally spaced on the parameter space of applied voltage and tip to collector distance. This reflects the non-linear current/distance and current/voltage relationships determined in Chapter 6.

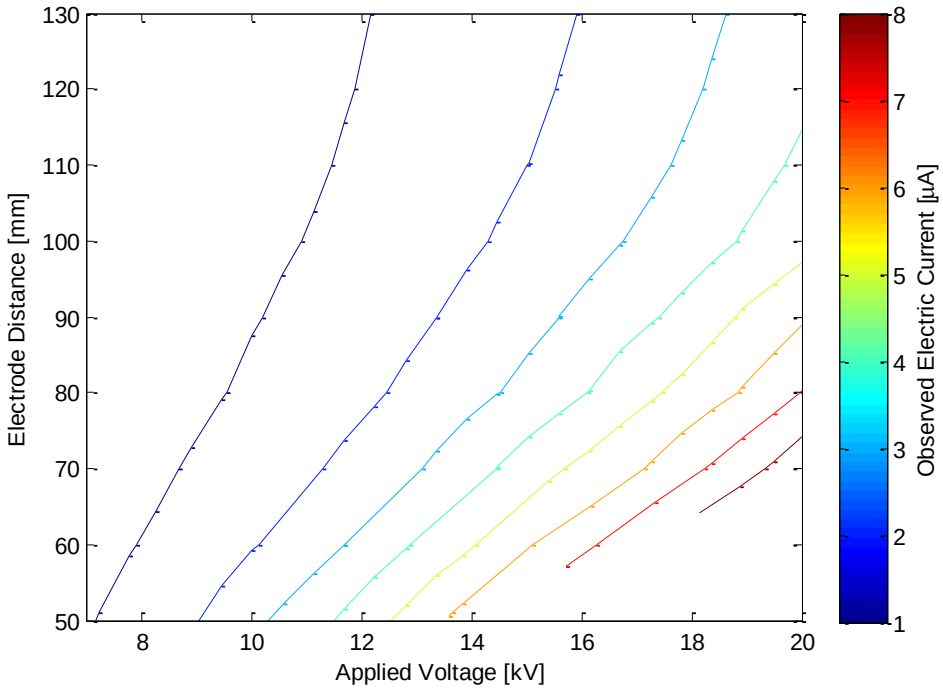

Figure 60: Contour plot of the observed high voltage electric current for 8% PVOH at all electrode distances and applied voltages.

8.4.2 Fitting an Electric Current Model

To transform the observed data into losses at lines of constant electric current, first the observed electric current data are interpolated using a 5th order polynomial with respect to applied voltage. This is chosen to accurately interpolate the raw data rather than to provide a theoretical description of the high voltage electric current as is explored later in this chapter. The 5th order polynomial fit can be seen on the accompanying plots in Figure 61. As 5th order polynomials are non-trivial to invert, the applied voltage required to observe a given high voltage current is iteratively found. Details of the process can be found in Appendix A. For a range of electrospinning distances this gives interpolated collector electric currents for fixed high voltage electric currents. The constant flow regimes were chosen to be 0.75, 1, 1.5, 2 and 3 µA. The result of this fitting process is shown in Figure 61. A selection of applied voltages and distances required to produce a constant flow regime are shown in Table 8.

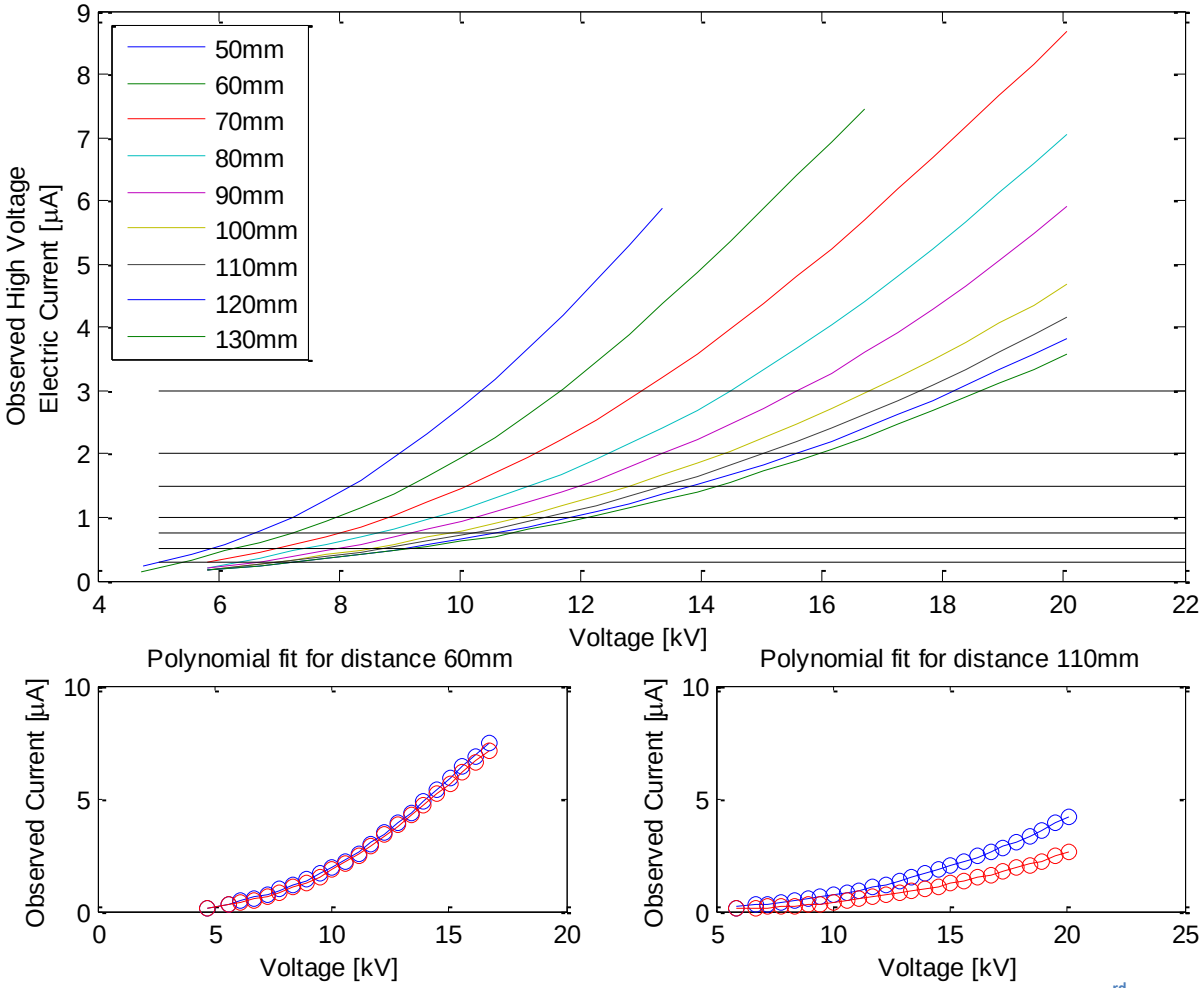

Figure 61: Polynomial fitting for interpolation of high voltage and collector electric current. Top plot shows 3rd order polynomial fits for high voltage electric current at all distances along with lines of constant current used in the analysis described in the text. The bottom plots show the quality of the polynomial fit with raw data as circles and the solid lines as the fitted function.

Table 8: Applied voltages and distances required to obtain a constant flow regime for electrospinning 8% PVOH. Each row represents one constant flow regime. Dashes represent data out of range of interpolation.

Current	Electrode distance								
µA	50 mm	60 mm	70 mm	80 mm	90 mm	100 mm	110 mm	120 mm	130 mm
0.75	6.62	7.20	7.97	8.58	9.20	9.81	10.20	10.62	10.85
1.00	7.22	7.97	8.80	9.58	10.25	10.95	11.45	11.88	12.18
1.50	8.20	9.18	10.14	11.19	11.97	12.82	13.43	13.90	14.25
2.00	9.01	10.14	11.23	12.47	13.37	14.33	15.03	15.54	15.92
3.00	10.35	11.67	13.02	14.48	15.61	16.80	17.60	18.20	18.66

Taking the fitted functions shown in Figure 61 and the values given in Table 8 allows the calculation of the loss rates at each distance for varying flow rates. The results of this calculation are shown in Figure 62. These interpolated charge loss rates can be considered equivalent to experimental data. It can be seen that for distances greater than 80 mm there is a linear relationship. The average linear gradient is -0.0086 mm^{-1}. Below this distance the loss rates start to asymptotically decrease to zero. This is unsurprising as the fraction lost would only decrease to exactly zero if there was a set of conditions where all losses could be eliminated. This suggests that under reasonable conditions there will always be some loss of charge from the jet. It is possible that at tip to collector distances of less than 80 mm a significant proportion of the created space charges are grounded through the collector. This would explain the deviation from the linear relationship as an increasing proportion of the charge lost at short tip to collector distances would be grounded through the collector. This would lead to a charge loss rate that was reported to be less than reality. Figure 62 also shows that the loss rates decrease with increasing mass flow rate (the bottom blue line is the lowest flow rate). Similar results are seen for 9% PVOH and 8% PVOH with salt. The fitted loss rates for 9% PVOH has an average linear gradient of -0.0071 mm^{-1} while 8% PVOH with salt has an average linear gradient of -0.0064 mm^{-1} (8% PVOH is -0.0086 mm^{-1}). The linear region extends a further 10 mm to 70 mm for both 9% PVOH and 8% PVOH with salt. The difference between the three PVOH solutions can be seen in Figure 63. Both 9% PVOH and 8% PVOH with salt also show that increasing mass flow rate increases the observed losses.

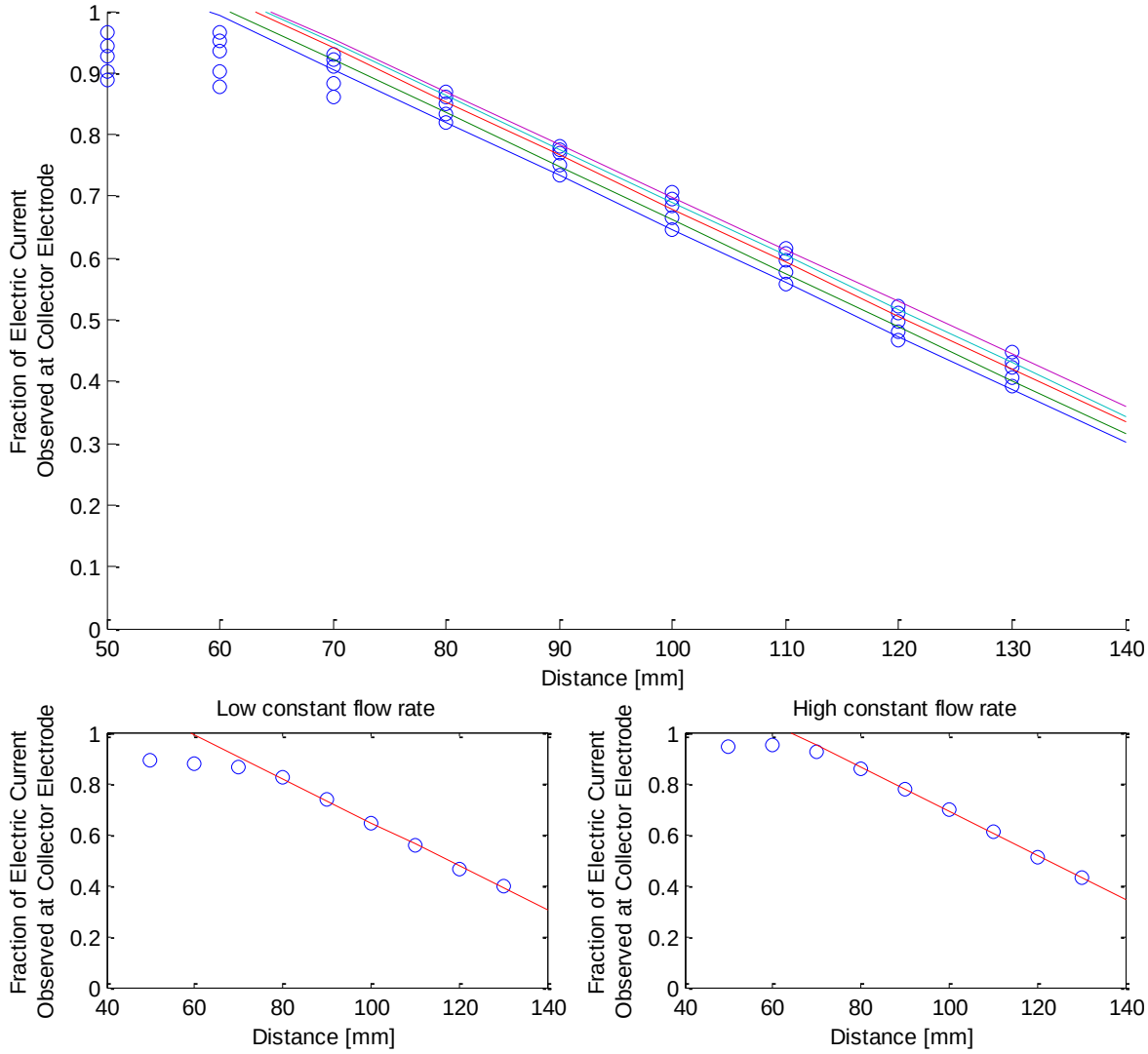

Figure 62: Relationship between electrode distance and fraction of electric current arriving at the collector for a range of constant flow regimes for 8% PVOH. Top plot shows this for all constant flow regimes chosen in the text with the lowest line corresponding to the lowest flow and the highest line corresponding to the highest flow. The bottom plots show a low flow regime on the left and a high flow regime on the right.

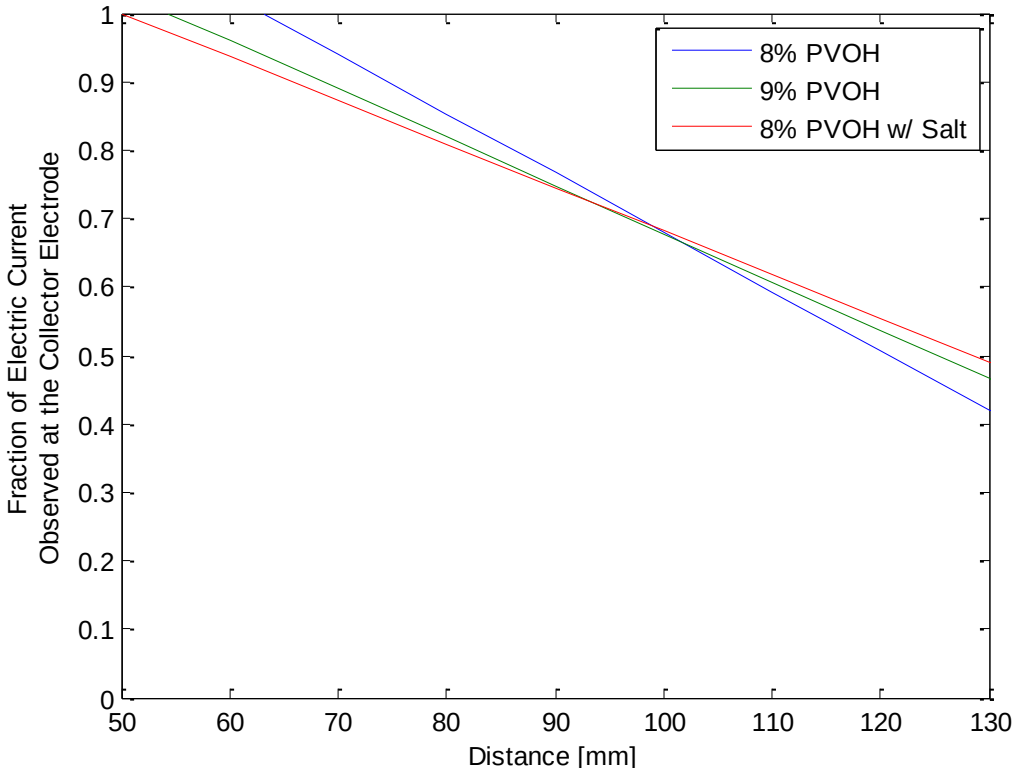

Figure 63: Comparison between loss rates for lines of constant flow (1.5 µA) for 8% PVOH, 8% PVOH with 0.3% wt KCl and 9% PVOH.

8.4.3 Poly(Vinyl Butyral) as an Alternative Polymer System

Figure 65 shows that when the polymer solution is changed to 18% PVB in ethanol the electric current behaviour appears to be different from PVOH (see Section 8.3.2). At low electric field strengths (low applied voltages and short distances) the whipping instability forms with the normal expanding helical envelope cone. This mode shall be referred to as the traditional spinning mode. At higher electric field strengths the mass flow rate appears to increase significantly due to the sudden increase in polymer supply pressure required. In this mode of electrospinning the whipping instability also takes on a characteristic cylindrical formation rather than the normal expanding envelope cone. This cylinder occurs at approximately the same position as the traditional whipping instability occurs. Unexpectedly the fibre appears to occasionally reverse direction towards the high voltage electrode at the formation of the whipping instability before returning on a path within the cylinder to the collector. This mode shall be referred to as the high volume throughput spinning mode. This mode also spontaneously generates free standing fibre structures to grow from the collector electrode towards the point of whipping instability (see Figure 64). This often results in small droplets being deposited on the collector without being converted to fibre. Eliminating this behaviour does not seem to alter the electric currents being observed compared with periodically destroying these structures when the Taylor cone is wiped free of dried material. It is possible to see the transition between different spinning modes discussed above at approximately 12 kV in both the high voltage and collector observed electric currents (see Figure 65). The electric current appears to

be a piecewise defined function that is at least C^0 continuous. At voltages below 12 kV it follows an approximately linear function while above 12 kV it appears to follow a function similar to that seen in PVOH. At the point, 12 kV, there is a transition point, likely related to the drastic change in the mass flow rate.

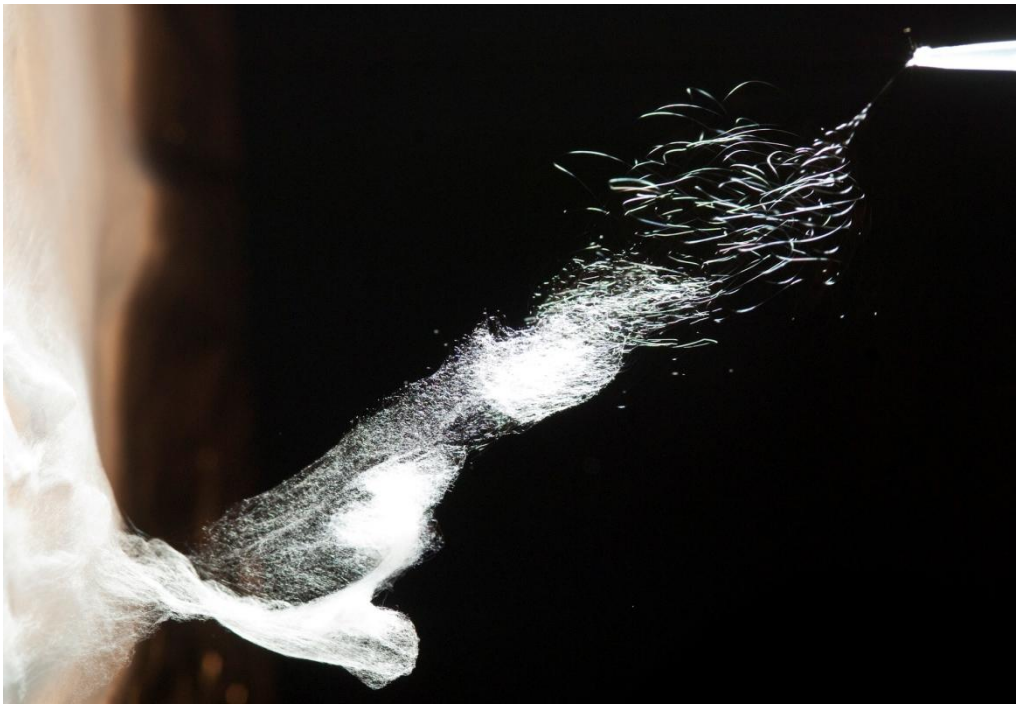

Figure 64: High speed photo of 18% PVB electrospinning under conditions to generate the high volume throughput mode, highlighting the spontaneous free standing structures that can be generated.

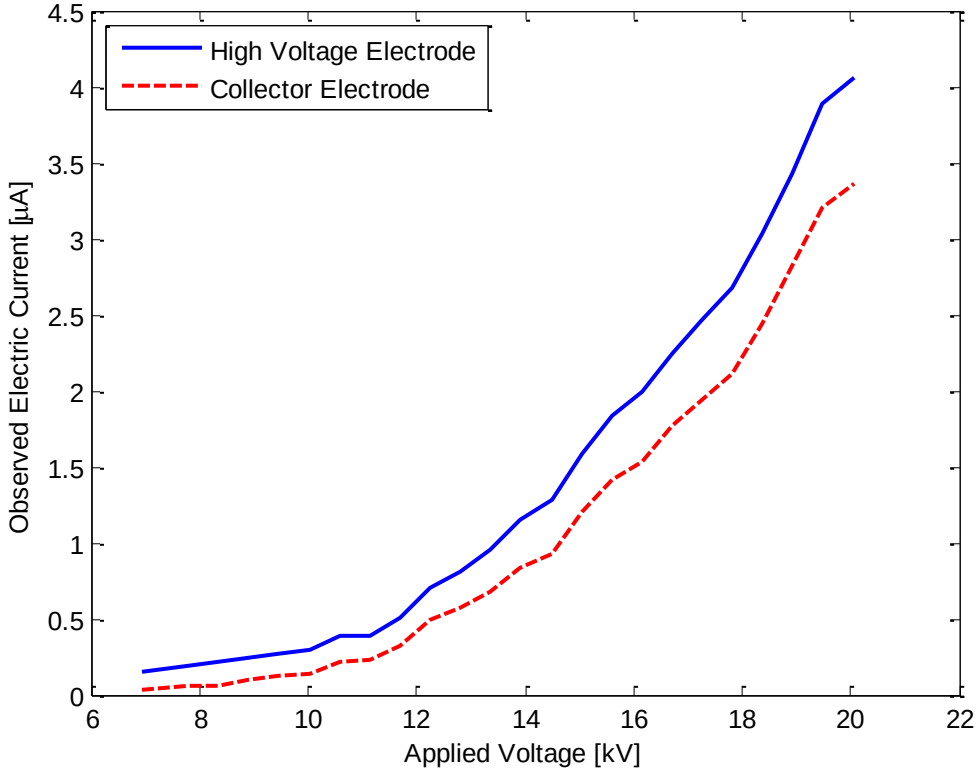

Figure 65: Observed electric current for 18% PVB in ethanol being electrospun at different applied voltages for a distance of 100 mm.

The difference in electric current, ΔI, for 18% PVB in ethanol (Figure 66) show a different form from PVOH (see Section 8.3.2). It appears to be two linear relationships intersecting at 12 kV. Under 12 kV the difference is constant, while above 12 kV it increases with increasing applied voltage.

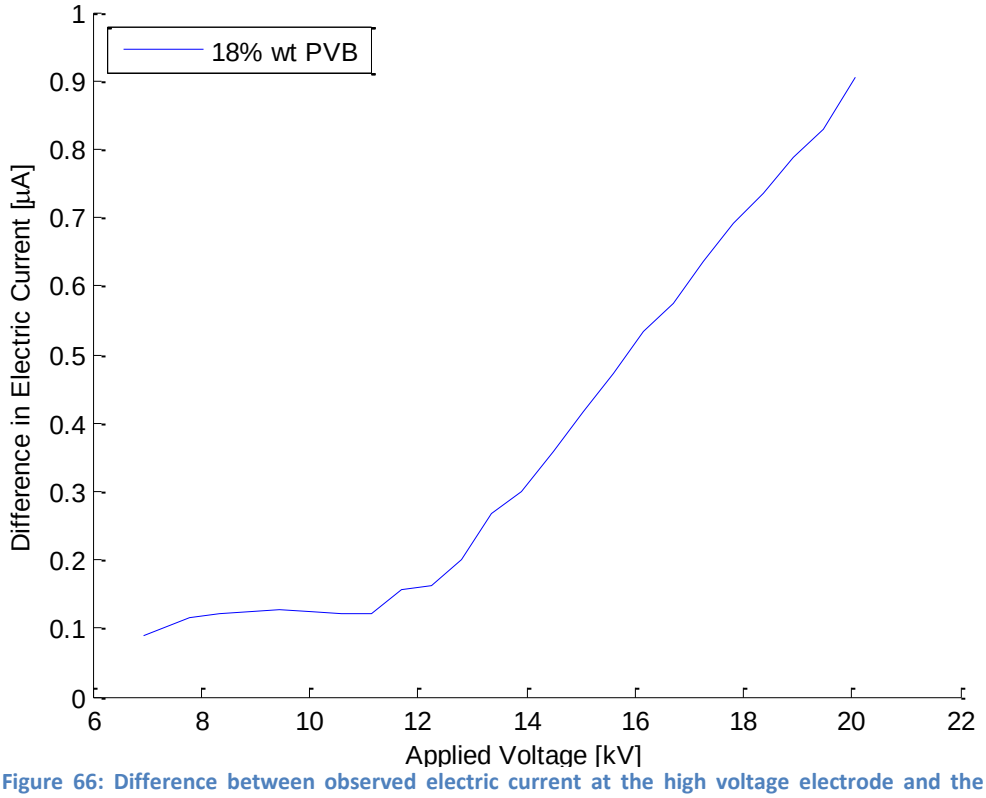

Figure 66: Difference between observed electric current at the high voltage electrode and the collector electrode for 18% PVB in ethanol being electrospun at different applied voltages for a distance of 100 mm.

As might be expected given the above reported results for 18% PVB, the fraction of electric current arriving at the collector for PVB is significantly different from that of PVOH. For electrospinning conditions above the transition point (i.e. 12 kV at 100 mm) in the high throughput mode the losses appear to be approximately constant like that of PVOH, although higher for each given TCD. This corresponds to the high volume throughput mode for PVB. The traditional spinning mode corresponds to much higher loss rates. Distances above 100 mm appear to have an unusual increase in the loss rate between 12 kV and 14 kV. Without further work it is unclear why this occurs, although the signal noise is much larger for PVB due to the need to clean the spinning tip from clogging which may account for unusual behaviour by introducing large spikes in the observed electric current.

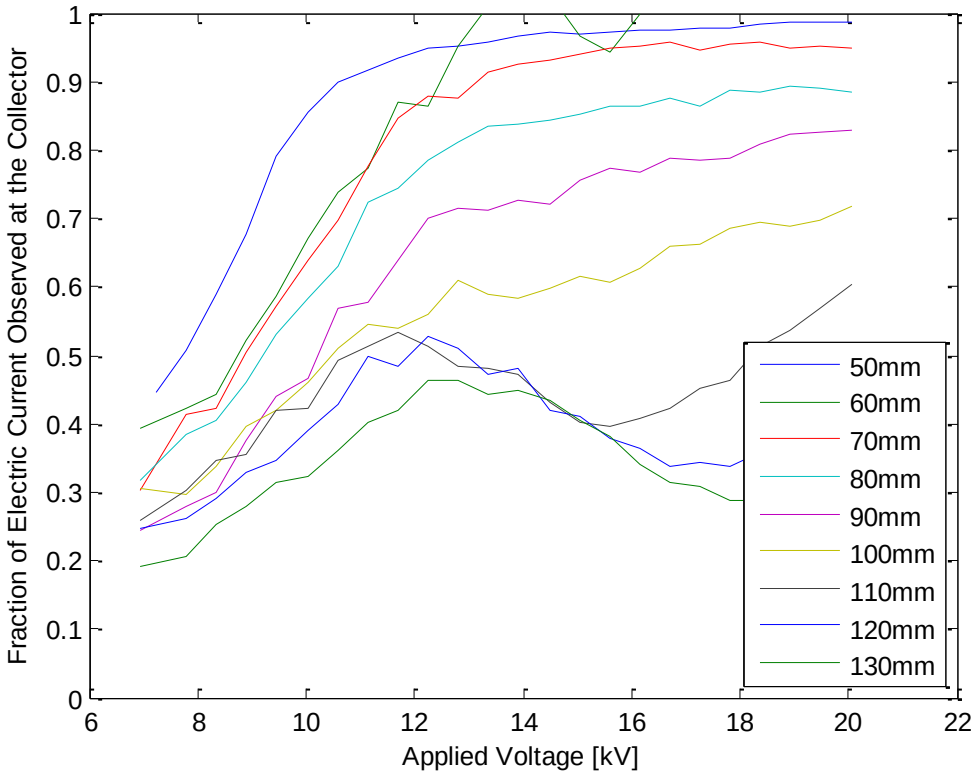

Figure 67: Fraction of electric current arriving at the collector electrode for 18% PVB at all distances.

The same analysis performed in Section 8.4.2 can be done for 18% PVB but may not be valid. The method requires the relationship between high voltage electric current and mass deposition rate to be linear (or at least well defined) which is untested for non-PVOH solutions. However, determining this is outside the scope of this work. As such it will be assumed that the constant charge density relationship holds for PVB in ethanol for both electrospinning modes. The resulting analysis shown in Figure 68 shows significantly different behaviour than PVOH (see Section 8.4.2). The first difference to observe is that unlike PVOH, the losses for lines of constant electric current do not all have the same gradient. It can be seen that for larger flow rates the gradient settles to a constant but at lower flow rates the gradient almost reaches zero (see Figure 69). This is likely due to the switch between different spinning modes, i.e. in the traditional spinning mode the losses are almost constant with respect to distance whereas with the high volume throughput mode the losses are similar to that for PVOH. The high volume throughput mode approaches a constant gradient of approximately -0.0116 mm^{-1} which is significantly steeper than that observed for PVOH (i.e. -0.0086 mm^{-1}, -0.0071 mm^{-1} or -0.0064 mm^{-1} for 8%, 9% PVOH and 8% PVOH with KCl, respectively). This analysis shows that the loss of charge phenomenon is likely to apply to all polymers rather than be specific to only aqueous PVOH.

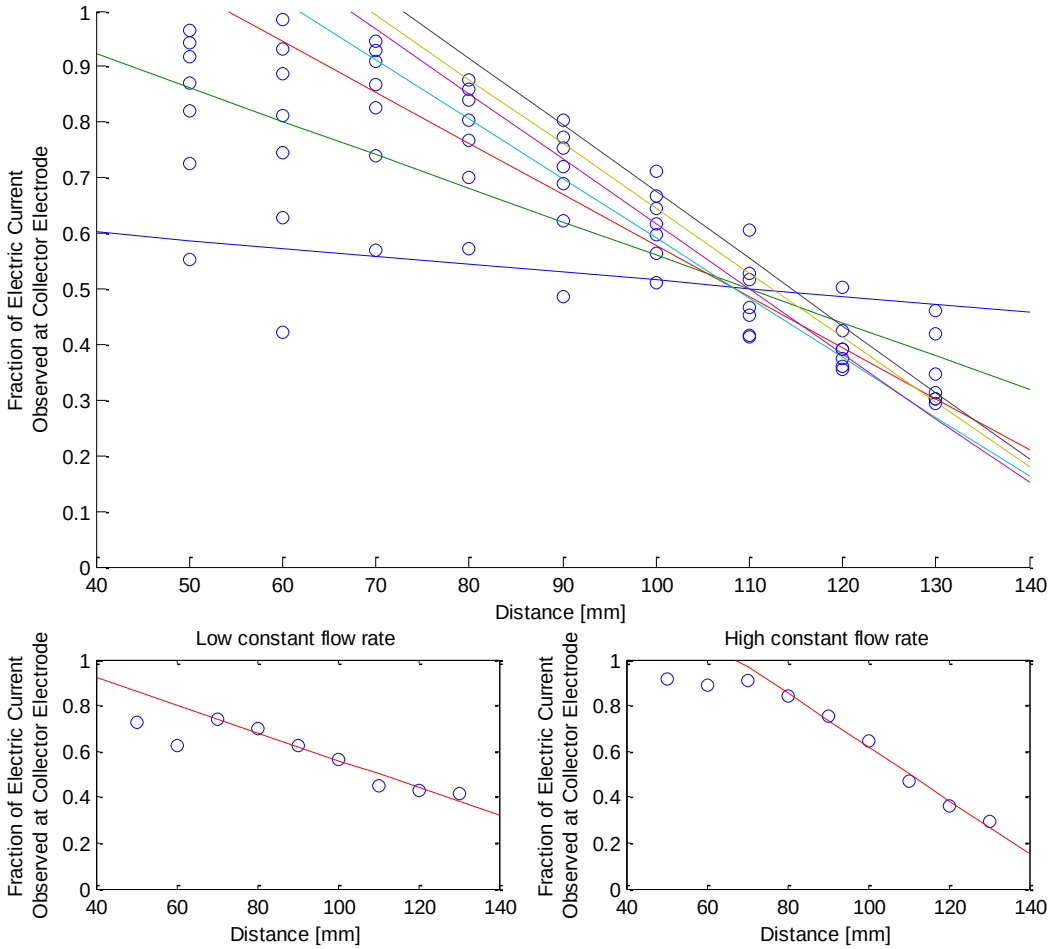

Figure 68: Relationship between electrode distance and fraction of electric current arriving at the collector for a range of constant flow regimes for 18% PVB. Top plot shows this for all constant flow regimes chosen in the text with the lowest line corresponding to the lowest flow and the highest line corresponding to the highest flow. The bottom plots show a low flow regime on the left and a high flow regime on the right.

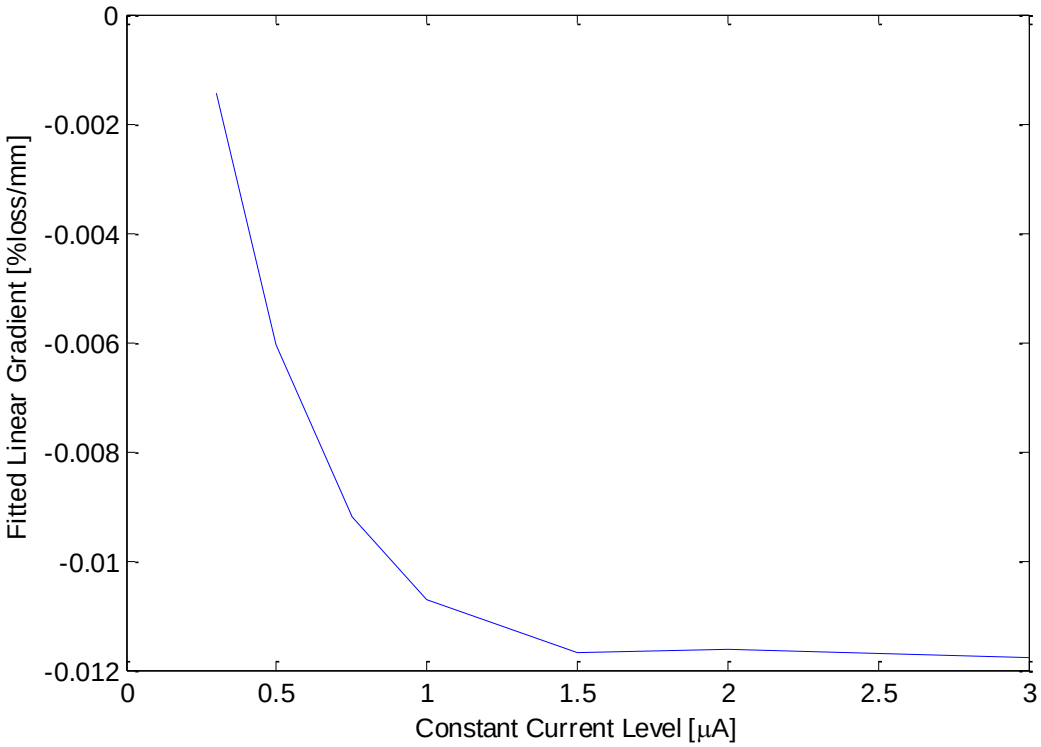

Figure 69: Relationship between linear gradient fitted to charge loss rates under a constant mass flow rate with varying electrode distance.

8.4.4 Solvent Evaporation as a Source of Charge Loss

Section 8.4 has so far demonstrated that in both aqueous and ethanol-based polymer-solvent systems charge is lost while in flight. Kalayci et al. (2005) states that using the quantum chemical concept, solvent evaporation does not remove charge from the jet in electrospinning; charged fluids evaporate losing mass without losing charge. If this is the case, solvent evaporation may still play a role in the loss of charge from the electrospinning jet. Section 4.3.4 demonstrated that the ambient humidity has an effect on the flow of current and the charge lost. At standard temperature and pressure, if the humidity is above 50% RH the current at the high voltage electrode will increase with increasing % RH as will the rate of charge loss. As the jet is continuously losing solvent while in flight, there would be a localized rise in humidity around the flight path of the jet. This could lead to solvent molecules in the atmosphere interacting with the jet to assist in transporting charge from the surface. However, without significantly more data for many more polymer-solvent systems it is not possible to draw any conclusions regarding solvent evaporation and charge loss. As such solvent evaporation will be assumed to not be involved in the charge loss process as per Kalayci et al. (2005).

8.4.5 Generalized Theoretical Model for Electric Current

In Chapter 6 it was shown that the observed electric current could be described by four parameters: α, β, V_{th} and H. These parameters are the exponents or coefficients from four different equations

used to model the high voltage electric current for 8% PVOH. Chapter 6 found that for 8% PVOH high voltage electric current Equation (8.54) offered the best fit.

$$I = A(V - V_{th})^2 d^{\beta} \tag{8.54}$$

For the four solutions and the two electrodes the parameters α, β, V_{th} and H were calculated (see Table 9) along with the associated quality of fit R^2 (see Table 10). It can be seen that for all three PVOH-based solutions, at the high voltage electrode, Equation (8.54) provides the best fit. However, for PVB, a slightly better fit is found by Equation (8.55).

$$I = A(V - V_{th})^2 e^{-d/H} \tag{8.55}$$

Both PVOH and PVB high voltage electric currents fit the $I = A(V - V_{th})^2$ model, which is related to the form used to predict current lost from electric discharge processes. The difference is in the distance term, of which $I = Ae^{-d/H}$ was originally proposed by Theron et al. (2004) in relation to electric current observations at the collector. There is no theoretical justification given for either of the distance relationships. Therefore, the differing quality of fit between two solutions demonstrates that each polymer/solution may not respond in the same way to changes in distance; reinforced by the observation that PVB has at least two distinct electrospinning modes while PVOH has only one. For PVB at short distances the high throughput mode dominates while at long distances the traditional spinning mode dominates which could lead to the importance of the distance relationship in the quality of fit.

Table 9: Model parameters fitted for the high voltage electric current for all four polymer solutions. Shaded areas indicate the best fit.

Solution / Electrode	Model parameters α	β	V_{th}	H
8% PVOH High Voltage	2.54	-1.49	2.76	66.30
9% PVOH High Voltage	2.41	-1.44	2.43	68.32
8% PVOH w/ salt High Voltage	2.49	-1.39	2.07	70.93
18% PVB High Voltage	2.53	-2.30	5.12	42.50

Table 10: Goodness of fit parameter, R^2, for the four models that were fitted to the high voltage electrode electric current for the four polymer solutions. Shaded areas indicate the best fit.

Solution	Model of high voltage electric current $AV^{\alpha}d^{\beta}$	$A(V - V_{th})^2 d^{\beta}$	$AV^{\alpha}e^{-d/H}$	$A(V - V_{th})^2 e^{-d/H}$
8% PVOH	0.9883	0.9909	0.9381	0.9446
9% PVOH	0.9955	0.9954	0.9571	0.9563
8% PVOH w/ salt	0.9943	0.9970	0.9587	0.9633
18% PVB	0.8941	0.9200	0.9711	0.9839

Knowing that the collector electric current will depend on the high voltage electric current and the expected loss rate it makes more sense to derive a function $I_{col} = f(V,d)I_{HV}$ rather than an independent function for I_{col}. If an independent function is fitted a similar goodness of fit can be achieved as found for the high voltage electric current. However, the collector electric current fits the distance model $I = Ae^{-d/H}$ proposed by Theron et al. (2004) far better than $I = Ad^{\beta}$ chosen for the high voltage electric current. This may be due to the loss rates being strongly dependent on the electrode distance (see Section 8.3.4 and 8.4.2) so requiring a function that can more rapidly change value over the range of distances. If we seek to provide a theoretical description for I_{col}, one that is derived from I_{HV} by losses, then the function $f(V,d)$ must be determined for each polymer system. The results from Section 8.3.4 and 8.4.2 show that for a simple first order approximation we can assume that the function is only dependent on the electrode distance giving $f(d)$. Taking the linear region fitted in Figure 62 and averaging the gradients and intercepts gives a function $f(d) = -0.00856d + 1.518$. Including this into the model provides a goodness of fit of R^2 = 0.9985 (see Figure 70) compared with R^2 = 0.9942 for the best arbitrary function. Examining the residuals from the fit of the model it is possible to see a slight upward trend with increasing distance that can be attributed to the averaging of the intercept for $f(d)$ when clearly it is a function of I_{HV} (see Figure 62). This shows that the model is not complete and is certainly omitting factors. Developing the model beyond the first approximation given above would require additional understanding of the theoretical mechanisms by which charge loss occur. These mechanisms are not clear from the data collected in this work and further data collection is beyond the scope of this thesis. The first approximation does provide a reasonable fit.

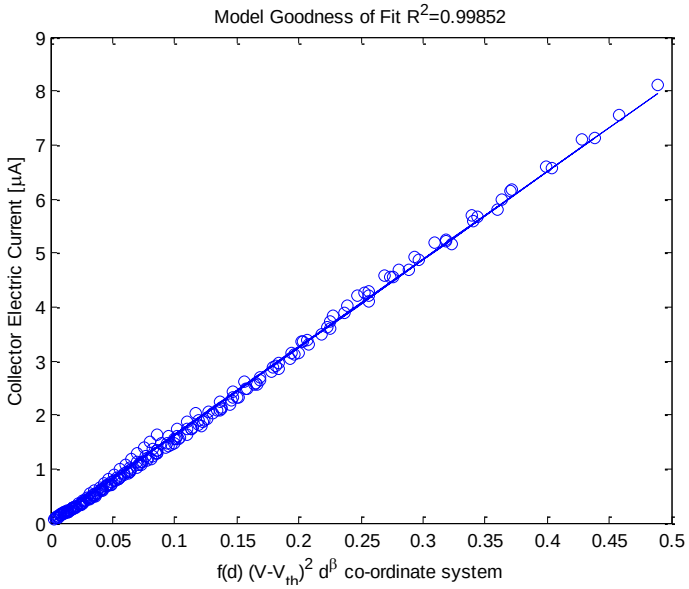

Figure 70: Quality of the fitted model for I_{col} compared with raw observed data. Open circles represent the raw data while the straight line represents the model predictions. The x axis is a single dimensional representation of the two-dimensional function of voltage and distance and has no physical meaning.

8.5 Conclusion

This chapter has presented a wide range of raw data for four polymer solutions, 8% PVOH, 9% PVOH 8% PVOH with ionic salt in water and 18% PVB in ethanol. In all cases there was a portion of charge that was not accounted for at the collector. This indicates that the charge loss phenomenon is a general one. In some cases the charge lost is as small as 1% of the total charge introduced into the system. However, in others the charge lost can be as high as 80%, though a typical range is between 5 and 60%. It was found that the loss rates showed little variation with changing applied voltage but had significant variation with changing tip to collector distance. In all cases, increasing the tip to collector distance increases the loss rates. It was found that for all cases increasing the mass flow rate increases the losses. For 18% PVB in ethanol, due to two different electrospinning modes existing there was different behaviour across the range of conditions studied compared with PVOH solutions in water. When describing the high voltage electric current, a different function gave a better fit for PVB than the three PVOH solutions. In both cases the electric discharge-like relationship to applied voltage gave the best fit. A function was found to describe the collector electric current in terms of the initial high voltage electric current and the amount of charge lost.

CHAPTER 9

AN EXHAUSTIVE DESCRIPTION OF THE ELECTROSPINNING PROCESS

9 An Exhaustive Description of the Electrospinning Process

9.1 Introduction

The electrospinning process is a complex interaction of many forces where any change to one initial condition often results in a number of other initial conditions changing as well. Much of the work to date on describing the process has either focused on a small aspect or has aimed at a mathematical description derived from theoretical considerations. Without a detailed background in electrohydrodynamics and rheology, this can act as a barrier to understanding the implications of the mathematics. This chapter aims to revisit the works presented in Chapter 3 in light of the phenomenological observations made in Chapters 4, 5, 6, 7 and 8 but refrain from presenting the description in the context of a detailed mathematical framework. Given the nature of the problem mathematics cannot be avoided; however, the emphasis will be on qualitative descriptions derived from empirical observations and theoretical study. The description will follow the transformation of a polymer solution into the Taylor cone, then into a straight jet, then destabilizing into the bending instability, then drying out into a solid fibre before depositing on the collector electrode. The reader should be cautioned when applying generalized models of electrospinning due to the interrelated nature of the parameters that affect the process (Patra, 2010, Patra et al., 2009b, 2010b). While it may be possible to describe much of the fundamental physics that leads to the electrospinning phenomenon, practical application of electrospinning has discovered numerous modifications or special cases of the process. This means that examples of electrospinning that operate solely on the primary physics of the phenomena are likely to be rare. When considering a specific case of electrospinning, care must be taken to account for any aspects unique to the specific case in question otherwise important interactions required to properly describe the process may be overlooked.

9.2 Taylor Cone Dynamics

The Taylor cone is the first moment where the electrospinning process deviates from simple polymer flows into electrohydrodynamics. In some cases it has a characteristic “onion dome” shape while in other cases the jet profile appears more like an exponential decay. In both cases the Taylor cone region is typically one of extreme thinning with the jet reducing by an order of magnitude within a few millimetres.

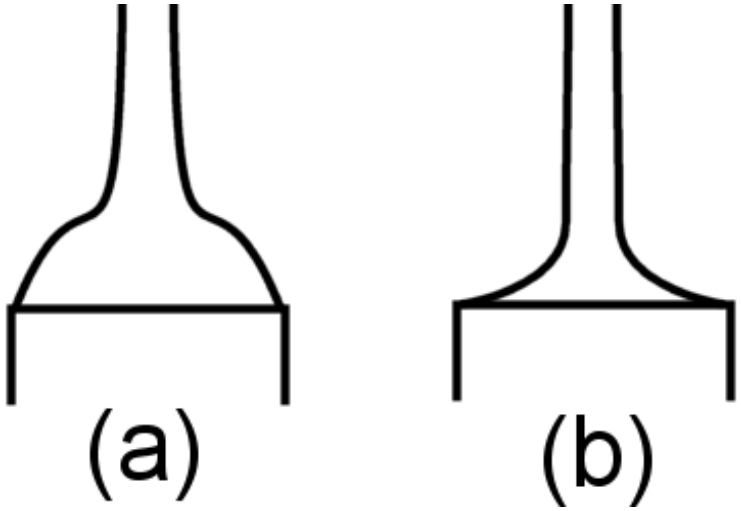

Figure 71: Example of the a) "onion dome" shape and the b) exponential decay shape of the Taylor cone

9.2.1 Fundamental Forces to Describe the Taylor Cone Shape

The fundamental forces that drive the shape of the Taylor cone are surface tension, viscoealsticity, internal fluid pressure and surface charge. The surface charge is what allows for the formation of the cone shape rather than a simple hemispherical droplet. Without surface charge the internal fluid pressure is balanced by surface tension and the solution adopts the familiar hemispherical droplet. Upon application of a suitable high voltage an electric charge will build up on the surface causing the hemispherical shape to adopt a more cone-like geometry. This is due to the Coulombic self-repulsion of the surface charges acting in the opposite fashion to surface tension. Whereas surface tension acts to reduce surface area, surface charge acts to increase it. If it is possible to find an energy balance this interplay will result in a static shape being obtained.

With sufficient surface charge the shape obtained will have enough concentration of charge at the tip of the cone geometry to cause the surface charge force to overcome entirely the surface tension resulting in the surface ejecting a constantly flowing jet of liquid. Once the fluid begins to flow viscoelastic forces come into prominence. The Taylor cone can now be viewed as a continually thinning flowing column of fluid. As such both surface tension and viscoelasticity will resist this thinning action. In the case of simple Newtonian viscosity an increase in the viscous nature of the polymer fluid will resist stretching resulting in a thicker jet and less curvature on the Taylor cone. If the polymer displays the non-Newtonian property of shear thinning then the Taylor cone begins to take on the more "onion dome" shape characterized in Taylor's original papers. This is due to a delay in the stretching where the greater the shear thinning the more the transition towards "onion dome" from the Newtonian case of exponential decay. A similar delayed stretching can occur due to increasing the polymer relaxation time leading to more of the "onion dome" shape. If the polymer solution instead undergoes shear thickening followed by shear thinning (typical of LDPE melts) then due to the initial thickening of the jet, the profile tends back towards the Newtonian case with less

of an "onion dome" shape. This is because the thinning in the later stages of higher shear cannot compensate for the low shear thickening within the Taylor cone. When experiencing strain hardening the Taylor cone undergoes an even greater rate of stretching, pushing the jet profile more towards the exponential decay shape than the Newtonian case. This is because as Feng (2002) states: "The initial growth in $\bar{\eta}^+$ implies an increase in T', be it positive or negative; an increasing T will increase more rapidly and a declining T will decline more slowly. This intensifies the initial stretching and sets up the conditions for greater suppression of stretching farther downstream" where $\bar{\eta}^+$ is the scaled extensional viscosity while T is the tensile force.

Gravity is the last force to consider for the Taylor cone and is generally ignored. This is because the magnitude of the force is at least an order of magnitude below the other forces above. In the case of the Taylor cone it is also because it is not critical to describe the dynamics observed. One can electrospin perpendicular to gravity, one can electrospin in the direction of gravity, or one can do so in direct opposition to gravity. This has little effect on the dynamics, rather being a more pragmatic force to consider due to its effect on the flow of any excess polymer possibly leading to drips on a fibre sample.

9.2.2 Charge Carriers and Charge Flow in the Taylor Cone

To the author's knowledge there is yet to be definitive experimental evidence that describes exactly how charge carriers behave in the electrospinning system. It is undeniable that charge is transferred across the gap between the electrodes, evidenced by the flow of electric current at both electrodes (see Chapter 4). However, this transfer can occur in two different ways: either by the transport of free charges or by the transport of induced dipoles. Some simulation work (Feng, 2002) found that for typical electrospinning the level of induced charge was approximately 1% of the total charge carried by the fibre.

Free charge carriers will be transported in two different modes, conduction and convection. Conduction has charge carriers moving through the fluid while convection has the fluid moving sufficiently fast that the charge is carried along with it. Which of the two states is dominant in the fluid can be found by looking at the characteristic relaxation times of the charge and the fluid. If the charge is able to move quicker than the fluid then it is dominantly in a conducting mode as it can reorganise itself into an equilibrium state before the fluid can. However, if the charge is unable to move faster than the fluid then it is dominantly in a convective mode as the fluid motion dictates the charge distribution. In the case of a fluid jet this would result in charge being forced to the surface as the fluid is only moving faster than the charge along the axis of travel, hence the equilibrium state of self-repulsion would force the charge to the surface. Analysis of the Taylor cone typically concludes that it is dominated by the conductive mode of charge transport for free charges. This is due to the

slow speed that fluid flows through the Taylor cone. In low conductivity cases there is still some convective transport; however, analysis of high conductivity shows that effectively zero charge is carried by the convective mode. It has been suggested by Carroll et al. (2011) that in these cases there must be some surface charge interacting otherwise the jet would behave just like a gravity drawn column of fluid which is obviously not the case. A solution to this, proposed by Carroll et al. (2011), is to invoke the Debye layer for the conduction mode, whereby conducted charges within a thin boundary layer near the surface can interact with external electric fields and each other.

The charge initially carried by the polymer solution as it forms the Taylor cone is a property of the solution rather than a property of the processing conditions. Chapter 6 demonstrates that for a range of applied voltages and electrode distances (hence a range of electric fields) the charge carried per unit mass was constant. An obvious solution property that would fit a constant charge per unit mass would be the concentration of ions in solution. This would fit well with work such as Stanger (2008) that shows that most properties of the electropun jet and final fibre are affected by changes in conductivity due to introducing more ions. Chapter 6 further explores this possibility by finding that if one assumes that the PVOH polymer molecules are carrying the charge then only one in ten molecules would carry a whole unit of charge (i.e. +1 ion).

The flow of charge can be studied by examining the flow of electric current. Examining the relationship between the applied voltage and the flow of current into the high voltage electrode in Chaper 6, it was found that it was similar to that for electric current discharged from a point in a corona discharge. Consider that electrospinning appears to be a relatively high energy process (albeit on a very small scale) whereby increasing the applied voltage slowly pushes a fluid droplet towards the Taylor cone shape until sufficient energy is built up that a charged jet is ejected from the tip of this cone. That the flow of current that results from this charged jet matches the approximate form for corona discharge could lead one to view electrospinning as another form of discharge from a high energy state, where the ejection of a charged jet occurs to return the system to a lower energy state rather than the ionization of air. If this is the case then the ejection of the jet would be occurring at a lower energy level than the corona discharge owing to the fluids ability to reshape its geometry by flowing.

9.2.3 Corona Discharge

The electric field conditions on the Taylor cone are intrinsically complex. To the author's knowledge there have been no studies that examine how the expected charge distribution on the Taylor cone would result in a local electric field. However, empirical observations have shown that under high applied voltages (where high depends on the electrode geometry used) an electrical discharge takes place. This appears to have the characteristic pink glow of a corona discharge indicating sufficient

electric field strength to ionize of the local air. In some cases this appears to be occurring either on the Taylor cone or just into the straight jet region. To explain this phenomenon we must consider the surface electric field on the jet.

It is expected that as the jet thins the electric field decreases. Consider a column of fluid that is carrying a charge that we assume is entirely distributed on the surface. The column has a known radius and a known length. Assuming that there is no significant solvent loss if the length of the column increases the radius decreases proportionately according to the conservation of mass. The surface area of the column increases as the length increases. Hence, as the electric field at the surface of the jet can be found from the surface charge (i.e. $E = \delta_q/\epsilon_0$) assuming no charge is lost then the electric field strength decreases as the jet gets thinner. However, as was discussed in Section 9.2.2 in regions near the Taylor cone it cannot be assumed that all the charge is at the surface. Some studies (Carroll et al., 2011, Reznik et al., 2004) have shown that charge migrates from purely conductive (limited surface charge) to purely convective with approximately 10 times the orifice size. This corresponds to the region where much of the corona discharges are seen and would logically be where the highest surface electric field concentration would exist. The exact location of the peak in surface electric field strength would depend both of the rates of thinning and the rate of migration of charge to the surface but is likely to occur near the transition point though not past it.

Chapter 8 showed that for all conditions considered there was always a minimum of approximately 5% of the total charge lost while in flight. Although the conditions in electrospinning are not always sufficient to observe the characteristic ionization of air for the corona discharge, there is a minimum loss which may occur at the same point where the maximum surface electric field would occur. This depends on determining if the loss is a slow rate over the entire flight time or is an instantaneous loss occurring at one point. The work in Chapter 8 would require further extension to answer this question. The possibility remains that near the Taylor cone there may always be a small loss of charge that significantly increases once surface electric field conditions reach the requirement for ionization.

9.3 Straight Jet Dynamics

For the purposes of this discussion the straight jet shall be defined as the axisymmetric region where the rate of thinning is small. This is distinct from the Taylor cone region that is typically characterized by high rates of thinning. From a practical stand point the Taylor cone has its own distinct geometry while at a distance far from the Taylor cone (i.e. greater than $\sim 10 - 20r_0$) one can typically identify a quasi-stable slowly thinning jet suspended in air that is the straight jet. The straight jet region ends with the onset of the bending instability.

9.3.1 Rheological Considerations

In general the viscous forces in the jet will resist the thinning action imposed by the electric forces. This resistance is joined by surface tension. The resistance by surface tension can be viewed as resisting the increase in surface area from thinning or from resisting the curvature created along the jet as thinning progresses. Both are valid and for an axisymmetric jet represent the action on a smooth jet. As the jet thins the polymer solution viscoelastic properties are key to understanding how the jets radius profile will vary. For a Newtonian jet an increase in the viscosity will create a thicker slower thinning jet. For a jet that undergoes non-Newtonian purely shear thinning, the shear experienced within the Taylor cone region results in sufficient shear thinning to negate the effect of reasonable changes in initial viscosity within the straight jet region. As such reasonable changes to the initial viscosity will result in near identical jet profiles beyond the Taylor cone region. For solutions that undergo shear thickening followed by shear thinning the behaviour depends on how much thickening occurs. If the thickening effect is sufficient to cancel out the thinning effect then the straight jet becomes thicker due to the increase viscous resistance to jet thinning. If the thickening effect is mild then outside of the Taylor cone region shear thinning takes over and jets are effectively the same as in the case of pure shear thinning. An interesting effect is that of strain hardening which increasing its effect results in a thicker straight jet despite starting with a smaller initial jet radius ejected from the Taylor cone. This is because increasing strain hardening will primarily affect the more severely stretched region of the straight jet as opposed to the mildly stretched region of the Taylor cone. It has been observed that as a general rule the straight jet appears to thin with the relationship $r \sim z^{-1/2}$ in the initial region followed by $r \sim z^{-1/4}$ once the strain in the jet reaches a high value and strain hardening becomes significant (Helgeson et al., 2008). An additional rheological parameter that becomes important for the straight jet is the viscoelastic relaxation time. The axisymmetric stability (i.e. not the off-axis stability of bending) of the straight jet depends somewhat on the viscoelastic relaxation time. Specifically, as the relaxation time increases the jet is further destabilized up until the point where the polymer relaxation time is on a similar order of magnitude to the flight time of the jet, at which point increases in relaxation time significantly stabilizes the jet. This is explained by the fact that as the shear rate within the jet decreases as the jet settles into steady state stretching, if the polymer molecules can relax then the jet loses its axisymmetric stability; whereas if the relaxation time is long enough then the polymer molecules stay aligned with the axis of the jet and the axisymmetric stability is preserved.

9.3.2 Charge Considerations

Section 9.2.2 introduced the concept of the transition from conduction to convection for charge transport. This transition occurs just outside of the Taylor cone, approximately near the beginning of the straight jet. This means that when considering the straight jet, it is generally more accurate to

see it as a moving flow of a charged insulator as opposed to a slow flowing conducting medium. As a result it is expected that all the charge carried by the fluid rests on or very near the surface of the jet. This transition may be responsible for the corona discharge discussed in Section 9.2.3. As was discussed in Section 9.2.3 the surface electric field decreases with increasing stretching. This assumes mass conservation which to a reasonable approximation is true for the Taylor cone; however, for the straight jet solvent loss cannot be ignored. The loss of solvent causes the volume of a unit of fluid travelling along the jet to decrease, effectively reducing the jet radius faster than pure thinning would account for. This decreases the surface area, increasing the surface charge and hence the surface electric field. As such further losses of charge (beyond the corona) may occur along the straight jet, especially as this increase in surface charge will be accompanied by higher concentration of solvent molecules in the local atmosphere around the jet which may help to remove charge from the surface. If the rate of stretching is sufficiently fast then the increase in surface area due to thinning of the jet may counter the effect of solvent loss, but as was discussed in Section 9.3.1 the straight jet is characterized by a slow rate of thinning. This can be easily understood when considering an equation for surface electric field strength modified from (Halliday et al., 2008) (see Equation (9.56)):

$$E_{surf} = \frac{q}{2\pi\epsilon_0 r_0 \sqrt{LV_f \ell}} \tag{9.56}$$

Where q is the charge carried by the unit of fluid, ϵ_0 is the permittivity of free space, r_0 is the initial diameter of the fluid unit and L is the initial length of the fluid unit which are all constants. This leaves only $1/\sqrt{\ell}$, the reciprocal of the current unit of fluid length and $1/\sqrt{V_f}$, the reciprocal of the remaining volume fraction of the unit of fluid as parameters that determine the surface electric field strength. As ℓ increases in value from an initial value to infinity while V_f decreases in value from 1 to the final dry volume fraction these elements work in opposition to each other. However, ℓ can theoretically increase indefinitely and hence given enough time results in a vanishing surface electric field. The final point regarding charge carried and lost by the straight jet is that when considering the charge being lost in relation to flight distance (see Chapter 8) very short distances (on the order of straight jet length) correspond to a minimum charge loss while long distances correspond to large losses of charge. This may indicate that while the slowly thinning jet is reducing the surface electric field the loss of solvent, which may culminate with the bending instability, could be responsible for the further charge loss. For all conditions, increasing electric current injected into the system results in more charge lost which can be explained by more charge on the surface leading to more opportunity for loss events.

9.3.3 Length of the Straight Jet

While the ejection of the jet from the Taylor cone can be understood as a concentration of electrical stresses leading to the ejection of charged material, the termination of the straight jet is less clear. In the works by Reneker et al. (2000) and Feng (2002) it is discussed that the straight jet may be a result of the internal tensile forces that stabilize the jet from off-axis perturbations. Alternatively, the straight jet may be limited by mechanical properties of the jet that change as the solution loses solvent. Empirical data collected by Kowalewski et al. (2005) shows that the length of the straight jet varies with applied voltage but that the relationship changes with the choice of polymer. Other empirical work by Qin et al. (2005) and observations by the author show that changing polymer concentration or increasing ionic salt addition leads to decreases in the straight jet length. This demonstrates that whatever causes the onset of the bending instability is related to the initial conditions.

9.4 Instability Dynamics

The electospun jet experiences three recognized classes of instability (see Figure 72). The first is an oscillation of the straight jet around the central axis of the two electrodes (Han et al., 2008a). This is slow enough that it can be observed by the human eye. The jet is ejected not from the centre of the Taylor cone but off to one side and then precesses around the central axis. The second is the axisymmetric instability of the jet which can lead to beaded fibre formation or to the jet breaking up into droplets (analogous to electrospraying). The third is the bending instability, where the jet is deflected from the central axis and its motion is reinforced by the self-repulsion of the charges carried by the jet. The result is a chaotic jet path that exists within a quasi-stable envelope cone. These final two instabilities will be discussed further below.

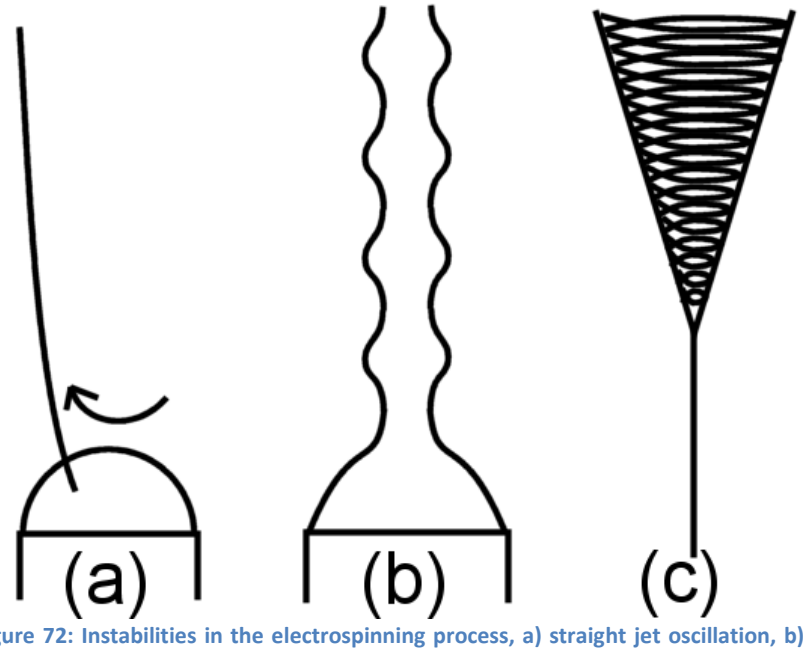

Figure 72: Instabilities in the electrospinning process, a) straight jet oscillation, b) axisymmetric instability and c) bending instability.

9.4.1 Axisymmetric Instabilities

In Section 9.3.1 it was discussed that a solution's viscoelastic relaxation time that was shorter than the total flight time that an axisymmetric instability may occur. Axisymmetric instabilities are characterized by a perturbation wave that runs along the length of the jet (Carroll et al., 2008); as the intensity of the wave grows the fibre becomes more like a string of beads than a smooth jet. If the instability growth rate is not sufficiently damped then the jet will eventually break up into droplets. The forces driving the formation of these instabilities depend on the fluid properties. For the case of low conductivity fluids the instability appears to be driven by surface tension. However, for highly conductive fluids the surface charge term becomes the dominant destabilizing force due to the significantly increased surface charge interactions. Exact predictions of the onset of an axisymmetric instability depend on the competition between the forces that drive the instability and the remaining forces that must damp the instability. If sufficient damping can be created then the jet will remain stable. Irrespective of the driving forces a low axial polymer stress along the jet typically leads to an instability onset as this provides an opportunity for the polymer molecules to relax and diminishes the non-Newtonian damping effect from the polymer molecules being elongated (Carroll et al., 2008).

9.4.2 Bending Instability

The bending instability is heavily reinforced by the same force that drives the stretching of the jet, Coulombic self-repulsion of surface charges. Reneker et al. (2000) also propose that the bending instability is caused by this exact same force. The reasoning is drawn from the Earnshaw theorem (Earnshaw, 1842) that states that any classically dynamic system governed only by electrostatic forces cannot exist in a stable equilibrium state. As such the smallest perturbations would force the system into a new state. So the theory states that the smallest laboratory noise (perturbation) would be sufficient to drive the jet into an off-axis bending mode that will be reinforced by the self-repulsion of the jet if sufficient conditions are met that the initial deflection is not damped. Reneker et al. (2000) presents a short discussion where it is proposed that the rapid decline in the longitudinal stress results in the jet becoming sufficiently undamped that the intrinsically unstable nature of the Coulomb force becomes subject to the laboratory noise perturbations.

Once the bending instability begins the growth rate of the loops of the jet will be dominated by the surface charge undergoing self-repulsion. This is because even with a non-uniform point plane electric field the fibre will still be travelling approximately perpendicular to the electric field from the applied voltage. Hence the only electric field to drive stretching once the jet is bent is that generated by the charge carried by the jet. This stretching will be limited by the viscoelastic and surface tension forces that, as for the straight jet, resist the thinning of the jet. Classically the bending instability has been shown to be an expanding helix formed by the fluid jet (Reneker et al., 2000). An alternative

view is one that involves random noise rather than a prescribed oscillation to generate the instability which results in a more chaotic jet path (Kowalewski et al., 2005). In this case the bending instability envelope cone is the maximum deflection the chaotic jet can achieve with the surface charge it carries. This matches well the observations seen in this thesis (see Chapter 3, Section 3.3.6.4). The reality is likely to be a mix of these two extremes where initially the expanding helix can be sustained, but as flight time increases the loops of the jet become less stable and collapse into a chaotic path. A key aspect of the bending instability for the production of nanofibre is that by stretching the fibre parallel to the collector plane it is possible to create a total jet path significantly longer than the distance between the electrodes. This allows for much more jet thinning than could be achieved by traditional methods within the same space.

9.4.3 Charge Loss and the Expected Effect on the Jet

For the case of the axisymmetric instability the loss of charge will stabilize the jet and reduce the onset of this instability which is typically desirable. Similarly, the loss of charge from the jet will decrease the forces driving the bending instability, effectively reducing its impact on the electrospun fibre which is typically undesirable. Chapter 8 demonstrates that the largest charge loss occurs when the bending instability is most significant (i.e. at large electrode distances). If it is the case that charge is predominantly lost in the bending instability region then both undesirable conditions are occurring. Charge loss does appear to depend somewhat on fluid properties and processing conditions (see Chapter 8) and hence further understanding of the charge loss phenomenon could allow the choice of conditions that either suppress the axisymmetric instability or enhance thinning occurring in the bending instability region. Chapter 8 also discusses the issues with space charge being formed by the charge loss process. This space charge may be responsible for the chaotic jet path observed using high speed photography.

9.5 Flight Dynamics and Phase Changes

9.5.1 Flight Time of the Jet

Some aspects of jet formation and flight are general and apply to the entire process rather than a specific region. Chapter 5 demonstrates that in tracking a single unit of fluid moving throughout its entire flight from one electrode to another that the flight time does not significantly vary with flight distance. Rather, flight time appears to be far more dependent on the applied voltage. As such, it cannot be argued that increasing the flight distance will allow more time for stretching to produce a thinner fibre as intuition might suggest. It is unlikely that changes to flight distance have no effect on the time taken for fluid to be transported from one electrode to another, simply that the effect from such a change is very small compared with the total flight time. Due to physical limitations in the electrospinning geometry it is not common for the electrospinning distance to double or triple. Due

to the point plane geometry, doubling the electrode distance does not correspond to halving the electric field strength in the initial period of acceleration where the jet's resistance to acceleration is low (see Chapter 5). However, the applied voltage can easily range from 5 kV to 30 kV, a six-fold increase in the force experienced by the jet along the z-axis (due to the Lorentz equation $F = Eq$). This again demonstrates the importance of a firm understanding of the electric fields that exist in the electrospinning process.

9.5.2 Change of Phase and the Physical Properties of the Jet

It was demonstrated by Yarin et al. (2001a) that the transition of the jet from a liquid to a solid fibre was vital in slowing the growth rate of a simulated bending instability to an observed range. As the jet loses solvent the viscosity will increase while the storage modulus will transition into an elastic modulus. For melt electrospinning a similar process will occur as the jet transitions from molten polymer to a solid. The simulation by Yarin et al. (2001a) simply increases the viscous resistance which slows down the growth rate sufficiently that the typical whipping envelope cone is formed. This change in phase is also likely to affect the charge carried by the jet. Once solvent is lost this marks the point where the volume stops decreasing and hence the surface electric field must decrease if the fibre continues to stretch (see Section 9.3.2). Without a solvent, if the charge is carried by ions, they become significantly less mobile.

9.6 Collector and Auxiliary Electric Field Dynamics

9.6.1 Collecting Dry Fibre

The final stage of the electrospinning process is the arrival of fibre at the collector. Typically the initial conditions are chosen to ensure the fibre arrives as dry polymer. It is possible to have a solution jet or gel-phase fibre arrive at the collector. If this occurs then often junctions where two or more fibres cross each other become fused creating a network of fibres rather than a mat of a single continuous fibre which may be desirable. Given the discussion in Section 9.5.1 the best approach to controlling the dry nature of the fibre is to vary the applied voltage to change the flight time or to modify the volatility of the jet either through solvent choice or creating higher surface area on the jet.

That it is possible to measure an electric current flowing from the collector electrode to ground and that the electrospinning process is quickly disrupted if this connection is severed indicates that charge picked up from the high voltage electrode is deposited on the collector along with the polymer fibre. Filatov et al. (2007) found that the electric current flowing from the collector appeared to be intermittent, with shortly interspaced spikes rather than a continuous flow. This suggests that some form of discharge process is occurring in the mat to facilitate charge transfer. Indeed small flashes of light were occasionally observed when electrospinning cellulose acetate.

However, from Chapter 7, even when examining the collector current at very high frequencies (10 kHz sample rate) there are no sudden discharges, only a continuous flow. As this was for poly(vinyl alcohol) electrospun from water it may be that for some suitable polymers there is sufficient residual conductivity in the fibres to enable charge to leak away at the required rate to prevent a build up. This lack of retention of charge is also demonstrated by Chapter 6 which shows that the mass deposition rate does not decrease over a 30-min period, where intuitively a build up of charge would decrease the deposition of more fibre. This is an unexpected aspect of the process as the technique of gap spinning demonstrates that charge will be retained by the deposited fibres. Gap spinning involves splitting the collector into two parts, each grounded, and allowing electrospun fibre to deposit bridging the gap. It has been observed and theoretically demonstrated that the retention of charge prevents multiple layers of fibre from being formed or the fibres from being laid down perfectly parallel (Liu et al., 2008). It is clear that the fibre carries charge due to the fact that fibre being formed by electrospinning is attracted to the grounded collector electrode. Given the range of observations it appears that indeed charge arrives at the collector on a fibre; however, if the polymer is not excessively insulating a number of leakage paths are found to enable charge arriving at the top to be dissipated into the conducting electrode.

9.6.2 Charge Loss Consequences when Interacting with Auxiliary Electric Fields

There are a number of examples of using auxiliary electric fields to influence the flight of electrospun fibre. An early example by Deitzel et al. (2001b) uses a series of rings to confine the bending instability and focus the deposition area. This was extended by Bellan et al. (2006a) to include two pairs of electrodes that were able to deflect the focused fibre either in the x or y axis. Later the work by Nurfaizey et al. (2012) used a single pair of electrodes with no focusing effect to quantify the deflection and confinement effect of auxiliary electric fields on the electrospun fibre. This technique will be strongly affected by the charge loss process. As the technique relies on the interaction between the electric field and the fibre, it relies on a significant amount of charge retained on the fibre. As Chapter 8 shows that as much as 60% of the charge carried by the fibre is lost in flight the electric field required to deflect the fibre would need to be increased in the regions where the charge is lost to get the same response. A potential additional concern is that the application of additional electric fields may result in higher peak electric fields allowing more charge to be lost.

9.7 Using Models of Electrospinning to Control Fibre Properties

As is discussed in Section 9.1, considerable caution must be exercised when applying generalized models of electrospinning. Within published literature there is significant disagreement between the effects of different parameters in electrospinning. Basu et al. (2011) provides specific examples of the effect of flow rate and applied voltage on fibre diameter. Some reports show that fibre diameter

increases with increasing flow rate (Du et al., 2008, Wang et al., 2006) with Heikkilä et al. (2008) showing the opposite trend, while Tan et al. (2005) shows there is no effect on fibre diameter at all. Similarly, for applied voltage, the effect on fibre diameter ranges from increasing (Cui et al., 2007, Du et al., 2008) to no effect (Gu et al., 2005, Tan et al., 2005, Wang et al., 2006) to decreasing (Ding et al., 2009, Li et al., 2006). The work by Patra (2010) or Coles et al. (2010) provides a useful insight into one possible explanation for these discrepancies, namely interaction between parameters. The classic parameters varied in electrospinning experiments such as electrode distance, applied voltage, polymer concentration or flow rate do not directly correlate to the underlying principles of physics that govern the electrospinning process. It is the interactions between these variable parameters that more usefully reflect the response of the process.

The example of polymer concentration shows how some of these parameters are quite closely related to the underlying physics of electrospinning. Increasing polymer concentration is generally taken to increase fibre diameter (Basu et al., 2011, Patra et al., 2009b). As polymer concentration increases there will be a larger volume fraction of polymer in the jet, such that once all solvent is lost (a typical assumption in successful electrospinning) one would expect a larger diameter fibre if the effect of fibre drawing is neglected. Similarly, the rheological properties suitable for electrospinning require that the polymer solution has a concentration sufficient to have approximately two times or greater than the entanglement concentration (Shenoy et al., 2005). Once a polymer is above the entanglement concentration it can be generally assumed that increases in concentration will lead to significant increases in viscosity that in turn would resist stretching leading to the formation of thicker fibres. This would happen without further consideration of molecular dynamics. As such, higher polymer concentration leading to thicker fibres would apply to all examples of electrospinning excluding certain special or unusual cases. This is why this general observation has become established in the literature.

The counter example of electrode distance shows how this parameter is quite far removed from the underlying physics of electrospinning, leading to an unclear effect on fibre diameter. If electrode distance is shortened then the electric field experienced by the fibre in flight will decrease (see Chapter 5). However, this will also change the shape of the electric field (again see Chapter 5), increasing or decreasing the effect of the electric field at different stages of the process. The extent of these changes will also depend on the electrode geometry used. Further to this, the onset of the whipping instability is approximately constant with respect to distance (Kowalewski et al., 2005). This means that changing the electrode distance also increases the proportion of the flight time spent in the whipping instability. This demonstrates that changes in electrode distance will indirectly affect the physics of the process, and as such the expected effect on fibre diameter would see

interactions between other parameters such as polymer concentration (for viscoelastic effects while undergoing thinning in the whipping region) or both applied voltage and electrode geometry.

Two methods can be used to address this problem. Previously published studies have taken the approach of treating each electrospinning experiment as an independent process, varying processing parameters to optimize the fibre properties for the chosen conditions (Coles et al., 2010, Patra et al., 2009b). This is done using a design-of-experiments approach both to minimize and statistically validate the work required to optimize the process. However, these results are not directly transferable to a new problem in electrospinning due to the strong interaction effects between parameters discussed above. This work then becomes of limited utility for engineering applications outside of the chosen set of conditions (often the specific polymer-solvent-geometry system).

This thesis has taken the approach to develop novel measurement techniques to observe the process to determine the underpinning physics of the process. This offers the possibility of defining new experimental regimes that will determine the relationship between classic processing parameters and the process physics that will lead to control of the fibre morphology. Two examples of this are the bulk charge density of the Taylor cone and the charge lost while in flight. The bulk charge density reflects the electrical energy available at the Taylor cone and hence is directly related to the energy available to initiate and sustain the process of electrospinning. Charge loss while in flight is a key physical process for electrospinning because once the jet enters the whipping instability mode the further thinning of the jet will be driven by self-repulsion of the jet. As such the effect of processing conditions on charge loss when taken with viscoelastic considerations could create a clear relationship between processing parameters and fibre morphology. Both of these examples, however, require significantly more data so that the effects from the underlying physics can be separated from other already established influencing factors such as polymer entanglement concentration.

9.8 Conclusion

This chapter demonstrates how further empirical observation can improve the understanding of the electrospinning process, specifically that further understanding of the role charge plays in the electrospinning process is vital to describing its dynamics. Electric charge is what separates the electrospinning process from other fibre production processes. By examining the flow of charge and the flow of mass it is possible to start to infer the nature of the charge transport. This leads to the view that the electrospinning process may be analogous to an electrical discharge process that occurs at a lower energy level than direct ionization discharges by using the ability of the solution to flow. The process is still a relatively high energy process (charge density of 7–96 C/kg) and as such undergoes losses of charge in flight. These losses will reduce the rate of stretching and the growth

rate of the various characteristic instabilities in the process, including the generally desirable whipping instability. This reduces the potential for electrospinning to form fibres at the nanoscale. Better understanding of these aspects of the process would enable better control of the electrospinning process extending the range of fibre properties that can be produced.

CHAPTER 10

CONCLUSION

10 Conclusion

This thesis provides an exhaustive description of the electrospinning process. The description has been constructed by reviewing existing mathematical models and from the novel experiments presented in this thesis. The differences between the two highlights the need for further experimental work to focus specifically on the electrospinning process so as to better understand how to gain control of the process.

This thesis presents a novel method of studying the electrospinning process by employing high frequency data capture measuring the electric current flow at the high voltage and collector electrodes. This technique has potential for use as a control feedback mechanism for electrospinning. As a versatile laboratory technique it has been used to study the charge density at the Taylor cone for a range of applied voltages and distances. Here the bulk charge density was found to be a constant 7.7 C/kg over the entire range. The current measurement technique was adapted to estimate the flight time of the electrospun fibre. High speed video was used to show that at jet initiation the leading edge behaves in a similar manner to the quasi-steady state of electrospinning. Here it was found that changing the electrode distance from 80 mm to 120 mm had no observable effect on the flight time of the leading edge. However, doubling the applied voltage from 7.5 kV to 15 kV reduced the flight time by a factor of three from 0.089s to 0.0277s. The current measurement technique is also able to quantify the charge lost from the fibre to the environment when electrospinning in the quasi-stable state. It was found that in all cases there was a minimum of 5% of the charge lost while in flight while some cases lost up to 80% of the initial charge. These losses were quantified for several polymer solutions, and solution composition was found to modify the magnitude of loss. Polymer type, concentration and dissolved ion concentration were all found to change the magnitude of the charge loss. The data set covered enough conditions to accurately fit models of electric current in response to applied voltage and electrode distance. It was found that a function of the form $I_{HV} = A(V - V_{th})^2 d^{\beta}$ gives the best fit for poly-vinyl alcohol (PVOH) while $I_{HV} = A(V - V_{th})^2 e^{-d/H}$ provides a better fit for poly-vinyl butyral (PVB). It was found that to describe the collector electrode current $I_{col} = f(V, d) I_{HV}$ the function $f(V, d)$ could be reduced to $f(d)$ and still provide a good fit, thus demonstrating that much of the magnitude of charge loss is dependent on electrode distance rather than applied voltage.

These results are incorporated into a new description of the electrospinning process with sufficient detail to inform a new generation of mathematical models, the construction of which is beyond the scope of this thesis. The implications of charge loss within the process is significant as the force due to the charge carried by the fibre is a significant part of what distinguishes the electrospinning

process from other fibre forming methods. This description can be used as a rapid introduction to electrospinning, and to inform design for industrial production of electrospun fibre.

V. Bibliography

Atten, P., Malraison, B. & Zahn, M. (1997). Electrohydrodynamic plumes in point-plane geometry. *Dielectrics and Electrical Insulation, IEEE Transactions on*, *4*(6), 710–718. IEEE.

Basu, S., Agrawal, A. K. & Jassal, M. (2011). Concept of minimum electrospinning voltage in electrospinning of polyacrylonitrile N, N-dimethylformamide system. *Journal of Applied Polymer Science*, *122*(2), 856–866. Wiley Online Library.

Baumgarten, P. K. (1971). Electrostatic spinning of acrylic microfibers. *Journal of colloid and interface science*, *36*(1), 71–79. Elsevier.

Bellan, L. M. & Craighead, H. (2006). Control of an electrospinning jet using electric focusing and jet-steering fields. *Journal of Vacuum Science \& Technology B: Microelectronics and Nanometer Structures*, *24*(6), 3179–3183. AVS.

Bellan, L. M., Joshua, D., Strychalski, E. A., Moran-Mirabal, J. & Craighead, H. (2006). Individually resolved DNA molecules stretched and embedded in electrospun polymer nanofibers. *Nano letters*, *6*(11), 2526–2530. ACS Publications.

Bergshoef, M. M. & Vancso, G. J. (1999). Transparent nanocomposites with ultrathin, electrospun nylon-4, 6 fiber reinforcement. *Advanced materials*, *11*(16), 1362–1365. Wiley Online Library.

Blonski, S., Blasinska, A. & Kowalewski, T. (2005). Electrospinning of liquid jets. *Mechanics of 21st Century, ICTAM2004 CD-ROM, edts. W. Gutkowski, TA Kowalewski, Springer Verlg*. Citeseer.

Boys, C. V. (1887). On the Production, Properties, and some suggested Uses of the Finest Threads. *Proceedings of the Physical Society of London*, *9*, 8–19. doi:10.1088/1478-7814/9/1/303

Buchko, C. J., Chen, L. C., Shen, Y. & Martin, D. C. (1999). Processing and microstructural characterization of porous biocompatible protein polymer thin films. *Polymer*, *40*(26), 7397–7407. Elsevier.

Carroll, C. P. & Joo, Y. L. (2006). Electrospinning of viscoelastic Boger fluids: Modeling and experiments. *Physics of Fluids*, *18*, 053102.

Carroll, C. P. & Joo, Y. L. (2008). Axisymmetric instabilities of electrically driven viscoelastic jets. *Journal of non-Newtonian fluid mechanics*, *153*(2), 130–148. Elsevier.

Carroll, C. P. & Joo, Y. L. (2009). Axisymmetric instabilities in electrospinning of highly conducting, viscoelastic polymer solutions. *Physics of Fluids*, *21*, 103101.

Carroll, C. P. & Joo, Y. L. (2011). Discretized modeling of electrically driven viscoelastic jets in the initial stage of electrospinning. *Journal of Applied Physics*, *109*(9), 094315–094315. AIP.

Casper, C. L., Stephens, J. S., Tassi, N. G., Chase, D. B. & Rabolt, J. F. (2004). Controlling surface morphology of electrospun polystyrene fibers: Effect of humidity and molecular weight in the electrospinning process. *Macromolecules*, *37*(2), 573–578. ACS Publications.

Chuangchote, S., Jitputti, J., Sagawa, T. & Yoshikawa, S. (2009). Photocatalytic activity for hydrogen evolution of electrospun TiO2 nanofibers. *ACS Applied Materials \& Interfaces*, *1*(5), 1140–1143. ACS Publications.

Coles, S. R., Jacobs, D. K., Meredith, J. O., Barker, G., Clark, A. J., Kirwan, K., Stanger, J., et al. (2010). A design of experiments (DoE) approach to material properties optimization of electrospun nanofibers. *Journal of Applied Polymer Science*, *117*(4), 2251–2257. Wiley Online Library.

Collins, G., Federici, J., Imura, Y. & Catalani, L. H. (2012). Charge generation, charge transport, and residual charge in the electrospinning of polymers: A review of issues and complications. *Journal of Applied Physics*, *111*(4), 044701–044701. AIP.

Cooley, J. F. (1900). Improved methods of and apparatus for electrically separating the relatively volatile liquid component from the component of relatively fixed substances of composite fluids. *UK Patent 6385*.

Cooley, J. F. (1902). Apparatus for electrically dispersing fluids. *US Patent 692,631*. Google Patents.

Costolo, M., Lennhoff, J., Pawle, R., Rietman, E. & Stevens, A. (2007). A nonlinear system model for electrospinning sub-100 nm polyacrylonitrile fibres. *Nanotechnology*, *19*(3), 035707. IOP Publishing.

Cui, W., Li, X., Zhou, S. & Weng, J. (2007). Investigation on process parameters of electrospinning system through orthogonal experimental design. *Journal of applied*

polymer science, *103*(5), 3105–3112. Wiley Online Library.

Deitzel, J., Kleinmeyer, J., Harris, D. & Beck Tan, N. (2001). The effect of processing variables on the morphology of electrospun nanofibers and textiles. *Polymer*, *42*(1), 261–272. Elsevier.

Deitzel, J. M., Kleinmeyer, J. D., Hirvonen, J. K. & Beck Tan, N. (2001). Controlled deposition of electrospun poly (ethylene oxide) fibers. *Polymer*, *42*(19), 8163–8170. Elsevier.

Demir, M. M., Yilgor, I., Yilgor, E. & Erman, B. (2002). Electrospinning of polyurethane fibers. *Polymer*, *43*(11), 3303–3309. Elsevier.

Ding, B., Kim, J., Miyazaki, Y. & Shiratori, S. (2004). Electrospun nanofibrous membranes coated quartz crystal microbalance as gas sensor for NH3 detection. *Sensors and Actuators B: Chemical*, *101*(3), 373–380. Elsevier.

Ding, Y., Zhang, P., Jiang, Y., Xu, F., Yin, J. & Zuo, Y. (2009). Mechanical properties of nylon-6/SiO< sub> 2</sub> nanofibers prepared by electrospinning. *Materials Letters*, *63*(1), 34–36. Elsevier.

Doshi, J. N. (1994). *The electrospinning process and applications of electrospun fibers*. Ph.D. Thesis, The University of Akron.

Drew, C., Wang, X., Senecal, K., Schreuder-Gibson, H., He, J., Kumar, J. & Samuelson, L. A. (2002). Electrospun photovoltaic cells. *Journal of Macromolecular Science, Part A*, *39*(10), 1085–1094. Taylor \& Francis.

Dror, Y., Kuhn, J., Avrahami, R. & Zussman, E. (2008). Encapsulation of enzymes in biodegradable tubular structures. *Macromolecules*, *41*(12), 4187–4192. ACS Publications.

Druesedow, C. J., Batur, C., Cakmak, M. & Yalcin, B. (2009). Pressure control system for electrospinning process. *Polymer Engineering & Science*, *50*(4), 800–810. Wiley Online Library.

Du, J., Shintay, S. & Zhang, X. (2008). Diameter control of electrospun polyacrylonitrile/iron acetylacetonate ultrafine nanofibers. *Journal of Polymer Science Part B: Polymer Physics*, *46*(15), 1611–1618. Wiley Online Library.

Earnshaw, S. (1842). On the nature of the molecular forces which regulate the constitution of the luminiferous ether. *Trans. Camb. Phil. Soc*, *7*, 97–112.

Eda, G., Liu, J. & Shivkumar, S. (2007). Solvent effects on jet evolution during electrospinning of semi-dilute polystyrene solutions. *European polymer journal*, *43*(4), 1154–1167. Elsevier.

Fallahi, D., Rafizadeh, M., Mohammadi, N. & Vahidi, B. (2008). Effect of applied voltage on jet electric current and flow rate in electrospinning of polyacrylonitrile solutions. *Polymer International*, *57*(12), 1363–1368. Wiley Online Library.

Feng, J. (2002). The stretching of an electrified non-Newtonian jet: A model for electrospinning. *Physics of Fluids*, *14*, 3912.

Feng, J. (2003). Stretching of a straight electrically charged viscoelastic jet. *Journal of non-newtonian fluid mechanics*, *116*(1), 55–70. Elsevier.

Filatov, Y., Budyka, A. & Kirichenko, V. (2007). *Electrospinning of Micro-And Nanofibers: Fundamentals and Applications in Separation and Filtration Processes*. Begell House.

Fong, H., Chun, I. & Reneker, D. (1999). Beaded nanofibers formed during electrospinning. *Polymer*, *40*(16), 4585–4592. Elsevier.

Formhals, A. (1934). Process and apparatus for preparing artificial threads. *US Patent, 1975504*.

Formhals, A. (1937). Production of artificial fibers. *US Patent 2,077,373*. Google Patents.

Formhals, A. (1938). Artificial fiber construction. *US Patent 2,109,333*. Google Patents.

Formhals, A. (1943). Production of Artificial Fibers from Fiber Forming Liquids. *US Patent 2,323,025*. Google Patents.

Formhals, A. (1944). Method and apparatus for spinning. *US Patent 2,349,950*. Google Patents.

Fridrikh, S. V., Yu, J. H., Brenner, M. P. & Rutledge, G. C. (2003). Controlling the fiber diameter during electrospinning. *Physical review letters*, *90*(14), 144502. APS.

Ganan-Calvo, A. M. (1997). On the theory of electrohydrodynamically driven capillary jets. *J. Fluid Mech*, *335*, 165. Cambridge Univ Press.

Gañán-Calvo, A. M. (1997). Cone-jet analytical extension of Taylor's electrostatic solution and the asymptotic universal scaling laws in electrospraying. *Physical review letters*, *79*(2), 217–220. APS.

Giesekus, H. (1982). A Simple Constitutive Equation for Polymer Fluids Based on the Concept of Deformation-Dependent Tensorial Mobility. *Journal of Non-Newtonian Fluid Mechanics*, *11*(1-2), 69–109. PO BOX 211, 1000 AE AMSTERDAM, NETHERLANDS: ELSEVIER SCIENCE BV. doi:10.1016/0377-0257(82)85016-7

Gu, S., Ren, J. & Vancso, G. (2005). Process optimization and empirical modeling for electrospun polyacrylonitrile (PAN) nanofiber precursor of carbon nanofibers. *European polymer journal*, *41*(11), 2559–2568. Elsevier.

Halliday, D., Resnick, R. & Walker, J. (2008). *Fundamentals of Physics Extended, 8th Ed*. Wiley India Pvt. Limited.

Han, T., Reneker, D. H. & Yarin, A. L. (2008). Pendulum-like motion of straight electrified jets. *Polymer*, *49*(8), 2160–2169. Elsevier.

Han, T., Yarin, A. L. & Reneker, D. H. (2008). Viscoelastic electrospun jets: Initial stresses and elongational rheometry. *Polymer*, *49*(6), 1651–1658. Elsevier.

Hartman, R., Brunner, D., Camelot, D., Marijnissen, J. & Scarlett, B. (1999). Electrohydrodynamic atomization in the cone-jet mode physical modeling of the liquid cone and jet. *Journal of Aerosol science*, *30*(7), 823–849. Elsevier.

He, J. H., Wan, Y. Q. & Yu, J. Y. (2004). Allometric scaling and instability in electrospinning. *International Journal of Nonlinear Sciences and Numerical Simulation 5 (3), 243-252, 2004*.

He, J. H., Wan, Y. Q. & Yu, J. Y. (2005). Scaling law in electrospinning: relationship between electric current and solution flow rate. *Polymer*, *46*(8), 2799–2801. Elsevier.

Heikkilä, P. & Harlin, A. (2008). Parameter study of electrospinning of polyamide-6. *European Polymer Journal*, *44*(10), 3067–3079. Elsevier.

Helgeson, M. E., Grammatikos, K. N., Deitzel, J. M. & Wagner, N. J. (2008). Theory and kinematic measurements of the mechanics of stable electrospun polymer jets. *Polymer*, *49*(12), 2924–2936. Elsevier.

Hohman, M. M., Shin, M., Rutledge, G. & Brenner, M. P. (2001). Electrospinning and electrically forced jets. I. Stability theory. *Physics of Fluids*, *13*, 2201.

Hong, Y., Shang, T., Li, Y., Wang, L., Wang, C., Chen, X. & Jing, X. (2006). Synthesis using electrospinning and stabilization of single layer macroporous films and fibrous networks of poly (vinyl alcohol). *Journal of membrane science*, *276*(1), 1–7. Elsevier.

Hsiao, H. Y., Huang, C. M., Liu, Y. Y., Kuo, Y. C. & Chen, H. (2012). Effect of air blowing on the morphology and nanofiber properties of blowing-assisted electrospun polycarbonates. *Journal of Applied Polymer Science*. Wiley Online Library.

Jarusuwannapoom, T., Hongrojjanawiwat, W., Jitjaicham, S., Wannatong, L., Nithitanakul, M., Pattamaprom, C., Koombhongse, P., et al. (2005). Effect of solvents on electro-spinnability of polystyrene solutions and morphological appearance of resulting electrospun polystyrene fibers. *European Polymer Journal*, *41*(3), 409–421. Elsevier.

Kalayci, V. E., Patra, P. K., Kim, Y. K., Ugbolue, S. C. & Warner, S. B. (2005). Charge consequences in electrospun polyacrylonitrile (PAN) nanofibers. *Polymer*, *46*(18), 7191–7200. Elsevier.

Keun Son, W., Ho Youk, J., Seung Lee, T. & Park, W. H. (2005). Effect of pH on electrospinning of poly (vinyl alcohol). *Materials letters*, *59*(12), 1571–1575. Elsevier.

Kim, C. H., Jung, Y. H., Kim, H. Y., Lee, D. R., Dharmaraj, N. & Choi, K. E. (2006). Effect of collector temperature on the porous structure of electrospun fibers. *Macromolecular Research*, *14*(1), 59–65. Springer.

Kim, G. T., Lee, J. S., Shin, J. H., Ahn, Y. C., Hwang, Y. J., Shin, H. S., Lee, J. K., et al. (2005). Investigation of pore formation for polystyrene electrospun fiber: Effect of relative humidity. *Korean Journal of Chemical Engineering*, *22*(5), 783–788. Springer.

Kim, J. & Reneker, D. H. (1999). Mechanical properties of composites using ultrafine electrospun fibers. *Polymer composites*, *20*(1), 124–131. Wiley Online Library.

Klein, S., Kuhn, J., Avrahami, R., Tarre, S., Beliavski, M., Green, M. & Zussman, E. (2009). Encapsulation of Bacterial Cells in Electrospun Microtubes. *Biomacromolecules*, *10*(7), 1751–1756. ACS Publications.

Kong, C., Jo, K., Jo, N. & Kim, H. (2008). Effects of the spin line temperature profile and melt index of poly (propylene) on melt-electrospinning. *Polymer Engineering \& Science*, *49*(2), 391–396. Wiley Online Library.

Koombhongse, S., Liu, W. & Reneker, D. H. (2001). Flat polymer ribbons and other shapes by electrospinning. *Journal of Polymer Science Part B: Polymer Physics*, *39*(21), 2598–2606. Wiley Online Library.

Koski, A., Yim, K. & Shivkumar, S. (2004). Effect of molecular weight on fibrous PVA produced by electrospinning. *Materials Letters*, *58*(3), 493–497. Elsevier.

Kowalewski, T., Barral, S. & Kowalczyk, T. (2009). Modeling Electrospinning of Nanofibers. *IUTAM Symposium on Modelling Nanomaterials and Nanosystems*, 279–292.

Kowalewski, T., Blonski, S. & Barral, S. (2005). Experiments and modelling of electrospinning process. *Technical Sciences*, *53*(4).

Larsen, G., Spretz, R. & Velarde-Ortiz, R. (2004). Use of coaxial gas jackets to stabilize Taylor cones of volatile solutions and to induce particle-to-fiber transitions. *Advanced Materials*, *16*(2), 166–169. Wiley Online Library.

Lee, J. S., Choi, K. H., Ghim, H. D., Kim, S. S., Chun, D. H., Kim, H. Y. & Lyoo, W. S. (2004). Role of molecular weight of atactic poly (vinyl alcohol)(PVA) in the structure and properties of PVA nanofabric prepared by electrospinning. *Journal of Applied Polymer Science*, *93*(4), 1638–1646. Wiley Online Library.

Li, D. & Xia, Y. (2004). Direct fabrication of composite and ceramic hollow nanofibers by electrospinning. *Nano Letters*, *4*(5), 933–938. ACS Publications.

Li, Y., Huang, Z. & Lǔ, Y. (2006). Electrospinning of nylon-6, 66, 1010 terpolymer. *European polymer journal*, *42*(7), 1696–1704. Elsevier.

Lim, J. M., Yi, G. R., Moon, J. H., Heo, C. J. & Yang, S. M. (2007). Superhydrophobic films of electrospun fibers with multiple-scale surface morphology. *Langmuir*, *23*(15), 7981–7989. ACS Publications.

Lin, Y., Yao, Y., Yang, X., Wei, N., Li, X., Gong, P., Li, R., et al. (2007). Preparation of poly (ether sulfone) nanofibers by gas-jet/electrospinning. *Journal of Applied Polymer Science*, *107*(2), 909–917. Wiley Online Library.

Liu, L. & Dzenis, Y. A. (2008). Analysis of the effects of the residual charge and gap size on electrospun nanofiber alignment in a gap method. *Nanotechnology*, *19*(35), 355307. IOP Publishing.

Lombardi, M., Palmero, P., Sangermano, M. & Varesano, A. (2011). Electrospun polyamide-6 membranes containing titanium dioxide as photocatalyst. *Polymer International*, *60*(2), 234–239. Wiley Online Library.

Luo, C., Nangrejo, M. & Edirisinghe, M. (2010). A novel method of selecting solvents for polymer electrospinning. *Polymer*, *51*(7), 1654–1662. Elsevier.

McClure, M. J., Simpson, D. G. & Bowlin, G. L. (2012). Tri-layered vascular grafts composed of polycaprolactone, elastin, collagen, and silk: Optimization of graft properties. *Journal of the Mechanical Behavior of Biomedical Materials*, *10*, 48–61. Elsevier.

Megelski, S., Stephens, J. S., Chase, D. B. & Rabolt, J. F. (2002). Micro-and nanostructured surface morphology on electrospun polymer fibers. *Macromolecules*, *35*(22), 8456–8466. ACS Publications.

Melcher, J. & Warren, E. (1971). Electrohydrodynamics of a current-carrying semi-insulating jet. *Journal of Fluid Mechanics*, *47*(01), 127–143. Cambridge Univ Press.

Mo, X., Xu, C., Kotaki, M., Ramakrishna, S. & others. (2004). Electrospun P (LLA-CL) nanofiber: a biomimetic extracellular matrix for smooth muscle cell and endothelial cell proliferation. *Biomaterials*, *25*(10), 1883–1890.

Nurfaizey, A., Stanger, J., Tucker, N., Buunk, N., Wallace, A. & Staiger, M. (2012). Manipulation of electrospun fibres in flight: the principle of superposition of electric fields as a control method. *Journal of Materials Science*, *47*(3), 1156–1163. Springer.

Onozuka, K., Ding, B., Tsuge, Y., Naka, T., Yamazaki, M., Sugi, S., Ohno, S., et al. (2006). Electrospinning processed nanofibrous TiO2 membranes for photovoltaic applications. *Nanotechnology*, *17*, 1026. IOP Publishing.

Pakravan, M., Heuzey, M. C. & Ajji, A. (2011). A fundamental study of chitosan/PEO electrospinning. *Polymer*, *52*(21), 4813–4824. Elsevier.

Patra, S. (2010). *Manufacturing and Characterisation of Electrospun Nanostructured Mats from Poly(lactic acid)*. Ph.D. Thesis, The University of Auckland.

Patra, S. & Bhattacharyya, D. (2010). Characterisation of Electrospun Poly (lactic acid) Nanofibre Networks. *Composite Interfaces*, *17*(2-3), 273–282. Taylor \& Francis.

Patra, S., Bhattacharyya, D., Ray, S. & Easteal, A. (2009). Electrospun poly (lactic acid) based conducting nanofibrous networks. *IOP Conference Series: Materials Science and Engineering*, *4*(1), 012020.

Patra, S., Easteal, A. & Bhattacharyya, D. (2009). Parametric study of manufacturing poly (lactic) acid nanofibrous mat by electrospinning. *Journal of materials science*, *44*(2), 647–654. Springer.

Patra, S., Lin, R. J. T. & Bhattacharyya, D. (2010). Regression analysis of manufacturing electrospun nonwoven nanotextiles. *Journal of materials science*, *45*(14), 3938–3946. Springer.

Pham, Q. P., Sharma, U. & Mikos, A. G. (2006). Electrospun poly (ε-caprolactone) microfiber and multilayer nanofiber/microfiber scaffolds: characterization of scaffolds and measurement of cellular infiltration. *Biomacromolecules*, *7*(10), 2796–2805. ACS Publications.

Qin, X. H., Wang, S. Y., Sandra, T. & Lukas, D. (2005). Effect of LiCl on the stability length of electrospinning jet by PAN polymer solution. *Materials Letters*, *59*(24-25), 3102–3105. Elsevier.

Ramakrishna, S., Fujihara, K., Teo, W. E., Lim, T. C. & Ma, Z. (2005). *An Introduction to Electrospinning And Nanofibers*. World Scientific.

Reneker, D. H. & Chun, I. (1999). Nanometre diameter fibres of polymer, produced by electrospinning. *Nanotechnology*, *7*(3), 216. IOP Publishing.

Reneker, D. H. & Yarin, A. L. (2008). Electrospinning jets and polymer nanofibers. *Polymer*, *49*(10), 2387–2425. Elsevier.

Reneker, D. H., Yarin, A. L., Fong, H. & Koombhongse, S. (2000). Bending instability of electrically charged liquid jets of polymer solutions in electrospinning. *Journal of Applied Physics*, *87*, 4531.

Reznik, S., Yarin, A., Theron, A. & Zussman, E. (2004). Transient and steady shapes of droplets attached to a surface in a strong electric field. *Journal of Fluid Mechanics*, *516*(1), 349–377. Cambridge Univ Press.

Rutledge, G., Shin, M., Warner, S. B., Buer, A. & Ugbolue, S. (2001). A fundamental investigation of the formation and properties of electrospun fibers. *National textile center annual report*, 83–90.

Shenoy, S. L., Bates, W. D., Frisch, H. L. & Wnek, G. E. (2005). Role of chain entanglements on fiber formation during electrospinning of polymer solutions: good solvent, non-specific polymer-polymer interaction limit. *Polymer*, *46*(10), 3372–3384. Elsevier.

Shin, Y., Hohman, M., Brenner, M. & Rutledge, G. (2001). Electrospinning: a whipping fluid jet generates submicron polymer fibers. *Applied Physics Letters*, *78*(8), 1149–1151. AIP.

Shin, Y., Hohman, M., Brenner, M. & Rutledge, G. (2001). Experimental characterization of electrospinning: the electrically forced jet and instabilities. *Polymer*, *42*(25), 09955–09967. Elsevier.

Song, W. & Xia, Z. (1994). A Phenomenoligical Viscosity Model for Polymeric Fluid. *Journal of Non-Newtonian Fluid Mechanics*, *53*, 151–163. PO BOX 211, 1000 AE AMSTERDAM, NETHERLANDS: ELSEVIER SCIENCE BV. doi:10.1016/0377-0257(94)85046-1

Spivak, A. & Dzenis, Y. (1999). A condition of the existence of a conductive liquid meniscus in an external electric field. *Journal of applied mechanics*, *66*, 1026.

Spivak, A., Dzenis, Y. & Reneker, D. (2000). A model of steady state jet in the electrospinning process. *Mechanics research communications*, *27*, 37–42. Pergamon.

Stanger, J. (2008). *Charge transfer mechanisms in Electrospinning*. Physics and Astronomy Department, Masters Thesis, University of Canterbury.

Stanger, J., Tucker, N., Fullick, S., Sellier, M. & Staiger, M. (2012). Insights into the power law relationships that describe mass deposition rates during electrospinning. *Journal of*

Materials Science, *47*(3), 1113–1118. Springer.

Stanger, J., Tucker, N., Kirwan, K. & Staiger, M. (2009). Effect of Charge Density on the Taylor cone in Electrospinning. *International Journal of Modern Physics B*, *23*(06n07), 1956–1961. World Scientific.

Stanger, J., Tucker, N. & Staiger, M. (2009). *Electrospinning*. Smithers Rapra Technology.

Stanger, J., Tucker, N., Staiger, M., Kirwan, K., Coles, S., Jacobs, D. & Larsen, N. (2009). Effect of salts on the electrospinning of poly (vinyl alcohol). *AIP Conference Proceedings*, *1151*, 118.

Stanger, J., Tucker, N., Staiger, M., Sellier, M., Wood, A., Phillips, J., Lamberts, R., et al. (2010). Characterization of the Electrospinning Process. *ElectroSpin2010, Melbourne, Australia*.

Stanger, J., Tucker, N., Wallace, A., Larsen, N., Staiger, M. & Reeves, R. (2009). The effect of electrode configuration and substrate material on the mass deposition rate of electrospinning. *Journal of Applied Polymer Science*, *112*(3), 1729–1737. Wiley Online Library.

Strutt, J. (1879). On the instability of jets. *Proc. R. Soc. London A*, *10*, 4–13.

Sun, Z., Deitzel, J. M., Knopf, J., Chen, X. & Gillespie Jr, J. W. (2012). The effect of solvent dielectric properties on the collection of oriented electrospun fibers. *Journal of Applied Polymer Science*. Wiley Online Library.

Tamura, T. & Kawakami, H. (2010). Aligned electrospun nanofiber composite membranes for fuel cell electrolytes. *Nano letters*, *10*(4), 1324–1328. ACS Publications.

Tan, S., Inai, R., Kotaki, M. & Ramakrishna, S. (2005). Systematic parameter study for ultra-fine fiber fabrication via electrospinning process. *Polymer*, *46*(16), 6128–6134. Elsevier.

Taylor, G. (1964). Disintegration of Water Drops in Electric Field. *Proceedings of the Royal Society of London. A. Mathematical and Physical Sciences*, *280*(1380), 383+. 6-9 CARLTON HOUSE TERRACE, LONDON SW1Y 5AG, ENGLAND: ROYAL SOC. doi:10.1098/rspa.1964.0151

Taylor, G. (1966). Force Exerted by an Electric Field on a Long Cylindrical Conductor. *Proceedings of the Royal Society of London. A. Mathematical and Physical Sciences*, *291*(1425), 145. 6 CARLTON HOUSE TERRACE, LONDON SW1Y 5AG, ENGLAND: ROYAL SOC LONDON. doi:10.1098/rspa.1966.0085

Taylor, G. (1969). Electrically driven jets. *Proceedings of the Royal Society of London. A. Mathematical and Physical Sciences*, *313*(1515), 453–475. The Royal Society.

Teo, W., Kotaki, M., Mo, X. & Ramakrishna, S. (2005). Porous tubular structures with controlled fibre orientation using a modified electrospinning method. *Nanotechnology*, *16*(6), 918. IOP Publishing.

Theron, S., Yarin, A., Zussman, E. & Kroll, E. (2005). Multiple jets in electrospinning: experiment and modeling. *Polymer*, *46*(9), 2889–2899. Elsevier.

Theron, S., Zussman, E. & Yarin, A. (2004). Experimental investigation of the governing parameters in the electrospinning of polymer solutions. *Polymer*, *45*(6), 2017–2030. Elsevier.

Thompson, C., Chase, G., Yarin, A. & Reneker, D. (2007). Effects of parameters on nanofiber diameter determined from electrospinning model. *Polymer*, *48*(23), 6913–6922. Elsevier.

Tomer, V., Teye-Mensah, R., Tokash, J., Stojilovic, N., Kataphinan, W., Evans, E., Chase, G., et al. (2005). Selective emitters for thermophotovoltaics: erbia-modified electrospun titania nanofibers. *Solar energy materials and solar cells*, *85*(4), 477–488. Elsevier.

Townsend-Nicholson, A. & Jayasinghe, S. N. (2006). Cell electrospinning: a unique biotechnique for encapsulating living organisms for generating active biological microthreads/scaffolds. *Biomacromolecules*, *7*(12), 3364–3369. ACS Publications.

Tripatanasuwan, S. & Reneker, D. H. (2009). Corona discharge from electrospinning jet of poly (ethylene oxide) solution. *Polymer*, *50*(8), 1835–1837. Elsevier.

Tripatanasuwan, S., Zhong, Z. & Reneker, D. H. (2007). Effect of evaporation and solidification of the charged jet in electrospinning of poly (ethylene oxide) aqueous solution. *Polymer*, *48*(19), 5742–5746. Elsevier.

Tucker, N., Stanger, J. J., Staiger, M. P., Razzaq, H. & Hofman, K. (2012). The History of the Science and Technology of Electrospinning from 1600 to 1995. *Journal of Engineered*

Fibers and Fabrics, *7*(2), 63–73.

Turnbull, R. (1989). Self-acceleration of a charged jet. *Industry Applications, IEEE Transactions on*, *25*(4), 699–704. IEEE.

De Vrieze, S., Van Camp, T., Nelvig, A., Hagström, B., Westbroek, P. & De Clerck, K. (2009). The effect of temperature and humidity on electrospinning. *Journal of materials science*, *44*(5), 1357–1362. Springer.

Wang, B., Yao, Y., Peng, J., Lin, Y., Liu, W., Luo, Y., Xiang, R., et al. (2009). Preparation of poly (ester imide) ultrafine fibers by gas-jet/electrospinning. *Journal of Applied Polymer Science*, *114*(2), 883–891. Wiley Online Library.

Wang, L., Xiao, Q., Li, Z., Lei, G., Wu, L., Zhang, P. & Mao, J. (2012). Synthesis of Li2CoTi3O8 fibers and their application to lithium-ion batteries. *Electrochimica acta*, *77*, 77–82. Elsevier.

Wang, T. & Kumar, S. (2006). Electrospinning of polyacrylonitrile nanofibers. *Journal of applied polymer science*, *102*(2), 1023–1029. Wiley Online Library.

Wang, X., Drew, C., Lee, S. H., Senecal, K. J., Kumar, J. & Samuelson, L. A. (2002). Electrospinning technology: a novel approach to sensor application. *Journal of Macromolecular Science, Part A*, *39*(10), 1251–1258. Taylor \& Francis.

Wu, C. M., Chiou, H. G., Lin, S. L. & Lin, J. M. (2012). Effects of electrostatic polarity and the types of electrical charging on electrospinning behavior. *Journal of Applied Polymer Science*. Wiley Online Library.

Yang, J., Zeng, Y., Pei, Z. & Wang, X. (2009). Effect of perturbation on the whipping motion in electrospinning. *Journal of Applied Polymer Science*, *115*(4), 2508–2513. Wiley Online Library.

Yarin, A., Koombhongse, S. & Reneker, D. (2001). Bending instability in electrospinning of nanofibers. *Journal of Applied Physics*, *89*, 3018.

Yarin, A., Koombhongse, S. & Reneker, D. (2001). Taylor cone and jetting from liquid droplets in electrospinning of nanofibers. *Journal of Applied Physics*, *90*(9), 4836–4846. AIP.

Yuan, X., Zhang, Y., Dong, C. & Sheng, J. (2004). Morphology of ultrafine polysulfone fibers prepared by electrospinning. *Polymer International*, *53*(11), 1704–1710. Wiley Online Library.

Zeleny, J. (1907). The discharge of electricity from pointed conductors differing in size. *Physical Review (Series I)*, *25*(5), 305. APS.

Zeleny, J. (1917). Instability of electrified liquid surfaces. *Physical review*, *10*(1), 1. APS.

Zeleny, J. (1920). Electrical discharges from pointed conductors. *Physical Review*, *16*(2), 102. APS.

Zeng, J., Xu, X., Chen, X., Liang, Q., Bian, X., Yang, L. & Jing, X. (2003). Biodegradable electrospun fibers for drug delivery. *Journal of Controlled Release*, *92*(3), 227–231. Elsevier.

Zhang, C., Yuan, X., Wu, L., Han, Y. & Sheng, J. (2005). Study on morphology of electrospun poly (vinyl alcohol) mats. *European Polymer Journal*, *41*(3), 423–432. Elsevier.

Zhao, S., Wu, X., Wang, L. & Huang, Y. (2003). Electrospinning of ethyl-cyanoethyl cellulose/tetrahydrofuran solutions. *Journal of Applied Polymer Science*, *91*(1), 242–246. Wiley Online Library.

Zong, X., Kim, K., Fang, D., Ran, S., Hsiao, B. S. & Chu, B. (2002). Structure and process relationship of electrospun bioabsorbable nanofiber membranes. *Polymer*, *43*(16), 4403–4412. Elsevier.

VI. Appendix A – Software Designed for this Thesis

compactDAQ Control Software

The compactDAQ control software written in LabVIEW™ is a simple algorithm that outputs through an analogue to digital converter (ADC) a calibrated 0–10 V signal that is fed into the Glassman MK50P1.5 high voltage power supply. This 0–10 V output produces a proportional output from the high voltage supply of 0–50 kV. The program will initialize then output a signal to produce the desired minimum high voltage output, wait a specified time period, step the output to a higher value, wait and repeat until the maximum high voltage output is reached, at which point the stepping direction will be reversed until the minimum is reached again. The waiting period provides a quasi-steady state observation of the electrospinning process under the applied voltage at that time. While all this is happening the digital to analogue converter (DAC) simultaneously records the voltage on three channels and logs it to a file. These three channels are time synchronised and represent the voltage feedback signal and the electric current feedback signal from the Glassman power supply and the voltage drop across the resistor between the collector and ground. As LabVIEW™ is a visual programming language a screenshot of the program is presented below:

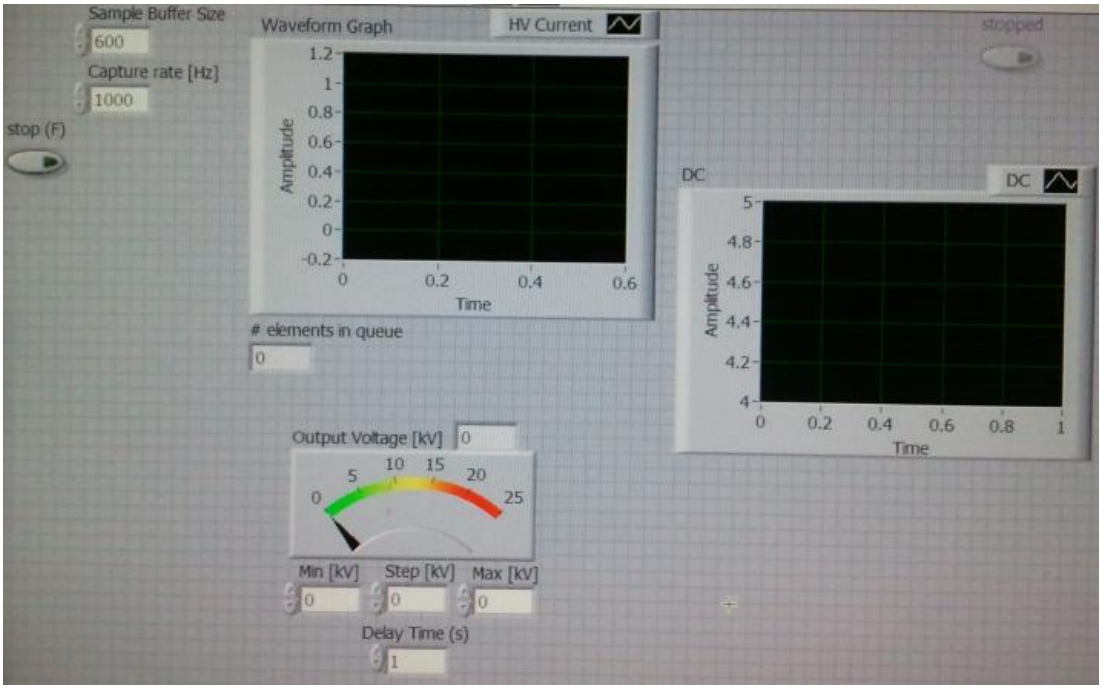

Program control panel

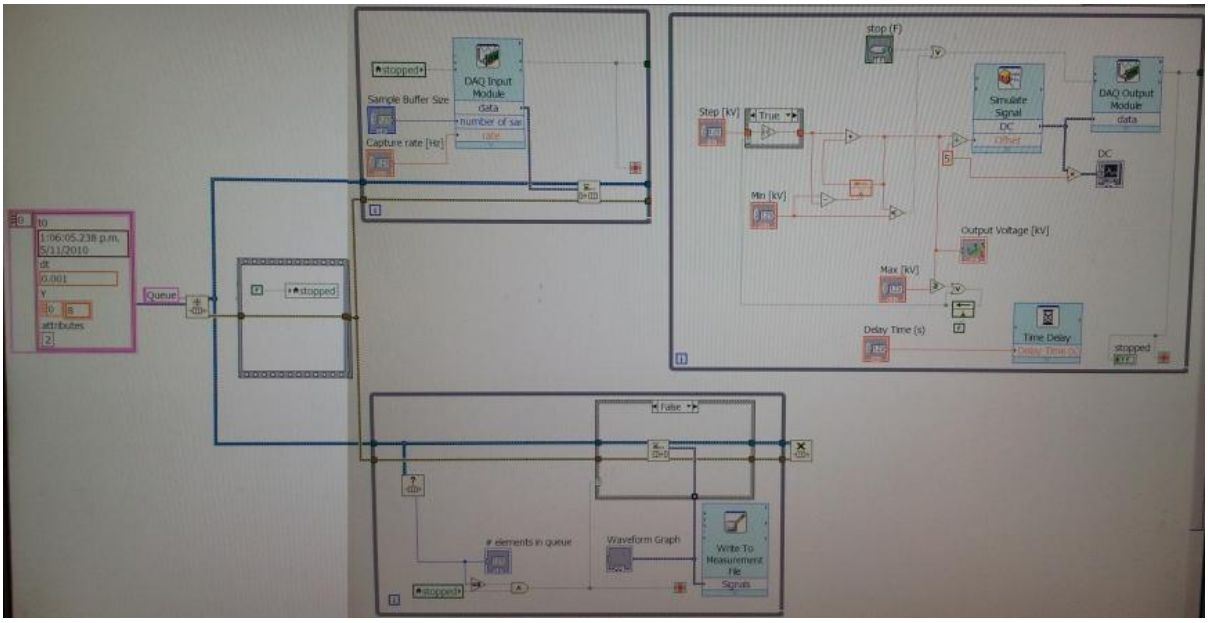

Program block diagram

Data Processing Program

The datasets produced by a typical experiment are of the order of 300,000 samples in three channels. This is more than Microsoft® Excel™ is designed to handle and so a script was written to automatically detect the step transitions in the applied voltage and extract the electric current data for the quasi-steady state condition and provide an output of the statistical properties of that quasi-steady state (i.e. average, standard deviation, etc. ...). This program does so by being told how large the voltage steps are, then applying a moving average to the signal then subtracting each point from its immediate neighbour and looking for the peaks that should be at least 50% of the voltage jump. Once these peaks have been found, a portion of the data on either side is rejected (as it is the transition) and the remaining section (approximately 4,500 samples per condition) is extracted and processed for output.

```
% Version 1.8
% - Added output for checking without debug mode running for faster
% processing
%
% Version 1.7
% - Added zero offset correction
% - Added data for new cDAQ chasis calibration
%
% Version 1.6
% - Added a variable 'excel' that contains all the parameters to copy to
% excel
% - Added a file open box rather than manual file name edit
% - Added a focus on figure 1 command
%
% Version 1.5
% - Added output for comment box to read atmosphric conditions more easily
% into excel
% - Added check to ensure that sampletime is the same as the datafile
% expects
% - Clear output variables each run
%
clear hvstats hvistats colistats
answer = 'n';
%filename = '2011-08-29-80mm.lvm';
filename = uigetfile('*.lvm','Select Data File');
```

```
disp(filename)
sampletime = 1/1000; % [s]
voltagesmoothing = 5;
gapsize = 99;
threshold = 0.4;
timestep = 5; %[s]
junkzone = 0.5; %[s]
diagnostics = 'n';

%rawdata = dlmread(filename,'\t',[23,1,267023,3]);
file = fopen(filename);
%temp = textscan(file,'%*[^\n]',23);
temp = textscan(file,'%*[^\n]',9);
dateoutput = textscan(file,'%[^\n]',1);
temp = textscan(file,'%*[^\n]',13);
disp(dateoutput{1,1}{1,1});
%readdata = textscan(file,'%f %f %f %f %f %*s','delimiter','\t');
readdata = textscan(file,'%f %f %f %f %f %f %s','delimiter','\t');
%readdata = textscan(file,'%f %f %f %f %f %f %f %*s','delimiter','\t');
fclose(file);
rawdata                                                
```

```
voltageconversionfactor = 5.63;  % cDAQ #3 4-slot  2011 +
% hviconversionfactor = 1.123;      % cDAQ #3 4-slot  2011 +
% coliconversionfactor = 1.118;      % cDAQ #3 4-slot  2011 +
hviconversionfactor = 1;      % cDAQ #3 4-slot  2011 +
%coliconversionfactor = 1.051;      % cDAQ #3 4-slot  2011 +
coliconversionfactor = 1.005387665;

figure(1)

smoothvoltage = smooth(rawdata(:,voltagechannel)*voltageconversionfactor,voltagesmoothing);
if diagnostics == 'y'
    while answer == 'n'
        plot(t,smoothvoltage);
        answer = input('Is this alright [y/n]? ','s');
        if isempty(answer)
            answer = 'n';
        end
        if answer == 'n';
            voltagesmoothing = input('Enter smoothing value for voltage: ');
            if isempty(voltagesmoothing)
                voltagesmoothing = 1;
            end
            smoothvoltage                                                                    =
smooth(rawdata(:,voltagechannel)*voltageconversionfactor,voltagesmoothing);
        end
    end
    answer = 'n';
else
    subplot(2,2,1)
    plot(t,smoothvoltage);
end

delta               =               smoothvoltage(1:max(size(rawdata))-gapsize)               -
smoothvoltage(gapsize+1:max(size(rawdata)));
if diagnostics == 'y'
    while answer == 'n'
        plot(t((gapsize+1)/2:max(size(t))-(gapsize+1)/2),abs(delta));
        answer = input('Is this alright [y/n]? ','s');
        if isempty(answer)
            answer = 'n';
        end
        if answer == 'n';
            gapsize = input('Enter new gapsize for edge detection (must be odd): ');
            if isempty(gapsize)
                gapsize = 1;
            end
            delta           =           smoothvoltage(1:max(size(rawdata))-gapsize)           -
smoothvoltage(gapsize+1:max(size(rawdata)));
        end
    end
    answer = 'n';
else
    subplot(2,2,2)
    plot(t((gapsize+1)/2:max(size(t))-(gapsize+1)/2),abs(delta));
end

ttemp = t((gapsize+1)/2:max(size(rawdata))- (gapsize+1)/2);
index = ((gapsize+1)/2:1:max(size(rawdata))- (gapsize+1)/2)';

if diagnostics == 'y'
    while answer == 'n'
        plot(t((gapsize+1)/2:max(size(t))-
(gapsize+1)/2),abs(delta),[min(t((gapsize+1)/2:max(size(t))-
(gapsize+1)/2)),max(t((gapsize+1)/2:max(size(t))-(gapsize+1)/2))],[threshold,threshold]);
        answer = input('Is this alright [y/n]? ','s');
        if isempty(answer)
            answer = 'n';
        end
        if answer == 'n';
            threshold = input('Enter threshold value for edge detection: ');
            if isempty(threshold)
                threshold = 1;
            end
        end
    end
    answer = 'n';
else
```

```
    subplot(2,2,3)
    plot(t((gapsize+1)/2:max(size(t))-
(gapsize+1)/2),abs(delta),[min(t((gapsize+1)/2:max(size(t))-
(gapsize+1)/2)),max(t((gapsize+1)/2:max(size(t))-(gapsize+1)/2))],[threshold,threshold]);
end
times = ttemp(abs(delta) > threshold);
timeindex = index(abs(delta) > threshold);

deltaT = times(1:max(size(times))-1) - times(2:max(size(times)));
if diagnostics == 'y'
    plot(deltaT)
else
   subplot(2,2,4)
   plot(deltaT)
end
%edge = [1; times(abs(deltaT) > timestep / 2)/sampletime; max(size(rawdata))];
edge = [1; timeindex(abs(deltaT) > timestep / 2); max(size(rawdata))];

for i = 1:max(size(edge))-1
    data(i).hv   =   voltageconversionfactor*rawdata(edge(i)+0.5*junkzone/sampletime:edge(i+1)-
0.5*junkzone/sampletime,voltagechannel);
    data(i).hvi   =  hviconversionfactor*150*rawdata(edge(i)+0.5*junkzone/sampletime:edge(i+1)-
0.5*junkzone/sampletime,hvichannel);
    data(i).coli = coliconversionfactor*100*rawdata(edge(i)+0.5*junkzone/sampletime:edge(i+1)-
0.5*junkzone/sampletime,colichannel);
    hvistats(i,1)                                                                          =
mean(hviconversionfactor*150*rawdata(edge(i)+0.5*junkzone/sampletime:edge(i+1)-
0.5*junkzone/sampletime,hvichannel));
    hvistats(i,2)                                                                          =
std(hviconversionfactor*150*rawdata(edge(i)+0.5*junkzone/sampletime:edge(i+1)-
0.5*junkzone/sampletime,hvichannel));
    colistats(i,1)                                                                         =
mean(coliconversionfactor*100*rawdata(edge(i)+0.5*junkzone/sampletime:edge(i+1)-
0.5*junkzone/sampletime,colichannel));
    colistats(i,2)                                                                         =
std(coliconversionfactor*100*rawdata(edge(i)+0.5*junkzone/sampletime:edge(i+1)-
0.5*junkzone/sampletime,colichannel));
    hvstats(i,1)                                                                           =
mean(voltageconversionfactor*rawdata(edge(i)+0.5*junkzone/sampletime:edge(i+1)-
0.5*junkzone/sampletime,voltagechannel));
    hvstats(i,2)                                                                           =
std(voltageconversionfactor*rawdata(edge(i)+0.5*junkzone/sampletime:edge(i+1)-
0.5*junkzone/sampletime,voltagechannel));
    hvstats(i,3)                                                                           =
max(size(voltageconversionfactor*rawdata(edge(i)+0.5*junkzone/sampletime:edge(i+1)-
0.5*junkzone/sampletime,voltagechannel)));
end
excel = [hvstats, hvistats, colistats];
```

Data Analysis Program

The process of transforming the electric current data from applied voltage to electrode distance, as seen in Section 8.4, is a complex one. First, the constant bulk charge density is used to transform the electric current flow into a mass flow rate. This then allows the selection of a range of fixed electric currents to be defined that represent fixed mass flow rates. Now the high voltage and collector electric current response to applied voltage is fitted using a fifth order polynomial. As fifth order polynomials are non-trivial to invert, for each distance the applied voltage required to give one of the fixed electric current values is found by scanning along the fifth order polynomial. This is done until a suitable value is found or the valid range of the polynomial is exceeded. If a valid value has been found then the fraction of charge lost is calculated for the associated applied voltage and electrode distance. This is stored and plotted.

```
myfitoptions = fitoptions('Method','NonlinearLeastSquares');                  %Use non-linear
least squares fitting method
%myfittype = fittype('a*x^b','coeff',{'a','b'},'options',myfitoptions);
myfittype      =      fittype('e*x^4      +      a*x^3      +      b*x^2      +      c*x      +
d','coeff',{'a','b','c','d','e'},'options',myfitoptions);  %Define fourth order polynomial fit
%fittype({'x','1'},'coefficients',{'m','c'},'options',myfitoptions);

varprefex = 'pvoh8pctsalt';   %Define Prefex for variables to be used
%isohvi = [0.75,1,1.5,2,3,4.5]';  %Define iso levels of HV current
isohvi = [0.3,0.5,0.75,1,1.5,2,3]';  %Define iso levels of HV current

figure          %Create new figure
hold on

clear excelmatrix isovolts isoloss excelmatrix2 hviploty        %Clear storage matrices
eval(sprintf('d = %sdistance(1,:);',varprefex));           % read in distance
eval(sprintf('inputvolts = %svoltage;',varprefex));         %read in the voltages


% 3rd order polynomial fit of the hv and collector data
% 1st set is HVi 2nd set is collector
for i = 1:max(size(d))
    subplot(5,2,i)
%    eval(sprintf('x = %shvi(:,i);',varprefex));
%    eval(sprintf('y = %svoltage(:,i);',varprefex));
    eval(sprintf('x = %svoltage(:,i);',varprefex));      %Read in voltage (i) for fitting x
axis
    eval(sprintf('y = %shvi(:,i);',varprefex));         % Read in hvi (i) for fitting
    eval(sprintf('y2 = %scoli(:,i);',varprefex));       % read in coli (i) for fitting
%    eval(sprintf('tmpvolt = %svoltage(i,1)'';',varprefex));

    %Perform Fit
    [myfi(i).cfun,gof(i),endoutput(i)] = fit(x,y,myfittype);
    [myfi2(i).cfun,gof2(i),endoutput2(i)] = fit(x,y2,myfittype);

    %Store data
    subfit(i).x = x;
    subfit(i).rawy = y;
    subfit(i).rawy2 = y2;
    subfit(i).fity = feval(myfi(i).cfun,x);  %Fit HV
    hviploty(i,:) = subfit(i).fity;
    subfit(i).fity2 = feval(myfi2(i).cfun,x);  %Fit col
    subfit(i).bounds = confint(myfi(i).cfun,0.95);
    excelmatrix(i,:) = [coeffvalues(myfi(i).cfun),gof(i).adjrsquare];
    hold on
    plot(x,subfit(i).fity)
    plot(x,y,'x')
    plot(x,subfit(i).fity2,'--r')
    plot(x,y2,'+r')
    xlabel('Voltage [kV]')
    ylabel('Observed Current [\muA]')
    title(sprintf('Distance %2.0fmm',d(i)))
    isovolts(:,i) = polyscan(myfi(i),isohvi);
    %isovolts(:,i) = nthroot((isohvi/excelmatrix(i,1)),excelmatrix(i,2));
    isoloss(:,i)                    =                    1-(feval(myfi(i).cfun,isovolts(:,i))-
feval(myfi2(i).cfun,isovolts(:,i)))./feval(myfi(i).cfun,isovolts(:,i));
end

%Plot fitted HV current against iso current lines
figure
subplot(3,2,1:4)
plot(inputvolts, hviploty')
hold on
for i = 1:max(size(isohvi))
    plot([5,22],[isohvi(i),isohvi(i)],'k')
end
xlabel('Voltage [kV]')
ylabel({'Observed High Voltage', 'Electric Current [\muA]'})
legend('50mm','60mm','70mm','80mm','90mm','100mm','110mm','120mm','130mm','Location','NorthWes
t')

%Plot short distance fitting
subplot(3,2,5)
i = int16(0.25*max(size(d)));
plot(subfit(i).x,subfit(i).fity,'b')
hold on
plot(subfit(i).x,subfit(i).rawy,'ob')
```

```
plot(subfit(i).x,subfit(i).fity2,'r')
plot(subfit(i).x,subfit(i).rawy2,'or')
ylim([0 10])
xlabel('Voltage [kV]')
ylabel('Observed Current [\muA]')
title(sprintf('Polynomial fit for distance %2.0fmm',d(i)))

%Plot long distance fitting example
subplot(3,2,6)
i = int16(0.75*max(size(d)));
plot(subfit(i).x,subfit(i).fity,'b')
hold on
plot(subfit(i).x,subfit(i).rawy,'ob')
plot(subfit(i).x,subfit(i).fity2,'r')
plot(subfit(i).x,subfit(i).rawy2,'or')
ylim([0 10])
xlabel('Voltage [kV]')
ylabel('Observed Current [\muA]')
title(sprintf('Polynomial fit for distance %2.0fmm',d(i)))

% Linear fit of the loss rate vs distance
myfitoptions = fitoptions('Method','NonlinearLeastSquares');
myfittype = fittype({'x','1'},'coefficients',{'m','c'},'options',myfitoptions);          %Fit
linear function
figure
isovolts = isovolts(:,1:9);
fitmn = 4;
fitmx = 9;
for i = 1:max(size(isohvi))
    subplot(4,2,i)
    eval(sprintf('x = %sdistance(i,1:9)'';',varprefex));
    limited = max(inputvolts(:,i));
    mydist = 0:10:140;
    sublinearfit(i).rawx = x;
    sublinearfit(i).rawy = isoloss(i,1:9)';
    y = isoloss(i,fitmn:fitmx)';
    x = x(fitmn:fitmx);
    [mylin(i).cfun,gof3(i),endoutput3(i)]                                                  =
fit(x(isovolts(i,fitmn:fitmx)'<limited),y(isovolts(i,fitmn:fitmx)'<limited),myfittype);
    sublinearfit(i).x = x(isovolts(i,fitmn:fitmx)'<limited);
    sublinearfit(i).fity = feval(mylin(i).cfun,mydist);
    sublinearfit(i).bounds = confint(mylin(i).cfun,0.95);
    sublinearfit(i).upfity                                                                 =
feval(myfittype,sublinearfit(i).bounds(1,1),sublinearfit(i).bounds(1,2),x);
    sublinearfit(i).lowfity                                                                =
feval(myfittype,sublinearfit(i).bounds(2,1),sublinearfit(i).bounds(2,2),x);
    hold on
    plot(sublinearfit(i).rawx,sublinearfit(i).rawy,'ob')
    plot(mydist,sublinearfit(i).fity,'-r')
    %plot(x,sublinearfit(i).upfity,'--r')
    %plot(x,sublinearfit(i).lowfity,'--r')
    xlabel('Distance [mm]','fontsize',12)
    ylabel({'Observed Current','Fraction lost in Flight'},'fontsize',12)
    title(sprintf('Constant Current %2.2fuA',isohvi(i)),'fontsize',12)
    ylim([0,1]);
    excelmatrix2(i,:) = [ coeffvalues(mylin(i).cfun),gof3(i).adjrsquare];
end

figure
subplot(3,2,1:4)
hold on
for i = 1:max(size(isohvi))
    lossploty(i,:) = sublinearfit(i).fity;
    plot(sublinearfit(i).rawx,sublinearfit(i).rawy,'ob')
end
xlabel('Distance [mm]')
ylabel({'Fraction of Electric Current','Observed at Collector Electrode'})
plot(mydist,lossploty)
ylim([0,1]);
xlim([40,140]);

subplot(3,2,5)
i = int16(0.25*max(size(isohvi)));
plot(sublinearfit(i).rawx,sublinearfit(i).rawy,'ob')
hold on
plot(mydist,sublinearfit(i).fity,'r')
title('Low constant flow rate')
```

```
xlabel('Distance [mm]')
ylabel({'Fraction of Electric Current','Observed at Collector Electrode'})
ylim([0,1]);
xlim([40,140]);

subplot(3,2,6)
i = int16(0.75*max(size(isohvi)));
plot(sublinearfit(i).rawx,sublinearfit(i).rawy,'ob')
hold on
plot(mydist,sublinearfit(i).fity,'r')
title('High constant flow rate')
xlabel('Distance [mm]')
ylabel({'Fraction of Electric Current','Observed at Collector Electrode'})
ylim([0,1]);
xlim([40,140]);
```

VII. Appendix B – Filter Design

The filter used to eliminate the noise on the data sampling channels as seen in Chapter 4 was a simple passive low pass filter. The circuit diagram is given below along with a diagram showing the calculated attenuation for high frequency signals through the filter. For this work a resistor value of 15 kΩ and a capacitor value of 10 nF was selected.

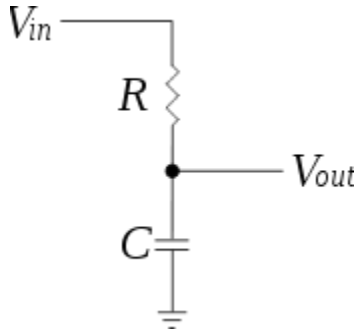

Circuit diagram for passive low pass filter

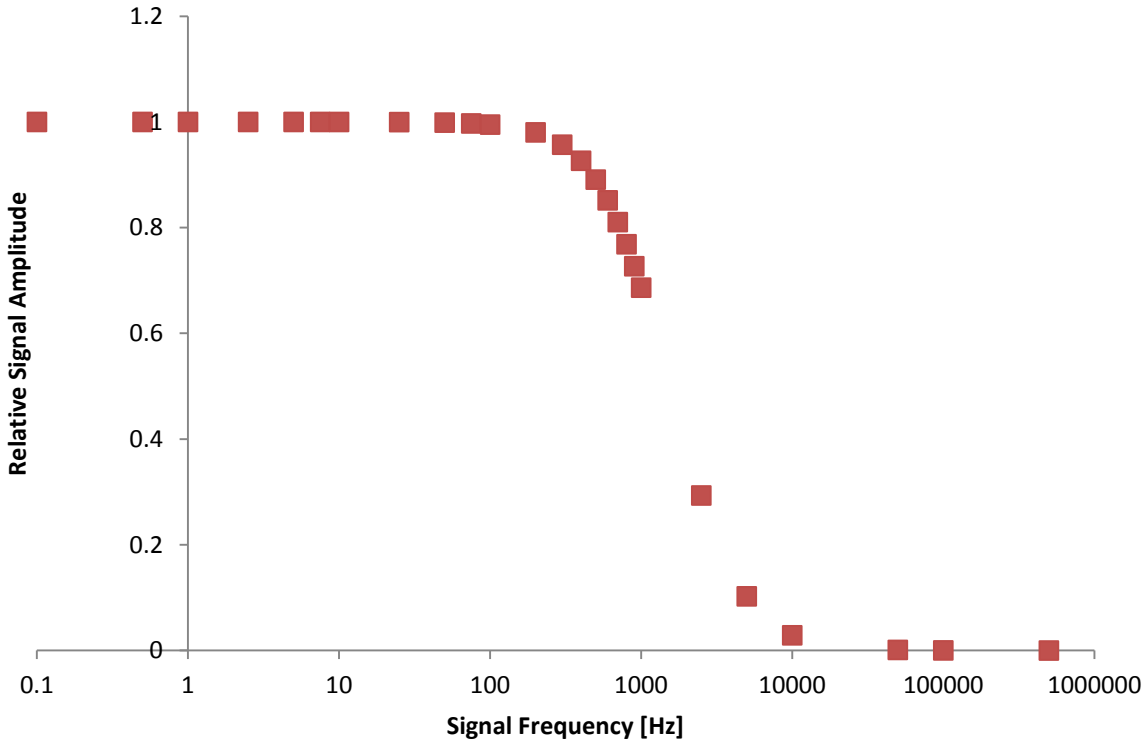

Theoretical attenuation of high frequency signals passing through the passive low pass filter.